

# **ACOUSTIC TRANSDUCTION – MATERIALS AND DEVICES**

**Period 1 January 1999 to 31 December 1999**

**Annual Report**

**VOLUME V**

**OFFICE OF NAVAL RESEARCH  
Contract No: N00014-96-1-1173**

**APPROVED FOR PUBLIC RELEASE –  
DISTRIBUTION UNLIMITED**

**Reproduction in whole or in part is permitted for any  
purpose of the United States Government**

**Kenji Uchino**

**20000815 042**

**PENNSSTATE**



**THE MATERIALS RESEARCH LABORATORY  
UNIVERSITY PARK, PA**

**DTIC QUALITY INSPECTED 4**

# REPORT DOCUMENTATION PAGE

Form Approved  
OMB No. 0704-0188

Public reporting burden for this collection of information is estimated to average 1 hour per response, including the time for reviewing instructions, searching existing data sources, gathering and maintaining the data needed, and completing and reviewing the collection of information. Send comments regarding this burden estimate or any other aspect of this collection of information, including suggestions for reducing this burden, to Washington Headquarters Services, Directorate for Information Operations and Reports, 1215 Jefferson Davis Highway, Suite 1204, Arlington, VA 22202-4302, and to the Office of Management and Budget, Paperwork Reduction Project (0704-0188), Washington, DC 20503.

1. AGENCY USE ONLY (Leave blank)		2. REPORT DATE 06/12/2000	3. REPORT TYPE AND DATES COVERED ANNUAL REPORT 01/01/2000-12/31/2000	
4. TITLE AND SUBTITLE  ACOUSTIC TRANSDUCTION -- MATERIALS AND DEVICES			5. FUNDING NUMBERS  ONR CONTRACT NO. N00014-96-1-11173	
6. AUTHOR(S)  KENJI UCHINO				
7. PERFORMING ORGANIZATION NAME(S) AND ADDRESS(ES)  Materials Research Laboratory The Pennsylvania State University University Park, PA 16802			8. PERFORMING ORGANIZATION REPORT NUMBER	
9. SPONSORING/MONITORING AGENCY NAME(S) AND ADDRESS(ES) Office of Naval Research    Office of Naval Research ONR 321SS                      Regional Office Chicago Ballston Centre Tower One 536 S Clark Str., RM 208 800 N Quincy Street        Chicago IL 60605-1588 Arlington VA 22217-5660			10. SPONSORING/MONITORING AGENCY REPORT NUMBER	
11. SUPPLEMENTARY NOTES				
12a. DISTRIBUTION / AVAILABILITY STATEMENT			12b. DISTRIBUTION CODE	
13. ABSTRACT (Maximum 200 words)  SEE FOLLOWING PAGE				
14. SUBJECT TERMS			15. NUMBER OF PAGES	
			16. PRICE CODE	
17. SECURITY CLASSIFICATION OF REPORT UNCLASSIFIED	18. SECURITY CLASSIFICATION OF THIS PAGE UNCLASSIFIED	19. SECURITY CLASSIFICATION OF ABSTRACT UNCLASSIFIED	20. LIMITATION OF ABSTRACT	

## GENERAL INSTRUCTIONS FOR COMPLETING SF 298

The Report Documentation Page (RDP) is used in announcing and cataloging reports. It is important that this information be consistent with the rest of the report, particularly the cover and title page. Instructions for filling in each block of the form follow. It is important to *stay within the lines* to meet optical scanning requirements.

**Block 1. Agency Use Only (Leave blank).**

**Block 2. Report Date.** Full publication date including day, month, and year, if available (e.g. 1 Jan 88). Must cite at least the year.

**Block 3. Type of Report and Dates Covered.** State whether report is interim, final, etc. If applicable, enter inclusive report dates (e.g. 10 Jun 87 - 30 Jun 88).

**Block 4. Title and Subtitle.** A title is taken from the part of the report that provides the most meaningful and complete information. When a report is prepared in more than one volume, repeat the primary title, add volume number, and include subtitle for the specific volume. On classified documents enter the title classification in parentheses.

**Block 5. Funding Numbers.** To include contract and grant numbers; may include program element number(s), project number(s), task number(s), and work unit number(s). Use the following labels:

C - Contract	PR - Project
G - Grant	TA - Task
PE - Program Element	WU - Work Unit Accession No.

**Block 6. Author(s).** Name(s) of person(s) responsible for writing the report, performing the research, or credited with the content of the report. If editor or compiler, this should follow the name(s).

**Block 7. Performing Organization Name(s) and Address(es).** Self-explanatory.

**Block 8. Performing Organization Report Number.** Enter the unique alphanumeric report number(s) assigned by the organization performing the report.

**Block 9. Sponsoring/Monitoring Agency Name(s) and Address(es).** Self-explanatory.

**Block 10. Sponsoring/Monitoring Agency Report Number.** (If known)

**Block 11. Supplementary Notes.** Enter information not included elsewhere such as: Prepared in cooperation with...; Trans. of...; To be published in... When a report is revised, include a statement whether the new report supersedes or supplements the older report.

**Block 12a. Distribution/Availability Statement.** Denotes public availability or limitations. Cite any availability to the public. Enter additional limitations or special markings in all capitals (e.g. NOFORN, REL, ITAR).

DOD - See DoDD 5230.24, "Distribution Statements on Technical Documents."

DOE - See authorities.

NASA - See Handbook NHB 2200.2.

NTIS - Leave blank.

**Block 12b. Distribution Code.**

DOD - Leave blank.

DOE - Enter DOE distribution categories from the Standard Distribution for Unclassified Scientific and Technical Reports.

NASA - Leave blank.

NTIS - Leave blank.

**Block 13. Abstract.** Include a brief (*Maximum 200 words*) factual summary of the most significant information contained in the report.

**Block 14. Subject Terms.** Keywords or phrases identifying major subjects in the report.

**Block 15. Number of Pages.** Enter the total number of pages.

**Block 16. Price Code.** Enter appropriate price code (*NTIS only*).

**Blocks 17. - 19. Security Classifications.** Self-explanatory. Enter U.S. Security Classification in accordance with U.S. Security Regulations (i.e., UNCLASSIFIED). If form contains classified information, stamp classification on the top and bottom of the page.

**Block 20. Limitation of Abstract.** This block must be completed to assign a limitation to the abstract. Enter either UL (unlimited) or SAR (same as report). An entry in this block is necessary if the abstract is to be limited. If blank, the abstract is assumed to be unlimited.

## ABSTRACT

This report describes the research performed over the period of 1 January 1999 to 31 December 1999 on a MURI under Office of Naval Research contract N00014-96-1-1173 on the topic "Acoustic Transduction: Materials and Devices" brings together work from the Materials Research Laboratory (MRL), the Applied Research Laboratory (ARL), and the Center for Acoustics and Vibrations (CAV) at The Pennsylvania State University. As has become customary over many years research on the program is described in detail in the 87 technical appendices to this report and only a brief narrative description connecting this research is given in the text.

Perhaps the most outstanding accomplishment of the year is a "spin on" from our earlier single crystal studies now involving Brookhaven National Laboratory and Professor Gonzalo's group in Madrid, Spain. Using exceptionally homogeneous polycrystal lead zirconate titanate samples prepared in MRL, precise synchrotron x-ray analysis has confirmed a new monoclinic phase at lower temperature in composition close to the important morphotropic phase boundary. This work demands a re-thinking of both intrinsic and extrinsic contributions to response in this most important practical transducer material family. Domain Engineering/Domain Averaging in lead zinc niobate:lead titanate (PZN:PT) in lead magnesium niobate:lead titanate (PMN:PT) and in barium titanate ( $\text{BaTiO}_3$ ) continues to offer single crystal systems with outstanding transducer and actuator properties and new insights into the field induced strain mechanisms in all perovskite type piezoelectrics. Excellent progress with the new high strain irradiated P(VDF:TrFE) relaxor ferroelectric copolymer system has helped catalyze a new DARPA initiative in this area and a re-awakening of interest in the whole area of electrostrictive polymer systems.

A primary objective of this MURI grouping was to help shorten the time constant for new materials and device concepts to be applied in practical Navy Systems. We believe this has now been realized in joint work on the composite cymbal type flexensional arrays for large area projectors, and in the progress made towards a micro-tonpils array system.

Original work on new step and repeat piezoelectric high strain systems continues to make good progress now using commercial motion rectifiers to produce both linear and rotary systems with high torque capability. New composite designs are pushing toward 1 mm diameter motors in the size regimen where there are real difficulties for conventional electromagnetic designs.

A new area of activity this year is in piezoelectric transformers where a circular symmetry design in conjunction with controlled inhomogeneous poling is shown to offer capabilities which are of real interest for energy recovery actuator power systems. Basic studies have evolved a new environmental SEM technique for high resolution domain wall studies without changing problems. Work is continuing on reliable measurements of electrostrictive constants in simple solids confirming by both direct and converse methods and permitting the first generalization of trends in these fundamentally important coupling constants.



# **ACOUSTIC TRANSDUCTION – MATERIALS AND DEVICES**

**Period 1 January 1999 to 31 December 1999**

**Annual Report**

**VOLUME V**

**OFFICE OF NAVAL RESEARCH  
Contract No: N00014-96-1-1173**

**APPROVED FOR PUBLIC RELEASE –  
DISTRIBUTION UNLIMITED**

**Reproduction in whole or in part is permitted for any  
purpose of the United States Government**

**Kenji Uchino**

## APPENDICES

### VOLUME I

#### GENERAL SUMMARY PAPERS

1. Cross, L.E., "Newnham Festschrift Introduction." Guest Editorial, Mat. Res. Innovations **2**, 251 (1999).
2. Newnham, R.E., "Ceramics into the Next Millennium," *British Ceramic Transactions* **98**(5), 251-255 (1999).
3. Uchino, K. and S. Takahashi, "New Trend in Multilayer Ceramic Actuators," Proc. Int'l Symp. Dielectric Ceramics, Amer. Ceram. Soc. '98; Ceramic Trans., Vol. 100, Dielectric Ceramic Materials, p.455 - 468 (1999).
4. Uchino, K., "Smart Composite Materials," Chap.5.19, Comprehensive Composite Materials, Elsevier Science, Oxford, UK (2000). [in press]
5. Kelly, A., R. Davidson, and K. Uchino "Smart Composite Materials Systems," Chap.5.20, Comprehensive Composite Materials, Elsevier Science, Oxford, UK (2000). [in press]
6. Fousek, J., L.E. Cross, and D.B. Litvin, "Possible Piezoelectric Composites Based on the Flexoelectric Effect." Materials Letters **39**, 287-291 (1999).

#### 2.0 MATERIALS STUDIES

##### 2.1 Polycrystal Perovskite Ceramics

7. Noheda, B., D.E. Cox, G. Shirane, J.A. Gonzalo, L.E. Cross, and S.-E. Park, "A Monoclinic Ferroelectric Phase in the  $\text{Pb}(\text{Zr}_{1-x}\text{Ti}_x)\text{O}_3$  Solid Solution." Applied Physics Letters **74**(14), 2059-2061 (1999).
8. Noheda, B., J.A. Gonzalo, R. Guo, S.-E. Park, L.E. Cross, D.E. Cox, and G. Shirane, "The monoclinic phase in PZT: new light on morphotropic phase boundaries," Proceedings of the Workshop on Fundamental Physical of Ferroelectrics, Aspen, CO (February 2000).
9. Noheda, B., J.A. Gonzalo, L.E. Cross, R. Guo, S.-E. Park, D.E. Cox, and G. Shirane, "Tetragonal-to-monoclinic phase transition in a ferroelectric perovskite: The structure of  $\text{PbZr}_{0.52}\text{Ti}_{0.48}\text{O}_3$ ," *Physical Review B* **61**(13), 8687 (April 2000).
10. Guo, R., L.E. Cross, S.-E. Park, B. Noheda, D.E. Cox, and G. Shirane, "Origin of the high piezoelectric response in  $\text{PbZr}_{1-x}\text{Ti}_x\text{O}_3$ ," *Physical Review Letters* **84**(23) (June 2000).
11. Zhang, Q.M., "Electromechanical Properties of Lead Zirconate Titanate Piezoceramics Under the Influence of Mechanical Stresses," IEEE Transactions on Ultrasonics, Ferroelectrics, and Frequency Control **46**(6) (November 1999).
12. Wang, H., W. Jiang, and W. Cao, "Characterization of Lead Zirconate Titanate Piezoceramic Using High Frequency Ultrasonic Spectroscopy," J. Appl. Phys. **85**, 8083-8091 (1999).
13. Zhao, J., V. Mueller, and Q.M. Zhang, "The Influence of External Stress on the Electromechanical Response of Electrostrictive 0.9PMN-0.1PT in the DC Field Biased State," J. Mater. Res. **14**, 948-956 (1999).

## 2.0 MATERIALS STUDIES

### 2.1 *Polycrystal Perovskite Ceramics (continued)*

14. Zhao, J., A.E. Glazounov, and Q.M. Zhang, "Change in Electromechanical Properties of 0.9PMN-0.1PT Relaxor Ferroelectric Induced by Uniaxial Compressive Stress Directed Perpendicular to the Electric Field," *Appl. Phys. Lett.* **74**, 436-438 (1999).
15. Albert, E.F., A.S. Bhalla, and T. Takenaka, "Large Hydrostatic Piezoelectric Constant and Temperature Dependence of the Piezoelectric Properties  $\text{Bi}(\text{Ni}_{1/2}\text{Ti}_{1/2})\text{O}_3\text{:PbTiO}_3$  Ceramics," *Ferroelectrics Letters* **25**, 45-52 (1999).
16. Alberta, E.F. and A.S. Bhalla, "Investigation of the Lead Indium Niobate-Lead Magnesium Niobate Solid Solution," *Materials Letters* **40**, 114-117 (1999).
17. Alberta, E.F. and A.S. Bhalla, "Electrical Properties of the Morphotropic Phase Boundary in  $\text{Pb}(\text{In}_{1/2}\text{Ta}_{1/2})\text{O}_3\text{-PbTiO}_3$  Ceramics," *Ferroelectrics Letters* **26**, 117-123 (1999).
18. Kim, J.S., S.J. Kim, H.G. Kim, D.C. Lee, and K. Uchino, "Piezoelectric and Dielectric Properties of  $\text{Fe}_2\text{O}_3$ -Doped  $0.57\text{Pb}(\text{Sc}_{1/2}\text{Nb}_{1/2})\text{O}_3\text{-}0.43\text{PbTiO}_3$  Ceramic Materials," *Jpn. J. Appl. Phys.* **38**(Part 1, No. 3A), 1433-1437 (1999).

## VOLUME II

19. Liu, S.F., I.R. Abothu, S. Komarneni, P. Poosanaas, D.S. Paik, Y. Ito, and K. Uchino, "PLZT Ceramics Prepared from Conventional and Microwave Hydrothermal Powders," *Ferroelectrics* **231**, 179-185 (1999).
20. Chen, Y. H., S. Hirose, D. Viehland, S. Takahashi, and K. Uchino, "Mn-Modified  $\text{Pb}(\text{Mg}_{1/3}\text{Nb}_{2/3})\text{O}_3\text{-PbTiO}_3$  Ceramics: Improved Mechanical Quality Factors for High Power Transduction Applications," *Jpn. J. Appl. Phys.* (1999). [accepted].
21. Chen, Y.H., S. Hirose, D. Viehland, and K. Uchino, "Doping Effects in  $\text{Pb}(\text{Mg}_{1/3}\text{Nb}_{2/3})\text{O}_3\text{-PbTiO}_3$  Ceramics for High Power Transduction Applications," *Mater. Res. Soc. Fall Mtg. '99*, LL.5.9, Boston (Nov. 29-Dec.3, 1999).
22. Du, X.H., Q.M. Wang, U. Belegundu, and K. Uchino, "Piezoelectric Property Enhancement in Polycrystalline Lead Zirconate Titanate by Changing Cutting Angle," *J. Ceram. Soc. Jpn.* **107**(2), 190-191 (1999).

### 2.2 *Single Crystal Systems*

23. Wada, S., S.E. Park, L.E. Cross, and T.R. Shrout, "Engineered Domain Configuration in Rhombohedral PZN-PT Single Crystals and their Ferroelectric Related Properties," *Ferroelectrics* **221**, 147-155 (1999).
24. Liu, S.-F., S.E. Park, T.R. Shrout, and L.E. Cross. "Electric Field Dependence of Piezoelectric Properties for Rhombohedral  $0.955\text{Pb}(\text{Zn}_{1/3}\text{Nb}_{2/3})\text{O}_3\text{-}0.045\text{PbTiO}_3$  Single Crystals," *Journal of Applied Physics* **85** (5), 2810-2814 (1999).
25. Erhart, J. and W. Cao, "Effective Material Properties in Twinned Ferroelectric Crystals," *J. Appl. Phys.* **86**, 1073- 1081 (1999).

## 2.0 MATERIALS STUDIES

### 2.2 *Single Crystal Systems (continued)*

26. Yin, J., B. Jiang, and W. Cao, "Elastic, Piezoelectric and Dielectric Properties of  $0.955\text{Pb}(\text{Zn}_{1/3}\text{Nb}_{2/3})\text{O}_3$ - $0.045\text{PbTiO}_3$  Single Crystal with Designed Multidomains," IEEE Transactions UFFC **47**, 285-291 (2000).
27. Wada, S., S.E. Park, L.E. Cross, and T.R. Shrout, "Defect-induced Domain Configuratrion in Relaxor PZN Single Crystal and Its Origin." Trans. of the Mat. Res. Soc. Of Japan **24**(1), 19-22 (1999).
28. Belegundu, U., X. Du, and K. Uchino, "Switching Current In  $\text{Pb}(\text{Zn}_{1/3}\text{Nb}_{2/3})\text{O}_3$ - $\text{PbTiO}_3$  Single Crystals, MRS Meeting, Boston (November 1999).
29. Park, S.-E., S. Wada, L.E. Cross, and T.R. Shrout, "Crystallographically Engineered  $\text{BaTiO}_3$  Single Crystals for High-Performance Piezoelectrics." Journal of Applied Physics **86**(5), 2746-2750 (1999).
30. Du, X.H., Q.M. Wang, U. Belegundu, A. Bhalla, and K. Uchino, "Crystal Orientation Dependence of Piezoelectric Properties of Single Crystal Barium Titanate," Mater. Lett. **40**, 109-113 (1999).
31. Lu, .Y., Z.-Y. Cheng, E. Park, S.F. Liu and Q.M. Zhang, "Linear Electro-optic Effect of  $0.88\text{Pb}(\text{Zn}_{1/3}\text{Nb}_{2/3})$ - $0.12\text{PbTiO}_3$  Single Crystal," Jpn. J. Appl. Phys. **39**, 141-145 (2000).

### 2.3 *High Strain Polymers*

32. Bharti, V., H.S. Xu, G. Shanthi, Q.M. Zhang, and K. Liang, "Polarization and Structural Properties of High Energy Electron Irradiated P(VDF-TrFE) Copolymer Films," J. Appl. Phys. **87**, 452-461 (2000).
33. Cheng, Z.-Y., T.-B. Xu, V. Bharti, S. Wang, and Q.M. Zhang, "Transverse Strain Response in the Electrostrictive P(VDF-TrFE) Copolymer," Appl. Phys. Lett. **74**, 1901-1903 (1999).
34. Cheng, Z.-Y., V. Bharti, T.B. Xu, S. Wang, Q.M. Zhang, T. Ramotowski, F. Tito, and R. Ting, "Transverse Strain Responses in Electrostrictive P(VDF-TrFE) Films and Development of a Dilatometer for the Measurement," J. Appl. Phys. **86**, 2208-2214 (1999).
35. Bharti, V., Z-Y Cheng, S. Gross, T.B. Xu, and Q.M. Zhang, "High Electrostrictive Strain under High Mechanical Stress in High Energy Electron Irradiated Poly(vinylidene fluoride-trifluoroethylene) Copolymer Films," Appl. Phys. Lett. **75**, 2653-2655 (1999).

## 3.0 TRANSDUCER STUDIES

### 3.1 *Composite Structures*

36. Geng, X. and Q.M. Zhang, "Resonance Modes and Losses in 1-3 Composites for Ultrasonic Transducer Applications," J. Appl. Phys. **85**, 1342-1350 (1999).
37. Tressler, J. and K. Uchino, "Piezoelectric Composite Sensors," Chap.5.25, Comprehensive Composite Materials, Elsevier Science, Oxford, UK (2000). [in press]
38. Tressler, J.F., S. Alkoy, A. Dogan, and R.E. Newnham, "Functional Composites for Sensors, Actuators and Transducers," Composites Part A: Applied Science & Manufacturing **30**, 477-482 (1999).

3.0 TRANSDUCER STUDIES

3.1 *Composite Structures (continued)*

39. Tressler, J.F. and R.E. Newnham, "Capped Ceramic Underwater Sound Projector: The "Cymbal" Transducer," J. of Acoustical Soc. America **105**(2), part 1, 591-600 (1999).

**VOLUME III**

40. Zhang, J., W.J. Hughes, P. Bouchilloux, R. Meyer Jr., K. Uchino, and R.E. Newnham, "A Class V Flexensional Transducer: The Cymbal," Ultrasonics **37**, 387-393 (1999).

41. Zhang, J., W.J. Hughes, R.J. Meyer Jr., K. Uchino, and R.E. Newnham, "Cymbal Array: A Broad Band Sound Projector," Ultrasonics **37**, 523-529 (2000).

3.0 TRANSDUCER STUDIES

3.1 *Composite Structures (continued)*

42. Zhang, J., W.J. Hughes, A.C. Hladky-Hennion and R.E. Newnham, "Concave Cymbal Transducers," Materials Research Innovations **2** (5), 252-255 (1999).

43. Alkoy, S., R.E. Newnham, A.C. Hladky, A. Dogan, and J.K. Cochran, Jr., "Piezoelectric Hollow Spheres for Microprobe Hydrophones," Ferroelectrics **226**, 11-25 (1999).

44. Carlson, W.B., R.E. Newnham and D.P. Williams, "Piezotensegritic Structures for Transducer Applications," Materials Research Innovations **3**, 175-178 (1999).

45. Newnham, R.E. and A. Amin, "Smart Systems: Microphones, Fish Farming, and Beyond," Chemtech **29**(12), 38-47 (1999).

3.2 *3-Dimensional Acoustic Intensity Probes*

46. Bastyr, K.J., G.C. Lauchle, and J.A. McConnell, "Development of a Velocity Gradient Underwater Acoustic Intensity Sensor," J. Acoust. Soc. Am. **106**, 3178-3188 (1999).

47. Lauchle, G.C. and W.A. Kargus, IV, "Scaling of Turbulent Wall Pressure Fluctuations Downstream of a Rearward Facing Step," J. Acoust. Soc. Am. **107**, L1-L6 (2000).

3.3 *Piezoelectric Transformers*

48. Koc, B., S. Alkoy, and K. Uchino, "A Circular Piezoelectric Transformer with Crescent Shape Input Electrodes," Proc. IEEE Ultrasonic Symp., Lake Tahoe, Nevada, Oct. 17-21 (1999).

49. Koc, B. and K. Uchino, "Disk Type Piezoelectric Transformer with Crescent Shape Input Electrodes," Proc. NATO- Advanced Research Workshop: Piezoelectric Materials, Advance in Science, Technology and Applications, Predeal, Romania (May 24-27, 1999).

#### 4.0 ACTUATOR STUDIES

##### 4.1 *Materials and Designs*

- 50. Uchino, K., "Recent Trend of Piezoelectric Actuator Developments," Proc. Int'l Symp. Micromechatronics and Human Science '99, p.3-9, Nagoya, Japan (Nov. 23-26, 1999).
- 51. Yao, K., W. Zhu, K. Uchino, Z. Zhang and L.C. Lim, "Design and Fabrication of a High Performance Multilayer Piezoelectric Actuator with Bending Deformation," **46** (4), 1020-1027 (1999).
- 52. Wang, Q.-M., X.-H. Du, B. Xu, and L.E. Cross, "Electromechanical Coupling and Output Efficiency of Piezoelectric Bending Actuators." IEEE Transactions on Ultrasonics, Ferroelectrics, and Frequency Control **46** (3), 638-646 (1999).
- 53. Wang, Q.-M. and L.E. Cross, "Analysis of High Temperature Reduction Processing of RAINBOW Actuator." Materials Chemistry and Physics **58**, 20-25 (1999).
- 54. Glazounov, A.E., Q.M. Zhang, and C. Kim, "Torsional Actuator Based on Mechanically Amplified Shear Piezoelectric Response," Sensors and Actuators A **79**, 22-30 (2000).
- 55. Yoo, J.-H., J.-I Hong, and W. Cao, "Piezoelectric Ceramic Bimorph Coupled to Thin Metal Plate as Cooling Fan for Electronic Devices," Sensors and Actuators **79**, 8-12 (1999).

##### 4.2 *Photostriction*

- 56. Poosanaas, P., K. Tonooka and K. Uchino, "Photostrictive Actuators," J. Mechatronics (1999) [in press].
- 57. Poosanaas, P. and K. Uchino, "Photostrictive Effect in Lanthanum-Modified Lead Zirconate Titanate Ceramics near the Morphotropic Phase Boundary," J. Mater. Chem. and Phys. **61**, 36-41 (1999).

### VOLUME IV

##### 4.3 *High Force Torsional Actuators*

- 58. Frank, J.E., G.H. Koopmann, W. Chen, and G.A. Lesieutre, "Design and Performance of a High Force Piezoelectric Inchworm Actuator," Proceedings of SPIE 6<sup>th</sup> Annual International Symposium on Smart Structures and Materials, 1999.
- 59. Koopmann, G.H., G.A. Lesieutre, J. Frank, and W. Chen, "Design and Performance of a Linear Piezoelectric Wedgeworm Actuator," Piezoelectric Materials: Advances in Science, Technology and Applications, 383-390 (2000).
- 60. Frank, J. E.M. Mockensturm, W. Chen, G.H. Koopmann, and G.A. Lesieutre, "Roller-Wedgeworm: A Piezoelectrically-Driven Rotary Motor," 10<sup>th</sup> International Conference on Adaptive Structures and Technologies, Paris (October 1999).

#### 4.4 Piezoelectric Mini Motors

61. Glazounov, A.E., S. Wang, Q.M. Zhang, and C. Kim, "High Efficiency Piezoelectric Motor Combining Continuous Rotation with Precise Control Over Angular Positioning," *Appl. Phys. Lett.* **75**, 862-864 (1999).
62. Uchino, K. and B. Koc, "Compact Piezoelectric Ultrasonic Motors," *Ferroelectrics* **230**, 73-86 (1999).
63. Kim, J.S., M.J. Park, and K. Uchino, "Composite Ultrasonic Motors Using a Piezoelectric Disk and an Elastic Body of "Windmill" Type," *Ferroelectrics* **232**, 185-190 (1999).
64. Koc, B., P. Bouchilloux, and K. Uchino, "Piezoelectric Micromotor Using A Metal-Ceramic Composite Structure," *IEEE Trans. Ultrasonic, Ferroelectrics, and Frequency Control* (1999).

#### 5.0 MODELING and CHARACTERIZATION

##### 5.1 Simulation

65. Cao, W., S. Tavener, and S. Xie, "Simulation of Boundary Condition Influence in a Second-Order Ferroelectric Phase Transition," *J. Appl. Phys.* **86**, 5739-5746 (1999).
66. Shen, M. and W. Cao, "Acoustic Band-Gap Engineering Using Finite Size Layered Structures of Multiple Periodicity," *Appl. Phys. Lett.* **75**, 3713-3715 (1999).
67. Uchino, K., and H. Aburatani, "Field Induced Acoustic Emission in Ferroelectric Ceramics," *Proc. 101st Annual Mtg. of Amer. Ceram. Soc., Symp. Dielectric Materials and Devices*, SE-56, Indianapolis, April 25 - 28 (1999). [accepted]
68. Uchino, K., J. Zheng, Y.H. Chen, X. Du, S. Hirose, and S. Takahashi, "Loss Mechanisms in Piezoelectrics—Extrinsic and Intrinsic Losses." *Mater. Res. Soc. Fall Mtg. '99, LL.1.6*, Boston, Nov. 29-Dec.3 (1999).
69. Uchino, K. and S. Hirose, "Loss Mechanisms in Piezoelectrics," submitted to *IEEE UFFC Transactions* (1999).

#### VOLUME V

70. Uchino, K., J. Zheng, Y.H. Chen, X. Du, and S. Hirose, "Loss Mechanisms in Piezoelectrics," *Mater. Res. Soc. Fall Mtg. '99*, Boston (Nov. 29-Dec.3, 1999).

##### 5.2 Thin and Thick Films

71. Abothu, I.R., Y. Ito, P. Poosanaas, S. Kalpat, S. Komarneni, and K. Uchino, "Sol-Gel Processing of Piezoelectric Thin Films," *Ferroelectrics* **232**, 191-195 (1999).
72. Kalpat, S., I.R. Abothu, A. Akiba, H. Goto, S. Trolrier-McKinstry, and K. Uchino, "Dielectric and Piezoelectric Property Dependence on Highly Textured (100), (111) and Random Thin Films Grown by RF Sputtering," *Symp. LL Proc., Mater. Res. Soc. Fall Mtg. '99, LL.1.3*, Boston, Nov. 29-Dec.3 (1999).
73. Xu, F., F. Chu, and S. Trolrier-McKinstry, "Longitudinal Piezoelectric Coefficient Measurement for Bulk Ceramics and Thin Films Using Pneumatic Pressure Rig," *J. Appl. Phys.* **86** (1) 588 -594 (1999).



## 5.0 MODELING and CHARACTERIZATION

### 5.2 *Thin and Thick Films (continued)*

- 74. Shepard, J. F., Jr., F. Chu, I. Kanno, and S. Trolier-McKinstry, "Characterization and Aging Response of the  $d_{31}$  Piezoelectric Coefficient of Lead Zirconate Titanate Thin Films," J. Appl. Phys. **85**(9), 6711-6716 (1999).
- 75. Xu, B., Y. Ye, L.E. Cross, J.J. Bernstein, and R. Miller, "Dielectric Hysteresis from Transverse Electric Fields in Lead Zirconate Titanate Thin Films." Applied Physics Letters **74** (23), 3549-3551 (1999).
- 76. Xu, B., R.G. Polcawich, S. Trolier-McKinstry, Y. Ye, L.E. Cross, J.J. Bernstein, and R. Miller, "Sensing Characteristics of In-Plane Polarized Lead Zirconate Titanate Thin Films," Applied Physics Letter **75** (26), 4180 (December 1999).
- 77. Xu, B., L.E. Cross, and D. Ravichandran, "Synthesis of Lead Zirconate Titanate Stannate Antiferroelectric Thick Films by Sol-Gel Processing." J. Am. Ceramic Soc. **82** (2), 306-312 (1999).
- 78. Xu, B., Y. Ye, Q.-M. Wang, and L.E. Cross, "Dependence of Electrical Properties on Film Thickness in Lanthanum-Doped Lead Zirconate Titanate Stannate Antiferroelectric Thin Films." Journal of Applied Physics **85** (7), 3753-3758 (1999).

### 5.3 *Domain Studies*

- 79. Belegundu, U., X.H. Du, A. Bhalla, and K. Uchino, "Effect of Electric Field on Domain Formation in Relaxor Based  $\text{Pb}(\text{Zn}_{1/3}\text{Nb}_{2/3})\text{O}_3\text{-PbTiO}_3$  Single Crystals," Ferroelectrics Letters **26** (5-6), 107-116 (1999).
- 80. Belegundu, U., X.H. Du, L.E. Cross and K. Uchino, "In Situ Observation of Domains in  $0.9\text{Pb}(\text{Zn}_{1/3}\text{Nb}_{2/3})\text{O}_3\text{-}0.1\text{PbTiO}_3$  Single Crystals," Ferroelectrics **221**, 67-71 (1999). (First Author Supervised by Candidate).
- 81. Hatch, D.M. and W. Cao, "Determination of Domain and Domain Wall Formation at Ferroic Transitions," Ferroelectrics **222**, 1-10 (1999).
- 82. Cao, W. and S.N. Zhu, "Observation of Ferroelectric Domains in  $\text{LiTaO}_3$ ," Ferroelectrics **226**, 27-35 (1999).
- 83. Zhu, S.N. and W. Cao, "Imaging of 180 Ferroelectric Domains in  $\text{LiTaO}_3$  by Scanning Electron Microscopy," Phys. Stat. Sol. (a) **173**, 495-502 (1999).
- 84. Mueller, V., H. Beige, and Q.M. Zhang, "Nonlinear Ferroelectric Domain Wall Response," Ferroelectrics **222**, 295-302 (1999).
- 85. Liu, R., R. Guo, A.S. Bhalla, L.E. Cross, M. Levy, and R.M. Osgood Jr., "Optical Observation of Dynamic Ferroelectric Phase Transition and Static Domain Structures in Crystal Ion Sliced (CIS)  $\text{LiNbO}_3$  Film." Materials Letters **39**, 264-267 (1999).

### 5.4 *Electrostriction*

- 86. Eury, S., R. Yimnirun, V. Sundar, P.J. Moses, S.J. Jang, and R.E. Newnham, "Converse Electrostriction in Polymers and Composites," Mat. Chem. and Phys. **61**, 18-23 (1999).
- 87. Yimnirun, R., S.M.-L. Eury, V. Sundar, P.J. Moses, S. Jang, and R.E. Newnham, "Electrostriction Measurement on Low Permittivity Dielectric Materials," Journal of European Ceramics Society **19**, 1269-1273 (1999).

# **MODELING and CHARACTERIZATION**

***(continued)***

# **APPENDIX 70**

## LOSS MECHANISMS IN PIEZOELECTRICS AND RESONANCE/ANTIRESONANCE

Kenji Uchino, Jiehui Zheng, Yun-Han Chen and Xiaohong Du  
International Center for Actuators and Transducers  
Materials Research Laboratory, The Pennsylvania State University  
University Park, Pa 16802

Seiji Hirose  
Faculty of Engineering, Yamagata University, Yonezawa 992, Japan

### ABSTRACT

Losses in piezoelectrics are considered in general to have three different mechanisms; dielectric, mechanical and piezoelectric losses. This paper deals with the phenomenology of losses, first, then how to measure these losses separately in experiments. We found that heat generation is caused mainly by dielectric loss  $\tan \delta'$  (i. e. P-E hysteresis loss), not by mechanical loss, and that a dramatical decrease in mechanical  $Q_m$  with an increase of vibration level was observed in resonant piezoelectric ceramic devices, which is due to an increase in the intrinsic dielectric loss, not in the intrinsic mechanical loss. Finally, we propose the usage of the antiresonance mode rather than the conventional resonance mode, particularly for high power applications, since the mechanical quality factor  $Q_B$  at an antiresonance frequency is larger than  $Q_A$  at a resonance frequency.

### INTRODUCTION

Loss or hysteresis in piezoelectrics exhibits both merits and demerits. For positioning actuator applications, hysteresis in the field-induced strain provides a serious problem, and for resonance actuation such as ultrasonic motors, loss generates significant heat in the piezoelectric materials. Further, in consideration of the resonant strain amplified in proportion to a mechanical quality factor, low (extrinsic) mechanical loss materials are preferred for ultrasonic motors. On the contrary, for force sensors and acoustic transducers, high mechanical loss, which corresponds to a low mechanical quality factor  $Q_m$ , is essential to widen a frequency range for receiving signals.

However, not much research effort has been put into systematic studies of the loss mechanisms in piezoelectrics, particularly in high voltage and high power range. Since not many comprehensive descriptions can be found in previous reports, this paper will clarify the loss mechanisms in piezoelectrics phenomenologically, describe heat generation processes and high power characteristics, and, finally, discuss the resonance and antiresonance vibration modes from a viewpoint of a quality factor.

### LOSS AND HYSTERESIS IN THE POLARIZATION CURVE

#### Relation between Hysteresis and Dissipation Factor

Let us start with loss and hysteresis in the electric displacement  $D$  (nearly equal to polarization  $P$ ) vs. electric field  $E$  curve without considering the electromechanical coupling. Figure 1 shows an example P-E hysteresis curve. When the  $D$  (or  $P$ ) traces a different line with increased and decreased applied electric field  $E$ , it is called *hysteresis*.

When the hysteresis is not very large, the electric displacement  $D$  can be expressed by using a slight phase lag to the applied electric field. Assuming that the electric field oscillates at a frequency  $f (= \omega/2\pi)$  as

$$E^* = E_0 e^{j\omega t}, \quad (1)$$

the induced electric displacement oscillates also at the same frequency under the steady state, but with some time phase delay  $\delta$ :

$$D^* = D_0 e^{j(\omega t - \delta)}. \quad (2)$$

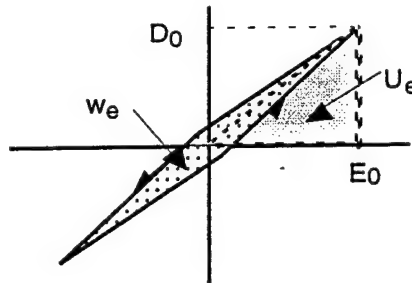


Fig.1 D (or P) vs. E hysteresis curve.

If we express the relation between  $D^*$  and  $E^*$  as

$$D^* = \epsilon^* \epsilon_0 E^*, \quad (3)$$

where the complex dielectric constant  $\epsilon^*$  is

$$\epsilon^* = \epsilon' - j \epsilon'', \quad (4)$$

and where

$$\epsilon'' / \epsilon' = \tan \delta. \quad (5)$$

Note that the negative connection in Eq.(4) comes from the time "delay", and that  $\epsilon' \epsilon_0 = (D_0/E_0) \cos \delta$  and  $\epsilon'' \epsilon_0 = (D_0/E_0) \sin \delta$ .

The area  $w_e$  corresponds to the consumed loss energy during an electric field cycle per unit volume of the dielectrics, and can be related in isotropic dielectrics with  $\epsilon''$  or  $\tan \delta$  as follows:

$$w_e = - \int_0^{2\pi/\omega} D \, dE = - \int_0^{2\pi/\omega} D \, (dE/dt) \, dt \quad (6)$$

Substituting the real parts in Eqs.(1) and (2) into Eq.(6),

$$w_e = \int_0^{2\pi/\omega} D_0 \cos(\omega t - \delta) (E_0 \omega \sin \omega t) \, dt$$

$$= E_0 D_0 \omega \sin \delta \int_0^{2\pi/\omega} \sin^2 \omega t \, dt = \pi E_0 D_0 \sin \delta \quad (7)$$

Or

$$w_e = \pi \epsilon'' \epsilon_0 E_0^2 = \pi \epsilon' \epsilon_0 E_0^2 \tan \delta \quad (8)$$

When there is no phase delay ( $\delta = 0$ ),  $w_e = 0$ ; i. e. the electrostatic energy stored in the dielectric will be recovered completely after a full cycle (100% efficiency). However, when there is a phase delay, the loss  $w_e$  will be accompanied per cycle, and the dielectric material generates heat. The  $\tan \delta$  is called *dissipation factor*, and its inverse value  $Q = 1/\tan \delta$  is called *electrical quality factor*.

In consideration of the stored electrostatic energy during a half cycle from  $-E_0$  to  $E_0$  ( $= 4 U_e$ , which is illustrated as an area in Fig. 1) provided by

$$\begin{aligned} 4 U_e &= (1/2)(2 E_0)(2 D_0 \cos \delta) \\ &= 2 E_0 D_0, \end{aligned} \quad (9)$$

the dissipation factor  $\tan \delta$  can be experimentally obtained by

$$\tan \delta = (1/2\pi) (w_e / U_e). \quad (10)$$

Note that  $w_e$  is the hysteresis in a full cycle and  $U_e$  is the stored energy in a quarter of cycle.

#### Temperature, Electric Field and Frequency Dependence of P-E Hysteresis

Figures 2, 3 and 4 show temperature, electric field and frequency dependence of the dissipation factor  $\tan \delta'$  calculated from the P-E hysteresis loss measured under stress free condition for a PZT-based ceramic.<sup>1)</sup> The loss  $\tan \delta'$  decreases gradually with increasing temperature, but is rather insensitive to frequency. On the contrary, the  $\tan \delta'$  increases initially in proportion to the applied electric field, exhibiting a saturation above a certain electric field. The value for  $E = 0$  (solid triangle mark in the figure) was obtained with an impedance analyzer.

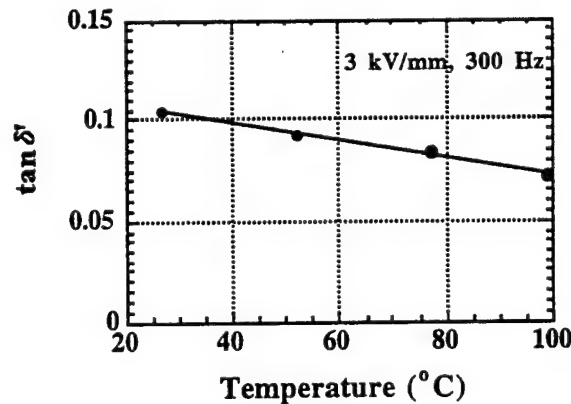


Fig.2 Loss  $\tan \delta'$  as a function of sample temperature (3 kV/mm, 300 Hz).

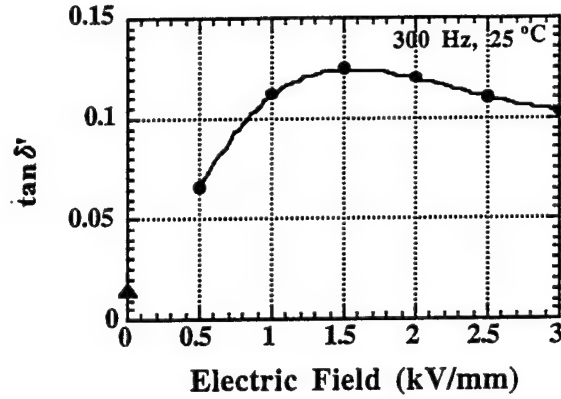


Fig.3 Loss  $\tan \delta'$  as a function of electric field ( $T = 25^\circ\text{C}$ ,  $f = 300 \text{ Hz}$ ).

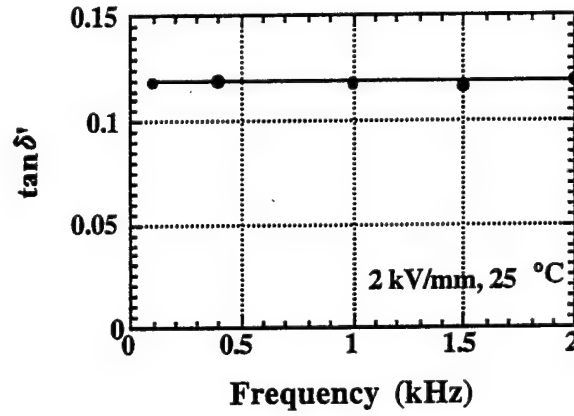


Fig.4 Loss  $\tan \delta'$  as a function of frequency ( $T = 25^\circ\text{C}$ ,  $E = 2 \text{ kV/mm}$ ).

#### GENERAL CONSIDERATION OF LOSS AND HYSTERESIS

Let us expand the above discussion into more general cases; i.e., piezoelectric materials. We will start from the Gibbs free energy  $G$  expressed by

$$dG = -x dX - D dE - S dT, \quad (11)$$

or

$$G = - (1/2) s^E X^2 - d X E - (1/2) \epsilon^X \epsilon_0 E^2. \quad (12)$$

Here,  $x$  is strain,  $X$ , stress,  $D$ , electric displacement,  $E$ , electric field,  $S$ , enthalpy and  $T$  is temperature. Temperature dependence is carried into the elastic compliance  $s^E$ , the dielectric



constant  $\epsilon^X$  and the piezoelectric constant  $d$ . We will obtain the following two piezoelectric equations:

$$x = -(\partial G / \partial X) = s^E X + d E, \quad (13)$$

$$D = -(\partial G / \partial E) = d X + \epsilon^X \epsilon_0 E. \quad (14)$$

Thermodynamical equations and the consequent piezoelectric equations (Eqs. (11)-(14)) cannot yield a delay-time related loss, without taking into account irreversible thermodynamic equations or dissipation functions. However, the latter considerations are mathematically equivalent to the introduction of complex physical constants into the phenomenological equations.

Therefore, we will introduce complex parameters  $\epsilon^{X*}$ ,  $s^{D*}$ ,  $\epsilon^{X*}$ ,  $s^{E*}$  and  $d^*$  in order to consider the hysteresis losses in electric, elastic and piezoelectric coupling energy:

$$\epsilon^{X*} = \epsilon^X (1 - j \tan \delta), \quad (15)$$

$$\epsilon^{X*} = \epsilon^X (1 - j \tan \delta'), \quad (16)$$

$$s^{D*} = s^D (1 - j \tan \phi), \quad (17)$$

$$s^{E*} = s^E (1 - j \tan \phi'), \quad (18)$$

$$d^* = d (1 - j \tan \theta). \quad (19)$$

$\theta$  is the phase delay of the strain under an applied electric field, or the phase delay of the electric displacement under an applied stress. Both delay phases should be exactly the same if we introduce the same complex piezoelectric constant  $d^*$  into Eqs. (13) and (14).  $\delta$  is the phase delay of the electric displacement to an applied electric field under a constant strain (i.e., zero strain or completely clamped) condition, and  $\phi$  is the phase delay of the strain to an applied stress under a constant electric displacement (i.e., open-circuit) condition. We will consider these phase delays as "intrinsic" losses. With this assumption, we can calculate the dissipation factors for  $\epsilon^{X*}$  (permittivity measured under constant stress) and  $s^{E*}$  (elastic compliance measured under constant electric field) which correspond to "extrinsic" losses. When an electric field is applied on a piezoelectric sample as illustrated in the top of Fig. 5, this state will be equivalent to the superposition of the following two steps: first, the sample is completely clamped and the field  $E_0$  is applied (pure electrical energy  $(1/2) \epsilon^X \epsilon_0 E_0^2$  is input); second, keeping the field at  $E_0$ , the mechanical constraint is released (additional mechanical energy  $(1/2) (d^2/s^E) E_0^2$  is necessary). The total energy should correspond to the total input electrical energy  $(1/2) \epsilon^X \epsilon_0 E_0^2$ ; thus, we obtain the relation,

$$\epsilon_0 \epsilon^X = \epsilon_0 \epsilon^{X*} + (d^2/s^E), \quad (20)$$

Similarly, from the bottom of Fig. 5,

$$s^E = s^{D*} + (d^2/\epsilon_0 \epsilon^X). \quad (21)$$

Replacing  $\epsilon^X$ ,  $\epsilon^{X*}$ ,  $s^E$ ,  $s^{D*}$ ,  $d$  in Eqs. (20) and (21) by the complex parameters in Eqs. (15) - (19), we obtain:

$$\epsilon^X / \epsilon^x = 1/(1 - k^2), \quad (22)$$

$$s^E / s^D = 1/(1 - k^2), \quad (23)$$

$$\tan \delta' = (1/(1 + k^2))[\tan \delta + k^2(2 \tan \theta - \tan \phi)], \quad (24)$$

$$\tan \phi' = (1/(1 + k^2))[\tan \phi + k^2(2 \tan \theta - \tan \delta)], \quad (25)$$

where

$$k^2 = d^2 / (s^E \epsilon_0 \epsilon^X). \quad (26)$$

This  $k$  is called the *electromechanical coupling factor*, and defined here as a real number. It is important that the extrinsic dielectric and elastic losses are mutually correlated with the intrinsic dielectric, elastic and piezoelectric losses through the electromechanical coupling  $k^2$ , and that the denominator  $(1 + k^2)$  comes basically from the  $\epsilon^X / \epsilon^x$  ratio and this real part reflects to the dissipation factor when the imaginary part is divided by the real part. Also note that depending on the vibration mode, the definition of electromechanical coupling  $k$  can be changed such as  $k^2 = d^2 / (s^D \epsilon_0 \epsilon^X)$ .

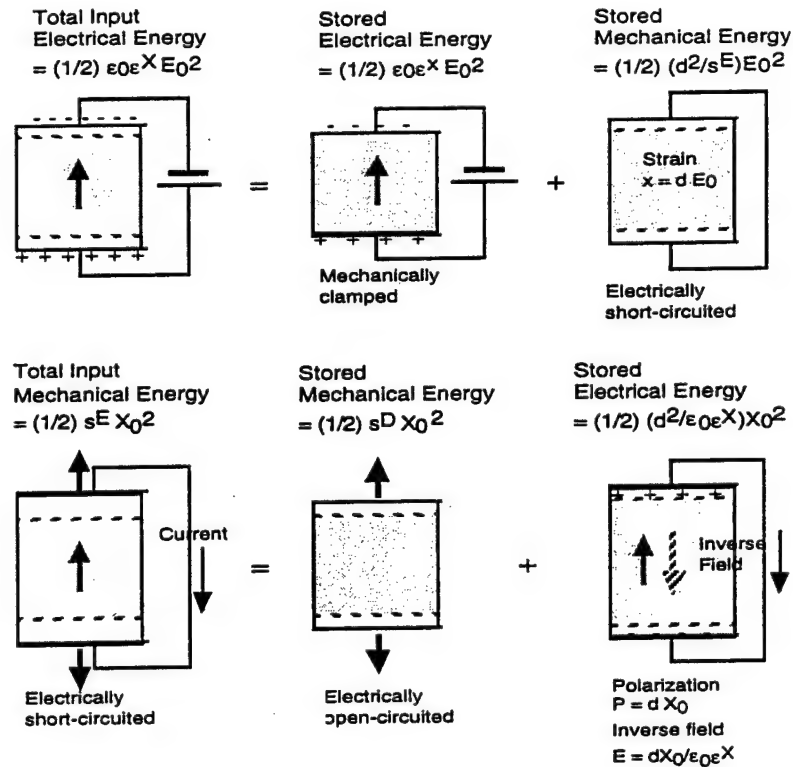


Fig. 5 Conceptual figure for explaining the relation between  $\epsilon^X$  and  $\epsilon^x$ ,  $s^E$  and  $s^D$ .

Figures 6(a) - 6(d) correspond to the model hysteresis curves for practical experiments: D vs. E curve under a stress-free condition, x vs. X under a short-circuit condition, x vs. E under a stress-free condition and D vs. X under an open-circuit condition for measuring charge (or under a short-circuit condition for measuring current), respectively.

In a similar fashion to the previous section, the stored energies and hysteresis losses for pure electrical and mechanical energies can be calculated as:

$$U_e = (1/2) \epsilon^X \epsilon_0 E_0^2, \quad (27)$$

$$w_e = \pi \epsilon^X \epsilon_0 E_0^2 \tan \delta', \quad (28)$$

$$U_m = (1/2) s^E X_0^2, \quad (29)$$

$$w_m = \pi s^E X_0^2 \tan \phi'. \quad (30)$$

The electromechanical loss, when measuring the induced strain under an electric field, is more complicated. Let us calculate the stored energy  $U_{em}$  during a quarter electric field cycle (i.e., 0 to  $E_0$ ), first :

$$\begin{aligned} U_{em} &= - \int x dX = (1/2) (x_0^2/s^E) = (1/2) (dE_0)^2/s^E \\ &= (1/2) (d^2/s^E) E_0^2 \end{aligned} \quad (31)$$

Replacing d and  $s^E$  by  $d^* = d(1 - j \tan \theta)$  and  $s^{E*} = s^E(1 - j \tan \phi)$ , we obtain

$$U_{em} = (1/2) (d^2/s^E) E_0^2, \quad (32)$$

and

$$w_{em} = \pi (d^2/s^E) E_0^2 (2 \tan \theta - \tan \phi'). \quad (33)$$

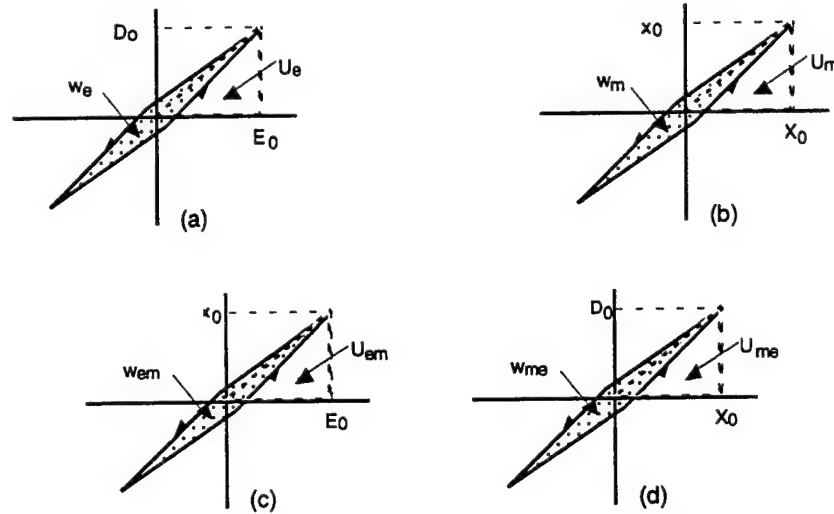


Fig.6 (a) D vs. E (stress free), (b) x vs. X (short-circuit), (c) x vs. E (stress free) and (d) D vs. X (open-circuit) curves with a slight hysteresis in each relation.

Note that the strain vs. electric field measurement seems to provide the piezoelectric loss  $\tan\theta$  directly, however, the observed loss should include an additional elastic loss because the strain should be delayed to the initial stress, which is needed to calculate energy.

Similarly, when we measure the induced charge under stress, the stored energy  $U_{me}$  and the hysteresis loss  $w_{me}$  during a quarter and a full stress cycle, respectively, are obtained as

$$U_{me} = (1/2) (d^2 / \epsilon_0 \epsilon^X) X_0^2, \quad (34)$$

and

$$w_{me} = \pi (d^2 / \epsilon_0 \epsilon^X) X_0^2 (2 \tan\theta - \tan\delta'). \quad (35)$$

Hence, from the measurements of  $D$  vs.  $E$  and  $x$  vs.  $X$ , we obtain  $\tan\delta'$  and  $\tan\phi'$ , respectively, and either the piezoelectric ( $D$  vs.  $X$ ) or converse piezoelectric measurement ( $x$  vs.  $E$ ) provides  $\tan\theta$  through a numerical subtraction.

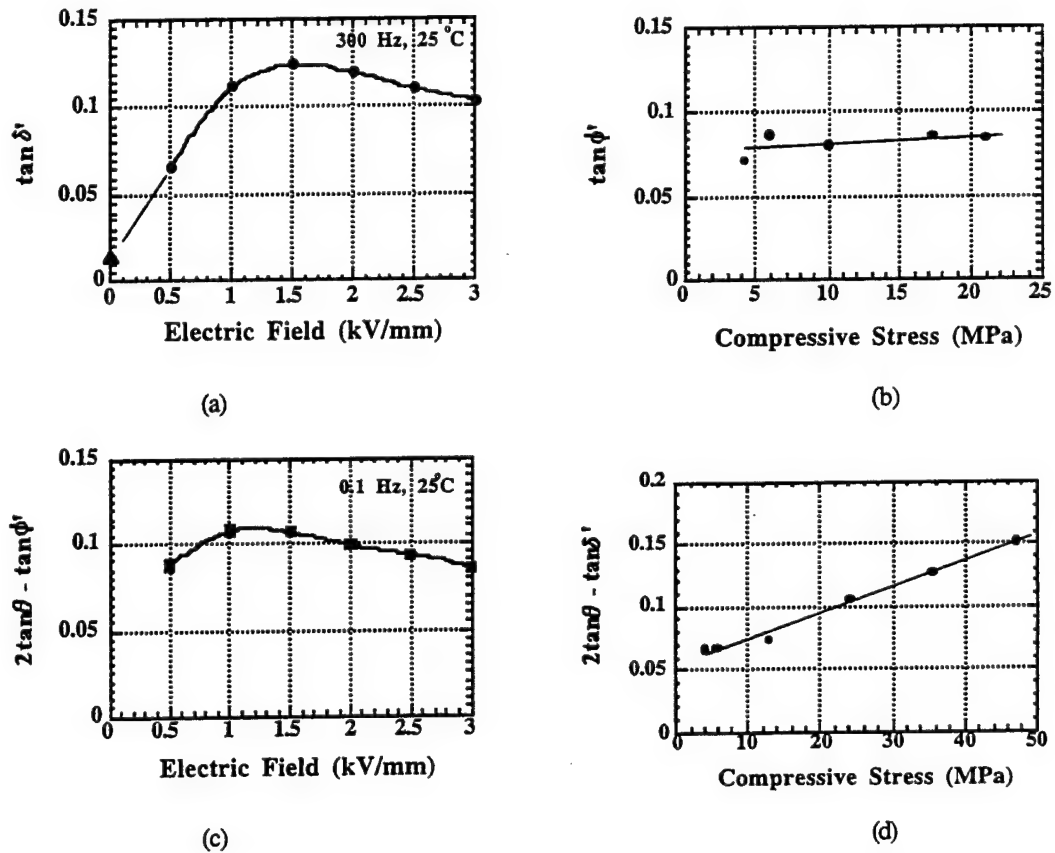


Fig.7 Dissipation factors determined from (a)  $D$  vs.  $E$  (stress free), (b)  $x$  vs.  $X$  (short-circuit), (c)  $x$  vs.  $E$  (stress free) and (d)  $D$  vs.  $X$  (open-circuit) curves for a PZT based actuator.

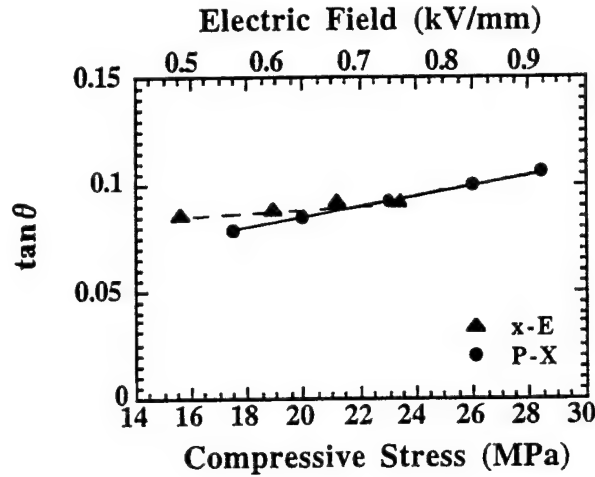


Fig.8 Piezoelectric dissipation factor  $\tan\theta$  as a function of electric field or compressive stress, measured for a PZT based actuator.

Figure 7 shows dissipation factors determined from (a)  $D$  vs.  $E$  (stress free), (b)  $x$  vs.  $X$  (short-circuit), (c)  $x$  vs.  $E$  (stress free) and (d)  $D$  vs.  $X$  (open-circuit) curves for a PZT based actuator. Figure 8 shows the result for the piezoelectric loss  $\tan\theta$ . We used the correlation factor between electric field and compressive stress given averagely by  $X = (\epsilon_0 \epsilon X_s E)^{1/2}$ . Note that the piezoelectric loss  $\tan\theta$  is not so small as previously believed, but comparable to the dielectric or elastic loss, and is insensitive to the field or stress. The experimental details will be reported in the successive papers.

When similar measurements to Figs. 6(a) and 6(b), but under constrained conditions; that is,  $D$  vs.  $E$  under a completely clamped state, and  $x$  vs.  $X$  under an open-circuit state, respectively, we can expect smaller hystereses; that is, intrinsic losses,  $\tan\delta$  and  $\tan\phi$ . These measurements are alternative methods to determine the three losses separately.

### LOSS AND HEAT GENERATION

Heat generation in various types of PZT-based actuators has been studied under a relatively large electric field applied (1 kV/mm or more) at an off-resonance frequency, and a simple analytical method was established to evaluate the temperature rise, which is very useful for the design of piezoelectric high-power actuators.

Zheng et al. reported the heat generation from various sizes of multilayer type piezoelectric ceramic actuators.<sup>1)</sup> Figure 9 shows the temperature change in the actuators when driven at 3 kV/mm and 300 Hz, and Fig. 10 plots the saturated temperature as a function of  $V_e/A$ , where  $V_e$  is the effective volume (electrode overlapped part) and  $A$  is the surface area. This linear relation is reasonable because the volume  $V_e$  generates the heat and this heat is dissipated through the area  $A$ . Thus, if we need to suppress the temperature rise, a small  $V_e/A$  design is preferred.

According to the law of energy conservation, the rate of heat storage in the piezoelectric resulting from heat generation and dissipation effects can be expressed as

$$q_g - q_{out} = V \rho c (dT/dt), \quad (36)$$

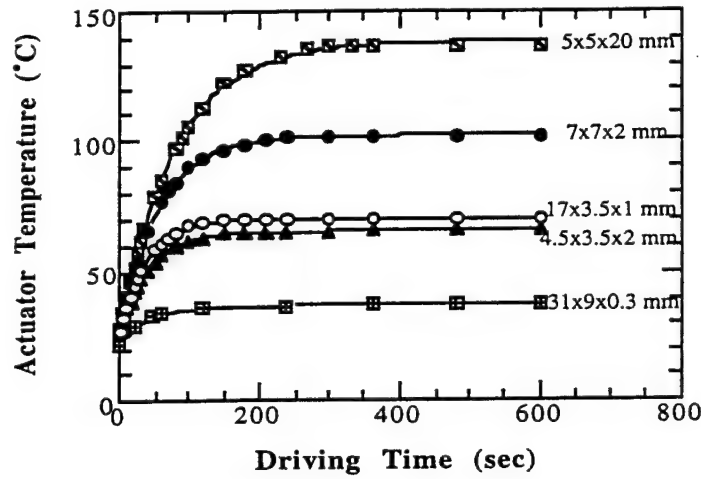


Fig.9 Temperature rise for various actuators while driven at 300 Hz and 3 kV/mm.

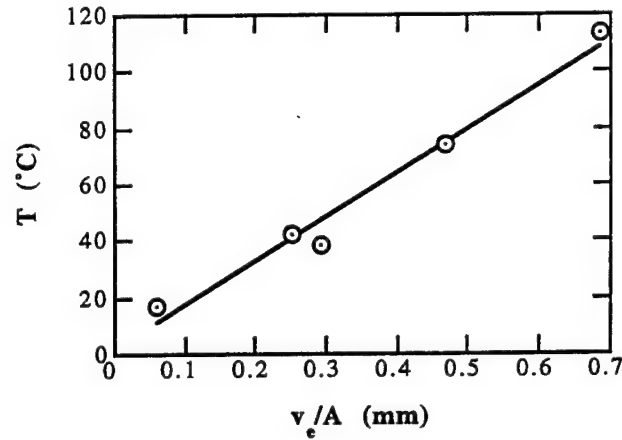


Fig.10 Temperature rise versus  $V_e/A$  (3 kV/mm, 300 Hz), where  $V_e$  is the effective volume generating the heat and  $A$  is the surface area dissipating the heat.

assuming uniform temperature distribution in the sample.  $V$ ,  $\rho$ ,  $c$  are total volume, density and specific heat, respectively. The heat generation is considered to be caused by losses. Thus, the rate of heat generation ( $q_g$ ) in the piezoelectric can be expressed as

$$q_g = u f V_e, \quad (37)$$

where  $u$  is the loss of the sample per driving cycle per unit volume,  $f$ , the driving frequency, and  $V_e$  is the effective volume where the ceramic is activated. According to the measuring condition,

this  $u$  corresponds to  $w_e$  of Eq. (28), which consists of the intrinsic electrical loss  $\tan \delta$  and the electromechanical loss  $(2 \tan \theta - \tan \phi')$  in the previous section:

$$\begin{aligned} u &= w_e = \pi \epsilon^X \epsilon_0 E_0^2 \tan \delta' \\ &= (1/(1 + k^2)) [\tan \delta + k^2(2 \tan \theta - \tan \phi)] \pi \epsilon^X \epsilon_0 E_0^2. \end{aligned} \quad (38)$$

Note that we do not need to add  $w_{em}$  explicitly, because the corresponding electromechanical loss is already included implicitly in  $w_e$ .

When we neglect the conduction heat transfer, the rate of heat dissipation ( $q_{out}$ ) from the sample is the sum of the rates of heat flow by radiation ( $q_r$ ) and convection ( $q_c$ ):

$$\begin{aligned} q_{out} &= q_r + q_c \\ &= \sigma e A (T^4 - T_0^4) + h_c A (T - T_0), \end{aligned} \quad (39)$$

where  $\sigma$  is the Stefan-Boltzmann constant,  $e$  is the emissivity of the sample,  $h_c$  is the average convective heat transfer coefficient, and  $A$  is the sample surface area.

Thus, Eq.(36) can be written in the form:

$$u f V - A k(T) (T - T_0) = V \rho c (dT/dt), \quad (40)$$

where

$$k(T) = \sigma e (T^2 + T_0^2)(T + T_0) + h_c \quad (41)$$

is defined as the overall heat transfer coefficient. If we assume that  $k(T)$  is relatively insensitive to temperature change, the solution to Eq.(40) for the piezoelectric sample temperature is given as a function of time ( $t$ ):

$$T - T_0 = [u f V_e / k(T) A] [1 - e^{-t/\tau}], \quad (42)$$

where the time constant  $\tau$  is expressed as

$$\tau = \rho c V / k(T) A. \quad (43)$$

As  $t \rightarrow \infty$ , the maximum temperature rise in the sample becomes

$$\Delta T = u f V_e / k(T) A. \quad (44)$$

As  $t \rightarrow 0$ , the initial rate of temperature rise is

$$(dT/dt) = u f V_e / \rho c V = \Delta T / \tau. \quad (45)$$

Figures 11 and 12 show the dependence of  $k(T)$  on applied electric field and frequency. Since  $k(T)$  is not really constant, we can calculate the total loss  $u$  of the piezoelectric through Eq.(45). The calculated results are shown in Table I. The experimental data of P-E hysteresis losses under a stress-free condition are also listed for comparison. It is seen that the P-E hysteresis extrinsic loss agrees well with the total loss contributing to the heat generation.



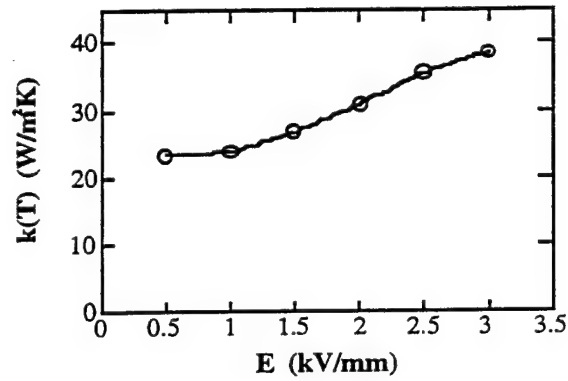


Fig.11  $k(T)$  as a function of applied electric field (400 Hz, data from the actuator with dimensions of 7 mm x 7 mm x 2 mm).

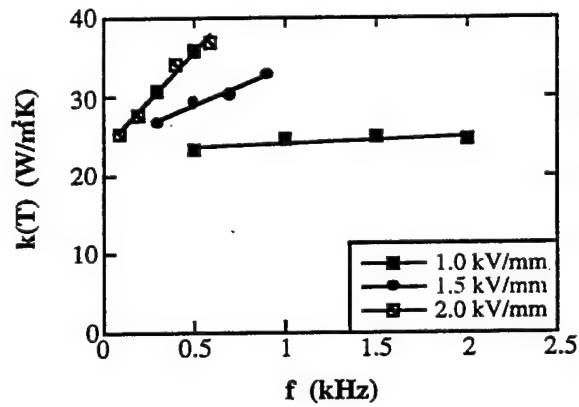


Fig.12 Overall heat transfer coefficient  $k(T)$  as a function of frequency.

Table I Loss and overall heat transfer coefficient for PZT multilayer samples ( $E = 3 \text{ kV/mm}$ ,  $f = 300 \text{ Hz}$ ).

Actuator	4.5x3.5x2 mm	7x7x2 mm	17x3.5x1 mm
Total loss ( $\times 10^3 \text{ J/m}^3$ )			
$u = \frac{\rho c v}{f v_e} \left( \frac{dT}{dt} \right)_{t \rightarrow 0}$	19.2	19.9	19.7
P-E hysteresis loss ( $\times 10^3 \text{ J/m}^3$ )	18.5	17.8	17.4
$k(T) \text{ (W/m}^2\text{K)}$	38.4	39.2	34.1

## LOSSES AT A PIEZOELECTRIC RESONANCE

So far, we have considered the losses for a quasi-static or off-resonance state. Problems in ultrasonic motors which are driven at the resonance frequency include significant distortion of the admittance frequency spectrum due to nonlinear behavior of elastic compliance at a high vibration amplitude, and heat generation which causes a serious degradation of the motor characteristics through depoling of the piezoceramic. Therefore, the ultrasonic motor requires a very hard type piezoelectric with a high mechanical quality factor  $Q$ , leading to the suppression of heat generation. It is also notable that the actual mechanical vibration amplitude at the resonance frequency is directly proportional to this  $Q$  value.

### Losses at a Piezoelectric Resonance

#### *Piezoelectric resonance without loss*

Let us consider the longitudinal mechanical vibration of a piezo-ceramic plate through the transverse piezoelectric effect ( $d_{31}$ ) as shown in Fig. 13. Assuming that the polarization is in the  $z$ -direction and  $x$ - $y$  planes are the planes of the electrodes, the extentional vibration in the  $x$  direction is represented by the following dynamic equation :

$$(\partial^2 u / \partial t^2) = F = (\partial X_{11} / \partial x) + (\partial X_{12} / \partial y) + (\partial X_{13} / \partial z), \quad (46)$$

where  $u$  is the displacement of the small volume element in the ceramic plate in the  $x$ -direction. When the plate is very long and thin,  $X_2$  and  $X_3$  may be set equal to zero through the plate, and the relations between stress, electric field (only  $E_z$  exists) and the induced strain are given by :

$$X_1 = x_1 / s_{11} E - (d_{31} / s_{11} E) E_z. \quad (47)$$

Introducing Eq.(47) into Eq.(46), and allowing for  $x_1 = \partial u / \partial x$  and  $\partial E_z / \partial x = 0$  (due to the equal potential on each electrode), leads to a harmonic vibration equation :

$$-\omega^2 \rho s_{11} E u = \partial^2 u / \partial x^2. \quad (48)$$

Here,  $\omega$  is the angular frequency of the drive field, and  $\rho$  is the density. Substituting a general solution  $u = u_1(x)e^{j\omega t} + u_2(x)e^{-j\omega t}$  into Eq.(47), and with the boundary condition  $X_1 = 0$  at  $x = 0$  and  $L$  (sample length), the following solutions can be obtained:

$$(\text{strain}) \quad \partial u / \partial x = x_1 = d_{31} E_z [\sin \omega(L-x)/v + \sin(\omega x/v)] / \sin(\omega L/v), \quad (49)$$

$$(\text{total displacement}) \quad \Delta L = \int_0^L x_1 dx = d_{31} E_z L (2v/\omega L) \tan(\omega L/2v). \quad (50)$$

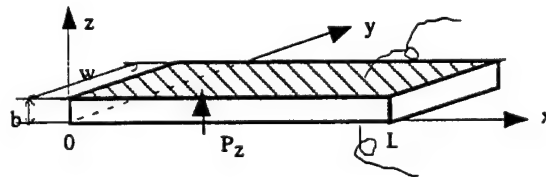


Fig.13 Longitudinal vibration through the transverse piezoelectric effect ( $d_{31}$ ) in a rectangular plate.

Here,  $v$  is the sound velocity in the piezoceramic which is given by

$$v = 1 / \sqrt{\rho s_{11}} E. \quad (51)$$

Since the total current is given by :

$$i = j\omega w \int_0^L D_3 dx = j\omega w \int_0^L [(\epsilon_0 \epsilon_{33} X - d_{31}^2 / s_{11} E) E_z + (d_{31} / s_{11} E) x_1] dx, \quad (52)$$

and using Eq. (49), the admittance for the mechanically free sample is calculated to be:

$$Y = (1/Z) = (i/V) = (i/E_z t) \\ = (j\omega w L / t) \epsilon_0 \epsilon_{33}^{LC} [1 + (d_{31}^2 / \epsilon_0 \epsilon_{33}^{LC} s_{11} E) (\tan(\omega L / 2v) / (\omega L / 2v))], \quad (53)$$

where  $w$  is the width,  $L$  the length,  $t$  the thickness of the sample, and  $V$  the applied voltage.  $\epsilon_{33}^{LC}$  is the permittivity in a longitudinally clamped sample, which is given by

$$\epsilon_0 \epsilon_{33}^{LC} = \epsilon_0 \epsilon_{33} X - (d_{31}^2 / s_{11} E) \\ = \epsilon_0 \epsilon_{33} X (1 - k_{31}^2). \quad (54)$$

The final transformation is provided by the definition,

$$k_{31} = d_{31} / \sqrt{s_{11} E \epsilon_0 \epsilon_{33} X}. \quad (55)$$

When the drive frequency is much lower than the resonance, taking  $\omega \rightarrow 0$  in Eq. (53) leads to  $Y = (j\omega w L / t) \epsilon_{33} X$  (corresponding to the normal capacitance). The piezoelectric resonance is achieved where the admittance becomes infinite or the impedance is zero. The resonance frequency  $f_R$  is calculated from Eq. (53), and the fundamental frequency is given by

$$f_R = v / 2L = 1 / (2L \sqrt{\rho s_{11}} E). \quad (56)$$

On the other hand, the antiresonance state is generated for zero admittance or infinite impedance:

$$(\omega_A L / 2v) \cot(\omega_A L / 2v) = -d_{31}^2 / \epsilon_{33}^{LC} s_{11} E = -k_{31}^2 / (1 - k_{31}^2). \quad (57)$$

The resonance and antiresonance states are described by the following intuitive model.<sup>2)</sup> In a high electromechanical coupling material with  $k$  almost equal to 1, the resonance or antiresonance states appear for  $\tan(\omega L / 2v) = \infty$  or 0 [i. e.,  $\omega L / 2v = (m-1/2)$  or  $m$  ( $m$ : integer)], respectively. The strain amplitude  $x_1$  distribution for each state [calculated using Eq. (49)] is illustrated in Fig. 14. In the resonance state, large strain amplitudes and large capacitance changes (called *motional capacitance*) are induced, and the current can easily flow into the device. Note that for a loss-free piezoelectric the strain is calculated to be infinite in Eq. (49). On the other hand, at antiresonance, the strain induced in the device compensates completely, resulting in no capacitance change, and

the current cannot flow easily into the sample. Thus, for a high  $k$  material the first antiresonance frequency  $f_A$  should be twice as large as the first resonance frequency  $f_R$ .

In a typical case, where  $k_{31} = 0.3$ , the antiresonance state varies from the above-mentioned mode and becomes closer to the resonance mode. The low-coupling material exhibits an antiresonance mode where capacitance change due to the size change is compensated completely by the current required to charge up the static capacitance (called *damped capacitance*). Thus, the antiresonance frequency  $f_A$  will approach the resonance  $f_R$ .

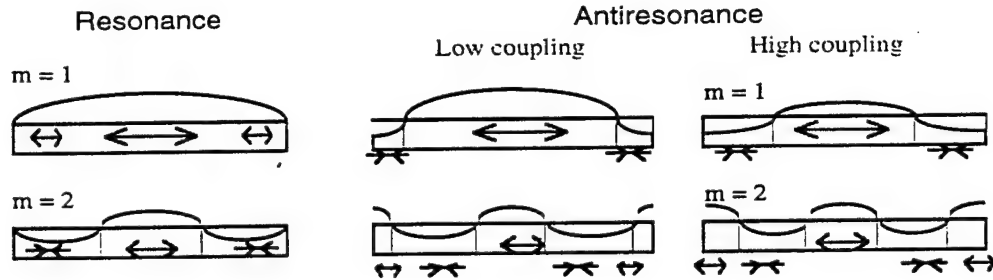


Fig.14 Strain generation in the resonance or antiresonance state.

When  $(f_A - f_R)$  is not very large due to a small electromechanical coupling, we can derive the following approximate expression for  $f_A$ . Assuming that  $\omega_A - \omega_R$  is much smaller than  $\omega_R (= \pi v / L)$ ,

$$(\omega_A L / 2v) \cot (\omega_A - \omega_R) L / 2v - \pi / 2 = -(\omega_A L / 2v) \sin (\omega_A - \omega_R) L / 2v / \cos (\omega_A - \omega_R) L / 2v$$

Thus,

$$\omega_A = (\pi v / L) [1 + (4 / \pi^2) K_{31}^2], \quad (59)$$

where we introduced a new parameter  $K_{31}$  as

$$K_{31}^2 = k_{31}^2 / (1 - k_{31}^2). \quad (60)$$

It is notable that for a piezoelectric sample with a typical  $k_{31}$  value, the two ends of the plate are not the nodal points, that is, we can expect rather large displacements, which can be applied for ultrasonic motors.

#### Piezoelectric resonance with losses

First, we will discuss the admittance curve. Similar to the treatment in Section 3, we will introduce the complex parameters  $\epsilon_{33}^{X*} = \epsilon_{33}^X (1 - j \tan \delta')$ ,  $s_{11}^{E*} = s_{11}^E (1 - j \tan \phi')$ , and  $d_{31}^* = d (1 - j \tan \theta)$  into Eq. (53):

$$\begin{aligned}
Y &= Y_d + Y_m \\
&= (j\omega L/t) \epsilon_0 \epsilon_{33} X (1 - k_{31}^2) [1 - j (1/(1 - k_{31}^2)) ((\tan \delta' - k_{31}^2 (2 \tan \theta - \tan \phi')))] \\
&\quad + (j\omega L/t) \epsilon_0 \epsilon_{33} X k_{31}^2 [(1 - j(2 \tan \theta - \tan \phi'))] [(\tan(\omega L/2 v^*) / (\omega L/2 v^*))] \\
&= j\omega C_d [1 - j (1/(1 - k_{31}^2)) ((\tan \delta' - k_{31}^2 (2 \tan \theta - \tan \phi')))] \\
&\quad + j\omega C_d K_{31}^2 [(1 - j(2 \tan \theta - \tan \phi'))] [(\tan(\omega L/2 v^*) / (\omega L/2 v^*))] \\
&= j\omega C_d (1 - j \tan \delta) + j\omega C_0 k_{31}^2 [(1 - j(2 \tan \theta - \tan \phi'))] [(\tan(\omega L/2 v^*) / (\omega L/2 v^*))], \quad (61)
\end{aligned}$$

where

$$C_0 = (\omega L/t) \epsilon_0 \epsilon_{33} X, \quad (62)$$

$$C_d = (1 - k_{31}^2) C_0. \quad (63)$$

Note that the loss for the first term (damped conductance) is represented by the intrinsic electric loss  $\tan \delta$ , not by the extrinsic loss  $\tan \delta'$ . Taking into account

$$v^* = 1/\sqrt{\rho s_{11}} E (1 - j \tan \phi') = v (1 + (1/2) j \tan \phi'), \quad (64)$$

we further calculate  $1/(\tan(\omega L/2 v^*))$  with an expansion-series approximation around  $(\omega L/2 v) = \pi/2$ . The resonance state is defined in this case for the maximum admittance point, rather than the infinite  $Y$ . We will use new frequency parameters,

$$\Omega = \omega L/2 v, \Delta\Omega = \Omega - \pi/2 \quad (<1). \quad (65)$$

$$\text{Since } \omega L/2 v^* = (\pi/2 + \Delta\Omega) [1 - (1/2) j \tan \phi'],$$

$$1 / (\tan(\omega L/2 v^*)) = -\Delta\Omega + j (\pi/4) \tan \phi'. \quad (66)$$

Thus, assuming  $K_{31}^2 = k_{31}^2/(1 - k_{31}^2)$ ,  $Y_m$  is approximated around the first resonance frequency by

$$\begin{aligned}
Y_m &= j\omega C_d K_{31}^2 [(1 - j(2 \tan \theta - \tan \phi'))] [(\tan(\omega L/2 v^*) / (\omega L/2 v^*))] \\
&= j\omega_0 C_d K_{31}^2 [(1 - j(2 \tan \theta - \tan \phi'))] [(-\Delta\Omega + j(\pi/4) \tan \phi') (\pi/2) (1 - (1/2) j \tan \phi')] \\
&= j(\pi^2/8) \omega_0 C_d K_{31}^2 [(1 + j((3/2) \tan \phi' - 2 \tan \theta)) / (- (4/\pi) \Delta\Omega + j \tan \phi')]. \quad (67)
\end{aligned}$$

The maximum  $Y_m$  is obtained at  $\Delta\Omega = 0$ :

$$Y_m^{\max} = (\pi^2/8) \omega_0 C_d K_{31}^2 (\tan \phi')^{-1}. \quad (68)$$

In order to obtain the mechanical quality factor, let us obtain  $\Delta\Omega$  which provides  $Y_m^{\max}/\sqrt{2}$ . Since  $\Delta\Omega = (\pi/4) \tan \phi'$  is obtained,

$$Q_m = \Omega_0 / 2\Delta\Omega = (\pi/2) / 2 (\pi/4) \tan \phi' = (\tan \phi')^{-1}. \quad (69)$$

This verifies the ready-used relation,  $Q_m = (\tan \phi')^{-1}$ .

Next, the displacement amplification is considered. From Eq. (50) also by using the complex parameters:

$$\begin{aligned}
 u(L) &= d_{31}^* E_z L (2v^* / \omega L) \tan(\omega L / 2v^*) \\
 &= 2d_{31}(1-j \tan \theta) E_z L [v(1+(1/2)j \tan \phi') / \omega L] \tan(\omega L / 2v^*) \\
 &= 2d_{31}(1-j \tan \theta) E_z L [v(1+(1/2)j \tan \phi') / \omega_0 L] / (-\Delta\Omega + j(\pi/4) \tan \phi').
 \end{aligned} \quad (70)$$

The maximum displacement  $u_{\max}$  is obtained at  $\Delta\Omega = 0$ :

$$u_{\max} = (\pi^2/8) d_{31} E_z L (\tan \phi')^{-1}. \quad (71)$$

The maximum displacement at the resonance frequency is  $(\pi^2/8) Q_m$  times larger than that at a non-resonance frequency ( $d_{31} E_z L$ ).

In a brief summary, when we observe the admittance or displacement spectrum as a function of drive frequency, and obtain the mechanical quality factor  $Q_m$  estimated from  $Q_m = \omega_0 / 2\Delta\omega$ , where  $2\Delta\omega$  is a full width of the 3 dB down (i.e.,  $1/\sqrt{2}$ ) of the maximum value at  $\omega = \omega_0$ , we will obtain the extrinsic mechanical loss  $\tan \phi'$ .

#### Equivalent Circuit

The equivalent circuit for the piezoelectric actuator is represented by a combination of L, C and R. Figure 15 (a) shows an equivalent circuit for the resonance state, which has very low impedance. Taking into account Eq. (61), we can understand that  $C_d$  and  $R_d$  correspond to the electrostatic capacitance (for a longitudinally clamped sample in the previous case) and the clamped (or intrinsic) dielectric loss  $\tan \delta$ , respectively, and the components  $L_A$  and  $C_A$  in a series resonance circuit are related to the piezoelectric motion. For example, in the case of the longitudinal vibration of the above rectangular plate through  $d_{31}$ , these components are represented by

$$L_A = (\rho / 8)(Lb / w)(s_{11}^E)^2 / d_{31}^2, \quad (72)$$

$$C_A = (8 / \pi^2)(Lw / b)(d_{31}^2 / s_{11}^E). \quad (73)$$

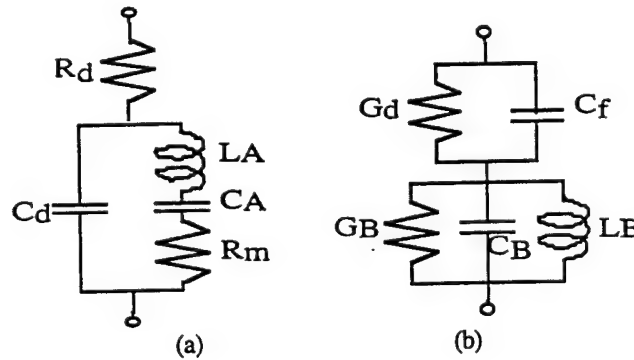


Fig.15 Equivalent circuit of a piezoelectric device for the resonance (a) and the antiresonance (b).

The total resistance  $R_A (= R_d + R_m)$  should correspond to the loss  $\tan \phi'$ , which is composed of the intrinsic mechanical loss  $\tan \phi$  and piezoelectric/dielectric coupled loss  $(2 \tan \theta - \tan \delta)$  (see Eq. (25)). Thus, roughly speaking,  $R_m$  corresponds to the intrinsic mechanical loss. Note that we introduced an additional resistance  $R_d$  to explain a large contribution of the dielectric loss when a vibration velocity is relatively large. In contrast, the equivalent circuit for the antiresonance state of the same actuator is shown in Fig. 15 (b), which has high impedance.

#### Losses as a Function of Vibration Velocity

Figure 16 shows the mechanical  $Q_m$  versus basic composition  $x$  at two effective vibration velocities  $v_0=0.05$  m/s and 0.5 m/s for  $\text{Pb}(\text{Zr}_x\text{Ti}_{1-x})\text{O}_3$  doped with 2.1 at.% of Fe.<sup>3)</sup> The decrease in mechanical  $Q_m$  with an increase of vibration level is minimum around the rhombohedral-tetragonal morphotropic phase boundary (52/48). In other words, the smallest  $Q$  material at a small vibration level becomes the best at a large vibration level, and the data obtained by a conventional impedance analyzer with a small voltage/power does not provide data relevant to high power materials.

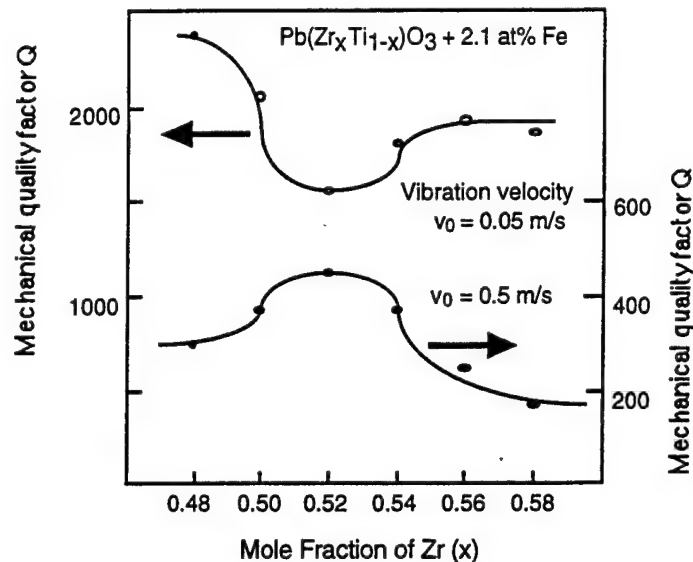


Fig.16 Mechanical  $Q_m$  versus basic composition  $x$  at two effective vibration velocities  $v_0=0.05$  m/s and 0.5 m/s for  $\text{Pb}(\text{Zr}_x\text{Ti}_{1-x})\text{O}_3$  doped with 2.1 at.% of Fe.

Let us consider here the degradation mechanism of the mechanical quality factor  $Q_m$  with increasing vibration velocity. Figure 17 shows an important notion on heat generation from the piezoelectric material.<sup>3)</sup> The damped and motional resistances,  $R_d$  and  $R_m$ , in the equivalent electrical circuit of a PZT sample are separately plotted as a function of vibration velocity. Note that  $R_m$ , mainly related to the mechanical loss, is insensitive to the vibration velocity, while  $R_d$ , related to the dielectric loss, increases significantly around a certain critical vibration velocity. Thus, the resonance loss at a small vibration velocity is mainly determined by the intrinsic



mechanical loss which provides a high mechanical quality factor  $Q_m$ , and with increasing vibration velocity, the intrinsic dielectric loss contribution significantly increases. After  $R_d$  exceeds  $R_m$ , we started to observe heat generation. Thus, we can conclude that heat generation is caused mainly by dielectric loss  $\tan \delta'$  (i. e. P-E hysteresis loss); this is not contradictory to the result in Section 4 where a high-voltage drive was conducted at an off-resonance frequency.

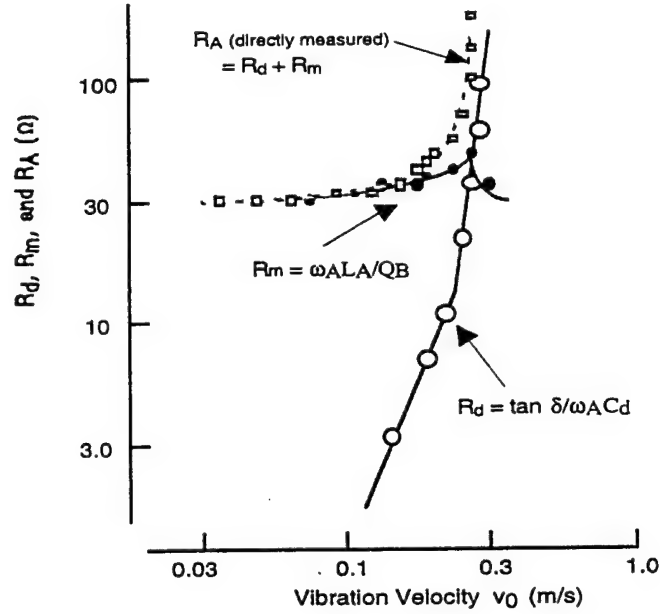


Fig.17 Vibration velocity dependence of the resistances  $R_d$  and  $R_m$  in the equivalent electric circuit for a PZT sample.

## LOSSES AT RESONANCE AND ANTIRESONANCE MODES

### Losses at a Piezoelectric Antiresonance State

We will consider the losses at the antiresonance frequency in comparison with the resonance mode. The antiresonance mode is obtained at a frequency which provides the minimum value of admittance  $Y$ , instead of zero of  $Y$  for the loss-free case. Taking an approximation technique on Eq. (61) around the antiresonance frequency  $\omega_A$ , similar to the previous section, we obtain:

$$\Omega_A = \omega_A L/2 \nu, \Delta\Omega = \Omega - \Omega_A (<<1). \quad (74)$$

If  $k_{31}$  is not very large, the following relationship is obtained:

$$\Omega_A = \omega_A L/2\nu = (\pi/2) (1 + (4/\pi^2) k_{31}^2) \quad (75)$$

In the following approximation, however, this relation is not used, but we will neglect the higher order of  $\Delta\Omega$  and  $\tan \phi'$  in Eq. (61):

$$Y = j\omega C_d \{ 1 + (k_{31}^2 / (1 - k_{31}^2)) \tan[(\Omega_A + \Delta\Omega) (1 - j (1/2) \tan\phi')] / [(\Omega_A + \Delta\Omega) (1 - j (1/2) \tan\phi')] \}. \quad (76)$$

Taking into account

$$\begin{aligned} & \tan[(\Omega_A + \Delta\Omega) (1 - j (1/2) \tan\phi')] \\ &= [(\Omega_A^2 - K_{31}^2 \Delta\Omega + j(1/2)\Omega_A \tan\phi' K_{31}^2) / [(-K_{31}^2 - \Omega_A \Delta\Omega) - j\Omega_A (1/2)\Omega_A \tan\phi']], \end{aligned} \quad (77)$$

$$\begin{aligned} Y &= j\omega C_d [- (\Omega_A^2 + K_{31}^2 + K_{31}^4) \Delta\Omega - j(1/2)\Omega_A \tan\phi' (\Omega_A^2 - K_{31}^2 - K_{31}^4) / \\ & [- K_{31}^2 \Omega_A - (\Omega_A^2 + K_{31}^2) \Delta\Omega - j(1/2)\Omega_A \tan\phi' (\Omega_A^2 - K_{31}^2)], \end{aligned} \quad (78)$$

where

$$K_{31}^2 = k_{31}^2 / (1 - k_{31}^2) \quad (79)$$

Then,  $Y_{\min}$  can be obtained at  $\Delta\Omega = 0$ :

$$Y_{\min} = \omega C_d (1/2) \tan\phi' (\Omega_A^2 - K_{31}^2 - K_{31}^4) / K_{31}^2. \quad (80)$$

$\sqrt{2} Y_{\min}$  can be obtained at

$$\Delta\Omega = (1/2) \Omega_A \tan\phi' (\Omega_A^2 - K_{31}^2 - K_{31}^4) / (\Omega_A^2 + K_{31}^2 + K_{31}^4). \quad (81)$$

Thus, mechanical quality factor at the antiresonance can be obtained as:

$$Q = \Omega_A / 2\Delta\Omega = [(\Omega_A^2 + K_{31}^2 + K_{31}^4) / (\Omega_A^2 - K_{31}^2 - K_{31}^4)] (\tan\phi')^{-1}. \quad (82)$$

Since  $(\Omega_A^2 + K_{31}^2 + K_{31}^4) / (\Omega_A^2 - K_{31}^2 - K_{31}^4)$  is larger than 1,  $Q_m$  can be verified to be larger than  $Q_m$  at the resonance  $(= (\tan\phi')^{-1})$ . When  $k_{31}$  is small, using Eq. (75) and neglecting  $k_{31}^4$  or higher orders,  $Q$  is approximated as

$$Q = (1 + (8/\pi^2) k_{31}^2) (\tan\phi')^{-1}. \quad (83)$$

Note that this  $Q$  is equal to the inverse value of the intrinsic mechanical loss,  $(\tan\phi')^{-1}$ .

#### Experimental Results

Figure 18 illustrates mechanical quality factors,  $Q_A$ ,  $Q_B$  and the temperature rise for the resonance (A-type) and the antiresonance (B-type) modes for a rectangular-shape har PZT resonator plotted as a function of vibration velocity.<sup>4)</sup> The sample size is indicated in the figure (43 mm x 7 mm x 2 mm). Note that an "effective" vibration velocity  $v_0$  is a material's constant independent of the sample size, and is defined as  $\sqrt{2} \pi f u_{\max}$  where  $f$  is the resonance or antiresonance frequency and  $u_{\max}$  is the maximum vibration amplitude of the piezoelectric device.<sup>5)</sup> It is again noteworthy that the mechanical quality factor decreases dramatically above a certain critical

vibration velocity (0.1 m/s), where a steep temperature rise starts. We have suggested that the heat generation is mainly attributed to a P-E hysteresis loss rather than the pure mechanical loss.<sup>1)</sup> Note also that  $Q_B$  is higher than  $Q_A$  over the entire vibration velocity range, and that the temperature rise of the sample is less for the B-type resonance (antiresonance) than for the A-type resonance for the same vibration level. This indicates an interesting idea that the antiresonance mode should be superior to the conventional resonance mode, particularly for high power applications such as ultrasonic motors. In a typical piezoelectric material with  $k_{31}$  around 30 %, the plate edge is not a vibration nodal point and can generate a large vibration velocity.

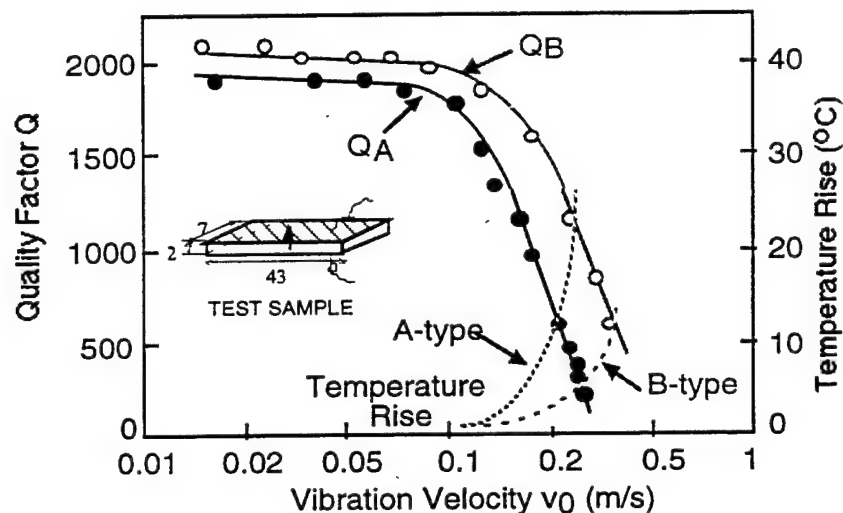


Fig.18 Vibration velocity dependence of the quality factor  $Q$  and temperature rise for both A (resonance) and B (antiresonance) type resonances of a longitudinally vibrating PZT ceramic transducer through transverse piezoelectric effect  $d_{31}$ .

## CONCLUSIONS

(1) Various techniques for measuring the electric, mechanical and piezoelectric coupling losses separately have been discussed:

- (a)  $D$  vs.  $E$ ,  $x$  vs.  $X$ ,  $x$  vs.  $E$  and  $D$  vs.  $X$  curves for electric, mechanical and piezoelectric losses
- (b) heat generation at an off-resonance frequency for an extrinsic electrical loss
- (c) resonance/antiresonance technique for intrinsic electric and extrinsic mechanical losses

By combining the above methods, we can investigate the loss mechanisms in practical piezoelectric materials.

(2) Heat generation is caused mainly by dielectric loss  $\tan \delta'$  (i.e., P-E hysteresis loss), not by mechanical loss. In order to suppress the temperature rise, a transducer design with larger surface area is recommended (for example, a tube rather than a rod).

(3) A dramatical decrease in mechanical  $Q_m$  with an increase of vibration level was observed in resonant piezoelectric ceramic devices, and the data obtained by a conventional impedance analyzer with a small voltage/power does not provide data relevant to high power materials.

(4) Since the mechanical quality factor  $Q_B$  at an antiresonance frequency is larger than  $Q_A$  at a resonance frequency, the antiresonance mode seems to be superior to the conventional usage of the resonance mode, particularly for high power applications such as ultrasonic motors.

#### REFERENCES

- <sup>1</sup>J. Zheng, S. Takahashi, S. Yoshikawa, K. Uchino and J. W. C. de Vries, *J. Amer. Ceram. Soc.*, **79**, 3193-98 (1996).
  - <sup>2</sup>K. Uchino, *Piezoelectric Actuators and Ultrasonic Motors*, (Kluwer Academic Publishers, Boston, 1997), pp. 197.
  - <sup>3</sup>S. Takahashi and S. Hirose, *Jpn. J. Appl. Phys.*, **32**, 2422-2425 (1993).
  - <sup>4</sup>S. Hirose, M. Aoyagi, Y. Tomikawa, S. Takahashi and K. Uchino, *Proc. Ultrasonics Int'l '95*, Edinburgh, pp. 184-87 (1995).
  - <sup>5</sup>K. Uchino, J. Zheng, A. Joshi, Y. H. Chen, S. Yoshikawa, S. Hirose, S. Takahashi and J. W. C. de Vries, *J. Electroceramics*, **2**, 33-40 (1998).
- For a general reference textbook:
- <sup>6</sup>T. Ikeda, *Fundamentals of Piezoelectric Materials Science*, (Ohm Publication Company, Tokyo, 1984), pp. 83.

# **MODELING and CHARACTERIZATION**

***Thin and Thick Films***

# **APPENDIX 71**

## Sol-Gel Processing of Piezoelectric Thin Films

ISAAC ROBIN ABOTHU<sup>ab</sup>, YUKIO ITO<sup>ab</sup>,  
PATCHARIN POOSANAAS<sup>b</sup>, SRIRAM KALPAT<sup>b</sup>,  
SRIDHAR KOMARNENT<sup>b</sup> and KENJI UCHINO<sup>b</sup>

<sup>a</sup>*Permanent address: Institute of Materials Research and Engineering (IMRE), National University of Singapore, Singapore -119260 and* <sup>b</sup>*Materials Research Laboratory, The Pennsylvania State University, University Park PA 16802, USA*

(Received December 8, 1998)

Lead zirconate titanate,  $\text{Pb}(\text{Zr}_x\text{Ti}_{1-x})\text{O}_3$  [PZT] rhombohedral thin films with [001] orientation were fabricated by sol-gel spin coating techniques. Using a methoxyethanol based precursor solution and rapid thermal annealing at 700°C for 30 seconds, crack free and homogeneous PZT thin films were successfully obtained. Preferred [001] oriented PZT thin films with  $x = 0.80$  showed a remanent polarization of 28  $\mu\text{C}/\text{cm}^2$  and a coercive field of 17 kV/cm.

**Keywords:** sol-gel processing; PZT thin films; MEMS

### INTRODUCTION

Micro-electro-mechanical system (MEMS) technology is a promising new high technology due to its wide range of applications for miniaturized sensors, analytical equipment and optical components etc. Commercial applications for MEMS now can be found in biomedical, manufacturing, information processing and automotive fields. Ferroelectric thin films fit naturally into the burgeoning field of MEMS, which combine Si-IC electronics with microsensors and microactuators. PZT films are promising candidates for MEMS applications, because of their strong piezoelectric behavior. To achieve high performance MEMS devices, high quality, crack free, homogeneous PZT thin films with excellent piezoelectric properties are desired. PZT thin films have been prepared by various methods including rf sputtering <sup>[1]</sup>, laser ablation <sup>[2]</sup>, metallo-organic decomposition <sup>[3]</sup> and the sol-gel process <sup>[4]</sup>. Sol-gel processing

of PZT thin films has gained much interest because of its (i) simplicity (ii) low processing temperature (iii) chemical homogeneity and stoichiometry control and (iv) ability to produce uniform film over a large area. The crystallization and the texture development of sol-gel PZT thin films as a function of pyrolysis and crystallization temperatures have been extensively investigated<sup>[5]</sup>.

Recently, one of the authors predicted theoretically that the maximum values of piezoelectric  $d_{33}$  constant and electromechanical coupling factor  $k_{33}$  occur for the rhombohedral PZT compositions at angles 50-60° canted from the spontaneous polarization direction [111], which correspond to the [001] orientation<sup>[6]</sup>. The [001] orientation is expected to enhance the piezoelectric constant of PZT by more than 3 times of the [111] orientation. Thus, if [001] oriented films with the rhombohedral phase could be produced, they would be expected to have superior piezoelectric properties.

In view of the above, an attempt is made here to fabricate highly [001] oriented rhombohedral PZT (80/20) sol-gel thin films on Pt/Si substrates using a methoxyethanol based precursor solution and rapid thermal annealing (RTA). This paper describes the fabrication and the characteristics of [001] oriented, rhombohedral PZT thin films using sol-gel and spin-coating techniques.

### **Experimental**

A precursor solution of PZT (80/20) was prepared using the procedure reported in our earlier work<sup>[7]</sup>. Figure 1 shows the flow chart for the fabrication of PZT thin film. Initially, PZT precursor solution was spin-coated on Pt(111)/Si substrate (supplied by Nova Electronics Comp. USA). The thickness of Pt was 150nm. Spin coating was done using a spin coater (P-6000, Integrated Technologies, Acushnet, MA) operated at 3000 rpm for 30 seconds. Before spin coating, the precursor solution was passed through 0.2  $\mu\text{m}$  nylon filter (Aldrich). Rapid pyrolysis of PZT gel films was achieved by placing on a hot plate at 350°C for 10 mins in air. By repeating this process, multilayer depositions (4 coatings)



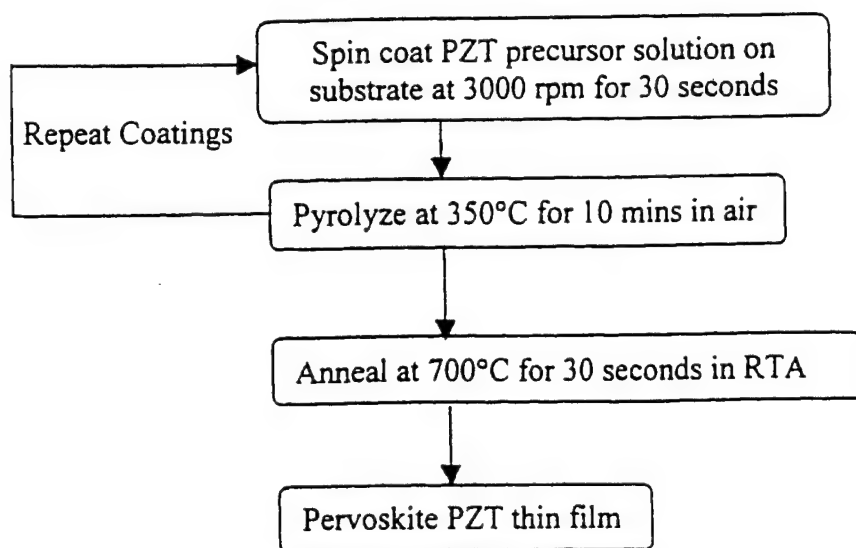


FIGURE 1. Flow chart for the fabrication of sol-gel PZT thin film

were performed to increase film thickness. These amorphous films were subsequently converted to crystalline  $\text{Pb}(\text{Zr}_{0.80}\text{Ti}_{0.20})\text{O}_3$  by annealing at  $700^\circ\text{C}$  for 30 seconds using rapid thermal annealing (RTA). Crystallization behavior of the films was studied using X-ray diffractometer (Scintag model DMC 105) with  $\text{CuK}\alpha$  radiation. The P-E hysteresis curves of these films were measured using a Radiant Technologies RT-66A Ferroelectric Tester.

### Results and discussion

The PZT (80/20) thin films were first deposited on Pt(111)/Si substrates using the sol-gel procedure mentioned above. Following pyrolysis of the fourth layer, the amorphous film was rapidly annealed at  $700^\circ\text{C}$  for 30 seconds, yielding a crystalline layer of  $0.3\mu\text{m}$  thickness. The film was crack free and homogenous. Figure 2 shows the XRD pattern of the PZT film. This pattern indicates that the film is a single phase PZT with a perovskite rhombohedral structure. However, [001] and [002] reflections are relatively strong. That is, preferred [001] oriented PZT film was obtained, even though Pt(111)/Si substrate was used. This preferred [001] oriented PZT film was characterized in terms of its polarization hysteresis loop.

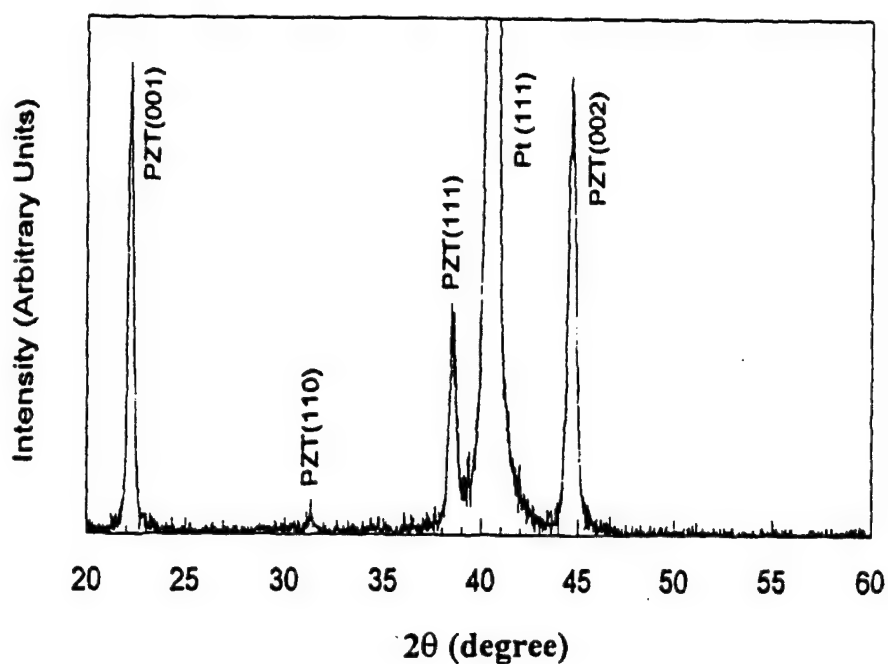


FIGURE 2. XRD pattern of PZT (80/20) film deposited on [111] oriented Pt/Si substrate.

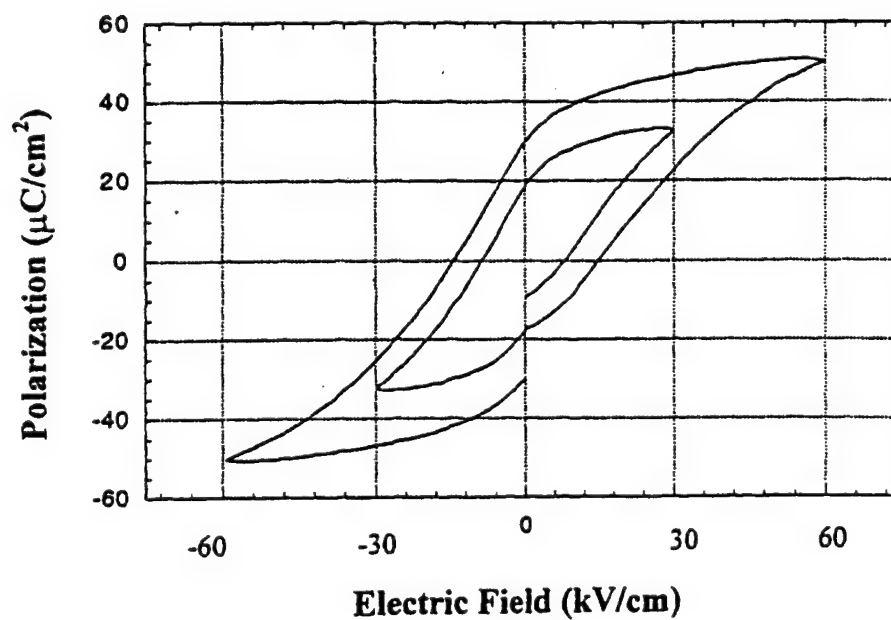


FIGURE 3. Ferroelectric hysteresis loop of [001] oriented PZT (80/20) thin film.

The result is shown in figure 3. The film showed well saturated hysteresis loop with a remanent polarization of  $28 \mu\text{C}/\text{cm}^2$  and a coercive field of  $17 \text{ kV}/\text{cm}$  comparable with PZT bulk ceramics. Further work related to the fabrication of [001] and [111] oriented rhombohedral PZT films and the comparison of their ferroelectric and piezoelectric properties will be explored in the future.

### Conclusions

Crack free, homogeneous PZT (80/20) thin films were fabricated on Pt(111)/Si substrates by sol-gel and spin-coating technologies. The films were annealed at  $700^\circ\text{C}$  for 30 seconds using RTA. Films were found to have preferred [001] orientation. These films showed a remanent polarization of  $28 \mu\text{C}/\text{cm}^2$  and a coercive field of  $17 \text{ kV}/\text{cm}$ .

### Acknowledgements

This research was supported by Institute of Materials Research and Engineering (IMRE), National University of Singapore, Singapore-119260.

### References

- [1] S.B. Krupanidhi and M. Sayer, *J. Vac. Sci. Technol. A*, **2**, 303 (1989).
- [2] D. Roy, S.B. Krupanidhi and J. Dougherty, *J. Appl. Phys.*, **69**, 7930 (1992).
- [3] R. Vest, *Ferroelectrics* **102**, 53 (1990).
- [4] S. L. Swartz, S.J. Bright, J.R. Busch and T.R. Shrout, *Ceram. Trans.*, **14**, 159 (1990).
- [5] S.Y. Chen and I.W. Chen, *J. Am. Ceram. Soc.*, **77**, 2332 (1994).
- [6] X.H. Du, U. Belegundu and K. Uchino, *Jpn. J. Appl. Phys.*, **36**, 5580 (1997).
- [7] U. Selvaraj, K. Brooks, A.V.P. Rao, S. Komarneni, R. Roy and L.E. Cross, *J. Am. Ceram. Soc.* **76**, 1441 (1993).

# **APPENDIX 72**

# DIELECTRIC PROPERTIES OF HIGHLY ORIENTED LEAD ZIRCONIUM TITANATE THIN FILMS PREPARED BY REACTIVE RF-SPUTTERING

S. Kalpat<sup>\*</sup>, X.Du<sup>\*</sup>, I.R.Abothu<sup>\*\*</sup>, A.Akiba<sup>\*\*\*</sup>, and H.Goto<sup>\*\*\*</sup>, S.Trolier McKnistry<sup>\*</sup> and K.Uchino<sup>\*</sup>

<sup>\*</sup> International Center for Actuators and Transducers, Materials Research Laboratory, The Pennsylvania State University, University Park, Pa 16802, <sup>\*\*</sup> Institute of Materials Research and Engineering, Kent Ridge, Singapore 119260, <sup>\*\*\*</sup> OMRON Corporation, Tsukuba city, Ibaraki-Pref, Japan 300-4247

## ABSTRACT

Highly (100) and (111) oriented lead zirconium titanate (PZT) thin films have been grown by using reactive rf-sputtering. PZT thin films with rhombohedral composition have been grown in different orientations using selective rapid thermal annealing cycles. The polarization versus electric field curves and the resistivity of the films were measured using a standardized RT66A ferroelectric test system. The dielectric constant and the loss were determined using an impedance analyzer. The PZT(100) oriented films showed larger dielectric constant and loss than the PZT(111) films. The PZT(100) films possessed sharper square-like hysteresis loops compared to the PZT(111) films, as expected from our phenomenological calculations.

## INTRODUCTION

Rooted in early research on materials and processes for the emerging field of integrated circuits in the late 1960's, there has been significant progress in the area of microelectromechanical systems (MEMS) in the past two decades[1,2]. During the past few years there has been an explosion of interest in MEMS, which has become a critical technology in the growth of various fields like medical, automotive, chemical, and space technology. PZT thin films hold great potential as actuator materials in MEMS devices[3]. Explicit knowledge of the dielectric and piezoelectric properties of PZT thin films at different crystal orientations needs to be investigated to enhance its performance and hence meet the challenging requirements of the MEMS industry.

Our group has previously reported theoretical calculations based on the phenomenological consideration of the crystal orientation dependence of the dielectric and piezoelectric properties in PZT thin films[4]. We have reported that for PZT 60/40 in the rhombohedral region of the phase diagram, the electric field induced polarization hysteresis loops are expected to be sharper and square-like for PZT(100) when compared to the smoother and slanted loops for PZT(111). The piezoelectric property dependence on crystal orientation has also been reported. Changing the crystal orientation dramatically enhances the effective piezoelectric constant  $d_{33}^{eff}$ . Figure 1 shows the change in  $d_{33}^{eff}$  with crystal orientation. Figure 2 gives the schematic explanation for this expectation. The  $d_{33}^{eff}$  value is three times larger for the [001] direction compared to that of the [111] direction. In the rhombohedral phase there are 8 possible polarization directions. Considering the (111) oriented films, the possible polarization directions 2,3, and 4 are equivalent and are about  $70.5^\circ$  away from the spontaneous polarization direction 1. The other possible directions are 6,7,8 and 5. When the electric field of a completely poled sample along axis 5, the polarization gets reversed, the polarization reversal has various possibilities 5-1; 5-(2,3,4), 5-(6,7,8); 5-(6,7,8)-1; 5-(6,7,8)-(2,3,4); 5-(2,3,4)-1 etc., hence the reverse segments in the polarization curves are inclined. In the (100) film, there are two sets of equivalent directions, (1,2,3,4) and (5,6,7,8). The polarization directions are  $54.7^\circ$  away from the normal of the film,

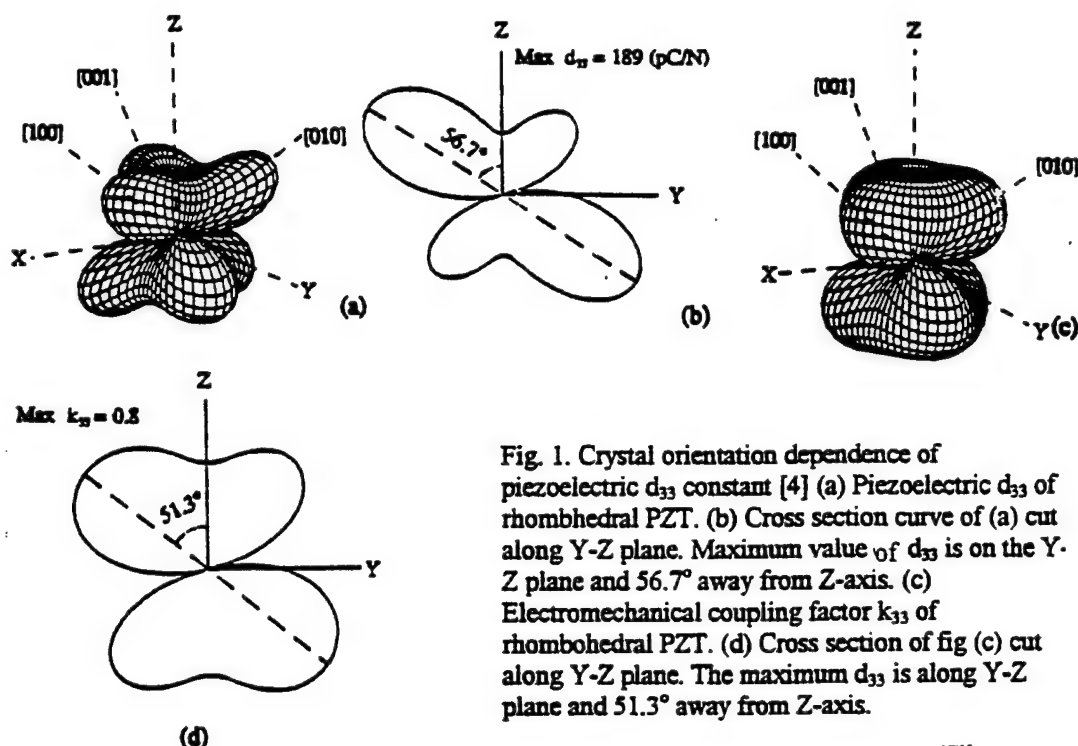


Fig. 1. Crystal orientation dependence of piezoelectric  $d_{33}$  constant [4] (a) Piezoelectric  $d_{33}$  of rhombohedral PZT. (b) Cross section curve of (a) cut along Y-Z plane. Maximum value of  $d_{33}$  is on the Y-Z plane and  $56.7^\circ$  away from Z-axis. (c) Electromechanical coupling factor  $k_{33}$  of rhombohedral PZT. (d) Cross section of fig (c) cut along Y-Z plane. The maximum  $d_{33}$  is along Y-Z plane and  $51.3^\circ$  away from Z-axis.

when the electric field  $E_3$  is switched from positive to negative, the domains along 1,2,3,4 are reversed at the same time leading to abrupt polarization reversal. Theoretically the remnant polarization of the (100) films is expected to be  $1/\sqrt{3}$  times that of (111) oriented films, a similar magnitude of the remnant polarization is expected due to the square-like hysteresis behavior of the (100) oriented films. Accordingly, we can expect an ideal strain curve like a butterfly hysteresis. Based on the above background we are investigating highly oriented PZT thin films in various crystal orientations. In this paper, the fabrication process and the dielectric property dependence of highly oriented PZT thin films will be discussed.

## EXPERIMENTATION

PZT thin films were deposited by reactive rf-sputtering using multielement metallic targets of lead, zirconium and titanium. A 3" circular target was made using individual wedges of the Pb, Zr and Ti. The target composition (Pb:Zr:Ti::4:8:9) was adjusted so as to fabricate a rhombohedral composition of PZT(70/30). Substrates used were highly (111) oriented platinum coated  $\text{SiO}_2/\text{Si}$  wafers. All the substrates were thoroughly cleaned with isopropyl alcohol and rinsed in deionized water prior to film deposition. The substrates were clamped to a stainless steel holder and heated by quartz lamps to  $450^\circ\text{C}$ . The rf-sputtering system (Anelva SPC-350) was evacuated to a base pressure of  $1 \times 10^{-4}$  Pa, the films were grown at 20 mTorr pressure with Ar/ $\text{O}_2$  ratio at 50/50. The films were grown at rf-power of 150 watts at a deposition rate of 0.1  $\mu\text{m/hr}$ . The as-deposited films were amorphous with some microcrystallization of the perovskite phase, annealed using rapid thermal annealing (RTA). The structural characterization of the films was made by X-ray diffraction using the Cu  $K\alpha$  radiation. For electrical characterization, the crystallized films were coated with 150 nm thick platinum top electrodes by dc sputtering using a shadow mask; the electrode area used was  $2.38 \times 10^{-3} - 1.77 \times 10^{-2} \text{ cm}^2$ . The polarization versus

electric field hysteresis loop, the quasi-static capacitance-voltage measurements, and the resistivity measurements were made using RT66A standardized hysteresis tester(Radiant Technologies). The quasi-static C-V measurements were made using the RT66A hysteresis tester at a frequency of 60 Hz. The dielectric constant and loss factor were measured as a function of frequency using an impedance analyzer(HP4192) in the frequency range between 10 Hz and 1 MHz.

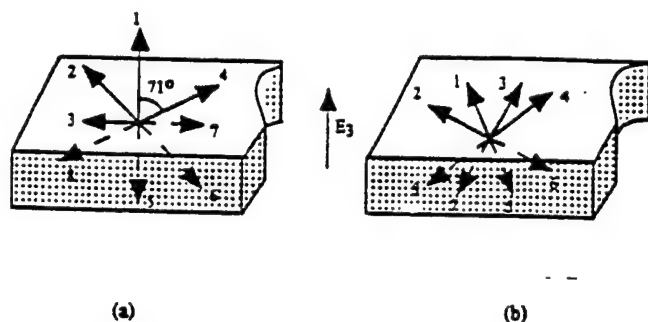


Fig 2. Possible spontaneous polarization directions[4] (a) (111) oriented films (b) (001) oriented films.

## RESULTS AND DISCUSSION

The XRD patterns of the annealed films are shown in Fig.3. The XRD patterns indicate that highly oriented PZT(100) and PZT(111) films have been fabricated. The degree of crystal orientation was calculated from the integrated intensity of the PZT(111) and PZT(100) peaks and can be expressed as  $\text{Int}_{(111)} = I(111)/[I(111) + I(100)]$ . The degree of crystal orientation obtained for  $\text{Int}_{(111)}$  was  $> 98\%$  and that for  $\text{Int}_{(100)}$  was  $> 95\%$ . The deposited films were annealed using a rapid thermal annealing(RTA) at different rates so as to crystallize the films to (100)/(111) perovskite structure. The crystal orientation of the substrate is critical in obtaining the desired orientation of the PZT films[5,6]. Highly oriented PZT(111) films can be easily grown on Pt(111)/SiO<sub>2</sub>/Si, but obtaining PZT(100) oriented film on Pt(111)/SiO<sub>2</sub>/Si substrate has not been widely reported[7,8]. The surface energy for the PZT(111) orientation is lower on Pt(111)/SiO<sub>2</sub>/Si as compared to that for PZT(100), hence the growth of PZT(111) is kinetically

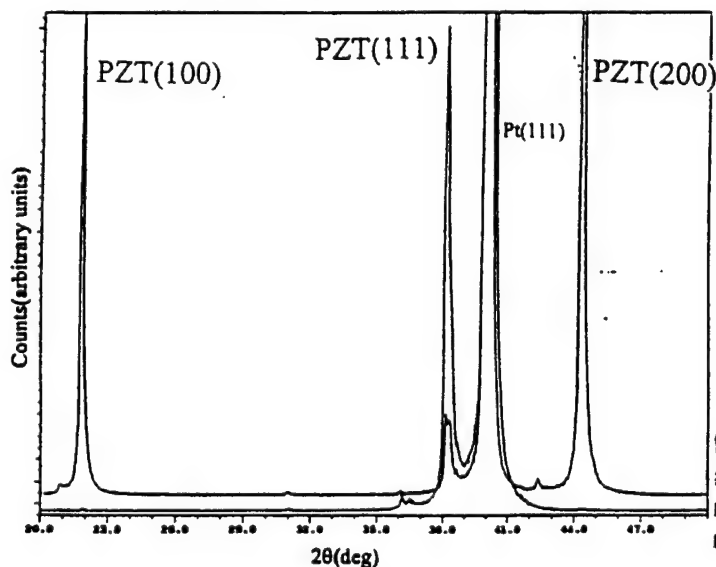


Fig. 3. XRD pattern of highly oriented PZT(111) and PZT(100) on Pt(111)/SiO<sub>2</sub>/Si in the rhombohedral composition 70/30 annealed using rapid thermal annealing(RTA).

However PZT(100) growth plane has the lowest activation energy for nucleation, and in the absence of any microcrystallization of pyrochlore phase, the nucleation of (100) orientation is easier and subsequent growth of the (100) plane is favored. Figure.4 shows the selective rapid thermal annealing(RTA) cycles for obtaining PZT(100) and PZT(111) on the same Pt(111)/SiO<sub>2</sub>/Si substrate.

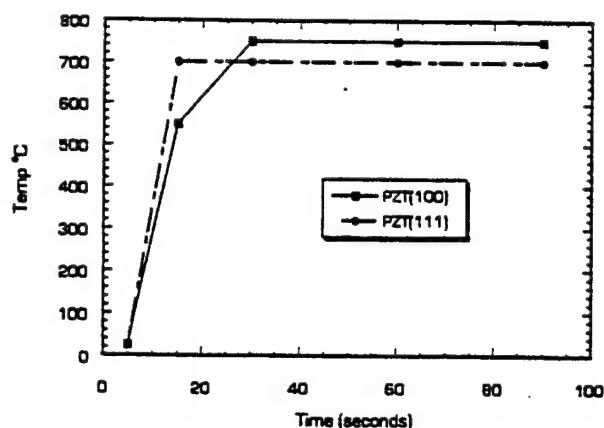


Fig. 4. Crystallization of highly oriented films using selective rapid thermal annealing cycles for PZT(111)/Pt/SiO<sub>2</sub>/Si and PZT(100)/Pt/SiO<sub>2</sub>/Si.

The electrical characterization of the films was made after making the top electrodes of platinum by dc sputtering using shadow masks. The dielectric constant and the loss factors are shown in fig.5 as a function of frequency for both the (111) and the (100) films. The films were poled with an electric field of 150 kV/cm for 30 minutes and then aged for an hour prior to measuring the dielectric constant at an oscillating ac frequency of 0.01 V. The dielectric constant and the loss factors are shown in Table 1, PZT(100) possess a larger dielectric constant and loss values compared to PZT(111). The loss values for the PZT(100) were in the range 0.03-0.035 and were larger than those for PZT(111) films which ranged from 0.02-0.03 at a frequency of 1 kHz. Figure 6 (a) and (b) show the P-E hysteresis loops and the quasi-static C-V curves(which is equivalent to the derivative of the P-E curves) for both PZT(111) and PZT(100) films.

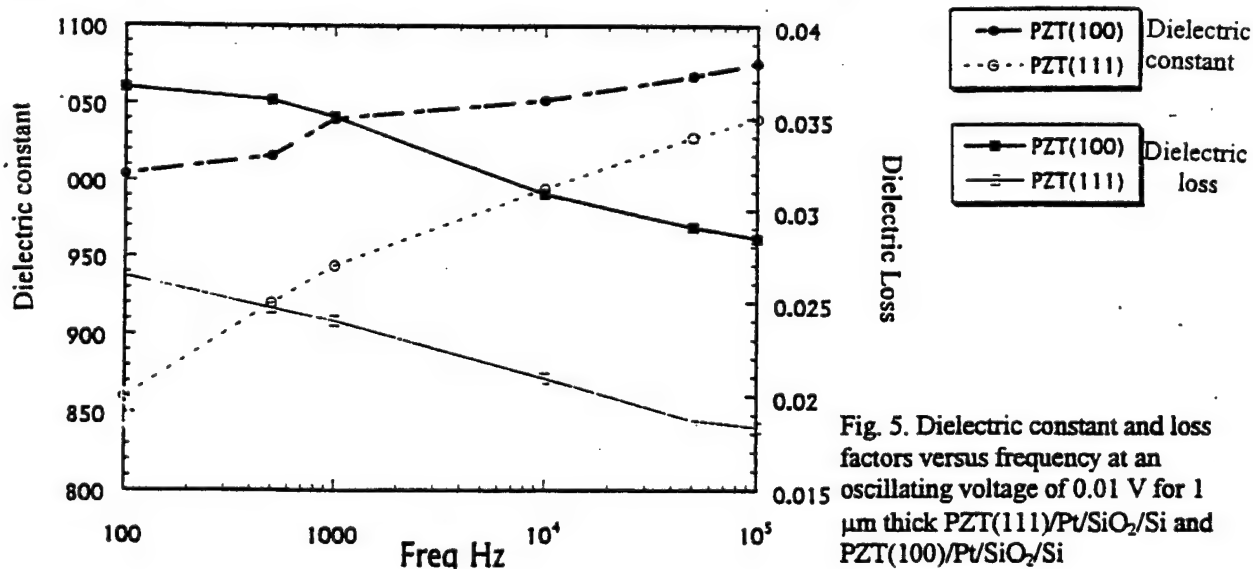


Fig. 5. Dielectric constant and loss factors versus frequency at an oscillating voltage of 0.01 V for 1  $\mu$ m thick PZT(111)/Pt/SiO<sub>2</sub>/Si and PZT(100)/Pt/SiO<sub>2</sub>/Si



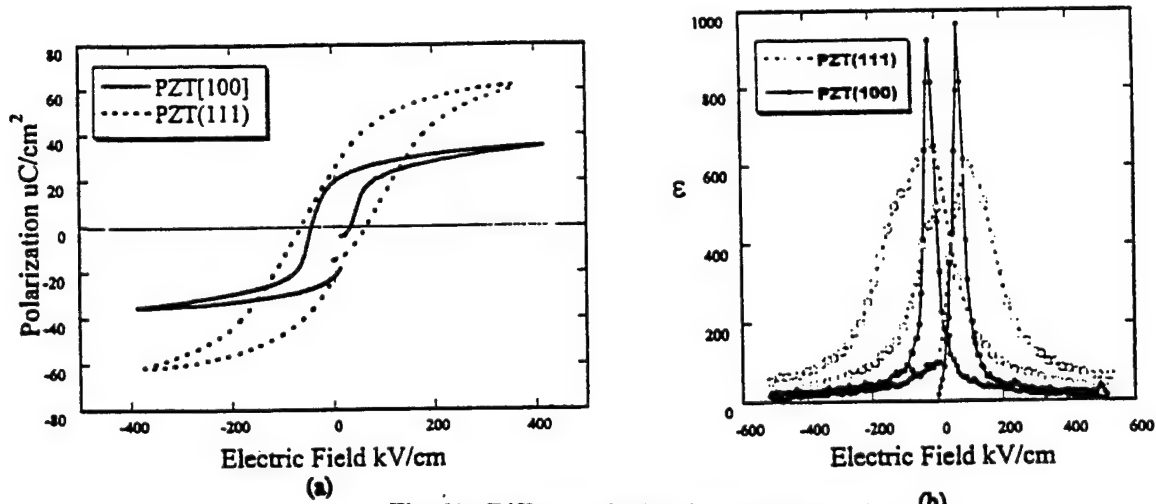


Fig. 6(a) Difference in the dielectric hysteresis between PZT(111) and PZT(100) measured using RT66A Ferroelectric tester. (b) Dielectric constant versus voltage characteristics of PZT(111) and PZT(100) 1  $\mu$ m thick films.

The saturation polarization values for PZT(111) oriented films are larger than those for the PZT(100) oriented films by a factor of  $\sqrt{3}$  as proposed by theoretical calculation[4]. The coercive field is smaller for the (100) films when compared to (111) films. From fig.7 it can be seen that there is an abrupt saturation of the coercive field value in PZT(100) films at an applied field of 150 kV/cm whereas the saturation is gradual in (111) films until breakdown. The polarization curve in the case of PZT(100) is abrupt and square-like and is relatively smooth in the case of PZT(111). This result is expected from our theoretical calculation. Figure 6(b) shows the C-V loops for PZT(100) and PZT(111). The (100) films have a higher maximum than the (111) films, which indicates that domain switching occurs readily near the coercive field for the (100) films. The (100) films have sharper peaks compared to the broader peaks for the (111) films.

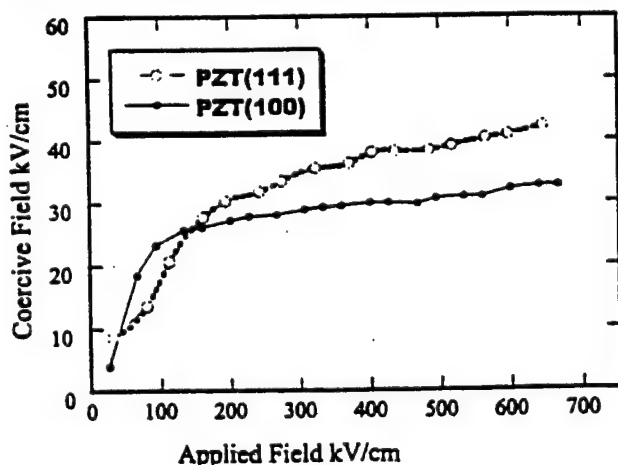


Fig. 7. Difference in the coercive field versus applied maximum field for PZT(100) and PZT(111) films.

Table 1 summarizes the dielectric constant, loss, coercive field, spontaneous polarization and remnant polarization for the PZT(100) and PZT(111) films. The piezoelectric characterization of the films is currently underway.

Table 1. Dielectric properties of PZT(111) and PZT(100) oriented films on Pt/SiO<sub>2</sub>/Si.

Property	Dielectric Constant	Dielectric loss factor @ 1 kHz	Spontaneous Polarization ( $\mu\text{C}/\text{cm}^2$ )	Remnant polarization ( $\mu\text{C}/\text{cm}^2$ )	Coercive Field (kV/cm)
PZT(111)	900	.025	55	25	65
PZT(100)	1050	.035	28	20	35

## CONCLUSIONS

Highly oriented PZT(100) and PZT(111) thin films have been grown by reactive rf magnetron sputtering using multielemental metallic targets. The crystal orientation dependence of the dielectric properties of PZT(111) and PZT(100) on Pt/SiO<sub>2</sub>/Si substrates has been investigated to compare the results with the reported theoretical calculation for PZT thin films. The dielectric constant and loss for PZT(100) were found to be larger than those for PZT(111). The P-E hysteresis loops and the C-V loops were found to be sharper for the (100) than for (111) indicating that the domain wall movement in (100) films occurs simultaneously at a particular field compared to the gradual switching of the (111) oriented films. The saturation polarization for PZT(111) is about  $1/\sqrt{3}$  times larger than that for PZT(100). The experimental observation seems to have good agreement with the reported theoretical calculations made for PZT thin films based on the phenomenology.

## REFERENCES

1. K.D.Wise, Proc. IEEE Micro Electro Mechanical Systems Workshop, Nara, p33-38, 1991
2. M.Mehgany, Circuits and Devices, pp14-22, 1993
3. D.L.Polla and P.J.Schiller, Integrated Ferroelectrics, Vol 7, pp 359-370, 1995
4. X.Du, U.Belegundu and K.Uchino, Jpn. J. Appl. Phy., Vol 36 Pt 1, No:9 A, pp 5580- 5587, 1997
5. K.Ijima, I.Ueda and K.Kugimiya, Jpn. J. Appl. Phy., Vol 30, No:9 B, pp2149-2151,1991
6. T.Ogawa, A.Senda, T.Kasanami, Jpn. J. Appl. Phy., Vol 30, No:9 B, pp 2145-2148, 1991
7. J.Senzaki, O.Mitsunaga, T.Uchida, T.Uena, K.Kuroiwa, Jpn. J. Appl. Phy., Vol 35, Pt 1, No:8, pp 4195-4198, 1996
8. A.Masuda, Y.Yamanaka, M.Tazoe, Y.Yonezawa, A.Morimoto, T.Shimiza, Jpn. J. Appl. Phy., Vol 34, pp 5154-5157, 1997

## ACKNOWLEDGEMENTS

The authors would like to thank the Office of Naval Research for supporting this work through the contract, N00014-91-J-4145.

# **APPENDIX 73**

## Longitudinal piezoelectric coefficient measurement for bulk ceramics and thin films using pneumatic pressure rig

F. Xu,<sup>a)</sup> F. Chu, and S. Trolier-McKinstry

*Materials Research Laboratory, The Pennsylvania State University, University Park, Pennsylvania 16802*

(Received 12 October 1998; accepted for publication 11 January 1999)

A pneumatic pressure rig was designed to measure the effective  $d_{33}$  coefficient of thin film piezoelectrics by applying a known stress and monitoring the induced charge. It was found that the stress state imposed included components both perpendicular and parallel to the film plane. The latter were due to friction and could largely be relieved through sliding of the O-rings to their equilibrium positions for a given pressure. The induced charge stabilized as equilibrium was reached and most of it was produced by the normal component of the stress. By minimizing the surface friction and compensating for the remnant in-plane stress, very good agreement was obtained among the  $d_{33}$  values measured by the Berlincourt method, double-beam interferometry and this method for a bulk lead zirconate titanate (PZT) sample. The  $d_{33}$  value of PZT thin films made by sol-gel processing was also measured. The as deposited films usually showed very weak piezoelectricity with  $d_{33}$  values ranging from 0 to 10 pC/N, indicating little pre-existing alignment of the domains. With increasing poling field, the  $d_{33}$  value also increased and saturated at poling fields exceeding three times the coercive field. Typically, films with thicknesses around 1  $\mu\text{m}$  had  $d_{33}$  values of 100 pC/N. Good agreement between double-beam interferometry and this technique was also obtained for thin films. The small difference between the two measurements is attributed to the effect of mechanical boundary conditions on the effective  $d_{33}$  coefficient. © 1999 American Institute of Physics. [S0021-8979(99)05813-2]

### I. INTRODUCTION

There has been a great deal of interest paid to the design and fabrication of microelectromechanical systems (MEMS) in recent years. Micromechanical actuators based on piezoelectricity are particularly attractive due to the high energy densities, and high-transmitted forces and torques which can be achieved.<sup>1,2</sup> Piezoelectric devices such as sensors and actuators can be fabricated at low cost using silicon technology designed for integrated circuits. A variety of applications for piezoelectric thin films integrated on silicon substrates, including micromotors,<sup>2,3</sup> accelerometers,<sup>4</sup> and microsonar arrays,<sup>5</sup> have been described.

For the design of miniature sensors and actuators, it is desirable to have a comprehensive knowledge of material properties such as the elastic and piezoelectric constants. However, for piezoelectric thin films, reliable measurements of the piezoelectric coefficients are still not widely available. Due to the constraints imposed by the substrate, the piezoelectric coefficients of thin films cannot be directly measured through standard resonance methods,<sup>6</sup> thus static or quasi-static methods have to be used. These methods can be categorized by whether the direct piezoelectric effect, i.e., applying a stress and measuring the induced charge, or the converse piezoelectric effect, i.e., applying a voltage and measuring the induced elongation, is used. It should be pointed out that in these measurements, the ratio between charge and stress (or strain and voltage) does not represent the piezoelectric coefficient of the free sample, but an effective

coefficient since the film is clamped to the substrate.

For converse measurements of the effective  $d_{33}$ , the longitudinal elongation of the film is on the order of 0.1–100 Å due to the small film thickness ( $\sim \mu\text{m}$ ). Laser interferometry has been used to measure these displacements.<sup>7,8</sup> Although reasonable values of effective  $d_{33}$  have been reported for both single-beam and double-beam interferometer systems,<sup>9,10</sup> reliable measurement using a single-beam instrument is very difficult because of both bending and backside motion of the sample.<sup>10,11</sup> Double-beam interferometry is able to measure the film dilatation accurately by eliminating the influence of substrate motion (including bending), but it requires a more sophisticated optical system and the measurement is strongly influenced by the optical alignment.

On the other hand, although the direct piezoelectric effect has been widely used in determining  $d_{33}$  for bulk piezoelectric materials, little success has been achieved for piezoelectric thin films. The major obstacle which prevents this kind of measurement for thin films is believed to be the simultaneous bending of the sample when force is applied perpendicular to the film plane to produce a uniaxial stress. In a thin film sample, a very thin layer of piezoelectric material is rigidly clamped to a much thicker substrate. As a result, even a small substrate bending can generate very large biaxial stresses in the piezoelectric thin film, which in turn produces a large amount of electrical charge through the transverse piezoelectric effect. This makes the accurate measurement of the charge induced by the applied uniaxial stress very difficult. Another problem for thin film  $d_{33}$  measurements is that the small thickness of the sample makes stress alignment very difficult.

<sup>a)</sup>Electronic mail: fxx101@psu.edu

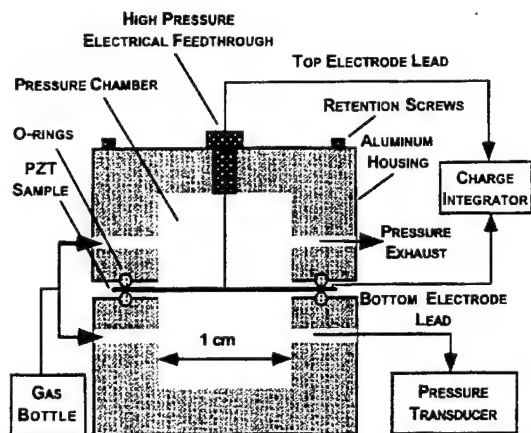


FIG. 1. Schematic drawing of the experimental setup for  $d_{33}$  measurement.

In this article, a pneumatic pressure rig designed to apply a uniaxial stress to piezoelectric thin films is described. The piezoelectric charge response of both bulk and thin film lead zirconate titanate (PZT) samples due to the applied stress was studied over the pressure range from 0 to 1.2 MPa. It was found that a component of in-plane stress led to inflated  $d_{33}$  values in both bulk and thin film samples. A measurement procedure which eliminated the error by self-compensating the remnant in-plane stress was then developed.

## II. EXPERIMENTAL PROCEDURE

The experimental setup developed in this work is shown schematically in Fig. 1. There were two major parts of this setup: a pneumatic pressure rig which was designed to apply a uniform uniaxial stress to the tested sample and a charge integrator. The stress rig consisted of two identical aluminum components machined with cavities 1 cm in diameter. The sample was placed between the aluminum fixtures with cavities both above and beneath it. The two cavities were connected so that the pressure inside them was always equal. O-rings were used on both sides of the sample for sealing. To reduce the surface friction, Parker O-lube lubricant was applied between the O-ring and the sample. By introducing high-pressure nitrogen gas into these cavities simultaneously, forces were imposed which acted uniformly and equally on both sides of the sample, thus a uniform uniaxial compressive stress was applied to it. Similarly, releasing the pneumatic pressure resulted in a uniaxial stress of opposite sign. The pressure inside the two cavities was measured using Omega PX602 pressure transducers. The pressure applied in this experiment was in the range from 0 to 1.2 MPa. Because the applied force was balanced everywhere across the faces of the sample, the application of pneumatic pressure would not bend the sample even if it had an initial curvature due to the thermal expansion coefficient mismatch between the piezoelectric film and the substrate. Another advantage of using pneumatic pressure is that a uniaxial stress can be obtained without the need to align the stress rig, even though the film thickness is much smaller than the lateral dimension

of the sample. Unlike the normal load method, because there is no solid contact between the sample surface and the gas, uniform stress can be produced easily on a sample with non-flat surfaces (which is usually the case for piezoelectric thin films due to the finite thickness of the top electrode).

The induced charge produced upon applying or releasing pressurized gas was collected using a charge integrator<sup>12</sup> which converted the collected charge into a variation of voltage on a capacitor of known size placed in series with the stressed sample. Since the circuit was in virtual ground mode, the voltage between the two electrodes of the sample was always zero, so that almost all the induced charge was driven to the capacitor. The voltage output from the charge integrator was monitored in real time using a Hewlett Packard 54600A oscilloscope.

The piezoelectric coefficient  $d_{33}$  (bulk material) or effective  $d_{33}$  (thin film) was calculated using the following equation:

$$d_{33} = \partial D_3 / \partial T_3 = \Delta Q / (\Delta P \cdot A), \quad (1)$$

where  $D_3$  and  $T_3$  are the electrical displacement and mechanical stress in thickness direction,  $\Delta P$  is the change of the cavity pressure,  $\Delta Q$  is the measured electric charge induced by that pressure change, and  $A$  is the area of the electrode.

The charge response of both a PZT bulk ceramic sample and PZT thin films were investigated in this work. The bulk ceramic studied was a piece of PZT-5A which was 25 mm by 25 mm by 2 mm in size and polished with 1  $\mu$ m alumina powder on both sides. A thin layer of Pt was sputtered on one entire face for the bottom electrode. On the other side, a 7.5 mm diameter top electrode was also formed with sputtered Pt. The sample was then poled at 100 °C for 10 min under an electric field of 20 kV/cm. PZT thin films were prepared by the sol-gel method. The procedure for the preparation of the sol-gel films can be found elsewhere.<sup>13</sup> The substrate used was platinum-coated, oxidized silicon wafer with a thin titanium adhesion layer. The composition of the film was  $\text{Pb}(\text{Ti}_{0.48}\text{Zr}_{0.52})\text{O}_3$ , which is at the morphotropic phase boundary. Top electrodes were formed by sputtering a thin platinum layer through a shadow mask with an array of 1.6 mm diameter holes. The back of the sample was polished with 1  $\mu$ m alumina powder. Air dry silver epoxy was used to contact the top and bottom electrodes of the thin film capacitor. Poling was performed at room temperature.

The double-beam interferometer measurements of  $d_{33}$  for both bulk and thin film PZT samples were made using a system described elsewhere.<sup>7,8</sup> A ZJ-2 piezoelectric  $d_{33}$  meter (Institute of Acoustics, Academia Sinica) was also used to measure the  $d_{33}$  value of the bulk PZT sample. The dielectric constant and loss factor were measured using an HP4192 LCR meter, and the ferroelectric hysteresis loop was measured using a RT66A ferroelectrics tester (Radiant Technologies).

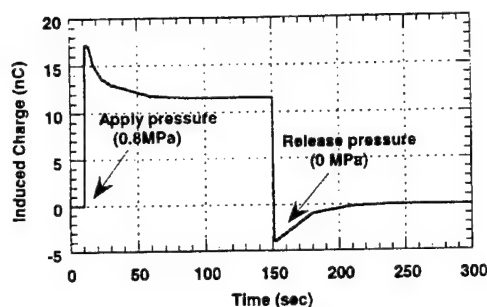


FIG. 2. Charge response of the bulk PZT sample to applied pneumatic pressure.

### III. RESULTS AND DISCUSSION

#### A. Measurements on bulk PZT

##### 1. Charge response and stress analysis

The charge response of the bulk PZT sample upon applying and releasing pressure was investigated first to study the stress state induced by pneumatic pressure. As shown in Fig. 2, when pressurized gas was introduced into the rig, the induced charge quickly reached a maximum, followed by a continuous asymptotic decrease, until it stabilized after about 90 s. The measured pressure in both cavities was equal and constant throughout the signal stabilization. The signal measured after releasing pressure was very similar to the signal on applying pressure, and the final values of the signal at stabilization were almost equal in magnitude, though opposite in sign. It should be emphasized here that the variation of the measured induced charge was not due to the leakage either from the PZT sample or the electronics. This was verified by applying a constant normal load to this sample. A step signal was indeed obtained, as expected. This result indicated that the time dependence of the induced charge observed on the oscilloscope was caused by some kind of change in the stress applied to the PZT sample. Since the pressure was constant inside the cavities, there was no change in the stress which was perpendicular to the sample plane. Obviously the pneumatic pressure also generated an additional stress component, and this stress was time dependent.

We have demonstrated that the in-plane stress induced by friction between the O-ring and the sample surface was the origin of the above observation.<sup>14</sup> The friction arises when there is a pressure change introduced into the cavities. Increasing the pressure increases the force acting on the O-ring parallel to the surface and pushes the O-rings outwards. This force generates surface friction on both sides of the sample, so that an equivalent tensile in-plane stress is created. The in-plane stress decreases over time as the pneumatic pressure acting on the O-ring leads to O-ring sliding. O-ring sliding reduces the net force acting on the O-ring by creating a restoring force via deformation. Eventually the in-plane stress stabilizes as a force balance on the O-ring is reached. The net result is that in addition to the desired compressive stress normal to the wafer surface created by pressurizing the cavities, remnant tensile in-plane stress is also

produced by the pneumatic pressure at the steady state. For the same reason, a compressive in-plane stress arises when pressure is released from the cavity, since the unbalanced O-ring restoring forces cause the O-rings to slide back towards their original positions. Since  $d_{31}$  and  $d_{33}$  have opposite signs in PZT, the piezoelectric charges induced by the normal component of the stress and the in-plane stresses add to each other. With the decrease in the in-plane stress over time, the total amount of induced charge also decreases. Finally, at steady state, both stresses are constant and the signal no longer changes with time. At this point, the in-plane stress was at its minimum since a majority of it had been released through O-ring deformation or recovery. Since the induced charge measured at this stage contains the smallest signal induced by the in-plane stress component, it was used to approximate the  $d_{33}$  coefficient using Eq. (1).

##### 2. Remnant in-plane stress analysis

To evaluate the remnant in-plane stress level at stabilization and the error in the calculated  $d_{33}$  introduced by that stress, a calibration was done by comparing the calculated  $d_{33}$  values with values measured by other techniques. A bulk PZT ceramic sample measured using the Berlincourt method and double beam interferometry gave  $d_{33}$  values of 305 and 302 pC/N, respectively, indicating a very good agreement between these two techniques. However, the calculated  $d_{33}$  from the pneumatic pressure method was always larger than those values, showing an appreciable amount of remnant in-plane stress present at stabilization. Depending on the experimental conditions which controlled the in-plane stress, the calculated  $d_{33}$  values were about 3%–10% larger than those measured by the other two techniques. To eliminate this error, a detailed investigation was made on both the factors which controlled the magnitude of the remnant in-plane stress as well as how to reduce it by optimizing the design of the pressure rig and the measurement procedure.

Since the frictional force is given by  $F = \mu N$ , where  $\mu$  is the friction coefficient between the two surfaces and  $N$  is the force parallel to the surface, any factor which influences  $\mu$  or  $N$  affects the friction. In our experiments, the following factors were found to be particularly important in friction control: the O-ring compression (i.e., the percentage reduction in dimension in the clamping direction), lubrication, sample surface roughness, the O-ring cross-sectional area and the O-ring hardness. Figure 3 shows how the measured pressure-induced charge was affected by O-ring compression. The results indicated that the remnant in-plane stress dropped with decreasing O-ring compression. This was due to a smaller  $\mu$  when the O-ring was less clamped. Therefore very small O-ring compression was favorable in this application, especially since a little leakage of gas from the cavities is permitted. Since rubber has an inherently high friction coefficient with almost all metallic and nonmetallic surfaces, adequate lubrication is very important, especially for pneumatic seal applications. A good lubricant can form a strong film on the sample surface which the O-ring cannot wipe away, thus reducing the friction coefficient. It was found in our experiment that the friction was greatly reduced by the application of lubricant, and reliable measurements were ob-

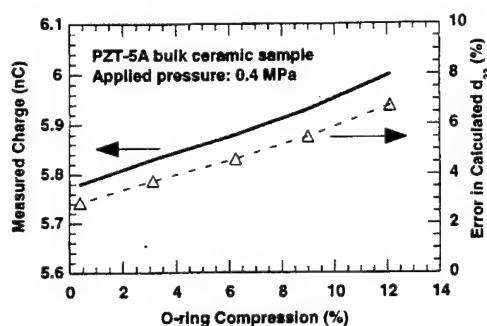


FIG. 3. Effect of O-ring compression on measured pressure-induced charge. O-ring compression was calculated as  $(d_0 - d_c)/d_0$ , where  $d_0$  is its original diameter and  $d_c$  is the dimension in the clamped direction. The error in the calculated  $d_{33}$ , was estimated by comparing the calculated  $d_{33}$  value with that measured by Berlincourt meter.

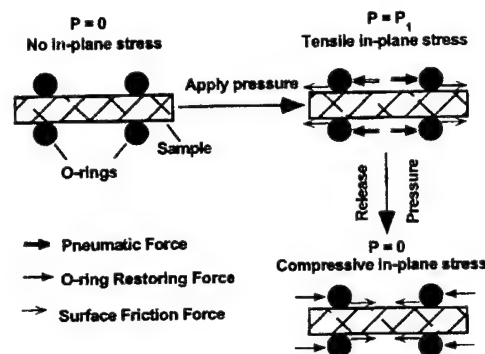
tained only when the sample was properly lubricated. Friction was also reduced by polishing the sample surfaces using  $1\ \mu\text{m}$  alumina powder. The smoother the surface, the smaller the remanent in-plane stress. Smaller remanent in-plane stresses were also obtained when an O-ring with a smaller cross-sectional area was used, since this reduced the pneumatic force acted on it. The reduction of friction through use of a harder O-ring is due to its smaller friction coefficient.

Under the best experimental conditions used to reduce the in-plane stress component, the  $d_{33}$  value calculated from the measured pressure-induced charge exceeded that measured by Berlincourt meter and interferometry by about 3%–4%. This suggests that the error in a  $d_{33}$  coefficient derived from this measurement would be under 5%. However, this optimized condition was not always readily achievable. As a result, there was a relatively larger scatter in the derived  $d_{33}$  value, and sometimes errors as large as 10%–15% were observed.

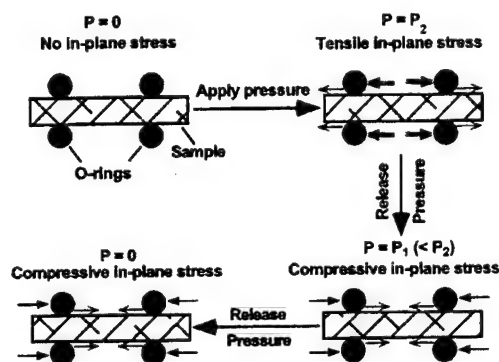
### 3. Self-compensation of remnant in-plane stress

To further improve the accuracy of the  $d_{33}$  measurement and more importantly, the reliability of this charge-pressure measurement technique, a measurement procedure for remnant in-plane stress self-compensation (RIPSSC) was developed. In this method, the charge contribution from the in-plane stress induced charge could be totally eliminated by manipulating the remnant stress levels. Figure 4 shows schematically how this method works.

In the previous section, where the induced charge was measured during switching the pressure between  $P=0$  and  $P=P_1$  [Fig. 4(a)], the remnant in-plane stress at the two steady states were of opposite sign. The change in in-plane stress between the two measurement states is fundamentally responsible for the inflated  $d_{33}$  values. The idea of the RIPSSC method is to tailor the remnant in-plane stress so that they are of the same sign and magnitude in the two steady states. If this is achieved, then there will be no change in in-plane stress between the two steady states. The induced charge is then only that due to the normal component of the



(a)



(b)

FIG. 4. Remnant in-plane stress produced by pneumatic pressure during (a) procedure in which pressure was switched between 0 and  $P_1$ , (b) procedure with a remnant in-plane stress self-compensation mechanism.

stress, and accurate  $d_{33}$  values can be obtained. One way to reach this condition is to preload the cavities with a pressure  $P=P_2$  which is higher than  $P_1$  and then reduce the pressure to  $P=P_1$  [Fig. 4(b)]. By doing so, a compressive remnant in-plane stress was imposed on the sample due to the O-ring recovery. After stabilization, the pressure is then released to  $P=0$  and the induced charge is measured between the steady states at  $P=P_1$  and  $P=0$ .

The dependence of the remnant in-plane stress at  $P_1$  on the preloading level  $P_2$  was investigated for the purpose of controlling the magnitude of the remnant in-plane stress. Figure 5 shows that the induced charge measured between  $P=P_1$  and  $P=0$  decreased with an increase in the preloading pressure (i.e., as  $P_2$  increased). If  $Q'$  is the charge which is due to the normal component of the stress (calculated using the  $d_{33}$  value obtained from the Berlincourt measurement), then the measured charge  $Q$  was equal to  $Q'$  when the preloading pressure  $P_2$  was about two times the value of  $P_1$ . This indicates that the remnant in-plane stress at  $P_1$  can be



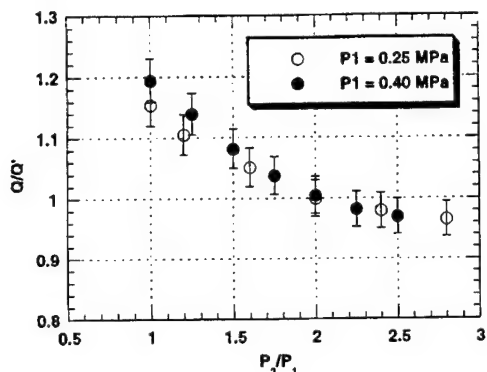


FIG. 5. Influence of the preloading pressure  $P_2$  on the measured charge for a pressure change from  $P = P_1$  to  $P = 0$ .  $Q$  is the measured pressure-induced charge, and  $Q'$  is the charge due to the normal component of the stress evaluated using the  $d_{33}$  value measured by Berlincourt meter.

controlled by the preloading pressure  $P_2$ , and the remnant in-plane stress level is controlled mainly by the pressure change between the two steady states. This is reasonable since the friction is proportional to the pressure change. Thus, one might expect that the remnant in-plane stress due to the friction would also be proportional to the change of pressure.

Using the RIPSSC method, a linear relationship between the induced charge and the applied pressure was obtained (see Fig. 6).  $d_{33}$  for the bulk PZT-5A ceramic sample derived from the slope of the curve was 304 pC/N, which was in very good agreement with the value obtained by both the Berlincourt method and interferometry, indicating that the influence of surface friction on the  $d_{33}$  measurement was eliminated by the RIPSSC method.

In addition to enhancing the measurement accuracy, the RIPSSC method also made the  $d_{33}$  measurement much less sensitive to variations in the remnant in-plane stress. Figure 7 shows the influence of the O-ring compression on the measurement results with and without remnant in-plane stress self compensation. In this experiment, very large compres-

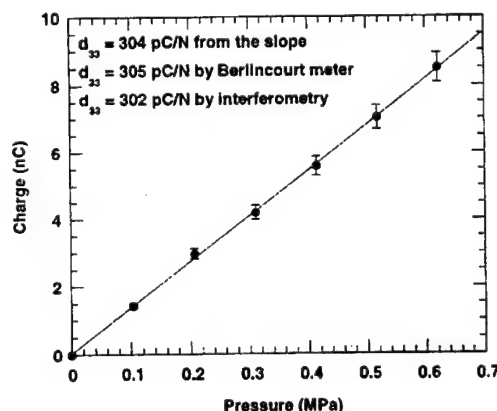


FIG. 6. Charge induced in a bulk PZT-5A ceramic specimen as a function of applied pressure. Measurements were made with the remnant in-plane stress self-compensation method.

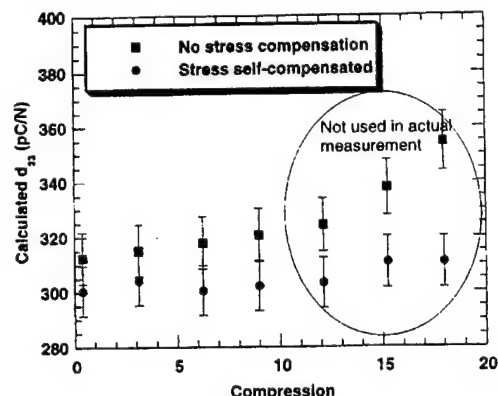


FIG. 7. Influence of O-ring compression on the measured  $d_{33}$  coefficient of bulk PZT-5A. The effectiveness of stress compensation is clear.

sions (which were not used in actual  $d_{33}$  measurements) were intentionally applied to the O-rings. As the O-ring compression increased, friction increased and so did the remnant in-plane stress, as indicated by a considerable increase (15%) in the calculated  $d_{33}$  value when the RIPSSC method was not employed. On the other hand, there was only a 2% variation in the measured  $d_{33}$  value from zero compression up to 17% compression when the RIPSSC method was used. Practically, this is very important in the routine application of the technique, making the measurements much more consistent and the measurement procedure much more convenient.

## B. Measurement on PZT thin films

The charge response of PZT thin films as the cavity pressure was changed was very similar to that observed in bulk samples (Fig. 2), indicating that the stress state applied to the thin film was the same as that for the bulk sample. Using the RIPSSC method described in the previous section, the  $d_{33}$  coefficient of several PZT thin films was measured. Figure 8 shows the induced charge as a function of the pressure change for a 1  $\mu\text{m}$  PZT film poled at 150 kV/cm for 1 min. The relative dielectric constant and the remanent polarization of the film were 930 and 22  $\mu\text{C}/\text{cm}^2$ , respectively. From the slope of the line, the effective  $d_{33}$  value of the thin film was

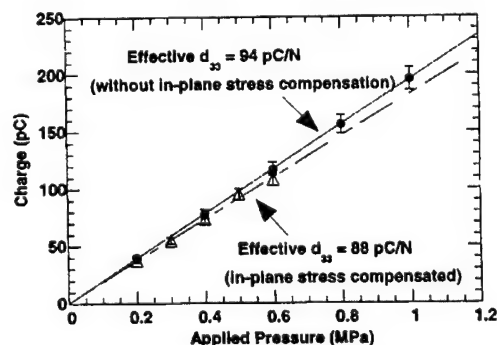


FIG. 8. Induced charge as a function of pressure change for a 1  $\mu\text{m}$  PZT film poled at 150 kV/cm for 1 min.



TABLE I. Elastic properties of PZT film and silicon substrate (see Refs. 16 and 17).

$S_{11}^E$ ( $10^{-12}$ m <sup>2</sup> /N)	$S_{12}^E$ ( $10^{-12}$ m <sup>2</sup> /N)	$S_{13}^E$ ( $10^{-12}$ m <sup>2</sup> /N)	$Y_{\text{Si}(100)}$ (GPa)	$Y_{\text{Si}(110)}$ (GPa)	$Y_{\text{ave}}$ (GPa)	$\nu_{\text{Si}(100)}$	$\nu_{\text{Si}(110)}$	$\nu_{\text{ave}}$
13.8	-4.07	-5.80	130	169.5	149.7	0.28	0.064	0.172

calculated to be 88 pC/N. Again a 7% error in the effective  $d_{33}$  value occurred when the RIPSSC method was not used.

Since double-beam interferometry is currently the most widely accepted technique for thin film  $d_{33}$  measurement and most of the  $d_{33}$  values reported in the literature were measured by that method, a direct comparison between the  $d_{33}$  value from our method and interferometry is necessary. The same electrode used for the data in Fig. 8 was measured using double beam interferometry. An effective  $d_{33}$  value of 84 pC/N was obtained. Again the two techniques gave very close  $d_{33}$  values, further confirming the validity of the charge measurement technique.

Given the fact that the RIPSSC method and interferometry yielded almost the same  $d_{33}$  value for a bulk PZT sample, it is our belief that the small difference in the  $d_{33}$  values obtained for the thin film was due to the different boundary conditions under which the two measurements were made. As was mentioned before, thin film piezoelectric measurements yield an effective value of the piezoelectric coefficient, due to the clamping effect of the substrate. The effective  $d_{33}$  value of a thin film on a substrate is related to the unclamped  $d_{33}$  value via the elastic and piezoelectric constants of the film and the substrate in a manner which depends on the boundary conditions. Since the boundary conditions for the direct piezoelectric measurement used here and a converse piezoelectric measurement such as interferometry are quite different, different effective  $d_{33}$  values are expected even when the same film is measured by the two techniques. Lefki and Dormans analyzed the boundary conditions for these two situations and predicted that the effective value given by the direct piezoelectric effect should be larger than the effective value given by the converse piezoelectric effect.<sup>15</sup> Our results agree with this prediction and are the first direct experimental observation of the influence of boundary conditions on the effective  $d_{33}$  of piezoelectric thin films.

To quantitatively evaluate the difference in the effective  $d_{33}$  measured by direct and converse methods, the model developed by Lefki and Dormans was adopted as a first approximation. In this model, the in-plane strain of the film was taken to be zero (assuming the film was totally clamped in-plane by the substrate) for the converse piezoelectric measurement, and it was equal to the in-plane strain of the substrate (assuming the substrate was free to expand and isotropic) for the direct piezoelectric measurement. The effective  $d_{33}$  for these two boundary conditions are given by<sup>15</sup>

$$d'_{33}(cp) = d_{33} - 2d_{31}S_{13}^E/(s_{11}^E + s_{12}^E), \quad (2)$$

$$d'_{33}(dp) = d_{33} - 2d_{31}(s_{13}^E + \nu/Y)/(s_{11}^E + s_{12}^E). \quad (3)$$

Here  $d'_{33}(cp)$  and  $d'_{33}(dp)$  represent the effective  $d_{33}$  measured by the converse and direct piezoelectric effect, respec-

tively,  $s_{ij}^E$  and  $d_{ij}$  are the compliances and piezoelectric coefficients of the thin film, and  $Y$  and  $\nu$  are Young's modulus and Poisson's ratio of the substrate. Because of the lack of compliance data for PZT thin films in the literature, data for an undoped bulk PZT ceramic with the same Zr/Ti ratio was used as an approximation.<sup>16</sup> For the calculation, the Young's modulus and Poisson's ratio of the substrate were taken as the average of the values in the  $\langle 100 \rangle$  direction and  $\langle 110 \rangle$  direction, which are the maximum and minimum in-plane values for a (100) silicon wafer.<sup>17</sup> Table I gives the values used for this work. Substituting them into Eqs. (2) and (3) yields:

$$d'_{33}(cp) = d_{33} + 1.19d_{31}, \quad (4)$$

$$d'_{33}(dp) = d_{33} + 0.96d_{31}. \quad (5)$$

Subtracting Eq. (4) from Eq. (5) yields

$$d'_{33}(dp) - d'_{33}(cp) = -0.23d_{31}. \quad (6)$$

Since the typical  $d_{31}$  value for these PZT films was around -40 to -50 pC/N,<sup>18</sup> the difference in effective  $d_{33}$  measured by direct piezoelectric effect and converse piezoelectric effect was estimated to be around 9-10 pC/N using Eq. (6).

However, in the real measurements, the boundary conditions deviate somewhat from the conditions used in the above model. Experimental results from single beam interferometry measurements indicate that the substrate is bent by the piezoelectric thin film during electrical excitation,<sup>10,11</sup> making the assumption that the in-plane strain was zero during the converse piezoelectric measurement invalid. In addition, during the direct piezoelectric measurement the substrate was not free to expand parallel to the plane because the periphery of the substrate was not subjected to the pneumatic pressure. Thus, the model represents two extremes for the boundary conditions and gives a maximum for the difference in effective  $d_{33}$ . The discrepancies between the measurements for the two techniques should and do fit between these bounds.

Kholkin *et al.* also used the above model to explain the difference between the  $d_{33}$  coefficients of bulk ceramic and thin film in PZT and Ca-modified lead titanate (PCT).<sup>19</sup> The  $d_{33}$  coefficient was significantly smaller in PZT thin films than that in PZT ceramics with the same composition, while in PCT, thin films and bulk material gave very similar  $d_{33}$  values. This was attributed to the effect of the boundary conditions on the  $d_{33}$  coefficient obtained in a converse piezoelectric measurement. For thin films, the effective  $d_{33}$  value is related to both the unclamped  $d_{33}$  and  $d_{31}$  of the piezoelectric material in a way similar to what is described in Eq. (4). However, PCT is a very anisotropic material and its  $d_{33}$  coefficient is about 20 times larger than the  $d_{31}$  coefficient.

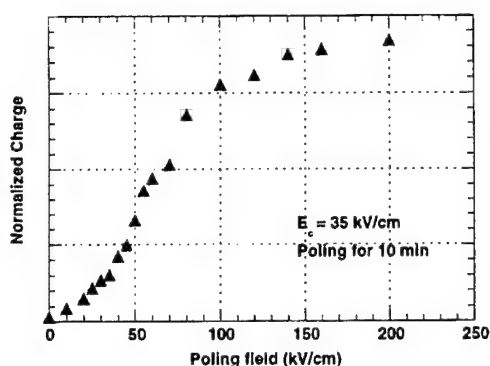


FIG. 9. Induced charge of a 1  $\mu\text{m}$  PZT 52/48 film as a function of poling field.

Therefore, the difference in the unclamped  $d_{33}$  and the effective  $d_{33}$  in PCT is negligible, while it is significant in PZT due to the larger  $d_{31}$ .

In this work the  $d_{33}$  of the as-deposited PZT thin films was also measured and values between 0 and 10 pC/N were obtained. This result indicated that there was little or no pre-existing alignment of the domains in the as-deposited films although all the films had strong preferred crystallographic orientation.<sup>13</sup> The dependence of the induced charge on the poling field was studied using another 1  $\mu\text{m}$  PZT film with (111) preferred orientation (Fig. 9). The coercive field of this sample was about 35 kV/cm. As expected, a considerable increase of the induced charge was observed when the poling field exceeded the coercive field of the film. It started to saturate at a poling field of about three times the coercive field. Poling in the opposite direction led to a reversal in the sign of the induced charge, but the  $d_{33}$  value was almost the same for the two poling directions.

#### IV. CONCLUSIONS

(1) A measurement technique which could accurately measure the  $d_{33}$  value of bulk and thin film piezoelectric materials was developed. Good agreement among this technique, the Berlincourt method and double beam interferometry was obtained.

(2) Surface friction between the sample and O-ring was the major source of error. By optimizing the design and operation of the pressure system, error from the surface friction could be reduced to less than 5%.

(3) The measurement error can be eliminated using the RIPSSC method and an accurate  $d_{33}$  value could be obtained even if there was an appreciable amount of friction present.

(4) As-deposited sol-gel 52/48 PZT thin films showed very weak piezoelectricity with a  $d_{33}$  value less than 10 pC/N. The  $d_{33}$  value increased with poling field and saturated when the poling field exceeded three times the coercive field. Typical  $d_{33}$  values at saturation for 1  $\mu\text{m}$  films were about 100 pC/N.

(5) A direct comparison between the  $d_{33}$  values measured by double-beam interferometry and this technique indicated the influence of the mechanical boundary conditions on the effective  $d_{33}$ . The effective  $d_{33}$  measured by the direct piezoelectric effect was slightly larger than that measured by the converse piezoelectric effect. A quantitative evaluation was made and the calculation was in agreement with the experimental result.

#### ACKNOWLEDGMENTS

The funding for this work is provided by the National Science Foundation under Contract No. DMR-9502431. The authors would also like to thank Dr. J. F. Shepard, Jr. and Dr. J. Zhao for their helpful assistance.

- <sup>1</sup>T. Tamagawa, D. L. Polla, and C. C. Hsueh, Proc. IEDM, pp. 26.2.1–26.2.4, 1990.
- <sup>2</sup>K. R. Udayakumar, J. Chen, A. M. Flynn, S. F. Bart, L. S. Tavrow, D. J. Ehrlich, L. E. Cross, and R. A. Brooks, *Ferroelectrics* **160**, 347 (1994).
- <sup>3</sup>P. Muralt, A. Kholkin, M. Kohli, T. Maeder, and N. Setter, *Microelectron. Eng.* **29**, 67 (1995).
- <sup>4</sup>Y. Nemirovsky, A. Nemirovsky, P. Muralt, and N. Setter, *Sens. Actuators A* **56**, 239 (1996).
- <sup>5</sup>J. J. Bernstein, S. L. Finberg, K. Houston, L. C. Niles, H. D. Chen, L. E. Cross, K. K. Li, and K. Udayakumar, *IEEE Trans. Ultrason. Ferroelectr. Freq. Control* **44**, 960 (1997).
- <sup>6</sup>IEEE Standard on Piezoelectricity, ANSI/IEEE Std., 1988, p. 176.
- <sup>7</sup>W. Y. Pan and L. E. Cross, *Rev. Sci. Instrum.* **60**, 2701 (1989).
- <sup>8</sup>Q. M. Zhang, W. Y. Pan, and L. E. Cross, *J. Appl. Phys.* **63**, 2492 (1988).
- <sup>9</sup>J. F. Li, D. D. Viehland, T. Tani, C. D. E. Lakeman, and D. A. Payne, *J. Appl. Phys.* **75**, 442 (1994).
- <sup>10</sup>A. L. Kholkin, C. Wutrich, D. V. Taylor, and N. Setter, *Rev. Sci. Instrum.* **67**, 1 (1996).
- <sup>11</sup>F. Xu and S. Troler-McKinstry, *Proceedings of 10th International Symposium on Applications of Ferroelectrics*, New Brunswick, New Jersey, 1996, p. 511.
- <sup>12</sup>J. F. Shepard, Jr., P. J. Moses, and S. Troler-McKinstry, *Sens. Actuators A* **71**, 133 (1998).
- <sup>13</sup>F. Chu, F. Xu, J. F. Shepard, Jr., and S. Troler-McKinstry, *Ferroelectric Thin Film VI [Mater. Res. Soc. Symp. Proc.]* **493**, 409 (1998).
- <sup>14</sup>F. Xu, J. F. Shepard, Jr., T. Su, and S. Troler-McKinstry, *Ferroelectric Thin Film VI [Mater. Res. Soc. Symp. Proc.]* **493**, 427 (1998).
- <sup>15</sup>K. Lefki and J. M. Dormans, *J. Appl. Phys.* **76**, 1764 (1994).
- <sup>16</sup>B. Jaffe, W. R. Cook, and H. Jaffe, *Piezoelectric Ceramics* (Academic, London, 1971), p. 19.
- <sup>17</sup>W. A. Brantley, *J. Appl. Phys.* **44**, 534 (1973).
- <sup>18</sup>J. F. Shepard, Jr., Ph.D. thesis, The Pennsylvania State University, 1998.
- <sup>19</sup>A. L. Kholkin, M. L. Calzada, P. Ramos, J. Mendiola, and N. Setter, *Appl. Phys. Lett.* **69**, 3602 (1996).

# **APPENDIX 74**

## Characterization and aging response of the $d_{31}$ piezoelectric coefficient of lead zirconate titanate thin films

Joseph F. Shepard, Jr.

*The Materials Research Laboratory, The Pennsylvania State University, University Park, Pennsylvania 16802*

Fan Chu

*Ramtron International Corporation, Colorado Springs, Colorado*

Isaku Kanno

*Matsushita Electric Industrial Company, Kyoto, Japan*

Susan Trolier-McKinstry<sup>a)</sup>

*The Materials Research Laboratory, The Pennsylvania State University, University Park, Pennsylvania 16802*

(Received 24 September 1998; accepted for publication 27 January 1999)

The wafer flexure technique was used to characterize the  $d_{31}$  coefficient of a number of sol-gel and radio frequency (rf) sputtered lead zirconate titanate (PZT) thin films with thicknesses between 0.6 and 3  $\mu\text{m}$ . Typical  $d_{31}$  values for well-poled 52/48 sol-gel films were found to be between  $-50$  and  $-60$  pC/N. The rf sputtered films possessed large as-deposited polarizations which produced  $d_{31}$  coefficients on the order of  $-70$  pC/N in some unpoled films. The subsequent poling of the material, in a direction parallel to the preferred direction increased the  $d_{31}$  coefficient to values of about  $-85$  pC/N. The aging behavior of the  $d_{31}$  coefficient was also investigated. For sol-gel films the aging rate was found to be independent of poling direction and to range from 4% per decade for a 2.5  $\mu\text{m}$  film to 8% per decade for a 0.6  $\mu\text{m}$  film. In contrast, the aging rate of sputtered films was strongly dependent on poling direction, with maximum and minimum rates of 26% and 2% per decade recorded. These aging rates are very high in light of the limited twin wall motion in PZT films, and are believed to result from the depolarizing effects of internal electric fields in the rf sputtered films and interfacial defects in the sol-gel films. © 1999 American Institute of Physics. [S0021-8979(99)04609-5]

### I. INTRODUCTION

The design and development of novel microelectromechanical systems which utilize piezoelectric thin films requires explicit knowledge of the material's longitudinal ( $d_{33}$ ) and transverse ( $d_{31}$  or  $d_{32}$ ) piezoelectric coefficients. When prepared in bulk ceramic form, piezoelectric coefficients are characterized by numerous methods, the most common of which are the resonance and dynamic load techniques (e.g., the Berlincourt meter). Those techniques however, are inadequate for the piezoelectric characterization of thin film materials and for that reason a number of alternative techniques have been proposed.<sup>1,2</sup>

Laser interferometers are the most well established method for the characterization of both the longitudinal and transverse piezoelectric coefficients of thin films. Interferometric methods however, require careful optical alignment and operation, and in the case of a  $d_{31}$  measurement, appropriate sample preparation (cantilever beam construction). In contrast, the wafer flexure technique was conceived as an alternative method for the characterization of the transverse piezoelectric coefficient ( $d_{31}$ ) of thin films.<sup>3</sup> The measurement is a direct technique (i.e., it utilizes the direct effect) and is based on measuring the charge produced as a film-coated wafer is flexed periodically. Details on the design and

calibration of the technique are given elsewhere.<sup>7</sup> The wafer flexure technique was used here to compare the properties of sol-gel and sputtered lead zirconate titanate (PZT) films.

### II. EXPERIMENTAL PROCEDURE

#### A. Sol-gel PZT thin films

PZT thin films were synthesized with 52/48 compositions using a variation of the procedure described earlier by Budd, Dey, and Payne.<sup>4</sup> Lead acetate trihydrate was dissolved in 2-methoxyethanol, distilled and refluxed at 110 °C, and combined with titanium-IV isopropoxide and zirconium-IV propoxide. Solutions were made in 0.5 molar concentrations and spin coated at 3000 rpm on platinized (100) silicon substrates. Each substrate had 1  $\mu\text{m}$  of thermal oxide sputter coated with a 200 Å titanium adhesion layer and 1500 Å of (111) platinum. Following pyrolysis at 300–360 °C, additional layers were spin coated to build up the desired thickness. Lead volatilization was discouraged (during the subsequent annealing step) with 12% excess lead in the solution. Films were crystallized in an AG Associates, Heatpulse 210 rapid thermal annealer at 700 °C for 60 s. Individual crystallization steps were conducted for thicker films after every fourth coating to minimize cracking of the resulting film. Final film thicknesses ranged from 0.6 to 2.5  $\mu\text{m}$ . Additional details on the processing are given

<sup>a)</sup>Electronic mail: stmckinstry@psu.edu

TABLE I. Sputtering conditions for the deposition of 4 in. PZT thin films.

Target	$[\text{Pb}(\text{Zr}_{0.51}, \text{Ti}_{0.49})\text{O}_3]0.8 + [\text{PbO}]0.2$ (Hot pressed)
Substrate	$\text{Pt/Ti}(\text{SiO}_2)/\text{Si}$ [Pt/Ti = 1000Å/500Å]
Stage temperature	600 °C
Target to substrate distance	10 cm
rf power	500 W
Gas flow	$\text{Ar}/\text{O}_2 = 9.5/0.5$ sccm
Pressure	1.0 Pa
Deposition rate	0.7–1.0 $\mu\text{m/h}$

elsewhere.<sup>5</sup> Pt top electrodes were sputtered through a 1.5-mm-diam shadow mask and postannealed at 400 °C for 60 s.

### B. rf magnetron sputtered 50/50 PZT films

Several 4-in.-diam radio frequency (RF) magnetron sputtered films were used in this investigation. The Zr/Ti ratio of the sputtered films was measured to be 50/50 using energy dispersive x ray. The two films studied were approximately 3.0 and 3.3  $\mu\text{m}$  thick and both displayed strong (111) textures. Details of the deposition procedure are given in Table I.<sup>6</sup> Pt top electrodes were sputtered through a 1.5-mm-diam shadow mask.

### C. Wafer flexure method for transverse piezoelectric characterization

The principle of operation for the wafer flexure method and the details of the hardware used have been reported elsewhere.<sup>7</sup> A schematic of the basic configuration is given in Fig. 1. In this investigation the uniform pressure rig was configured for both 3 and 4 in. wafer characterization. Fundamentally, the technique utilizes the direct piezoelectric effect. The audio speaker was excited with the reference signal [ $0.4 V_{\text{rms}}$  (rms=root mean square) at 4 Hz] from an EG&G 7260 lock-in amplifier fed through a Harman/Kardon HK770 stereo amplifier. The output of the audio speaker is fed to a cavity in the aluminum housing over which the film-coated wafer is fixed. The resulting pressure oscillation flexes the wafer, which subjects the film to a controlled planar stress, and induces a charge via the  $d_{31}$  coefficient of the film. The charge from the PZT sample is converted to a rms voltage (via the charge integrator) and together with the voltage from

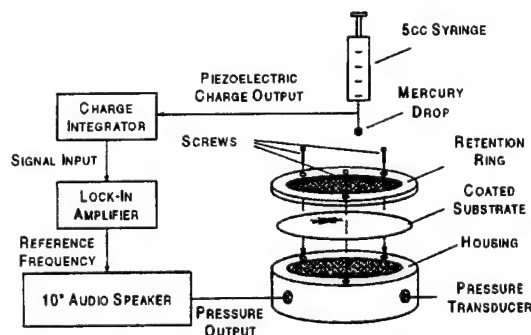


FIG. 1. Wafer flexure method for the transverse piezoelectric characterization of piezoelectric thin films.

a piezoresistive pressure transducer (Omega PX 170, 0.26 psig full scale) is fed into the lock-in and measured with respect to the internal reference. From the lock-in data, output charge and applied pressure are then calculated and used to determine; (1) the stress applied to the film (using classical mechanical plate theory), and (2) the film's  $d_{31}$  coefficient.

### D. Effects of poling time and poling direction on the $d_{31}$ coefficient

The wafer flexure technique was used to characterize the  $d_{31}$  coefficient of a number of PZT thin films. As a general rule, each PZT sample was characterized as a function of poling time and poling direction at room temperature. The magnitude of the poling field was typically two to three times the coercive voltage (as measured from the polarization hysteresis loop) and poling was done in 5 or 15 min increments to a maximum of 1 h. By analogy with piezoelectric ceramics,<sup>8</sup> results from the experiments were expected to show a logarithmic increase with poling time. As such, data from the poling experiments were used to check the health of the  $d_{31}$  meter, the quality of the PZT films, and to identify/confirm the existence of internal bias fields (the  $d_{31}$  response is strongly asymmetric with respect to poling direction for films with large internal bias fields).

### E. Aging rate of the $d_{31}$ coefficient of PZT thin films

The aging of the piezoelectric response under closed circuit conditions without a direct current bias was measured and is reported as a function of film thickness and poling direction. A number of 3 in. sol-gel and 4 in. rf sputtered samples were tested. For each test, samples were poled with an electric field (typically two or three times their coercive field) for a time of 1–2 min. At the end of the poling period the oscillation on the measurement rig was started and the test begun. The output from the test capacitor was monitored continuously on the lock-in display and the voltages recorded every 5 min for times of 1–60 min after poling. Care was taken to insure that the pressure applied to the plate was the same over the course of the experiment.

## III. RESULTS AND DISCUSSION

### A. Effects of poling time on the $d_{31}$ coefficient of PZT thin films

Four rapid thermally annealed sol-gel films with thicknesses of 0.6–2.5  $\mu\text{m}$  were characterized in terms of their  $d_{31}$  coefficients as a function of both poling direction and poling time. The poling fields used for the experiments were taken to be three times the coercive field of the capacitor tested (where  $E_c$  was calculated from the average of the  $\pm E_c$ 's reported during earlier polarizing-electric field (P-E) measurements). The same spot on the sample was then poled for increasing lengths of time, up to 31 min, at this field level. For each set of experiments a virgin electrode was used. The results from the experiments with the top electrode made positive are given in Fig. 2 and show that the piezoelectric coefficient of all films tested increases in a logarithmic

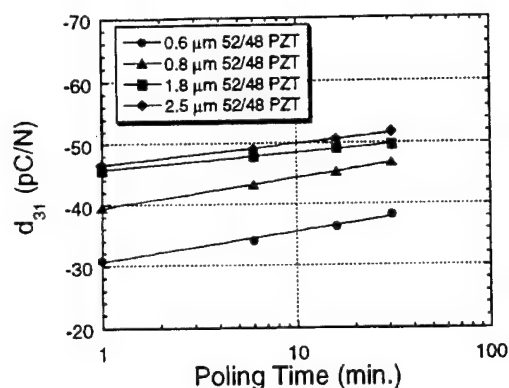


FIG. 2. Variation of  $d_{31}$  as a function of film thickness and poling time with the top electrode positive. Films tested had 52/48 compositions and were poled with fields equal to three times the coercive field of the film.

mic fashion with poling time. The maximum  $d_{31}$  coefficient was recorded for the 2.5- $\mu\text{m}$ -thick film and had a magnitude on the order of  $-50$  pC/N. Results collected with the top electrode made negative showed a similar response with the magnitudes comparable to those given in Fig. 2.

The piezoelectric characterization of the 50/50 rf sputtered films indicated that the films had large spontaneous polarizations which produced as-deposited  $d_{31}$  coefficients between  $-45$  and  $-70$  pC/N.  $d_{31}$  data taken from a 3.3- $\mu\text{m}$ -thick film are presented in Fig. 3 as a function of poling time at  $\pm 60$  kV/cm. (This poling field is close to the average coercive field; higher fields could not be used due to delamination of the top electrode after prolonged high field exposure.) In Fig. 3, the data for the top electrode negative follow the expected logarithmic increase with poling time. However, poling the film for 1 min with the top electrode positive was insufficient to reverse the original polarization direction. As a result, the magnitude of  $d_{31}$  decreased from  $-70$  to  $-20$  pC/N, but the phase of the response with respect to the applied stress was unchanged. Only with extended poling did the remanent polarization change sign. For these longer times, the phase of the  $d_{31}$  response with the applied stress

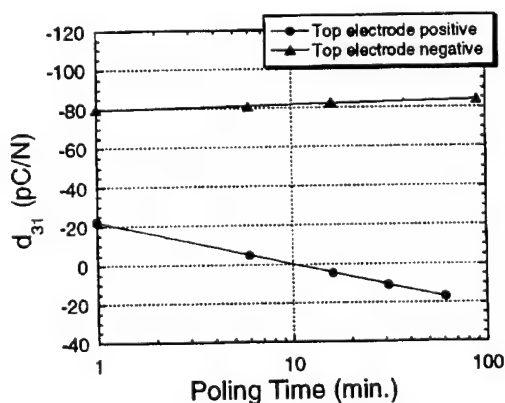


FIG. 3. Change of the  $d_{31}$  coefficient of a 3.3- $\mu\text{m}$ -thick 50/50 sputtered film with poling time. The data show a strong sensitivity to poling direction. As-deposited values of  $d_{31}$  were measured at about  $-70$  pC/N.

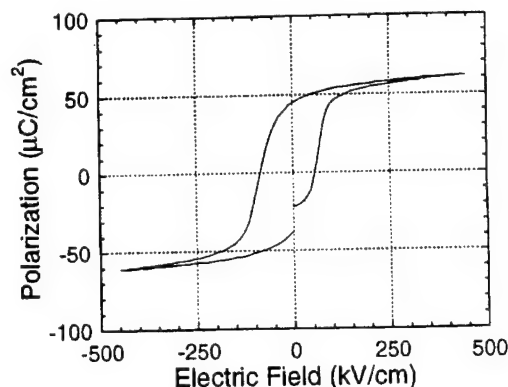


FIG. 4. Polarization hysteresis loop for a  $\sim 3$ - $\mu\text{m}$ -thick 50/50 rf sputtered PZT film. The plot shows the average remanent polarization of the film is  $41$   $\mu\text{C}/\text{cm}^2$  and the average coercive field is  $70$  kV/cm. The internal bias field is calculated from the offset on the field axis to be  $15$  kV/cm.

changed by approximately  $180^\circ$ . To show that the degree of poling did, in fact, increase logarithmically with time, all of the  $d_{31}$  data are shown with negative values in the graph; zero marks the point at which the phase of the response changed.

The data presented in Fig. 3 illustrate a number of striking results. The first is the large value ( $-70$  pC/N) of the  $d_{31}$  coefficient in the as-deposited films.  $d_{31}$  increased with poling to values which approached  $-85$  pC/N. Those numbers are themselves encouraging because they represent some of the largest  $d_{31}$  values reported for polycrystalline PZT films. Furthermore, there is significant asymmetry in the  $d_{31}$  coefficient as a function of the poling direction. When poled with the top electrode negative, the  $d_{31}$  increased by about 20% for poling times of 60 min. In contrast, poling the sample in the opposite direction changed the  $d_{31}$  coefficient by a factor of 2.

The large as-deposited  $d_{31}$  and the strong asymmetry in the poling behavior are probably related to an internal electric field in the film. The existence of internal bias fields have been well documented for PZT ceramics<sup>9</sup> and thin films<sup>10</sup> and their presence is usually manifested as a shift in the polarization hysteresis loop or an asymmetry in the current-voltage ( $I$ - $V$ ) curve. In thin films, such internal fields have been reported to result in preferred polarization directions and asymmetry in the piezoelectric response as a function of poling direction.<sup>11,12</sup> The  $P$ - $E$  loop for the 50/50 film is given in Fig. 4. The  $P$ - $E$  hysteresis loop is shifted  $15$  kV/cm along the field axis, which is assumed to be equal to the film's internal field. It is expected that the bias field poles the material as it cools from its deposition temperature ( $600^\circ\text{C}$ ) which leads to a large as-deposited polarization and an appreciable piezoelectric effect. The subsequent application of a poling field in excess of, and in a direction parallel to, the internal bias yields only minimal gains in the  $d_{31}$  coefficient. The application of a field in a direction antiparallel to the internal field however, results in appreciable changes of the as-deposited polarization and therefore, the film's  $d_{31}$  coefficient. There is also the possibility that the preferred polarization direction is the result of a strain gradient in the film,

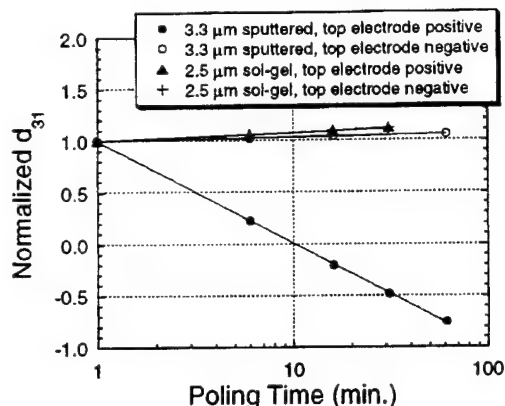


FIG. 5. Normalized  $d_{31}$  coefficients as a function of poling time. Data for both a 2.5  $\mu\text{m}$  sol-gel film and a 3.3  $\mu\text{m}$  sputtered film are shown. Note that the response of the sol-gel film is nearly symmetrical with respect to poling direction, so that the two curves for the sol-gel films are superimposed.

though given the distance between the film and the neutral axis of the film/substrate system, a large strain gradient seems unlikely. For simplicity therefore, the mechanism responsible for the shift in the hysteresis loop will be described as an internal field.

The effect of the preferred polarization direction is illustrated most clearly in Fig. 5, which plots the response of both the 2.5  $\mu\text{m}$  52/48 sol-gel film and the 50/50 sputtered film as a function of poling time. The strong contrast between the poling behavior of the two types of films is believed to result from the relative magnitude of the film's internal bias fields.

The internal bias of the sputtered film was calculated to be about 15 kV/cm, which is an order of magnitude larger than the  $\sim 1$ –2 kV/cm internal bias in the sol-gel films. The large internal field in the sputtered films poles the material almost completely as the material is cooled through  $T_c$ . The sputtered films therefore, display only a small increase in the magnitude of  $d_{31}$  when poled in a direction parallel to the internal bias and show large changes when poled antiparallel to the preferred direction. In contrast, the internal fields of the sol-gel films are much lower (than the sputtered films). The net polarization produced in either direction is therefore comparable and the response produced is symmetric.

### B. Aging behavior of the transverse ( $d_{31}$ ) piezoelectric coefficient

The aging rates of the transverse piezoelectric coefficients for both sol-gel and sputtered PZT films were measured using the wafer flexure technique. The  $d_{31}$  coefficients were monitored at regular intervals after poling and their decay plotted versus the logarithm of time.

Experiments were conducted with sol-gel films poled in either direction at room temperature with fields equal to three times their coercive field strength. Poling times for the experiments conducted were either 1 or 2 min. Figure 6 gives the aging data from the experiments conducted with the top electrode made negative (tests with the top electrode positive were also conducted and the response was similar to that shown). The rates for all experiments (including those con-

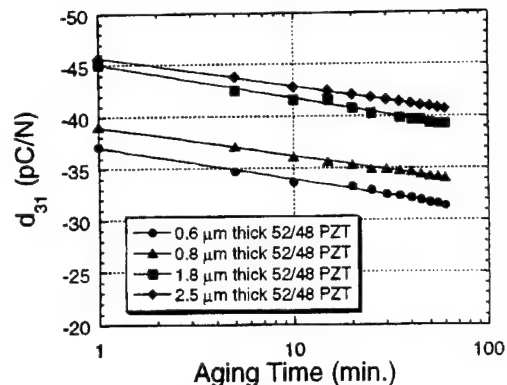


FIG. 6. Aging of the  $d_{31}$  coefficient for four sol-gel films ranging in thickness from 0.6 to 2.5  $\mu\text{m}$ . Samples were all poled with three times the coercive field for 1 min with the top electrode negative.

ducted with the top electrode positive) are tabulated from the slopes of the fitted logarithmic curves and are given in Table II.

Similar experiments were conducted on a 4 in. rf sputtered 50/50 PZT film. The film investigated was 3.0  $\mu\text{m}$  thick with an as-deposited  $d_{31}$  coefficient of about  $-45$  pC/N. Test capacitors were poled with an electric field of 150 kV/cm, which was approximately equal to two times the coercive field strength. The aging rate was evaluated as a function of poling time and direction with the data taken from different test capacitors on the same film.

Figure 7 is a plot of the decay of the transverse piezoelectric coefficient for the sputtered film poled with a field of  $\pm 150$  kV/cm for 1 min at room temperature. The plot shows a strong asymmetry in the film's aging rate, with the sample poled at  $-150$  kV/cm (top electrode negative) measured at 2% per decade while the sample poled in the opposite direction decayed at 26% per decade. When the samples were poled for 15 min, the data showed an aging rate of 4% per decade when poled with the top electrode negative and an aging rate of 20% per decade when poled with the top electrode positive.

The aging data collected from both the sol-gel and rf sputtered films make an interesting contrast to data reported for bulk ceramics. In bulk materials, the decay of the dielectric and piezoelectric constants and the evolution of constricted  $P$ – $E$  loops are attributed to ferroelastic stress relief and domain stabilization.<sup>13</sup> Because extrinsic contributions

TABLE II. Aging rates (percent per decade) of the  $d_{31}$  coefficient of 52/48 sol-gel PZT thin films.

Film thickness ( $\mu\text{m}$ )	Poling time: 1 min Top electrode (+)	Poling time: 1 min Top electrode (–)	Poling time: 2 min Top electrode (+)
0.6	8%	8%	7%
0.8	7%	7%	5%
1.8	7%	7%	5%
2.5	6%	7%	4%



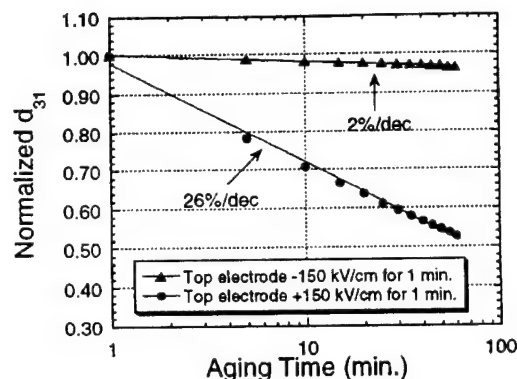


FIG. 7. Aging rate of the  $d_{31}$  coefficient of a 3.0- $\mu\text{m}$ -thick 50/50 rf sputtered PZT film. The film had been poled for 1 min with a field of  $\pm 150$  kV/cm.

to the dielectric and piezoelectric characteristics are limited in these films<sup>14</sup> and the decay of the dielectric constant proceeds at only a few percent per decade,<sup>12,15</sup> the mechanism(s) responsible for the decay of the electromechanical constants has been attributed to the reduction of the film's remanent polarization.<sup>12</sup>

In this work, the aging data collected show a correlation with the presence of an internal bias field. The rf sputtered films ( $E_{\text{bias}} = 15\text{--}20$  kV/cm) show accelerated aging when the polarization vectors are misaligned with the internal field. Removal of the poling field results in the rapid reorientation of switched domains (i.e., the film begins to switch back to the original orientation) and a rapid decrease of the film's  $d_{31}$  coefficient. In contrast to the rf sputtered films, the net internal fields of the sol-gel films ( $E_{\text{bias}} = 1\text{--}2$  kV/cm) are smaller, and as a result their response is independent of poling direction. This behavior is in agreement with that reported by Kholkin *et al.*,<sup>12</sup> although the asymmetries observed here for the sputtered films are appreciably larger.

The symmetric aging response of the sol-gel films suggests that depolarization does not result from a net internal electric field. Earlier work on PZT ceramics has shown that large mechanical stresses can result in significant amounts of depolarization<sup>16,17</sup> however, data presented elsewhere<sup>14</sup> show that the effects of mechanical stress are less pronounced in PZT films. In addition, the limited extrinsic contributions in these PZT films suggest that depolarization results from the backswitching of aligned domains and not non-180° reorientation or domain wall pinning. Because 180° switching is not a stress relief mechanism, mechanical depolarization cannot be responsible for the aging behavior of thin films. Rather, it is expected that the origins of the accelerated aging rates are related to interfacial or defect-related effects comparable to those responsible for the polarization degradation of ferroelectric non-volatile memory devices.<sup>18</sup>

Extensive work has been conducted on degradation mechanisms in films, with both lead and oxygen vacancies identified as potential sources of the problem(s).<sup>18</sup> It is expected that the high volatility of lead oxide at the elevated crystallization temperatures (typically 600–700 °C) results in large concentrations of charged defects in a shallow layer at

the film's surface.<sup>19</sup> There are several possible consequences of this. First, the defective material could form a discrete semiconducting layer at the film surface. Earlier work has suggested that a low- $\epsilon_r$  region at one of the film's surfaces results in the reduced dielectric constant of thin (submicron thickness) PZT films.<sup>20</sup> A similar region may be responsible for the spontaneous depolarization of the material. In particular, it is suggested that when subjected to large poling fields, charge is injected through this layer and domain reversal is possible. After the voltage is removed however, a depolarization field is created which cannot be compensated effectively by the defective layer. In the absence of an external voltage, the limited conductivity of the lead deficient layer prevents additional charge from being transported to compensate the depolarization field. As a result the material depoles, which leads to the accelerated decay of the film's piezoelectric coefficient.

A second possibility is that  $V_{\text{pb}}'' - V_{\text{O}}'$  defect dipoles in the near surface regime align with respect to the ferroelectric dipoles on cooling through the transition. Since the domain structure is initially random, there is little net internal bias. If the field associated with these dipoles is not too high, then the material could be poled. However, at room temperature it is unlikely that all of the defects would be reoriented (especially for short poling times). Thus, after poling they would act to drive the film back to its original random domain configuration, which would result in accelerated piezoelectric aging.

There are data presented both here and elsewhere<sup>12</sup> which suggest that the aging rates of the piezoelectric coefficients can be decreased with increased poling times (Table II). The beneficial effects of poling time can be explained within the framework of imprint phenomena which attributes the voltage offset of the  $P$ - $E$  loop (i.e., the imprint) to the alignment of defect dipoles with the film's polarization vector.<sup>21</sup> With increased poling times the defects (predominantly oxygen vacancies) which are responsible for imprint have time to migrate through the film. The migration and reorientation of defect dipoles stabilize the film's domain structure, which prevents depolarization and reduces the aging rate.

The asymmetric aging rates of the  $d_{31}$  coefficient of the rf sputtered films are comparable to behavior which has been reported by Maria for epitaxial lead magnesium niobate-lead titanate films.<sup>22</sup> The source of the aging behavior in those films was attributed to the presence of a large internal bias which shifted the  $P$ - $E$  loops to one side of the origin, i.e., both coercive fields had the same sign. Maria speculated that energetic bombardment, either through implantation or ion peening, was responsible for a displacement of the oxygen sublattice. The shift of the oxygen atoms led to a preferred polarization direction and thus produced the large internal field (and the asymmetry in the aging rates) in the as-deposited films. A similar mechanism could explain why the sputtered films in this work showed asymmetric aging rates while the sol-gel films (which never see bombardment) did not.



#### IV. CONCLUSIONS

The wafer flexure method was used to characterize the  $d_{31}$  coefficients and monitor their aging rates for a number of 52/48 sol-gel and 50/50 rf sputtered PZT films. Piezoelectric characterization indicated an increase of  $d_{31}$  with poling time (at room temperature) to maximum values of about  $-50$  pC/N for the  $2.5\text{-}\mu\text{m}$ -thick sol-gel film and  $-85$  pC/N for  $\sim 3\text{-}\mu\text{m}$ -thick rf sputtered film. Aging results showed that the  $d_{31}$  coefficient decreased in a linear fashion with the logarithm of time. The aging rates measured for the sol-gel films were found to be between 4% and 10% per decade with the thickest films tested ( $2.5\text{ }\mu\text{m}$ ) displaying the smallest rates. Similar experiments were conducted on rf sputtered PZT films. In contrast to the aging behavior of the sol-gel films, the aging rates of the sputtered samples showed a strong anisotropy of the decay rate. Rates were measured at as much as 26% per decade when the sample was poled against the as-deposited polarization and as little as 2% per decade when poled in the preferential direction.

The aging rates of PZT films are large when compared to the few percent per decade reported for bulk ceramics. The mechanism responsible for the piezoelectric aging of the PZT films is believed to be depolarization of the material. The rf magnetron sputtered films display large asymmetries in their aging response which is probably the result of a large internal field present in the film. When poled in a direction parallel to the internal bias, the film's polarization is stable and the aging rates are modest. If however, the films are poled antiparallel to the internal field, the remanent polarization is unstable and the aging rates are accelerated. In contrast to the sputtered films, the aging rates of the sol-gel samples were independent of poling direction. The symmetry of aging rate indicated that the net internal fields in the sol-gel films, which were about an order of magnitude less than those in the rf sputtered films, were not the predominant depolarization mechanism in the material. The origin of the

aging response in the sol-gel samples was attributed to charged defects or a defective layer which resulted in the backswitching of domains.

#### ACKNOWLEDGMENTS

This work is funded by DARPA under Contract No. DABT63-95-C-0053 and NSF under Grant No. EEC-9526808.

- <sup>1</sup>J. L. Deschanvres, P. Rey, G. Delabouglise, M. Labeau, J. C. Joubert, and J. C. Peuzin, *Sens. Actuators A* **33**, 43 (1992).
- <sup>2</sup>M. Toyama, R. Kubo, E. Takata, K. Tanaka, and K. Ohwada, *Sens. Actuators A* **45**, 125 (1994).
- <sup>3</sup>J. F. Shepard, Jr., P. J. Moses, and S. Trolier-McKinstry, *Mater. Res. Soc. Symp. Proc.* **459**, 225 (1996).
- <sup>4</sup>K. D. Budd, S. K. Dey, and D. A. Payne, *Br. Ceram. Proc.* **36**, 107 (1985).
- <sup>5</sup>F. Chu, F. Xu, J. Shepard, Jr., and S. Trolier-McKinstry, *Mater. Res. Soc. Symp. Proc.* **492**, 409 (1998).
- <sup>6</sup>I. Kanno, S. Fujii, T. Kamada, and R. Takayama, *Appl. Phys. Lett.* **70**, 1378 (1997).
- <sup>7</sup>J. F. Shepard, Jr., P. J. Moses, and S. Trolier-McKinstry, *Sens. Actuators A* **71**, 133 (1998).
- <sup>8</sup>B. Jaffe, J. W. R. Cook, and H. Jaffe, *Piezoelectric Ceramics* (R.A.N., India, 1971).
- <sup>9</sup>S. Takahashi, *Ferroelectrics* **41**, 143 (1982).
- <sup>10</sup>W. L. Warren, D. Dimos, G. E. Pike, B. A. Tuttle, and M. V. Raymond, *Appl. Phys. Lett.* **67**, 866 (1995).
- <sup>11</sup>A. L. Kholkin, K. G. Brooks, D. V. Taylor, S. Hiboux, and N. Setter, *Int. Ferro.* (submitted).
- <sup>12</sup>A. Kholkin, E. Colla, K. Brooks, P. Murali, M. Kohli, T. Maeder, D. Taylor, and N. Setter, *Microelectron. Eng.* **29**, 261 (1995).
- <sup>13</sup>W. A. Schulze and K. Ogino, *Ferroelectrics* **87**, 361 (1988).
- <sup>14</sup>J. F. Shepard, Jr., J. P. Maria, B. Xu, and S. Trolier-McKinstry, *J. Mater. Res.* (submitted).
- <sup>15</sup>J. F. Shepard, Jr. and S. Trolier-McKinstry (unpublished).
- <sup>16</sup>R. F. Brown, *Can. J. Phys.* **39**, 741 (1961).
- <sup>17</sup>H. H. A. Krueger, *J. Acoust. Soc. Am.* **42**, 636 (1967).
- <sup>18</sup>W. L. Warren, D. Dimos, and R. Waser, *MRS Bull.* **21**, 40 (1996).
- <sup>19</sup>T. Tani and D. A. Payne, *J. Am. Ceram. Soc.* **77**, 1242 (1994).
- <sup>20</sup>K. R. Udayakumar, P. J. Schuele, J. Chen, S. B. Krupanidhi, and L. E. Cross, *J. Appl. Phys.* **77**, 3981 (1995).
- <sup>21</sup>G. E. Pike, W. L. Warren, D. Dimos, B. A. Tuttle, R. Ramesh, J. Lee, V. G. Keramidas, and J. T. Evans, *Appl. Phys. Lett.* **66**, 484 (1995).
- <sup>22</sup>J. P. Maria, Ph.D. thesis, The Pennsylvania State University, 1998.

# **APPENDIX 75**

## Dielectric hysteresis from transverse electric fields in lead zirconate titanate thin films

Baomin Xu,<sup>a)</sup> Yaohong Ye, and L. Eric Cross

*Materials Research Laboratory, Pennsylvania State University, University Park, Pennsylvania 16802*

Jonathan J. Bernstein and Raanan Miller

*The Charles Stark Draper Laboratory, 555 Technology Square, Cambridge, Massachusetts 02139*

(Received 9 March 1999; accepted for publication 13 April 1999)

Excellent symmetric dielectric hysteresis is observed from lead zirconate titanate (PZT) thin films using transverse electric fields driven by interdigitated surface electrodes. The 1- $\mu\text{m}$ -thick PZT films with a Zr/Ti ratio of 52/48 are prepared on  $\text{ZrO}_2$  buffered, 4-in.-diam silicon wafers with a thermally grown  $\text{SiO}_2$  layer. Both the  $\text{ZrO}_2$  buffer layer and PZT film are deposited by using a similar sol-gel processing. Remanent polarization of about  $20 \mu\text{C}/\text{cm}^2$  with coercive field less than  $40 \text{ kV}/\text{cm}$  is obtained as measured using a triangle wave at 50 Hz. Thicker films are being developed and retention for the transversely polarized state is currently under study. One of the objectives of this study is to develop a large array of  $d_{33}$ -driven unimorph sensing elements for a high-resolution acoustic imaging system. © 1999 American Institute of Physics. [S0003-6951(99)03123-X]

Because the  $d_{33}$  and  $k_{33}$  values of most ceramics are almost two times of the  $d_{31}$  and  $k_{31}$  values, respectively,<sup>1</sup> recent studies in macroscopic systems have highlighted the strong advantages for unimorph bending actuators with a transversely polarized lead zirconate titanate (PZT) layer, which can be driven electromechanically through the piezoelectric  $d_{33}$  mode rather than the conventional  $d_{31}$  mode.<sup>2,3</sup> Here, the  $d_{33}$  mode means that both the polarization and applied field are along the surface of the piezoelectric layer (that is, transverse direction). This  $d_{33}$  unimorph structure should also be significant for microelectromechanical systems (MEMS) applications because many micromachined unimorph transducers for various MEMS devices have been developed by combining silicon microelectronics technology and on-chip ferroelectric lead zirconate titanate films.<sup>4-6</sup> In addition, we believe the transverse polarization configuration will be more attractive for micromachined unimorph diaphragm pressure sensors, since diaphragm thickness and electrode spacing are now independent variables. Particularly important is the fact that newer field-effect transistors are available with ultralow input capacitance, matching well the very low self-capacitance of the unimorph structures with wider electrode separation, and consequently, higher intrinsic voltage sensitivity. As a first step towards producing  $d_{33}$ -mode unimorph bending transducers on silicon substrates, ferroelectric PZT films have to be deposited on an insulating buffer layer with a low dielectric constant instead of the conventional platinum buffer layer. In this letter we report that PZT thin films can be prepared on  $\text{ZrO}_2$ -buffered silicon substrates and strong symmetric hysteresis is observed for transverse fields generated from interdigitated surface electrodes, indicating the excellent ferroelectric properties of the films.

Both the  $\text{ZrO}_2$  and PZT films were deposited by multiple sol-gel spin-on procedures, and their solutions were pre-

pared using an acetic acid process modified from former reports in the literature.<sup>7,8</sup> To prepare the  $\text{ZrO}_2$  solution, zirconium *n*-propoxide was added to the glacial acetic acid and the mixture was refluxed at  $105^\circ\text{C}$  for 1 h. Ethylene glycol and deionized water were also added during the reflux to control the viscosity and concentration of the solution. To prepare the PZT (52/48) solution, lead acetate trihydrate, with 20 mol % excess lead content, was initially dissolved in acetic acid and the associated water was removed during a period of distillation at  $150^\circ\text{C}$ . After cooling to room temperature, zirconium *n*-propoxide and titanium isopropoxide were added to the solution and the mixture was refluxed at  $80^\circ\text{C}$  for 1 h. Again, ethylene glycol and deionized water were added during the reflux process. The concentrations of the final solutions were adjusted to be 0.75 M for the  $\text{ZrO}_2$  solution and 0.90 M for the PZT solution. The substrate was 4-in.-diam, *n*-type, (100)-oriented silicon wafers with a 0.4- $\mu\text{m}$ -thick thermally grown  $\text{SiO}_2$  layer. For the preparation of the  $\text{ZrO}_2$  film, the samples were pyrolyzed at  $600^\circ\text{C}$  for 0.1 h after the deposition of each layer and annealed at  $700^\circ\text{C}$  for 3 h after the fifth layer deposition. After the annealing of the  $\text{ZrO}_2$  film, another five layers of PZT solution were coated layer by layer in the same way but the final annealing condition was changed to  $700^\circ\text{C}$  for 1 h.

The phase structures of the films were analyzed by using an x-ray diffractometer and the results are shown in Fig. 1. It can be seen that the  $\text{ZrO}_2$  film is mainly amorphous after annealing but the PZT film is a well-formed perovskite structure phase. The peak with the highest intensity in the x-ray diffraction pattern of the PZT film is indexed as the (101) plane, indicating that the film is mostly random oriented. This is not surprising considering the PZT film was grown on an amorphous surface. The surface and cross-sectional microstructures of the films were studied under scanning electron microscopy (SEM) and the results are given in Fig. 2. The SEM surface micrograph of the PZT film suggests a grain aggregate structure of the 3–5  $\mu\text{m}$  scale, but obvious substructure, and x-ray line broadening indicate that the true

<sup>a)</sup>Corresponding author. Electronic mail: bxx2@psu.edu

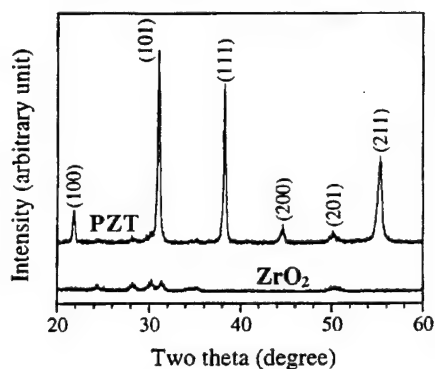


FIG. 1. X-ray diffraction patterns of the films.

grain size is significantly smaller. The SEM cross-sectional microstructure [Fig. 2(b)] shows the clear multilayer PZT,  $\text{ZrO}_2$ ,  $\text{SiO}_2$ , Si structure and the very sharp interface between the PZT and  $\text{ZrO}_2$  films. The thicknesses of the PZT and  $\text{ZrO}_2$  films are about 1 and  $0.4 \mu\text{m}$ , respectively. These results have verified that the  $\text{ZrO}_2$  film can work as an effective buffer layer preventing the reaction and interdiffusion between the PZT film and silicon substrate.

In order to measure the hysteresis loops under transverse electric field, the Ti/Pt/Au interdigitated electrodes were sputtered on the surface of the PZT film and a sketch map of the electrode patterns is shown in Fig. 3. A conventional photoresister lift-off process was used to define the finger width of  $10 \mu\text{m}$  and electrode separations (finger gaps) of 5, 10, and  $20 \mu\text{m}$ , respectively. The electrode arrays with various patterns were written within the outline of about  $1.55 \times 1.33 \text{ mm}$  as shown in Fig. 3(a).

The hysteresis loops of the films were measured using a modified Sawyer–Tower circuit with 50 Hz, triangle wave-

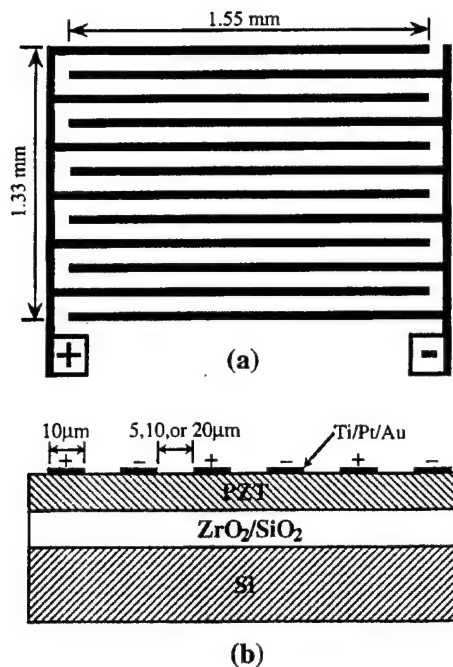


FIG. 3. Sketch map of the surface interdigitated electrode patterns: (a) top view and (b) cross-sectional view.

form driving signals. Direct electrical hysteresis between the induced charge and applied voltage in the  $5\text{-}\mu\text{m}$ -gap electrode system is given in Fig. 4(a). If it is assumed that the area switched is the product of the length of the electrode

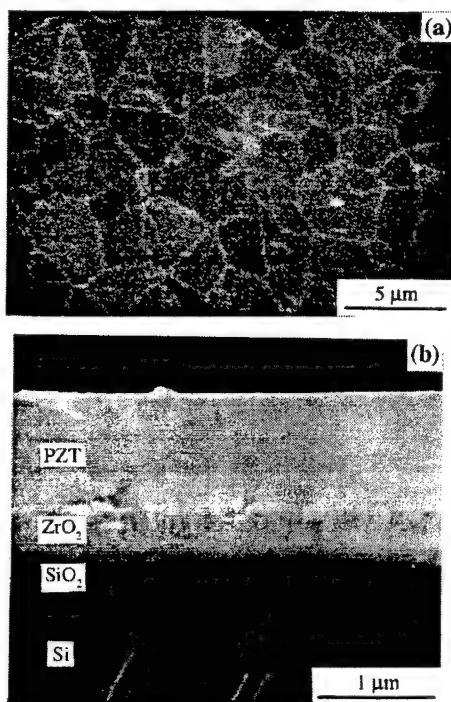
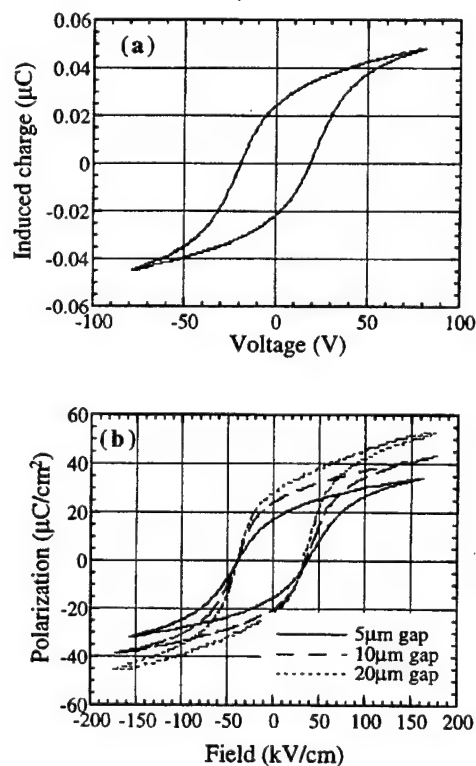


FIG. 2. SEM micrographs of the sample. (a) Surface microstructure of the PZT film. (b) Cross-sectional microstructure.

FIG. 4. Field-induced charge and polarization of the PZT film using the surface interdigitated electrodes. (a) Direct voltage–charge relationship for the  $5 \mu\text{m}$  gap electrode system. (b) Field-induced polarization for the electrode patterns with various finger gaps.

fingers and film thickness and that the field is uniform across the electrode gap, the data may be converted to a  $P$  (polarization) versus  $E$  (field) scale. Figure 4(b) shows the loops superposed for the 5, 10, and 20  $\mu\text{m}$  finger gaps under such assumptions. Clearly, there will be fringing fields associated with the finger terminations which will affect the calculated polarization and electric-field values. However, it is encouraging to find the remanent polarization ( $P_r$ ) of order 20  $\mu\text{C}/\text{cm}^2$  and the coercive field ( $E_c$ ) of order 40 kV/cm, which are close to the corresponding values of PZT films deposited on platinum-buffered silicon substrates using similar sol-gel processing.<sup>8</sup>

In summary, PZT (52/48) films with the thickness of about 1  $\mu\text{m}$  have been prepared on  $\text{ZrO}_2$ -buffered silicon substrates. Both the  $\text{ZrO}_2$  and PZT films were deposited using a similar sol-gel processing. The results indicate that the deposited  $\text{ZrO}_2$  film can work effectively as a buffer layer. The strong symmetric hysteresis loops measured by using interdigitated electrodes on the surface of the PZT film sug-

gest very good transverse coherence in the film. Current work is concerned with studying the retention of polarization along the transverse direction and the related piezoelectric effect, and developing PZT films with thickness up to 5  $\mu\text{m}$  in order to construct micromachined unimorph transducer arrays with a working frequency at the MHz range for hand-held underwater three-dimensional imaging systems.

<sup>1</sup>A. J. Moulson and J. M. Herbert, *Electroceramics* (Chapman and Hall, London, 1990), Chap. 6.

<sup>2</sup>V. D. Kugel, S. Chandran, and L. E. Cross, Appl. Phys. Lett. **69**, 2021 (1996).

<sup>3</sup>V. D. Kugel, S. Chandran, and L. E. Cross, Proc. SPIE **3040**, 9 (1997).

<sup>4</sup>D. L. Polla and L. F. Francis, MRS Bull. **21**, 59 (1996).

<sup>5</sup>J. J. Bernstein, S. L. Finderg, K. Houston, L. C. Niles, H. D. Chen, L. E. Cross, K. K. Li, and K. R. Udayakumar, IEEE Trans. Ultrason. Ferroelectr. Freq. Control **44**, 960 (1997).

<sup>6</sup>P. Luginbuhl, G.-A. Racine, P. Lerch, B. Romanowicz, K. G. Brooks, N. F. de Rooij, P. Renaud, and N. Setter, Sens. Actuators A **54**, 530 (1996).

<sup>7</sup>G. Yi, Z. Wu, and M. Sayer, J. Appl. Phys. **64**, 2717 (1988).

<sup>8</sup>H. D. Chen, K. R. Udayakumar, C. J. Gaskey, L. E. Cross, J. J. Bernstein, and L. C. Niles, J. Am. Ceram. Soc. **79**, 2189 (1996).

# **APPENDIX 76**

## Sensing characteristics of in-plane polarized lead zirconate titanate thin films

Baomin Xu,<sup>a)</sup> Ronald G. Polcawich, Susan Troler-McKinstry, Yaohong Ye,  
and L. Eric Cross

*Materials Research Laboratory, Pennsylvania State University, University Park, Pennsylvania 16802*

Jonathan J. Bernstein and Raanan Miller

*The Charles Stark Draper Laboratory, 555 Technology Square, Cambridge, Massachusetts 02139*

(Received 30 September 1999; accepted for publication 30 October 1999)

The sensing characteristics of in-plane polarized lead zirconate titanate (PZT) thin films were studied and compared with the through-thickness polarized PZT films. The in-plane polarized PZT films were deposited on  $\text{ZrO}_2$ -passivated silicon substrates and had interdigitated electrode systems on the top surface; hence, they can be polarized in the film plane. This in-plane polarization configuration separates the electrode spacing and film thickness as independent variables; thus, the voltage sensitivity can be increased by using wider electrode spacing even for fixed film thickness. The results show that for films with a thickness of  $1\text{ }\mu\text{m}$  the voltage sensitivity of in-plane polarized PZT films can be more than 20 times higher than that of the conventional, through-thickness polarized PZT films which were deposited on Pt-buffered silicon substrates. © 1999 American Institute of Physics. [S0003-6951(99)01152-3]

Ferroelectric thin films such as lead zirconate titanate (PZT) have been intensively studied for sensor and actuator applications in microelectromechanical systems (MEMS) because they offer much higher piezoelectric activity than traditional piezoelectric films such as ZnO and AlN.<sup>1,2</sup> At present, many designs for piezoelectric MEMS devices utilize the bending of cantilever or diaphragm structures. Typically, the bending element consists of a layer of PZT film with both top and bottom electrodes (and so, poled through the thickness) and a thin structural membrane supporting the PZT film. Such structures can be easily realized using silicon micromachining technology. Mechanical bending of the structure can greatly amplify the displacement generated by the PZT films for actuator applications or the applied stress on the PZT films for sensor applications. Thus, many bending-type cantilever or diaphragm MEMS devices are under development for accelerometers, force sensors, pressure and acoustic sensors, microvalves, micropumps, and other microactuators.<sup>2-6</sup>

It should be noticed that the conventional bending unimorph structure utilizes a  $d_{31}$  mode, that is, the polarization direction is through the film thickness and perpendicular to the film plane, but the generated displacement to be used, or the applied stress to be detected, is in the film plane. Because the  $d_{33}$  coefficient of most perovskite-structure piezoelectric ceramics is approximately twice as large as  $d_{31}$ , the use of PZT films which can be polarized in the film plane instead of through the thickness enables the  $d_{33}$  mode to be employed. This, in turn, leads to perform once improvements. As a first step to approach this objective, PZT films were successfully deposited on  $\text{ZrO}_2$ -passivated silicon substrates and shown to possess excellent in-plane polarization.<sup>7</sup> In this letter, the sensing characteristics of such in-plane polarized PZT films

are studied and compared to the conventional, through-thickness polarized PZT films deposited on Pt-buffered silicon substrates.

Both the PZT film and the  $\text{ZrO}_2$  passivation layer were deposited on the silicon substrate through acetic acid-based sol-gel processing; the thickness of the PZT film was  $1\text{ }\mu\text{m}$ . After film deposition, Ti/Pt/Au electrodes were sputtered on the top surface of the PZT film. A photoresist lift-off process was used to define the interdigitated electrodes with a finger width of  $10\text{ }\mu\text{m}$  and finger gaps (electrode spacings) of 5, 10, and  $20\text{ }\mu\text{m}$ , respectively, as shown in Fig. 1. The dielectric properties and hysteresis loops of the films were measured using an HP 4274A LCR meter and a modified Sawyer-Tower circuit. Additional details on processing and hysteresis loops can be found in Ref. 7.

The sensing effect of the PZT film was characterized using the modified wafer flexure technique developed by Shepard, Moses, and Troler-McKinstry and Maria.<sup>8,9</sup> As shown in Fig. 2, after poling the PZT film at 5 times the coercive field (voltage) for 15 min, a small piece of sample was glued on a 3-in.-diam silicon wafer. This was then suspended over a cylinder cavity. By modulating the air pressure in the cavity using the output of an audio speaker, the silicon wafer and PZT film were flexed periodically. This generated a biaxial, transverse stress in the film, and hence, a piezoelectrically induced charge which can be detected by the charge amplifier. Then, the voltage generated in the film was determined by dividing the induced charge by the measured film capacitance. Finally, the voltage sensitivity, which is defined here as the generated voltage per unit change of rms air pressure modulation in the cavity, was calculated by dividing the generated voltage by the pressure value read from the digital pressure transducer.

Shown in Fig. 3(a) are the capacitances and induced charge values of the in-plane polarized film with various electrode spacings under a fixed pressure oscillation level.

<sup>a)</sup>Corresponding author; electronic mail: bxx2@psu.edu

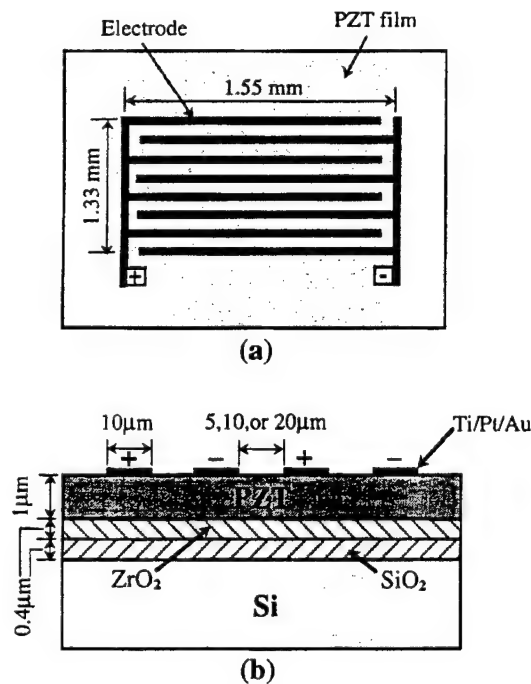


FIG. 1. Sketch of top surface interdigitated electrode pattern and film structure (a) top view and (b) cross-sectional view.

The capacitance continually decreases with an increase of electrode spacing from 5 to 20  $\mu\text{m}$ , but the induced charge remains almost the same as the electrode spacing increases from 10 to 20  $\mu\text{m}$ . While there is some reduction of induced charge when the electrode spacing increases from 5 to 10  $\mu\text{m}$ , the decrease of capacitance is much larger. This leads to a monotonic increase in voltage sensitivity with an increase in electrode spacing, as shown in Fig. 3(b).

The voltage sensitivity of a through-thickness polarized PZT film measured under the same conditions is also given in Fig. 3(b). This PZT film was deposited on a Pt-buffered silicon substrate and the film thickness was also 1  $\mu\text{m}$ . It can be seen that the voltage sensitivity of the in-plane polarized PZT film is much larger than that of the through-thickness polarized PZT film, especially as wider electrode spacing is used for the in-plane polarized film. The sensitivity of the in-plane polarized PZT film with a 20  $\mu\text{m}$  electrode spacing can be more than 20 times larger than that of the through-thickness polarized film.

The air pressure modulation in the cavity is amplified and transferred to the biaxial, transverse stress on the PZT films through flexing the sample. The small deflection plate theory is valid for the present experiment because the applied

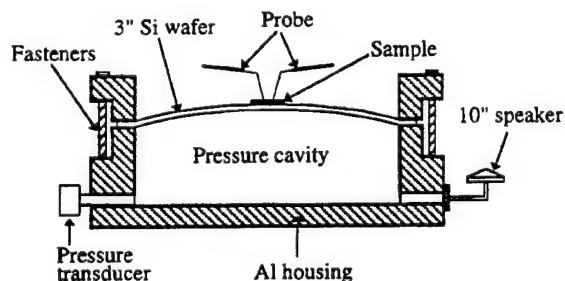


FIG. 2. Setup of the wafer flexure technique (after Maria, see Ref. 9).

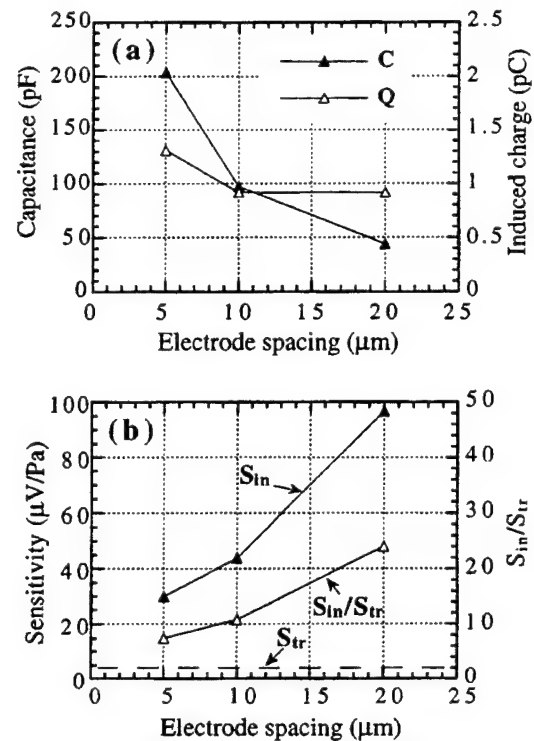


FIG. 3. (a) Film capacitance and induced charge of in-plane polarized PZT film with various electrode spacing for a fixed excitation condition. (b) Voltage sensitivity of in-plane and through-thickness polarized films and their ratios.  $S_{in}$ : sensitivity of in-plane polarized film.  $S_{tr}$ : sensitivity of through-thickness polarized film.

pressure modulation is very small. Thus, the relationship between the transverse stress ( $T$ ) and the rms air pressure modulation ( $P$ ) can be simply expressed as:  $T = cP$ , where  $c$  is a constant and only depends on the elastic properties of the silicon wafer and PZT film.<sup>8</sup> Hence, a comparison of the sensing mechanism of these two kinds of PZT films can be simplified to a comparison of the sensitivity of free-standing, in-plane polarized, and through-thickness polarized PZT thin films under a biaxial stress. As shown in Fig. 4, if we define

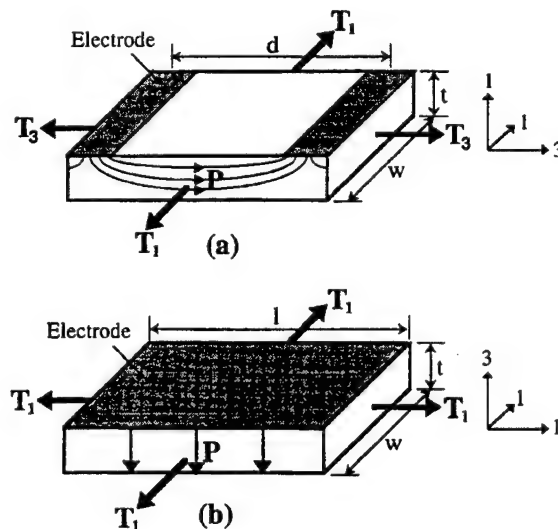


FIG. 4. Schematic of free-standing films under biaxial stress condition: (a) in-plane polarized film and (b) through-thickness polarized film.



the poling direction as the "3" direction, for the in-plane polarized PZT film, the relationship between stress and the rms air pressure modulation can be written as

$$T_{3,in} = c_{3,in}P, \quad T_{1,in} = c_{1,in}P, \quad (1)$$

where the constant  $c_{3,in}$  and  $c_{1,in}$  may be different because the PZT film is anisotropic in the film plane after polarization. The subscript *in* represents in-plane polarization. Supposing that the fringing effect close to the electrode can be neglected and that the polarization is homogeneous in the film between the electrodes, the capacitance and induced charge are [referring to Fig. 4(a)]

$$C_{in} = \epsilon_{33,in}\epsilon_0 tw/d, \quad (2)$$

$$Q_{in} = D_{in}tw = (d_{33,in}T_{3,in} + d_{31,in}T_{1,in})tw. \quad (3)$$

Therefore, the induced voltage and voltage sensitivity will be

$$V_{in} = Q_{in}/C_{in} = [(d_{33,in}T_{3,in} + d_{31,in}T_{1,in})/(\epsilon_{33,in}\epsilon_0)]d, \quad (4)$$

$$\begin{aligned} \text{sensitivity } (S_{in}) &= V_{in}/P \\ &= [(d_{33,in}c_{3,in} + d_{31,in}c_{1,in})/(\epsilon_{33,in}\epsilon_0)]d. \end{aligned} \quad (5)$$

For the through-thickness polarized PZT film, the relationship between stress and the rms air pressure modulation can be written as

$$T_{1,tr} = c_{1,tr}P, \quad (6)$$

where the subscript *tr* represents through-thickness polarization. Referring to Fig. 4(b), the capacitance and induced charge are

$$C_{tr} = \epsilon_{33,tr}\epsilon_0 l w/t, \quad (7)$$

$$Q_{tr} = D_{tr}lw = (2d_{31,tr}T_{1,tr})lw. \quad (8)$$

Hence, the generated voltage and voltage sensitivity will be

$$V_{tr} = Q_{tr}/C_{tr} = [(2d_{31,tr}T_{1,tr})/(\epsilon_{33,tr}\epsilon_0)]t, \quad (9)$$

$$\text{sensitivity } (S_{tr}) = V_{tr}/P = [(2d_{31,tr}c_{1,tr})/(\epsilon_{33,tr}\epsilon_0)]t. \quad (10)$$

Comparing Eq. (2) with Eq. (7), it can be found that as the in-plane polarization configuration separates the film thickness and electrode spacing as independent variables, the capacitance is conversely proportional to the electrode spacing rather than film thickness. Thus, the voltage sensitivity of the in-plane polarized film is proportional to the electrode spacing rather than film thickness [comparing Eq. (5) with Eq. (10)], because the induced charge does not depend on the electrode spacing [Eq. (3)]. The experimental data may not give as simple quantitative relationships as the theoretical analysis due to the fringing effect and relatively large finger width (compared to the finger gap) of the interdigitated electrode system used. Nevertheless, Figs. 3(a) and 3(b) do show, respectively, the obvious decrease of film capacitance and increase of voltage sensitivity with wider electrode spacing. Figure 3(a) also shows that the induced charge is almost the same for the 10- and 20- $\mu\text{m}$ -gap electrode systems. The change in induced charge for the 5- $\mu\text{m}$ -gap electrode system may be attributed to the more severe fringing effect with

smaller electrode spacing.<sup>10</sup> On the other hand, to increase the voltage sensitivity of through-thickness polarized films one has to increase the film thickness [see Eq. (10)]. This is limited both by processing technology, because it is more difficult to prepare thicker films, and by device design, because in many cases the total thickness of a device is determined by the resonant frequency required by the application.

Finally, we point out that the sensing characteristics demonstrated here are general for all bending-type devices because all of them use a similar mechanism to detect force or pressure as in this experiment. In addition, because on-chip buffer amplifiers can have ultralow input capacitance (e.g., as low as 0.1 pF),<sup>11</sup> for integrated devices it is also practical to use a wider electrode spacing for in-plane polarized films. Furthermore, for real devices a normal interdigitated electrode system can be used for cantilever structures and an annular top electrode system can be used for diaphragm structures. The annular electrode system will have one inner electrode in the center of the diaphragm and one outer electrode near the edge of the diaphragm and the polarization can be set between these two electrodes. This will enable the  $(d_{31,in}T_{1,in})$  term in Eq. (4) or the  $(d_{31,in}c_{1,in})$  term in Eq. (5) to be eliminated, which means the devices will use a pure  $d_{33}$  mode and the sensitivity can be further increased ( $d_{31}$  has the opposite sign as  $d_{33}$ ).

In summary, in this letter the sensing characteristics of in-plane polarized PZT thin films which were deposited on  $\text{ZrO}_2$ -passivated silicon substrates has been demonstrated. Because the in-plane polarization configuration separates the film thickness and electrode spacing as independent variables, for a fixed film thickness the voltage sensitivity of the films can be increased by using wider electrode spacing. This makes the voltage sensitivity of in-plane polarized PZT films much larger (e.g., 20 times) than that of the conventional, through-thickness polarized PZT films deposited on Pt-buffered silicon substrates. The voltage sensitivity can be further increased by using suitable electrode systems for special device structures so that a pure  $d_{33}$  mode can be employed. Further work is being developed on constructing devices such as diaphragm sensors for underwater acoustics and cantilever accelerometers by using the in-plane polarized PZT films through silicon micromachining technology.

<sup>1</sup>L. E. Cross and S. Trolier-McKinstry, *Encl. Appl. Phys.* **21**, 429 (1997).

<sup>2</sup>D. L. Polla and L. F. Francis, *MRS Bull.* **21**, 59 (1996).

<sup>3</sup>J. H. Kim, L. Wang, S. M. Zurn, L. Li, Y. S. Yoon, and D. L. Polla, *Integr. Ferroelectr.* **15**, 325 (1997).

<sup>4</sup>J. J. Bernstein, S. L. Finberg, K. Houston, L. C. Niles, H. D. Chen, L. E. Cross, K. K. Li, and K. R. Udayakumar, *IEEE Trans. Ultrason. Ferroelectr. Freq. Control* **44**, 960 (1997).

<sup>5</sup>P. Luginbuhl, G.-A. Racine, P. Lerch, B. Romanowicz, K. G. Brooks, N. F. De Rooij, P. Renaud, and N. Setter, *Sens. Actuators A* **54**, 530 (1996).

<sup>6</sup>C. Lee, T. Itoh, and T. Suga, *IEEE Trans. Ultrason. Ferroelectr. Freq. Control* **43**, 553 (1996).

<sup>7</sup>B. Xu, Y. Ye, L. E. Cross, J. J. Bernstein, and R. Miller, *Appl. Phys. Lett.* **74**, 3549 (1999).

<sup>8</sup>J. F. Shepard, Jr., P. J. Moses, and S. Trolier-McKinstry, *Sens. Actuators A* **71**, 133 (1998).

<sup>9</sup>J. P. Maria, Ph.D. dissertation, The Pennsylvania State University, 1998.

<sup>10</sup>V. M. Ristic and A. M. Hussein, *IEEE Trans. Microwave Theory Tech.* **27**, 897 (1979).

<sup>11</sup>See, for example, Interfet IF 140 JFET (Interfet Corp., [www.inferfet.com](http://www.inferfet.com)).

# **APPENDIX 77**

# Synthesis of Lead Zirconate Titanate Stannate Antiferroelectric Thick Films by Sol-Gel Processing

Baomin Xu,\* L. Eric Cross,\* and Duraiswamy Ravichandran\*

Intercollege Materials Research Laboratory, Pennsylvania State University, University Park, Pennsylvania 16802

The effects of different sintering procedures on the preparation of antiferroelectric thick films and the structure-property relations in these films were studied. An acetic acid-based sol-gel processing with multistep annealing and suitable lead oxide overcoat layers was developed to fabricate both niobium-doped and lanthanum-doped lead zirconate titanate stannate antiferroelectric thick films. The 5- $\mu\text{m}$ -thick  $\text{Pb}_{0.99}\text{Nb}_{0.02}(\text{Zr}_{0.85}\text{Sn}_{0.13}\text{Ti}_{0.02})_{0.98}\text{O}_3$  films demonstrate typical square hysteresis loops with a maximum polarization of  $40 \mu\text{C}/\text{cm}^2$ , zero remanent polarization, an antiferroelectric-to-ferroelectric phase transition field of  $153 \text{ kV}/\text{cm}$ , and a ferroelectric-to-antiferroelectric phase transition field of  $97 \text{ kV}/\text{cm}$ . The dielectric constant and dielectric loss are 283 and 1.7%, respectively. The 5- $\mu\text{m}$ -thick  $\text{Pb}_{0.97}\text{La}_{0.02}(\text{Zr}_{0.65}\text{Sn}_{0.31}\text{Ti}_{0.04})\text{O}_3$  films display typical slanted hysteresis loops with very small hysteresis, a maximum polarization of  $35.0 \mu\text{C}/\text{cm}^2$ , and zero remanent polarization. The dielectric constant and dielectric loss are 434 and 2.0%, respectively.

## I. Introduction

ANTIFERROELECTRIC ceramic materials in the lead zirconate titanate stannate ( $\text{Pb}(\text{Zr},\text{Sn},\text{Ti})\text{O}_3$ ) family have been studied extensively over the past several decades for applications as energy storage capacitors and high-strain transducers/actuators.<sup>1-6</sup> In these ceramics, the free energy difference between the antiferroelectric and ferroelectric states may be modified compositionally to such an extent that a phase transition between the antiferroelectric state and the ferroelectric state can be forced by an applied electric field. This field-induced phase transition is accompanied by a volume expansion due to the larger volume of the ferroelectric phase; hence, large strains can be expected concurrent with the phase transition. In fact, the phase transition strain can be 3 to 4 times larger than the strain levels in conventional piezoelectric materials.<sup>5</sup> Depending on composition and temperature, the antiferroelectric-to-ferroelectric phase transition can occur as a step function of electric field or can change gradually with electric field. These two types of transitions are characterized by "square" and "slanted" hysteresis loops,<sup>3</sup> which allow for digital or analog mechanical motions. Since the phase transition fields must be smaller than the dielectric breakdown strength and low driving voltages are desirable for applications, the most interesting compositions of bulk-type antiferroelectric materials in the  $\text{Pb}(\text{Zr},\text{Sn},\text{Ti})\text{O}_3$  family are in the tetragonal region close to the phase boundary between ferroelectric rhombohedral phase and antiferroelectric tetragonal phase.<sup>5,6</sup>

Antiferroelectric thin films (film thickness  $< 1 \mu\text{m}$ ) have

been studied since the 1990s for microactuation applications in microelectromechanical systems (MEMS)<sup>7-9</sup> and decoupling capacitor applications in advanced multichip modules (MCMs).<sup>10,11</sup> Since thin films have the advantages of high dielectric strength and low operation voltage, antiferroelectric thin films can have rather high phase transition fields and compositions can be extended to the orthorhombic region with very high Zr content.<sup>10</sup> However, most antiferroelectric thin films have slanted hysteresis loops and some remanent polarization, which is believed to be due to the retention of ferroelectric phase after field removal.<sup>9</sup> Our group recently reported that antiferroelectric thin films with square hysteresis loops and zero remanent polarization can be made from modified sol-gel methods.<sup>10,11</sup>

As many MEMS devices require larger displacements than can be generated in thin films,<sup>12</sup> the preparation of ferroelectric PZT thick films (film thickness  $> 1 \mu\text{m}$ ) through sol-gel processing have been reported by several groups.<sup>13-15</sup> However, few reports are given on the preparation of antiferroelectric thick films in spite of the fact that much higher strain levels can be reached in bulk-type antiferroelectric materials. Akiyama *et al.* reported<sup>16</sup> that they could make niobium-doped lead zirconate titanate stannate antiferroelectric films with thicknesses of up to  $4.8 \mu\text{m}$ , but electrical property data were given only for the  $2.4\text{-}\mu\text{m}$ -thick films. In addition, their films displayed some remanent polarization when the electric field was removed.

One of the main problems in preparing lead-containing ferroelectric and antiferroelectric films is lead oxide (PbO) evaporation.<sup>17</sup> The lead deficiency caused by lead oxide evaporation can result in the presence of pyrochlore or fluorite phase within the film which is detrimental to film properties.<sup>18,19</sup> This phenomenon is more severe in high Zr content compositions.<sup>19,20</sup> However, most antiferroelectric phase compositions have rather high Zr contents.<sup>2</sup> This is one of the main reasons that the fabrication of antiferroelectric films is more difficult than ferroelectric films. In addition, most antiferroelectric materials have more complex compositions compared to ferroelectric PZT materials.

Adding excess lead precursor in the starting solution and using rapid thermal annealing are the most typical methods to control lead oxide evaporation and limit the formation of second phases.<sup>21-25</sup> The excess lead can also enhance perovskite phase formation and improve the ferroelectric properties.<sup>21,22</sup> Recently, Tani and Payne<sup>26</sup> proposed a PbO overcoat technique to prevent lead loss. The technique involves the deposition of a single layer of an unhydrolyzed PbO precursor solution after all the required solution depositions. It has been used to prepare PLZT ferroelectric and  $\text{Pb}_{0.99}\text{Nb}_{0.02}[(\text{Zr}_{0.58}\text{Sn}_{0.42})_{0.96}\text{Ti}_{0.04}]_{0.98}\text{O}_3$  (denoted as PZST 42/4/2) antiferroelectric thin films with a 2-methoxyethanol-based sol-gel method,<sup>9,26</sup> but there are no reports on the preparation of antiferroelectric thick films using the lead oxide overcoat method.

In this paper, we demonstrate that both niobium-doped and lanthanum-doped lead zirconate titanate stannate antiferroelectric thick films can be produced from an acetic acid-based sol-gel processing, with emphasis on the effects of the PbO overcoat and sintering procedure. The thicknesses of the films

P. P. Phule—contributing editor

Manuscript No. 190524. Received December 4, 1997; approved June 3, 1998.  
Supported by the Charles Stark Draper Laboratory, Boston, MA.  
\*Member, American Ceramic Society.

Phase analyses of the films were performed using an X-ray diffractometer (XDS 2000, Scintag, Inc., CA). The microstructures were studied using scanning electron microscopy (DS 130, Kevex Instruments, CA). The film thickness was determined with a surface profilometer (Alpha-step 500, Tencor Instruments, NH). To measure the electrical properties of the films, platinum top electrodes with a diameter of 1.6 mm and thickness of 0.05  $\mu\text{m}$  were deposited by the rf sputtering method. The weak-field dielectric properties were measured by using an HP 4274A LCR meter with an oscillating field of about 1 mV/ $\mu\text{m}$  and a frequency of 1 kHz. Polarization-



Table I. Characteristics of Samples

Sample	Composition <sup>a</sup>	Total coating layers <sup>b</sup>	Processing remarks
PN-1	PNZST	25	Single annealing
PN-2	PNZST	25	Multistep annealing (every 5 PN layers)
PN-3	PNZST	25	Multistep annealing with 0.4M PbO solution coatings (every 5 PN layers)
PN-4	PNZST	25	Multistep annealing with 0.8M PbO solution coatings (every 5 PN layers)
PL-1	PLZST	30	Single annealing
PL-2	PLZST	30	Multistep annealing (every 6 PL layers)
PL-2B	PLZST	30	Multistep annealing (every 6 layers) with 0.8M PbO solution coating (for last layer)
PL-3	PLZST	30	Multistep annealing with 0.4M PbO solution coatings (every 6 PL layers)
PL-4	PLZST	30	Multistep annealing with 0.8M PbO solution coatings (every 6 PL layers)

<sup>a</sup>The PNZST composition is  $\text{Pb}_{0.99}\text{Nb}_{0.02}(\text{Zr}_{0.85}\text{Sn}_{0.13}\text{Ti}_{0.02})_{0.98}\text{O}_3$  and the PLZST composition is  $\text{Pb}_{0.97}\text{La}_{0.02}(\text{Zr}_{0.65}\text{Sn}_{0.31}\text{Ti}_{0.04})\text{O}_3$ . <sup>b</sup>The PbO solution overcoat layers are not counted.

electric field characteristics were evaluated by means of a modified Sawyer-Tower circuit, and a triangular waveform voltage was applied at a frequency of 50 Hz. All of the measurements were done at room temperature.

### III. Results

#### (1) Phase Characterization

The X-ray diffraction patterns of the PNZST and PLZST samples are given in Figs. 2 and 3, respectively. The lattice indexes of the peaks are given according to pseudocubic (perovskite) structure rather than orthorhombic structure.<sup>28</sup> (100), (110), (111), and (200) peaks were detected for the PNZST samples, and (100), (111), and (200) peaks were detected for the PLZST samples. The split of the (100) and (200) peaks was probably caused by the tetragonal distortion of the pseudocubic lattice, as observed in bulk-type  $\text{PbZrO}_3$  by Fujishita *et al.*<sup>29</sup> All of the samples show very strong (111) preferred orientation, which is the (202) plane in the orthorhombic structure. It is clear that the strengths of the (100), (200), (110) peaks for the PNZST samples and the (100), (200) peaks for the PLZST samples are gradually increased from PN-1 to PN-4 and PL-1 to PL-4, respectively. The same trend is also observed for the (111) peak for all of the samples (the strengths of the (111) peak of PN-1 and PN-4, and PL-1 and PL-4 are shown in the small figures inserted in Figs. 2 and 3, respectively). This indicates that the crystallization of the perovskite

phase is gradually enhanced from samples PN-1, PL-1, to PN-4 and PL-4.

Although the XRD patterns do not clearly display the existence of the second phase in sample PN-1 (the broad peak around  $2\theta = 30^\circ$  is not obvious), a secondary phase is observed in its photomicrograph (see the photomicrograph of PN-1 below). The similar phenomenon exists for samples PN-2 and PL-1. On the other hand, there is a broad peak around  $2\theta = 30^\circ$  on the XRD patterns of samples PN-3, PL-2, PL-2B, and PL-3, which means that there is some second phase with nanocrystalline fluorite structure in these samples, as has been discussed in thin films.<sup>9</sup> Only samples PN-4 and PL-4 have pure and highly crystallized perovskite phase.

#### (2) Microstructure Analysis

Figure 4 is the surface microstructure of samples PN-1 and PN-4. The photomicrograph of sample PN-1 shows that the grains on the surface are not closely packed and that a second phase exists that may have nanocrystalline fluorite structure.<sup>19</sup> This verifies that the excess lead oxide content in sample PN-1 is not enough to suppress the formation of second phase and to compensate the lead oxide evaporation from the surface. On the other hand, when an extra PbO overcoat layer is used before annealing, sample PN-4 displays a dense, homogeneous, and single-phase surface structure as shown by Fig. 4(b). The cross-sectional photomicrograph of sample PN-4 is given in Fig. 5. It exhibits a dense structure with a film thickness of about 4  $\mu\text{m}$ . Clear columnar structure can also be found in Fig.

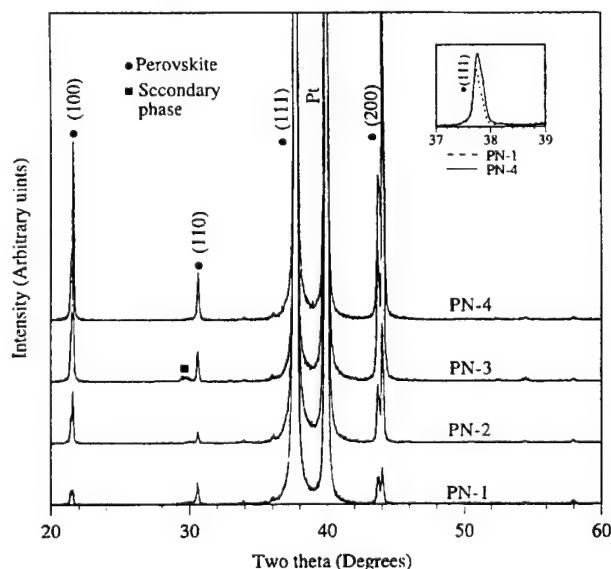


Fig. 2. XRD patterns of the PNZST thick films.

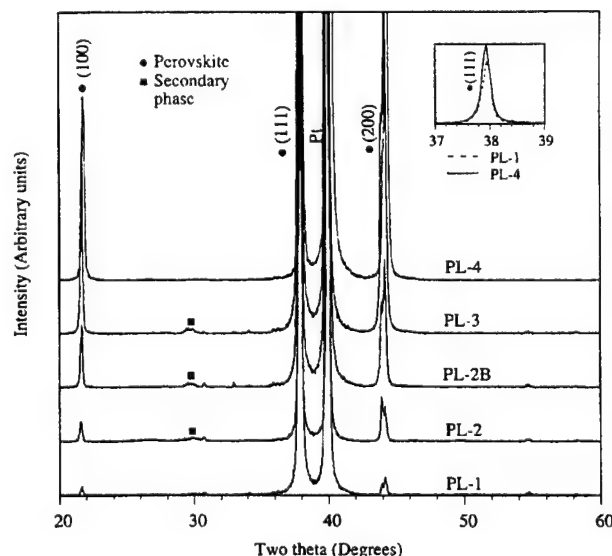


Fig. 3. XRD patterns of the PLZST thick films.

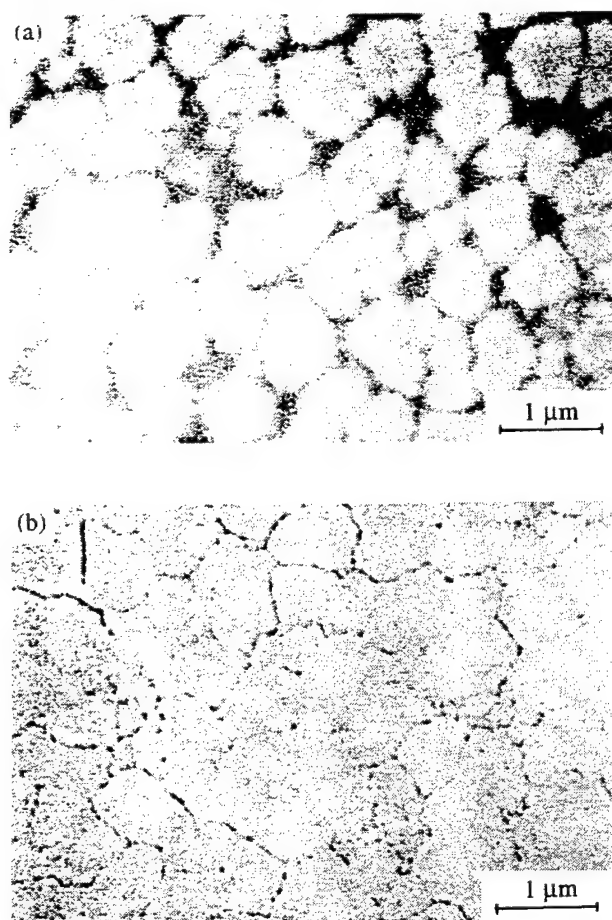


Fig. 4. Surface microstructures of the PNZST thick films: (a) sample PN-1, (b) sample PN-4.

5. This indicates that the perovskite grains nucleate at the film-electrode interface and grow through the film to the free surface, as reported in PZT thin films.<sup>30</sup> Although no surface treatments were done on the samples with PbO overcoat layers after annealing, we did not find any residual PbO from the surface and cross-sectional microstructure analysis. Therefore, most of the PbO evaporated to air or diffused to the earlier PNZST or PLZST layers during the annealing process.

### (3) Film Thickness and Electrical Properties

The total film thickness, average single layer thickness, and the dielectric properties of the samples are given in Table II. The results show that coating of extra PbO layers decreases the film thickness rather than increases the film thickness. The film thickness decreases with the samples prepared by a single annealing process, a multistep annealing process, and a multistep annealing process with PbO overcoat layers. This means that the sintering density increases from samples PN-1 to PN-4 and PL-1 to PL-4. Because of the higher sintering density and the gradually enhanced crystallization of the perovskite phase, the dielectric loss decreases and the dielectric constant increases from samples PN-1 to PN-4 and PL-1 to PL-4, and the dielectric loss of samples PN-4 and PL-4 is smaller than or equals 2.0%.

Figure 6 is the field-induced polarization (hysteresis loops) of the PNZST samples. It can be seen that samples PN-1 and PN-2 have some remanent polarization after the electric field is removed, the quality of their hysteresis loops is very poor, and the maximum polarizations are smaller than those of samples PN-3 and PN-4 when the same driving field (200 kV/cm) is



Fig. 5. Cross-section microstructure of sample PN-4.

used. Although sample PN-3 has a square hysteresis loop with zero remanent polarization, its maximum polarization is still smaller than that of sample PN-4 under the same driving field. Increasing the driving field to 300 kV/cm can make sample PN-3 have the same maximum polarization, but this also causes the sample to have some remanent polarization. Sample PN-4 has a square hysteresis loop with very sharp phase transitions, zero remanent polarization, and a maximum polarization of  $38.5 \mu\text{C}/\text{cm}^2$ . Similar behavior is displayed by the PLZST samples, as shown in Fig. 7, but all the PLZST samples have slanted rather than square hysteresis loops. This means that the shape of hysteresis loops strongly depends on film compositions. Sample PL-4 has a slanted hysteresis loop with very small hysteresis, zero remanent polarization, and a maximum polarization of about  $40 \mu\text{C}/\text{cm}^2$ .

## IV. Discussion

Generally, 5 to 10 mol% excess lead is added to the starting solution to make thin films,<sup>22,23</sup> and more excess lead (10 to 20 mol%) is necessary to make thick films.<sup>14-16</sup> In this work, 25 mol% excess lead was put in the starting solution. This value is almost the maximum amount of excess lead which can be used for the present processing because the addition of 30 mol% or more excess lead is seen to cause cracks in the films even when a single layer is coated. However, this 25 mol% excess lead is still not enough to suppress the formation of the second phase, as proved by the microstructure analysis of sample PN-1. Furthermore, samples PN-1 and PL-1 show relatively weaker crystallization of the perovskite phase and lower sintering density as compared to other samples, which result in samples PN-1 and PL-1 having higher dielectric loss, lower dielectric constant, poor hysteresis loops with some remanent polarization, and lower maximum polarization. In order to enhance the crystallization of the perovskite phase and film density, a multistep annealing process is used instead of a single annealing process.

Table II. Film Thicknesses and Dielectric Properties

Sample	Total film thickness ( $\mu\text{m}$ )	Average single layer thickness ( $\mu\text{m}$ )	$\epsilon_r$ at 1 kHz	$\tan \delta$ at 1 kHz (%)
PN-1	4.875	0.195	207	4.1
PN-2	4.706	0.188	215	3.2
PN-3	4.500	0.180	245	2.2
PN-4	4.201	0.168	262	1.8
PL-1	4.802	0.160	303	4.4
PL-2	4.460	0.149	343	2.9
PL-2B	4.336	0.144	360	2.8
PL-3	4.054	0.135	385	2.2
PL-4	3.659	0.122	406	2.0



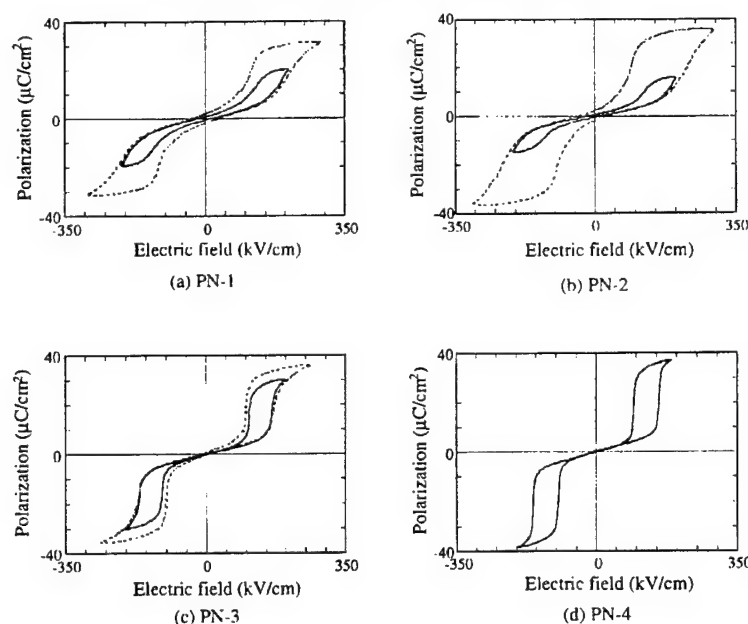


Fig. 6. Electric-field-induced polarization of the PNZST thick films.

The results of samples PN-2 and PL-2 show that simply using multistep annealing can improve the crystallization of the perovskite phase, film density, and electrical properties, but the effect is rather limited. Moreover, multistep annealing may cause more lead oxide evaporation because the annealing tem-

perature is higher than pyrolysis temperature and the soaking time is much longer. This has been proved by the existence of the second phase on the XRD pattern of sample PL-2. Clearly this cannot be overcome by adding more excess lead in the starting solution. Although coating a single PbO cover layer

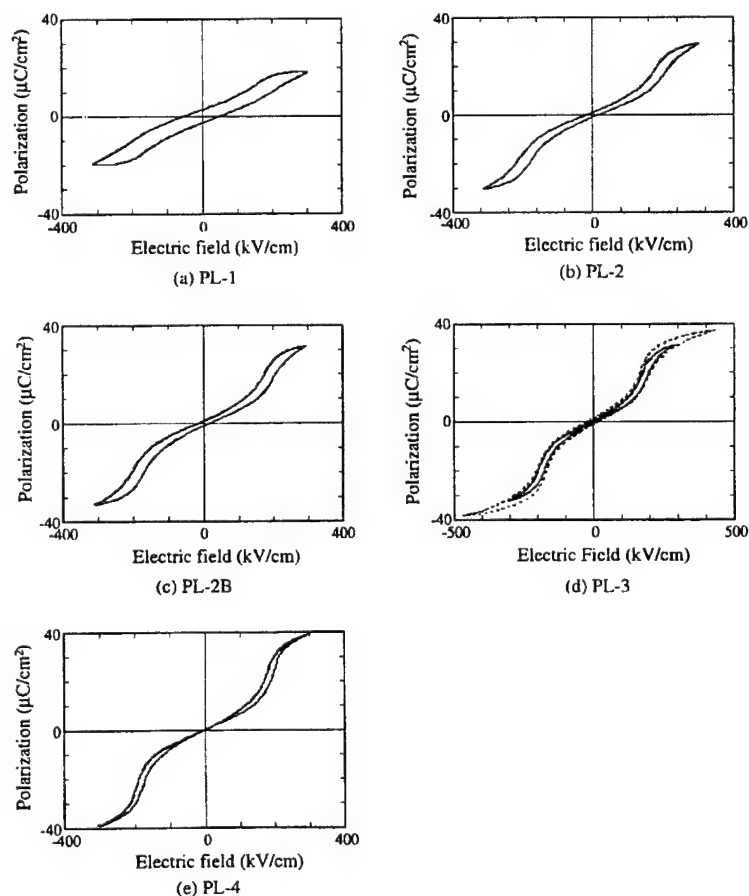


Fig. 7. Electric-field-induced polarization of the PLZST thick films.

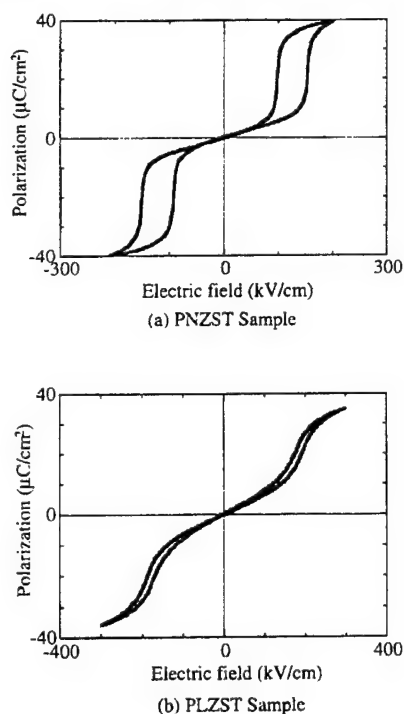


Fig. 8. Electric-field-induced polarization of the 5- $\mu\text{m}$ -thick PNZST and PLZST films: (a) PNZST sample, (b) PLZST sample.

can prevent the formation of the second phase and accelerate the crystallization of the perovskite phase in the preparation of PZST 42/4/2 antiferroelectric thin films (0.5  $\mu\text{m}$  thick),<sup>9</sup> the results of sample PL-2B show that its effectiveness is not so obvious in the preparation of thick films.

Considering all of these factors, a multistep annealing process with multiple PbO overcoat layers (0.8M PbO solution) was developed to prepare antiferroelectric films with thicknesses greater than 3  $\mu\text{m}$ . Its success in producing high-quality antiferroelectric thick films was demonstrated by the results of samples PN-4 and PL-4. Comparing samples PN-4 and PL-4 with other samples, it can be found that this method improved the structure and electrical properties of antiferroelectric thick films in four aspects: (1) It obviously diminished the formation of second phases. (2) It prevented lead oxide evaporation from the PNZST or PLZST surface layer so that a dense surface microstructure could be obtained. (3) It enhanced the crystallization of the perovskite phase. (4) It promoted sintering and increased film density, which was proved by the fact that the average single-layer thicknesses of samples PN-4 and PL-4 were smaller than those of other samples.

The former work has shown that, by using the similar acetic acid-based sol-gel route with 20 mol% excess lead in the starting solution, PZT films with thicknesses of up to 12  $\mu\text{m}$  can be made on platinum-buffered silicon substrates.<sup>14</sup> The present work reveals that the preparation of antiferroelectric thick films is more difficult and complicated. This may be due to the high Zr content and low Ti content in these compositions, that is, the very high Zr/Ti ratio. Although the role of Sn in the nucleation-growth process in these antiferroelectric films is not clear, many investigators have reported that, in PZT systems, a high Zr/Ti ratio will reduce the perovskite crystallization rate.<sup>19,20,30</sup> More recently, Lefevre, Speck, *et al.*<sup>30</sup> have indicated that, for films with columnar microstructure, the perovskite grains nucleate at film/substrate interfaces then grow through the nanocrystalline fluorite to the free surface. Therefore, the films with high Zr/Ti ratios need more time for the perovskite crystallization front to reach the surface, causing more lead loss and resulting in the retained fluorite phase at the surface.

Schwartz<sup>31</sup> has found that, in the preparation of PZT 95/5 thin films, simply adding excess lead in the starting solution cannot balance the lead loss and crystallization process and a PbO overcoat must be used. The antiferroelectric films in this work have Zr/Ti ratios of 85/2 for the PNZST samples and 65/4 for the PLZST samples (Sn has not been counted). The perovskite crystallization rate in these films may be rather slow; hence, in order to get films with single perovskite phase, high density, and good electric properties, PbO overcoats are necessary even though we have added excess lead in the starting solution.

This kinetic effect is also affected by the film thickness and the concentration of PbO overcoat solution. Lefevre, Speck, *et al.*<sup>30</sup> have reported that, to prepare PZT films with a fired thickness of about 0.4  $\mu\text{m}$ , 0.4M PbO overcoat solution is enough to compensate for the lead loss. In our case, the fired thickness of five PNZST coating layers is at least 0.84  $\mu\text{m}$  (the average single layer thickness of PN-4  $\times$  5) and that of six PLZST coating layers is at least 0.73  $\mu\text{m}$  (the average single layer thickness of PL-4  $\times$  6). The results of samples PN-3 and PL-3 show that the 0.4M PbO solution is not enough to compensate the lead loss, as proved by the existence of the second phase in these samples. This can be attributed to the following reason: In thicker films, longer time will be spent for the perovskite phase (which nucleates at the film/electrode interface) to grow through the film and reach the film surface, thus allowing more time for lead loss and requiring more PbO at the film surface for compensation. It is not difficult to conclude that, if the film thickness is greater than 4  $\mu\text{m}$ , it will be very difficult to compensate the lead loss by simply coating one PbO layer before the annealing, as proved by the results of sample PL-2B. This is why multiple PbO overcoat (0.8M PbO solution) layers are necessary to prepare these antiferroelectric thick films.

Finally, using the same procedure to prepare samples PN-4 and PL-4, 5- $\mu\text{m}$ -thick PNZST and PLZST samples were prepared by coating more layers (30 PNZST coating layers and 42 PLZST coating layers). The hysteresis loops of these 5- $\mu\text{m}$ -thick samples are given in Fig. 8, and the electrical properties are summarized in Table III. The phase transition fields of PNZST sample were determined by extrapolating the steepest sections of the hysteresis loop and obtaining their intersections with the horizontal axis. The phase transition fields of PLZST sample cannot be determined because of the slanted shape of the hysteresis loop. To the best of our knowledge, this is the first time that the preparation of 5- $\mu\text{m}$ -thick antiferroelectric films have been reported, with zero remanent polarization, typical square hysteresis loops with very sharp phase transitions, or typical slanted hysteresis loops with very small hysteresis.

## V. Summary

The effects of lead oxide overcoat layers and various sintering conditions on the preparation of antiferroelectric thick films by acetic acid-based sol-gel processing were systematically investigated. The processing-structure-property relations in the films were studied for films with thicknesses between 3.6 and 5  $\mu\text{m}$ . A multistep annealing process with multiple PbO overcoat layers (0.8M PbO solution) was developed to produce high-quality antiferroelectric thick films because it can effectively limit the formation of the second phase, promote the formation of dense surface structure, enhance the crystallization of the perovskite phase, and improve the film density.

Table III. Electrical Properties of 5- $\mu\text{m}$ -Thick Films

Composition	$\epsilon_r$ at 1 kHz	$\tan \delta$ (%)	$E_{\text{AFE} \rightarrow \text{FE}}$ (kV/cm)	$E_{\text{FE} \rightarrow \text{AFE}}$ (kV/cm)	$P_{\text{max}}$ ( $\mu\text{C}/\text{cm}^2$ )
PNZST	283	1.7	153	97	40
PLZST	434	2.0	†	†	35

†Cannot be determined because of the slanted shape of the hysteresis loop.



The 5- $\mu\text{m}$ -thick  $\text{Pb}_{0.99}\text{Nb}_{0.02}(\text{Zr}_{0.85}\text{Sn}_{0.13}\text{Ti}_{0.02})_{0.98}\text{O}_3$  films demonstrate square hysteresis loops with very sharp phase transition, zero remanent polarization, and a maximum polarization of 40  $\mu\text{C}/\text{cm}^2$ , which is suitable for digital electromechanical response applications. The antiferroelectric-to-ferroelectric and the ferroelectric-to-antiferroelectric phase transition fields are 153 and 97 kV/cm, respectively. The weak-field dielectric constant is about 283, and the dielectric loss is about 1.7%. The 5- $\mu\text{m}$ -thick  $\text{Pb}_{0.97}\text{La}_{0.02}(\text{Zr}_{0.65}\text{Sn}_{0.31}\text{Ti}_{0.04})\text{O}_3$  films demonstrate slanted hysteresis loops with very small hysteresis, zero remanent polarization, and a maximum polarization of 35  $\mu\text{C}/\text{cm}^2$ , which is suitable for analog electromechanical response applications. The weak field dielectric constant is about 434 and the dielectric loss is about 2.0%.

## References

- <sup>1</sup>B. Jaffe, "Antiferroelectric Ceramics with Field-Enforced Transitions: A New Nonlinear Circuit Element," *Proc. IRE*, **49**, 1264–67 (1961).
- <sup>2</sup>D. Berlincourt, H. H. A. Krueger, and B. Jaffe, "Stability of Phase in Modified Lead Zirconate with Variation in Pressure, Electric Field, Temperature and Composition," *J. Phys. Chem. Solids*, **25**, 659–74 (1964).
- <sup>3</sup>D. Berlincourt, "Transducers Using Forced Transitions between Ferroelectric and Antiferroelectric States," *IEEE Trans. Sonics Ultrason.*, **13**, 116–24 (1966).
- <sup>4</sup>K. Uchino and S. Nomura, "Shape Memory Effect Associated with the Forced Phase Transition in Antiferroelectrics," *Ferroelectrics*, **50**, 517–21 (1983).
- <sup>5</sup>W. Y. Pan, C. Q. Dam, Q. M. Zhang, and L. E. Cross, "Large Displacement Transducers Based on Electric Field Forced Phase Transitions in the Tetragonal  $(\text{Pb}_{0.97}\text{La}_{0.02})(\text{Ti,Zr,Sn})\text{O}_3$  Family of Ceramics," *J. Appl. Phys.*, **66**, 6014–23 (1989).
- <sup>6</sup>K. Markowski, S. E. Park, S. Yoshikawa, and L. E. Cross, "Effect of Compositional Variations in the Lead Lanthanum Zirconate Stannate Titanate System on Electrical Properties," *J. Am. Ceram. Soc.*, **79**, 3297–304 (1996).
- <sup>7</sup>K. G. Brooks, J. Chen, K. R. Udayakumar, and L. E. Cross, "Electric Field Forced Phase Switching in La-Modified Lead Zirconate Titanate Stannate Thin Films," *J. Appl. Phys.*, **75**, 1699–704 (1994).
- <sup>8</sup>K. K. Li, F. Wang, and G. H. Haertling, "Antiferroelectric Lead Zirconate Thin Films Derived from Acetate Precursors," *J. Mater. Sci.*, **30**, 1386–90 (1995).
- <sup>9</sup>S. S. Sengupta, D. Roberts, J. F. Li, M. C. Kim, and D. A. Payne, "Field-Induced Phase Switching and Electrically Driven Strains in Sol-Gel Derived Antiferroelectric  $(\text{Pb,Nb})(\text{Zr,Sn,Ti})\text{O}_3$  Thin Layers," *J. Appl. Phys.*, **78**, 1171–77 (1995).
- <sup>10</sup>C. J. Gaskey, K. R. Udayakumar, H. D. Chen, and L. E. Cross, "'Square' Hysteresis Loops in Phase-Switching Nb-Doped Lead Zirconate Stannate Titanate Thin Films," *J. Mater. Res.*, **10**, 2764–69 (1995).
- <sup>11</sup>B. Zu, N. G. Pai, and L. E. Cross, "Lanthanum-Doped Lead Zirconate Titanate Stannate Antiferroelectric Thin Films from Acetic Acid-Based Sol-Gel Method," *Mater. Lett.*, **35**, 157–60 (1998).
- <sup>12</sup>L. E. Cross and S. Trolier-McKinstry, "Thin Film Integrated Ferroelectrics," *Encycl. Appl. Phys.*, **21**, 429–51 (1997).
- <sup>13</sup>G. Yi and M. Sayer, "Sol-Gel Processing of Thick PZT Films," pp. 289–92 in Proceedings of the Eighth IEEE International Symposium on Applications of Ferroelectrics (Greenville, SC, 1992). Edited by M. Liu, A. Safari, A. Kingon, and G. Haertling. Institute of Electrical and Electronic Engineers, Piscataway, NJ, 1992.
- <sup>14</sup>H. D. Chen, K. R. Udayakumar, C. J. Gaskey, L. E. Cross, J. J. Bernstein, and L. C. Niles, "Fabrication and Electrical Properties of Lead Zirconate Titanate Thick Films," *J. Am. Ceram. Soc.*, **79**, 2189–92 (1996).
- <sup>15</sup>Y. L. Tu and S. J. Milne, "Processing and Characterization of  $\text{Pb}(\text{Zr,Ti})\text{O}_3$  Films, Up to 10  $\mu\text{m}$  Thick, Produced from a Diol Sol-Gel Route," *J. Mater. Res.*, **11**, 2556–64 (1996).
- <sup>16</sup>Y. Akiyama, S. Kimura, and I. Fujimura, "Development of  $(\text{Pb,Nb})(\text{Zr,Sn,Ti})\text{O}_3$  Film Using a Sol-Gel Process and Resulting Antiferroelectric Properties," *Jpn. J. Appl. Phys.*, **32**, 4154–57 (1993).
- <sup>17</sup>B. A. Tuttle and R. W. Schwartz, "Solution Deposition of Ferroelectric Thin Films," *MRS Bull.*, **21** [6] 49–54 (1996).
- <sup>18</sup>L. N. Chapin and S. A. Mayers, "Microstructure Characterization of Ferroelectric Thin Films Used in Non-volatile Memories—Optical and Scanning Electron Microscopy," pp. 153–58 in *Ferroelectric Thin Films*, Proceedings of the Materials Research Society Symposium (San Francisco, CA, April 1990), Vol. 200. Edited by E. R. Myers and A. I. Kingon. Materials Research Society, Pittsburgh, PA, 1990.
- <sup>19</sup>A. P. Wilkinson, J. S. Speck, A. K. Ceetham, S. Natarajan, and J. M. Thomas, "In Situ X-ray Diffraction Study of Crystallization Kinetics in  $\text{PbZr}_{1-x}\text{Ti}_x\text{O}_3$  (PZT,  $x = 0.0, 0.55, 1.0$ )," *Chem. Mater.*, **6**, 750–59 (1994).
- <sup>20</sup>A. H. Carim, B. A. Tuttle, D. H. Doughty, and S. L. Martinez, "Microstructure of Solution-Processed Lead Zirconate Titanate (PZT) Thin Films," *J. Am. Ceram. Soc.*, **74**, 1455–58 (1991).
- <sup>21</sup>S. D. Bernstein, Y. Kisler, J. M. Wahl, S. E. Bernacki, and S. R. Collins, "Effects of Stoichiometry on PZT Thin Film Capacitor Properties," pp. 373–78 in *Ferroelectric Thin Films II*, Proceedings of the Materials Research Society Symposium (Boston, MA, December 1991), Vol. 243. Edited by A. I. Kingon, E. R. Myers, and B. A. Tuttle. Materials Research Society, Pittsburgh, PA, 1992.
- <sup>22</sup>B. A. Tuttle, R. W. Schwartz, D. H. Doughty, and J. A. Voigt, "Characterization of Chemically Prepared PZT Thin Films," pp. 159–65 in *Ferroelectric Thin Films*, Proceedings of the Materials Research Society Symposium (San Francisco, CA, April 1990), Vol. 200. Edited by E. R. Myers and A. I. Kingon. Materials Research Society, Pittsburgh, PA, 1990.
- <sup>23</sup>I. M. Reaney, K. Brooks, R. Klissurska, C. Pawlaczyk, and N. Setter, "Use of Transmission Electron Microscopy for the Characterization of Rapid Thermally Annealed, Solution-Gel, Lead Zirconate Titanate Films," *J. Am. Ceram. Soc.*, **77**, 1209–16 (1994).
- <sup>24</sup>L. Shi, S. B. Krupanidhi, and G. H. Haertling, "Development of Ferroelectric  $\text{Pb}(\text{Zr,Ti})_{1-x}\text{O}_3$  by Metallo-organic Decomposition Process and Rapid Thermal Annealing," *Integr. Ferroelectr.*, **1**, 111–27 (1992).
- <sup>25</sup>L. F. Francis, Y.-J. Oh, and D. A. Payne, "Sol-Gel Processing and Properties of Lead Magnesium Niobate Powders and Thin Layers," *J. Mater. Sci.*, **25**, 5007–13 (1990).
- <sup>26</sup>T. Tani and D. A. Payne, "Lead Oxide Coatings on Sol-Gel-Derived Lead Lanthanum Zirconium Titanate Thin Layers for Enhanced Crystallization into the Perovskite Structure," *J. Am. Ceram. Soc.*, **77**, 1242–48 (1994).
- <sup>27</sup>G. Yi, Z. Xu, and M. Sayer, "Preparation of  $\text{Pb}(\text{Zr,Ti})\text{O}_3$  Thin Films by Sol-Gel Processing: Electrical, Optical, and Electro-optic Properties," *J. Appl. Phys.*, **64**, 2717–24 (1988).
- <sup>28</sup>F. Jona, G. Shirane, F. Mzaai, and R. Pepinsky, "X-ray and Neutron Diffraction Study of Antiferroelectric Lead Zirconate,  $\text{PbZrO}_3$ ," *Phys. Rev.*, **105**, 849–56 (1957).
- <sup>29</sup>H. Fujishita, Y. Shiozaki, and E. Sawaguchi, "Lattice Distortion of  $\text{PbZrO}_3$ ," *J. Phys. Soc. Jpn.*, **46**, 1391–92 (1979).
- <sup>30</sup>M. J. Lefevre, J. S. Speck, R. W. Schwartz, D. Dimos, and S. J. Lockwood, "Microstructural Development in Sol-Gel Derived Lead Zirconate Titanate Thin Films: The Role of Precursor Stoichiometry and Processing Environment," *J. Mater. Res.*, **11**, 2076–84 (1996).
- <sup>31</sup>R. W. Schwartz, "Chemical Solution Deposition of Perovskite Thin Films," *Chem. Mater.*, **9**, 2325–40 (1997). □

# **APPENDIX 78**

# Dependence of electrical properties on film thickness in lanthanum-doped lead zirconate titanate stannate antiferroelectric thin films

Baomin Xu,<sup>a)</sup> Yaohong Ye, Qing-Ming Wang, and L. Eric Cross  
*Intercollege Materials Research Laboratory, Pennsylvania State University,  
University Park, Pennsylvania 16802*

(Received 1 October 1998; accepted for publication 4 January 1999)

Lanthanum-doped lead zirconate titanate stannate antiferroelectric thin films with compositions in antiferroelectric orthorhombic region have been prepared on Pt-buffered Si substrates by the sol-gel method, with the film thickness from 0.1 to 1.0  $\mu\text{m}$ . The dependence of dielectric and ferroelectric properties on film thickness have been studied, with the emphasis on field-induced phase switching. The dielectric constant and maximum polarization decrease with the reduction of film thickness, which are similar to ferroelectric thin films. However, the decrease of film thickness also leads to the decrease of the phase switching fields, the appearance of remanent polarization in the hysteresis loops, and the smearing of antiferroelectric-ferroelectric phase switching. These phenomena are believed to be caused mainly by the stress effect between the film and substrate. Due to thermal mismatch, the films are under high tensile stress after annealing, and the stress effect becomes more significant with the decrease of film thickness. This makes the thinner films more preferable to the ferroelectric phase and causes the retention of ferroelectric phase in the films with thickness less than 0.4  $\mu\text{m}$ . © 1999 American Institute of Physics. [S0021-8979(99)03707-X]

## I. INTRODUCTION

Ferroelectric thin films have been under intensive investigation because of their extensive applications in microelectronics, microelectromechanical systems (MEMS), and electro-optics. These applications include ferroelectric non-volatile memories, high density dynamic random access memories, infrared pyroelectric detectors, decoupling capacitors, microsensors and microactuators, electro-optical switches and modulators, and optical waveguide devices.<sup>1,2</sup> Many researchers have found that the electrical properties of ferroelectric thin films are quite different from that of bulk materials and significantly depend on the thickness of films. These so-called "size effects" in thin films, especially in lead zirconate titanate (PZT) ferroelectric thin films, have been widely studied.<sup>3-7</sup> Generally, with the decrease of film thickness the size effects lead to the decrease of dielectric constant and remanent polarization, the increase of coercive field, and the smearing of the ferroelectric-paraelectric phase transition. Another phenomenon related to size effects in thin films is the domain switching. It has been reported that, mainly due to the small grain size and residual stresses, the non-180° domain wall motion is very limited in PZT thin films.<sup>8-10</sup> Hence, the extrinsic factors make modest contributions to the dielectric and piezoelectric properties in thin films, which leads to the inferior dielectric and electromechanical properties of ferroelectric thin films compared to bulk ceramics.<sup>10</sup> This implies that it will be difficult to fabricate high-strain microactuators based only on the ferroelectric PZT thin films.

Because high-strain thin films are very important for microactuation applications in MEMS, it is necessary to develop other thin film materials which can generate high-strain levels. The antiferroelectric-to-ferroelectric phase switching thin films may be one of the alternatives. Unlike PZT ferroelectric materials, the strain or displacement of antiferroelectric materials originates from the antiferroelectric-to-ferroelectric phase switching because the unit cell of the ferroelectric phase is larger than that of the antiferroelectric phase. Therefore, it is possible to keep the strain level of thin film-type materials as that of bulk-type materials. In bulk-type antiferroelectric materials, a strain level as high as 0.8% has been reported, and the strain level of 0.4% can be easily reproduced.<sup>11,12</sup>

As a matter of fact, the study on the antiferroelectric thin films for microactuator applications began in the early 1990s.<sup>13</sup> However, most of the antiferroelectric thin films demonstrate some remanent polarization after the electric field is removed, which is believed to be due to the retention of the ferroelectric phase.<sup>14</sup> The strain levels of these thin films just reach about 0.2%.<sup>14</sup> Until recently, our group reported that the antiferroelectric thin films with zero remanent polarization and "square" hysteresis loops (that is, very sharp phase switching) can be prepared from the 2-methoxyethanol based or acetic acid based sol-gel method.<sup>15,16</sup> The strain levels of these thin films can reach about 0.4%, which is very promising for microactuator applications.<sup>17</sup> In addition, the energy storage density of these thin films can be higher than 7 J/cm<sup>3</sup>, and half of the stored charge can be released in 10 ns, demonstrating another potential application as decoupling capacitors in high-speed multichip modules.<sup>18</sup>

<sup>a)</sup>Author to whom correspondence should be addressed; Electronic mail: bxx2@psu.edu

Compared to PZT ferroelectric thin films, the study on the size effects in antiferroelectric thin films is very limited. In 1995, Kanno *et al.* reported the field-induced polarization in  $\text{PbZrO}_3$  thin films with different thicknesses.<sup>19</sup> These films were deposited on Pt-buffered MgO or Si substrates by a multi-ion-beam sputtering technique. They found that the films 177 nm thick show antiferroelectric hystereses (double hysteresis loops) while films 87.5 nm thick show ferroelectric hystereses. More recently, Chattopadhyay and Ayyub *et al.* also reported the thickness dependence of hysteresis loops in  $\text{PbZrO}_3$  thin films which were directly deposited on Si (100) substrates using the laser ablation method, and they found that the films are ferroelectric below a thickness of about 500 nm and antiferroelectric at higher thickness.<sup>20,21</sup> However, for the more widely used lead zirconate titanate stannate (PZST) system, the size effects in their thin films have not been reported. In this article the thickness-dependent electrical properties in lanthanum-doped PZST antiferroelectric thin films have been reported for the first time. The emphasis is put on the thickness dependence of field-induced phase switching, which is very important for antiferroelectric thin films but cannot exist in ferroelectric thin films. We also point out that the residual stress due to the thermal mismatch between the film and substrate is the most important factor affecting the thickness dependence of field-induced phase switching in antiferroelectric thin films.

## II. EXPERIMENTAL PROCEDURE

The compositions used in this work are  $\text{Pb}_{0.97}\text{La}_{0.02}(\text{Zr}_{0.85}\text{Sn}_{0.13}\text{Ti}_{0.02})\text{O}_3$  (abbreviated as PL-1) and  $\text{Pb}_{0.97}\text{La}_{0.02}(\text{Zr}_{0.65}\text{Sn}_{0.31}\text{Ti}_{0.04})\text{O}_3$  (abbreviated as PL-2), and both of them are located in the antiferroelectric orthorhombic region in the phase diagram. The substrates are (100) oriented, *n*-type silicon wafers with a 0.5  $\mu\text{m}$ -thick thermally grown-on  $\text{SiO}_2$  layer, a 0.02- $\mu\text{m}$ -thick sputtered titanium layer, and a 0.15- $\mu\text{m}$ -thick sputtered platinum layer as the bottom electrode. Samples were prepared from the acetic acid based sol-gel method. The flow chart to prepare films is given in Fig. 1, and details of the processing can be found in Ref. 16. Lead acetate trihydrate, lanthanum ethoxide, and tin acetate were initially dissolved in acetic acid, and the associated water was removed during a period of distillation at 150 °C. After cooling to room temperature, titanium isopropoxide and zirconium *n*-propoxide were added to the solution and mixed in the flask at 105 °C for 1 h. Ethylene glycol and de-ionized water were also added during reflux to control the concentration and viscosity of the solution. A multiple spin coating procedure was used for the samples to reach desired thickness. The films were pyrolyzed at 600 °C for 0.1 h after the deposition of each layer and annealed at 700 °C for 1 h after the final layer deposition. Both pyrolysis and annealing were conducted in a commercial box furnace.  $\text{PbO}$  overcoat solution, which was made from lead acetate trihydrate, was prepared using the similar procedure. An extra  $\text{PbO}$  solution layer was coated before final annealing of the films with thickness equal to or larger than 0.7  $\mu\text{m}$ . This is because in thicker films, a longer time will be spent for the perovskite phase (which nucleates at the film/electrode inter-

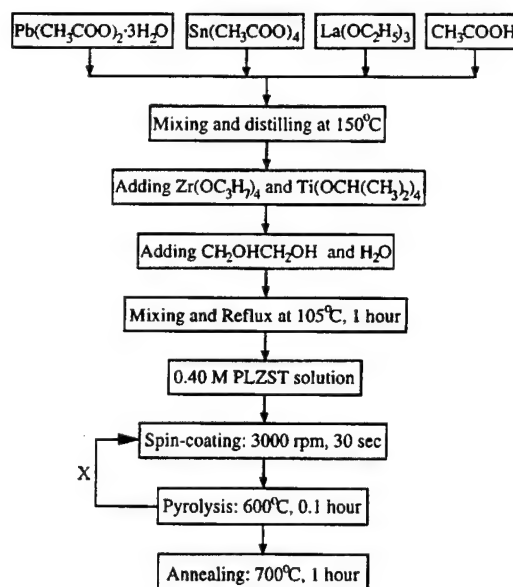


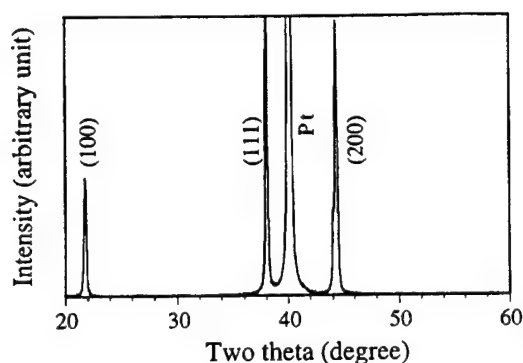
FIG. 1. Flow chart to prepare the antiferroelectric films.

face) to grow through the film and reach the film surface, thus allowing more time for lead evaporation and requiring more  $\text{PbO}$  at the film surface for compensation. Only by using the  $\text{PbO}$  overcoat layer procedure can the films (which are thicker than 0.7  $\mu\text{m}$ ) be obtained with single perovskite phase and dense surface microstructure. This is also a critical technique to prepare antiferroelectric “thick” films (the film thickness is about 5  $\mu\text{m}$ ). The discussion on the effect of  $\text{PbO}$  overcoat layers is not the objective of this article and will be published separately.<sup>22</sup>

Crystallization of the films after annealing was examined by a Scintag x-ray diffractometer (XDS 2000, Scintag) using  $\text{Cu K}\alpha$  radiation ( $\lambda = 1.5418 \text{ \AA}$ ). The x-ray diffraction (XRD) patterns were recorded at a rate of 2°/min with the  $2\theta$  range from 20° to 60°. The microstructure of the films was studied using a scanning electron microscope (DS 130, Kevex Instruments, CA). The thickness of the films was measured by a surface profilometer (Alpha-step 500, Tencor Instruments, NH) with the films partially etched by using the  $\text{HF-HNO}_3$  solution. In order to measure the electrical properties, platinum top electrodes with a diameter of 1.6 mm were deposited by the rf sputtering method. The low field dielectric properties were measured using an HP 4274A LCR meter with an oscillating field of about 10 mV/ $\mu\text{m}$ . The field-induced polarization (hysteresis loop) was measured using a modified Sawyer-Tower circuit with a 50 Hz, triangular wave form driving signal. All the measurements were conducted at room temperature.

## III. RESULTS

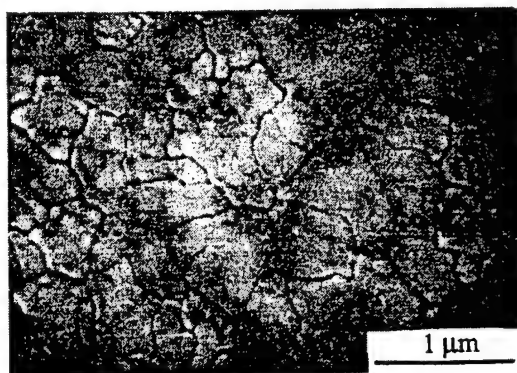
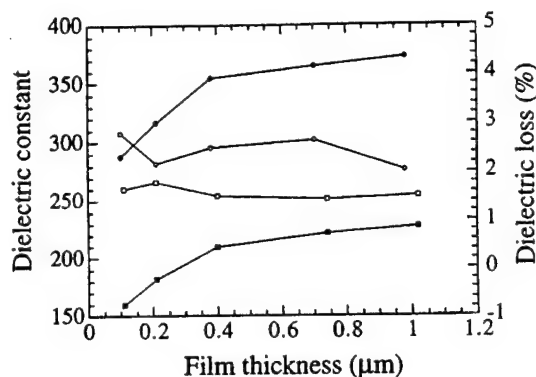
The x-ray analyses demonstrate that all the films are single perovskite structure after the annealing at 700 °C. Figure 2 is the XRD pattern of the 0.74- $\mu\text{m}$ -thick PL-1 film. The lattice indexes of the peaks are given according to pseudocubic (tetragonal) structure rather than orthorhombic structure. Preferred (111) orientation is observed for all the samples, which is (202) plane in the orthorhombic structure.

FIG. 2. XRD configuration of the 0.74- $\mu\text{m}$ -thick PL-1 film.

The similar preferred orientation is also reported by other groups and is believed to be due to the diffusion of Ti into the Pt layer, which changed the surface energy and lattice parameters and promoted the crystallization of (111) perovskite by epitaxial nucleation and growth.<sup>14,23</sup> Figure 3 is the scanning electron microscope (SEM) picture of the 0.74- $\mu\text{m}$ -thick PL-1 film, which shows the presence of single-phase and dense grains with the typical grain size from 0.4 to 0.6  $\mu\text{m}$ . This dense, close-packed surface structure is common to the films in the thickness range studied.

The thickness dependence of dielectric properties for the PL-1 and PL-2 films is shown in Fig. 4. The dielectric loss values are not as sensitive to the film thickness, and are between 1% and 2% for the PL-1 films and between 2% and 3% for the PL-2 films. However, the dielectric constant decreases with the reduction of film thickness, and this decreasing tendency is more obvious for the films with thickness below a critical value of about 0.4  $\mu\text{m}$ .

The field-induced polarization of PL-1 and PL-2 samples with various thicknesses are given in Figs. 5 and 6, respectively. All these films demonstrate double hysteresis loops, which confirms their antiferroelectric characteristic. The quality of the hysteresis loops depends strongly on film thickness, and the contrast is very explicit for the films with thicknesses below and above 0.4  $\mu\text{m}$ : The films with thickness equal to or larger than about 0.4  $\mu\text{m}$  demonstrate zero remanent polarization, while the remanent polarization is observed on the hysteresis loops for the films with the thickness less than 0.4  $\mu\text{m}$ , which implies the retention of ferroelectric

FIG. 3. Surface microstructure of the 0.74- $\mu\text{m}$ -thick PL-1 film.FIG. 4. Thickness dependence of dielectric properties for the PL-1 and PL-2 films: (—●—) PL-1,  $\epsilon_r$ , (—○—) PL-1,  $\tan \delta$ , (—■—) PL-2,  $\epsilon_r$ , (—□—) PL-2,  $\tan \delta$ .

phase in these films.<sup>14</sup> Moreover, the reduction of film thickness leads to the decrease of maximum polarization (Fig. 7), and there is a sharp drop on the maximum polarization for the films with thickness less than about 0.4  $\mu\text{m}$ . The smearing or diffusion of field-induced phase switching for the films with thickness less than 0.4  $\mu\text{m}$  can also be found in Figs. 5 and 6. This phenomenon is especially distinctive for the PL-1 samples because of the "square" hysteresis loop characteristic for this composition. Typical "slanted" hysteresis loops with gradual phase switching are observed for the PL-2 samples with thickness larger than about 0.4  $\mu\text{m}$ . This kind of material is suitable for analog electromechanical response applications. On the other hand, the films with PL-1 composition and thickness larger than 0.4  $\mu\text{m}$  show typical "square" hysteresis loops with sharp phase switching. They are suitable for digital electromechanical applications and energy-storage capacitor applications.

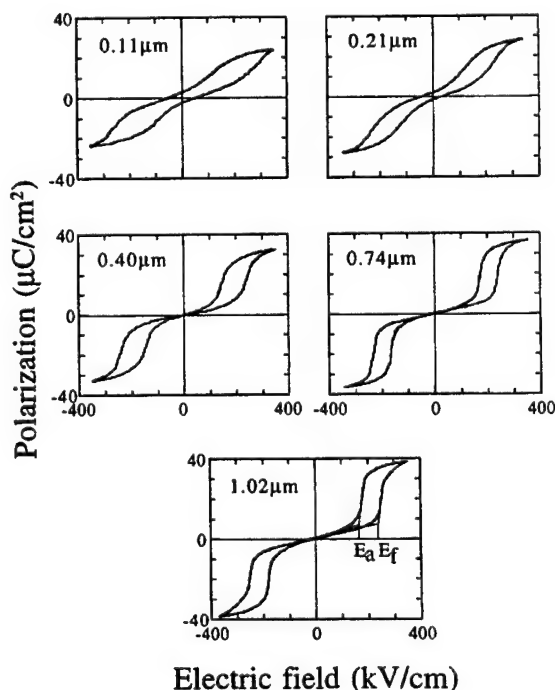


FIG. 5. Electric field-induced polarization of the PL-1 films with various thicknesses.

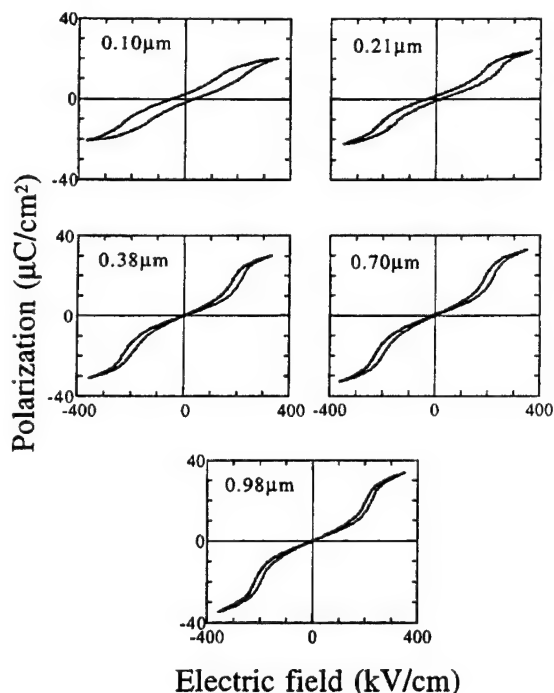


FIG. 6. Electric field-induced polarization of the PL-2 films with various thicknesses.

The phase switching fields for the PL-1 films with thickness larger than  $0.4 \mu\text{m}$  are rather explicit, but they are not so distinctive for the films with thickness less than  $0.4 \mu\text{m}$  because of the smearing of the field-induced phase switching. In order to study the thickness dependence of phase switching fields in the whole thickness range, we determine the phase switching fields for all the PL-1 films using the method introduced by Brook *et al.* in Ref. 13. That is, the antiferroelectric-to-ferroelectric ( $\text{AF} \rightarrow \text{F}$ ) and the ferroelectric-to-antiferroelectric ( $\text{F} \rightarrow \text{AF}$ ) phase switching fields are determined as the intersections of the two lines representing the steepest and flattest sections on the forward part and backward part, respectively, of the hysteresis loops. One example to determine the phase switching fields is shown in the hysteresis loop of the  $1.02\text{-}\mu\text{m}$ -thick PL-1 film ( $E_f$  represents  $E_{\text{AF} \rightarrow \text{F}}$  and  $E_a$  represents  $E_{\text{F} \rightarrow \text{AF}}$ ). According to this definition it is clear that the  $\text{AF} \rightarrow \text{F}$  phase switching field

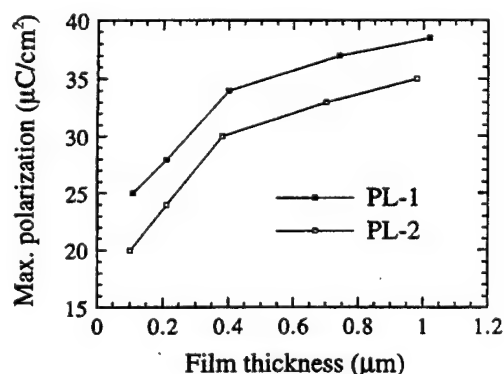


FIG. 7. Thickness dependence of maximum polarization for the PL-1 and PL-2 films.

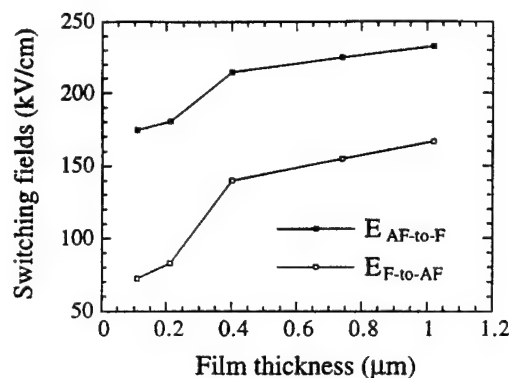


FIG. 8. Thickness dependence of phase switching fields for the PL-1 films.

represents the field at which the  $\text{AF} \rightarrow \text{F}$  phase switching begins to happen and the  $\text{F} \rightarrow \text{AF}$  phase switching field represents the field at which the  $\text{F} \rightarrow \text{AF}$  phase switching is finished. The thickness dependence of the phase switching fields for the PL-1 films are given in Fig. 8. It can be seen that the phase switching fields also decrease with the reduction of film thickness and there is a sharp drop for the films with thickness less than  $0.4 \mu\text{m}$ . This means that for the thinner films, much lower fields are required to induce the  $\text{AF} \rightarrow \text{F}$  phase switching and to keep the films in ferroelectric phase. Due to the slanted hysteresis characteristic of PL-2 films, we do not define their phase switching fields in this work.

#### IV. DISCUSSION

The reduction in film thickness causes the decrease of dielectric constant and maximum polarization in these antiferroelectric thin films, which is similar to the variations of dielectric constant and remanent polarization with film thickness in PZT ferroelectric films. It has been suggested that these thickness-dependent properties can be attributed to a number of factors such as electrode/film interface layers,<sup>5,6</sup> stresses,<sup>4,24</sup> domain structure transitions,<sup>9</sup> and grain size variation with film thickness.<sup>25</sup> Although the exact influence of each of these factors is still under study, some researchers believe that the interface layer between the film/electrode is the dominant factor,<sup>5,6</sup> and the property changes with thickness can be treated as a simple two-capacitor series circuit: One represents the PZT layer and another represents the interface layer. The decrease of the dielectric constant and remanent polarization with the decrease of film thickness is due to the low dielectric constant and nonferroelectric characteristic of the interface layer. Using this approach, there should be a linear relationship between  $1/\epsilon_r$  and  $1/t$ , where  $t$  is the film thickness. However, the plot of  $1/\epsilon_r$  vs  $1/t$  for these antiferroelectric thin films indicates an obvious deviation from linearity, as shown in Fig. 9. This means that, except for the electrode/film interface layer, other factors such as stresses and grain size variations may also strongly affect the thickness dependence of dielectric constant and maximum polarization in the antiferroelectric thin films, while to distinguish the effect of each factor is beyond the scope of this article.



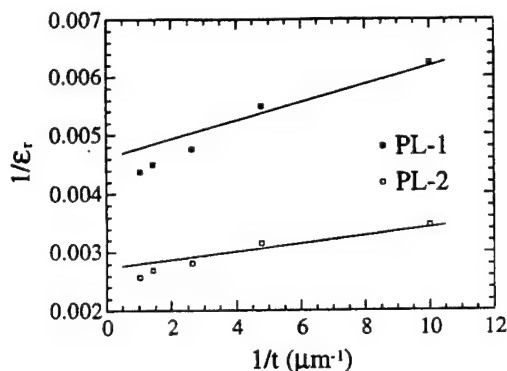


FIG. 9. Relationship between  $1/\epsilon_r$  and  $1/t$  for the PL-1 and PL-2 films.

As previously mentioned, the emphasis investigated in this work is the thickness dependence of field-induced phase switching. We have noticed that the reduction in film thickness leads to the appearance of remanent polarization in the hysteresis loops and the smearing of field-induced phase switching. In addition, the phase switching fields also decrease with the decrease of film thickness, which gives the opposite tendency compared to the coercive field change in ferroelectric thin films. This proved that the thickness-dependent phase switching is not dominated by the interface layer: If it is interface layer dominated, the phase switching fields should increase with the decrease of film thickness because more applied voltage will drop on the nonferroelectric interface layer when the films become thinner.

We propose that, for these antiferroelectric thin films, the residual tensile stress due to the thermal mismatch between the film and substrate is the most important factor in affecting the variation of field-induced phase switching with film thickness. Although we do not know the thermal expansion coefficient of these antiferroelectric thin films exactly, Berlincourt reported the thermal expansion behavior of a kind of bulk-type antiferroelectric material with the composition close to PL-1, as shown in Fig. 10.<sup>26</sup> The thermal expansion coefficients calculated from Fig. 10 are almost the same for the paraelectric cubic phase  $P_C$ , antiferroelectric tetragonal phase  $A_T$ , and antiferroelectric orthorhombic phase  $A_O$ , with the value of about  $8 \times 10^{-6}/^\circ\text{C}$ . In addition,

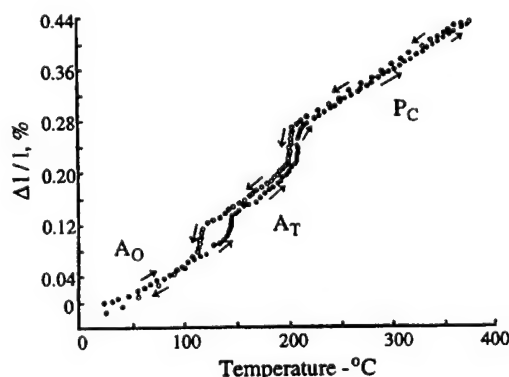


FIG. 10. Thermal expansion behavior of  $\text{Pb}_{0.97}\text{La}_{0.02}(\text{Zr}_{0.935}\text{Ti}_{0.04}\text{Sn}_{0.025})\text{O}_3$  antiferroelectric material (after Berlincourt, Ref. 26).

there are sharp contractions of about 0.055% and 0.04% when the material transfers from  $P_C$  to  $A_T$  and from  $A_T$  to  $A_O$ , respectively. This sharp contraction at the phase transition temperature is common for all the antiferroelectric materials in PZST system because the unit cell always decreases from  $P_C$  to  $A_T$  and to  $A_O$ .<sup>26</sup> Sawaguchi *et al.* also reported that the linear thermal coefficients of  $\text{PbZrO}_3$  are  $8.4 \times 10^{-6}/^\circ\text{C}$  in both phases above and below the Curie point, and there is a sharp volume contraction of about 0.27% when the material transfers from paraelectric cubic phase to antiferroelectric orthorhombic phase.<sup>27</sup> Considering the high Zr contents in the PL-1 and PL-2 compositions and that both of them are located in the antiferroelectric orthorhombic region, their thermal expansion coefficients should be close to these reported data. This indicates that the thermal expansion coefficients of these antiferroelectric films are much larger than that of the Si substrate (the thermal expansion coefficient of Si is  $2.6 \times 10^{-6}/^\circ\text{C}$ ).<sup>28</sup> Due to the larger thermal expansion coefficients and the volume contraction when transferred from high temperature paraelectric phase to low temperature antiferroelectric phase, the films will be under a high tension state when cooled down from high temperature after annealing.

Because the  $\text{AF} \rightarrow F$  phase switching will cause the unit cell to expand, the tensile stress will make the films favor the ferroelectric phase with respect to the increase of volume, as indicated by Berlincourt *et al.* for the bulk-type antiferroelectric materials.<sup>29</sup> Clearly the stress will be highest in the regions of the antiferroelectric films closest to the substrate and gradually decrease further away from the substrate. Therefore, the effect of tensile stress becomes more significant with the reduction of film thickness, which means that the thinner films are more prone to the ferroelectric phase. This implies that less energy is necessary to keep the thinner films in ferroelectric phase, hence the phase switching fields should decrease with the decrease of film thickness, which is consistent with our experimental results. The effect of tensile stress in the thinner films (0.1- and 0.2- $\mu\text{m}$ -thick films) is so strong that it may retain part of the films in the ferroelectric phase after the field is removed, which causes the existence of remanent polarization in the hysteresis loops.<sup>14</sup> In addition, part of the films in the ferroelectric phase and more preference to the ferroelectric phase also cause the field-induced phase switching to be smeared in thinner films. Due to the gradually weaker tension effect with the increase of film thickness, the remanent polarization is gradually decreased with film thickness and diminished completely in the relatively thicker films (thickness  $\geq 0.4 \mu\text{m}$ ).

## V. SUMMARY

Lanthanum-doped PZST antiferroelectric thin films with compositions in the antiferroelectric orthorhombic region have been prepared on Pt-buffered silicon wafers using sol-gel method with acetic acid as a solvent. The films show dense surface microstructure and pure perovskite structure with preferred (111) orientation. The thickness dependence of electrical properties has been studied with the thickness range from 0.1 to 1.0  $\mu\text{m}$ . Similar to the variations of dielec-

tric constant and remanent polarization in ferroelectric thin films, the dielectric constant and maximum polarization in antiferroelectric thin films decrease with the reduction of film thickness. However, the reduction of film thickness also leads to the decrease of phase switching fields, the retention of ferroelectric phase, or the appearance of remanent polarization in the hysteresis loops, and the smearing of field-induced phase switching. These phenomena related to the thickness dependence of field-induced phase switching are explained in view of the high tensile stress on the films due to the thermal mismatch between films and Si substrates, which causes the films to prefer the ferroelectric state.

## ACKNOWLEDGMENT

This work was supported by the Office of Naval Research.

- <sup>1</sup>J. F. Scott, *Ferroelectrics Rev.* **1**, 1 (1998).
- <sup>2</sup>L. E. Cross and S. Trolier-McKinstry, *Ency. Appl. Phys.* **21**, 429 (1997).
- <sup>3</sup>K. R. Udayakumar, P. J. Schuele, J. Chen, S. B. Krupanidhi, and L. E. Cross, *J. Appl. Phys.* **77**, 3981 (1995).
- <sup>4</sup>R. E. Newnham, K. R. Udayakumar, and S. Trolier-McKinstry, in *Chemical Processing of Advanced Materials*, edited by L. L. Hench and J. K. West (Wiley, New York, 1982), pp. 379–393.
- <sup>5</sup>Y. Sakashita and H. Segawa, *J. Appl. Phys.* **73**, 7857 (1993).
- <sup>6</sup>P. K. Larsen, G. J. M. Dormans, D. J. Taylor, and P. J. van Veldhoven, *J. Appl. Phys.* **76**, 2405 (1994).
- <sup>7</sup>G. H. Haertling, *Integr. Ferroelectr.* **14**, 219 (1997).
- <sup>8</sup>S. Trolier-McKinstry, C. A. Randall, J. P. Maria, C. Theis, D. G. Schlom, J. Shepard, Jr., and K. Yamakawa, *Mater. Res. Soc. Symp. Proc.* **433**, 363 (1996).
- <sup>9</sup>S. B. Ren, C. J. Lu, J. S. Liu, H. M. Shen, and Y. N. Wang, *Phys. Rev. B* **55**, 3485 (1997).
- <sup>10</sup>S. Trolier-McKinstry, P. Aungkavattana, F. Chu, J. Lacey, J.-P. Maria, J. F. Shepard, Jr., T. Su, and F. Xu, *Mater. Res. Soc. Symp. Proc.* **493**, 59 (1998).
- <sup>11</sup>W. Y. Pan, Q. M. Zhang, A. S. Bhalla, and L. E. Cross, *J. Am. Ceram. Soc.* **72**, 571 (1989).
- <sup>12</sup>K. Markowski, S.-E. Park, S. Yoshikawa, and L. E. Cross, *J. Am. Ceram. Soc.* **79**, 3297 (1996).
- <sup>13</sup>K. G. Brooks, J. Chen, K. R. Udayakumar, and L. E. Cross, *J. Appl. Phys.* **75**, 1699 (1994).
- <sup>14</sup>S. S. Sengupta, D. Roberts, J.-F. Li, M. C. Kim, and D. A. Payne, *J. Appl. Phys.* **78**, 1171 (1995).
- <sup>15</sup>C. J. Gaskey, K. R. Udayakumar, H. D. Chen, and L. E. Cross, *J. Mater. Res.* **10**, 2764 (1995).
- <sup>16</sup>B. Xu, N. G. Pai, and L. E. Cross, *Mater. Lett.* **34**, 157 (1998).
- <sup>17</sup>B. Xu, N. G. Pai, Q.-M. Wang, and L. E. Cross, *Integr. Ferroelectr.* **22**, 545 (1998).
- <sup>18</sup>B. Xu, P. Moses, N. G. Pai, and L. E. Cross, *Appl. Phys. Lett.* **72**, 593 (1998).
- <sup>19</sup>I. Kanno, S. Hayashi, M. Kitagawa, R. Takayama, and T. Hirao, *Appl. Phys. Lett.* **66**, 145 (1995).
- <sup>20</sup>S. Chattopadhyay, *Nanostruct. Mater.* **9**, 551 (1997).
- <sup>21</sup>P. Ayyub, S. Chattopadhyay, R. Pinto, and M. S. Multani, *Phys. Rev. B* **57**, R5559 (1998).
- <sup>22</sup>B. Xu, L. E. Cross, and D. Ravichandran, *J. Am. Ceram. Soc.* (in press).
- <sup>23</sup>T. Tani, Z. Xu, and D. A. Payne, *Mater. Res. Soc. Symp. Proc.* **310**, 269 (1993).
- <sup>24</sup>H. D. Chen, K. K. Li, C. J. Gaskey, and L. E. Cross, *Mater. Res. Soc. Symp. Proc.* **433**, 325 (1996).
- <sup>25</sup>J. Zhu, X. Zhang, Y. Zhu, and S. B. Desu, *J. Appl. Phys.* **83**, 1610 (1998).
- <sup>26</sup>D. Berlincourt, *IEEE Trans. Sonics Ultrason.* **SU-13**, 116 (1966).
- <sup>27</sup>E. Sawagushi, G. Shirane, and Y. Takagi, *J. Phys. Soc. Jpn.* **6**, 333 (1951).
- <sup>28</sup>S. A. Campbell, *The Science and Engineering of Microelectronic Fabrication* (Oxford University Press, 1996), p. 516.
- <sup>29</sup>D. Berlincourt, H. H. A. Krueger, and B. Jaffe, *J. Phys. Chem. Solids Suppl.* **25**, 659 (1964).



# **MODELING and CHARACTERIZATION**

***Domain Studies***

# **APPENDIX 79**

## Effect of Electric Field on Domain Formation in Relaxor Based $\text{Pb}(\text{Zn}_{1/3}\text{Nb}_{2/3})\text{O}_3$ - $\text{PbTiO}_3$ Single Crystals

UMA BELEGUNDU, X. H. DU, AMAR BHALLA and KENJI UCHINO

*International Center for Actuators and Transducers Materials Research  
Laboratory, The Pennsylvania State University, University Park, PA 16802 U. S. A*

Communicated by Dr George W. Taylor

(Received April 15, 1999)

Domain switching has been observed in 0.9PZN – 0.1PT single crystals under the influence of electric field. The crystal being near the morphotropic phase boundary contains two phases – rhombohedral and tetragonal. The electric field was applied along two principal directions [001] and [111]. Their formation as the temperature is reduced with the electric field is discussed here. For electric field along [001], it was found that a single domain could be induced in tetragonal phase. When the electric field was applied along [111], the formation of domains as temperature is reduced are shown to be remarkably similar to those formed when the temperature is fixed and the concentration of PT varied. This type of domain hierarchy may be a contributing factor for the high  $k$  (electromechanical factor) observed in these crystals.

### INTRODUCTION

Relaxor materials such as  $\text{Pb}(\text{Zn}_{1/3}\text{Nb}_{2/3})\text{O}_3$  (PZN),  $\text{Pb}(\text{Mg}_{1/3}\text{Nb}_{2/3})\text{O}_3$  (PMN),  $\text{Pb}(\text{Sc}_{1/3}\text{Nb}_{2/3})\text{O}_3$  (PSN) and their solid solutions with  $\text{PbTiO}_3$  have come into prominence due to their very high electromechanical coupling factors  $k^{1-4}$ . Strain levels of 1.7% have been observed<sup>2, 3</sup> in such single crystals. Currently, these materials are being studied intensively for actuator / transducer applications in medical imaging. Among the materials mentioned above, the solid solution of  $\text{Pb}(\text{Zn}_{1/3}\text{Nb}_{2/3})\text{O}_3$  -  $\text{PbTiO}_3$  (PZN -PT) single crystals have the highest reported value of piezoelectric coefficient  $d_{33} \cong 2000$  pC/N and electromechanical coupling factors  $k_{33} \cong 94\%$ <sup>1,2</sup>. The phase diagram for this system is shown in figure 1. One of the end members of the

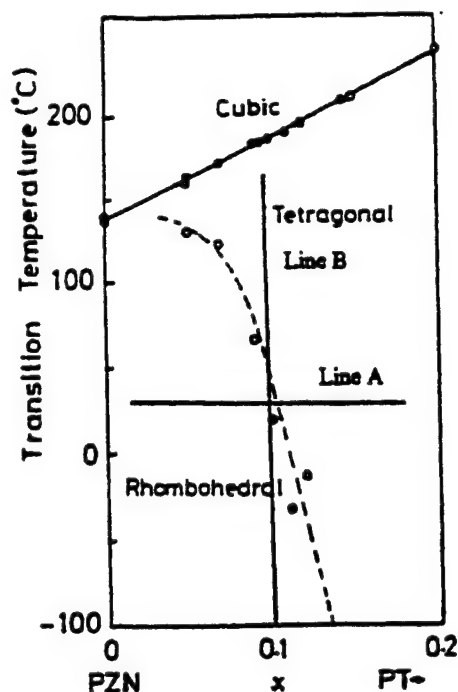


Figure 1 Phase diagram<sup>1</sup> of the (1-x) PZN - x PT system near the MPB region. The changes in the domain configuration along the lines A and B are discussed in this paper.

system-PZN, is a relaxor. The relaxor ferroelectrics are characterized by large frequency dependence of the permittivity, broad phase transition region, tapering off of the polarization charge. The other end member, lead titanate, (PT) is regular ferroelectric characterized by the sharp phase transition and frequency independent permittivity. The solid solution of this system forms a morphotropic phase boundary (MPB) near PT = 0.09 which show the high values of  $k_{33}$ ,  $d_{33}$  and elastic constants<sup>5</sup>. An issue of great importance is the direction in which the crystal must be poled to obtain highest  $k_{33}$  value. These values are obtained when the crystals of rhombohedral composition poled along [001]. The spontaneous polarization direction for the rhombohedral compositions is along [111] and for tetragonal compositions is along [001]. However, the mechanism relating this poling direction and  $k$ -value is not very clear. Two aspects for this explanation can be considered- the crystal orientation dependence of the piezoelectric properties and the domain motion in relaxor ferroelectrics and possibly their behavior under the electric field.

Systematic calculations<sup>6</sup> for the orientation dependence of piezoelectric properties have been made for PZT. The results show that the maximum  $k_{33}$  and  $d_{33}$  occur in the direction canted about 50°—60° from the spontaneous polarization direction. Domain motions in relaxor ferroelectrics contribute towards the piezoelectric properties.

The other aspect, is the domain motion in these relaxor ferroelectric systems under the influence of electric field. In the present paper, domain motion under the influence of electric field along [001] and [111] and with varying temperature is discussed for crystals of composition 0.90PZN - 0.10PT. As the composition of the crystal lies near MPB, the formation of domains when the field is applied along [001] and [111] need to be studied to have a better understanding of the switching behaviour. As mentioned before [111] is the spontaneous polarization direction for rhombohedral phase and [001] is the spontaneous polarization direction for the tetragonal phase. Static domains have been observed by etching methods<sup>7</sup> and TEM<sup>8</sup>. In the domain studies on PZN - PT crystals reported earlier, dynamic switching of domains have not been reported. Study of dynamic domain switching would give us a better understanding of the role of domains in affecting the piezoelectric properties of the material.

#### EXPERIMENTAL DETAILS

Single crystals of 0.90PZN - 0.10PT were grown by the flux method. Crystallographic direction [111] and [110] were then determined using Laue X-ray diffractometer. The crystal was then thinned down to 90  $\mu\text{m}$ . Sputtered gold was used as electrodes. The figures shown have the following crystallographic directions. The plane of the paper is perpendicular to [110] direction. The other directions such as [001] and [111] lie in the plane of the paper. The electrodes lie at the top and bottom of each picture and the direction of the field lies in the plane of the paper.

The domain observation was carried out using Nikon Transmission Microscope under crossed polarizers. A temperature controlled sample stage (Linkam) was used to vary the temperature. A deep focal lens of the objective allowed the electric field to be applied to the sample. A VCR with the monitor connected to the microscope allowed the data to be recorded continuously. A function generator was used to apply a triangular wave with a frequency of 0.05HZ.

## RESULTS

The results are discussed in three parts - domain formation with varying temperature and no electric field, domain switching with varying temperature and electric field along [001] and [111] direction.

### Domain Formation with Varying Temperature and No Electric Field

The present crystal has co-existence of two phases rhombohedral and tetragonal on a very fine scale. The rhombohedral domains have spindle like morphology and the tetragonal domains show clear stripe pattern. At room temperature co-existence of both phases were observed. As the crystal was heated or cooled down between the two transitions, rhombohedral phase at lower temperature and tetragonal phase at higher temperature were observed as is expected from the phase diagram. The domain formation with varying temperature showed the morphotropic phase boundary to be a region rather than a sharp separation.

### Domain Switching with Varying Temperature and Electric Field along [001]

The crystal was initially heated to 230°C ( above Curie temp ) and then cooled down with the electric field. Fig 2 shows the typical domain formation observed during switching with field along [001] direction and essentially follows the line B in Fig. 1. Initially, color changes associated with the birefringence are observed. As the temperature was reduced further to tetragonal phase, the whole region between the electrodes switched in a uniform

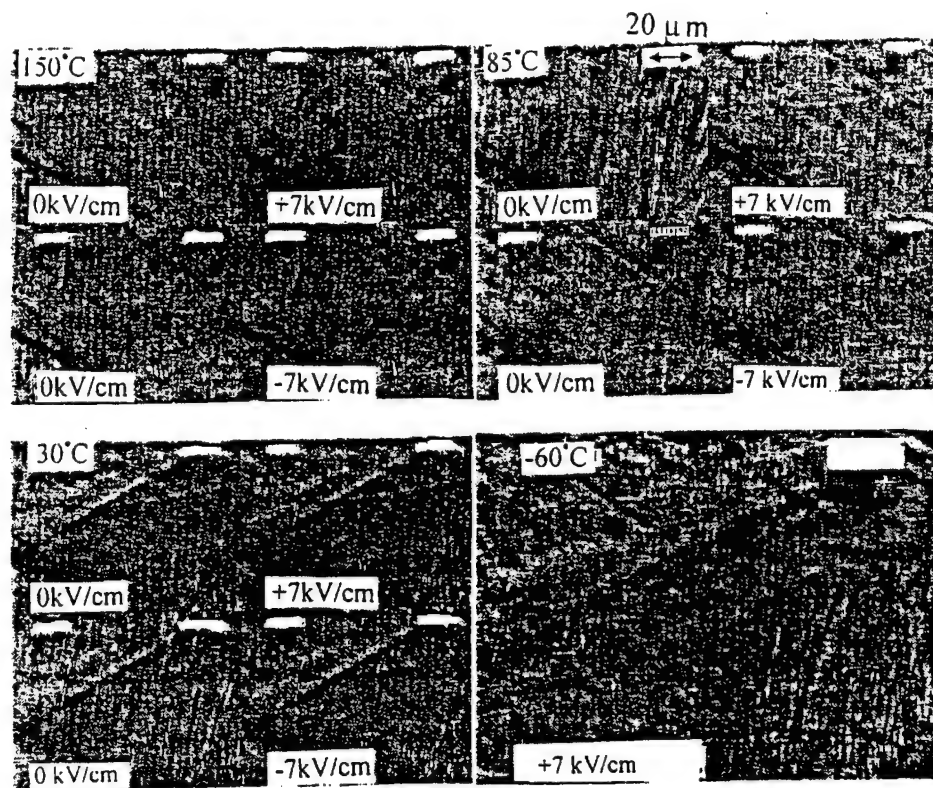


Figure 2 Domain formation in 0.9PZN - 0.1PT single crystals with field along [001] direction. The figures are shown for one cycle of electric field at different temperatures of the phase diagram.

manner. It appears that a single domain was induced with field along [001]. As the temperature is reduced to the co-existence region, the width of the domains reduced and the stripe pattern associated with the tetragonal phase could be observed. For one complete cycle of the electric field, rhombohedral phase was induced for zero field values as the temperature was lowered further. The switching of these domains continued till -25°C whereupon the freezing of domains occurred.

#### Domain Switching with Varying Temperature and Electric Field along [111]

Figures 3 show the typical domain configuration observed during switching while reducing temperature for 0.90PZN — 0.10 PT single crystals. Here again the crystal was initially heated to 230°C and cooled with the field along [111] direction essentially following the line B in Fig. 1. The field value is 3 kV/cm. At very high temperature, clear stripe pattern corresponding to tetragonal state was observed only at the zero field value of the electric field cycle as the field is applied along [111] direction. As the temperature reduced to 75°C, corresponding to co-existence region, the stripe pattern disappeared and long spindle like domains with high aspect ratio and oriented along [111] were observed. During an electric field cycle, these domains switched between the top and the bottom surface of the crystal - domains that were darker during the positive value of the field became lighter during the negative value of the field. The switching of these domains became slower as the temperature was reduced. Also, the sharpness of these domains reduces with decreasing temperature. Instead, small spindle like domains with smaller aspect ratio emerge in between and almost perpendicular the larger domains. The switching of these smaller domains occur in wave like fashion during the maximum value of the field. The switching speed reduces as the temperature is reduced the domains oriented along [111] disappear completely and are replaced by domains of smaller aspect ratio. A typical domain configuration is shown at -40°C. The domain motion freezes below -30°C.



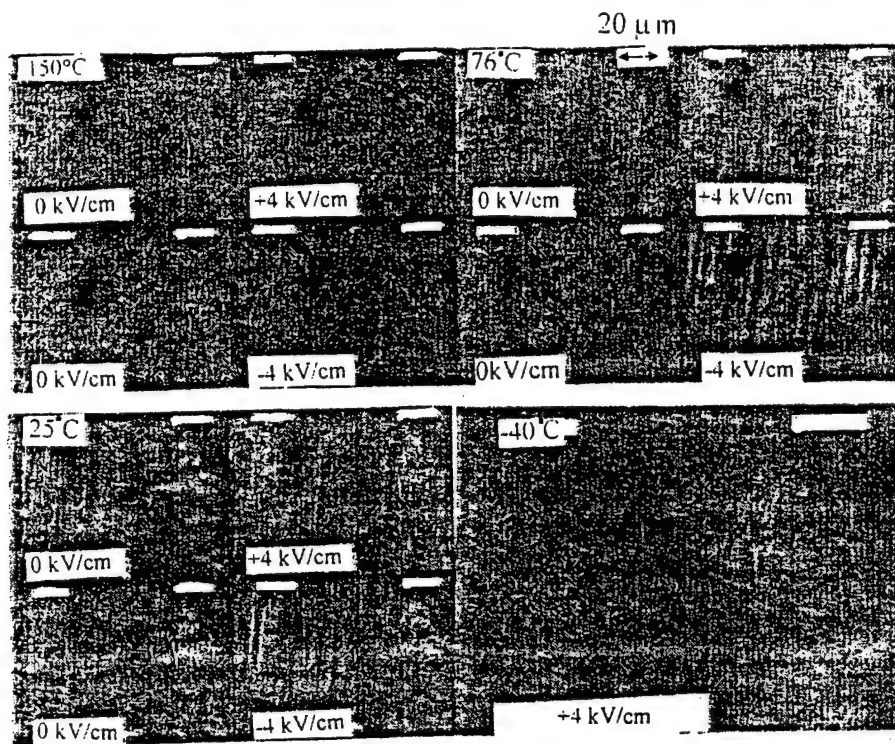


Figure 3 Domain formation in 0.9PZN - 0.1PT single crystals with field along [111] direction. The figures are shown for one cycle of electric field at different temperatures of the phase diagram.

## DISCUSSION

Some interesting results are obtained when the figures in 4a - 4d are compared to figs 4e-4h. Figures 4e-4h show the domain evolution as the concentration of PT is changed from  $x = 0.20$  to 0 in  $(1-x)\text{PZN} - x \text{PT}$  single crystals. All the figures are taken from reference 9 at room temperature with the field of 12kV/cm essentially following the line A in Fig. 1.

Fig. 2a is for  $x = 0.2$  and shows clearly the tetragonal domains formation. As the  $x$  is reduced to 0.11 (Fig. 2b) and  $x = 0.05$  (Fig 2c), the configuration becomes more complex. The domain pattern consists of stripes and the spindles showing the co-existence of both the phases.

The similarities between the two sets of the domain configuration are quite clear. Figures 4a to 4d show the domain configuration for decreasing amount of PT content from  $x = 0.20$  to  $x = 0.0$  ( PZN ); Figures 4e to 4h show the domain changes in the domain configuration while changing the temperature for one composition of  $x = 0.10$ . Clear stripe pattern corresponding to tetragonal phase are observed at room temperature for high content of PT ( $x = 0.2$ ) and at high temperature (  $223^\circ\text{C}$  ) for  $x = 0.10$  ( MPB composition). As the temperature is lowered, small spindle with smaller aspect ratio are observed in between the spindles having larger aspect ratio corresponding to the domain pattern for composition  $x = 0.05$  and finally, only the smaller domains remain at very low temperatures which corresponds to the domain pattern of pure PZN.

## SUMMARY

The 0.9PZN - 0.1PT showed the co-existence of both rhombohedral and tetragonal phase at room temperature. The MPB was found to be a region rather than a sharp line.

With the application of field along [001], single domains could be induced at higher temperature. For one complete cycle of the electric field, rhombohedral phase was induced for zero field values at lower temperatures in the co-existence region.

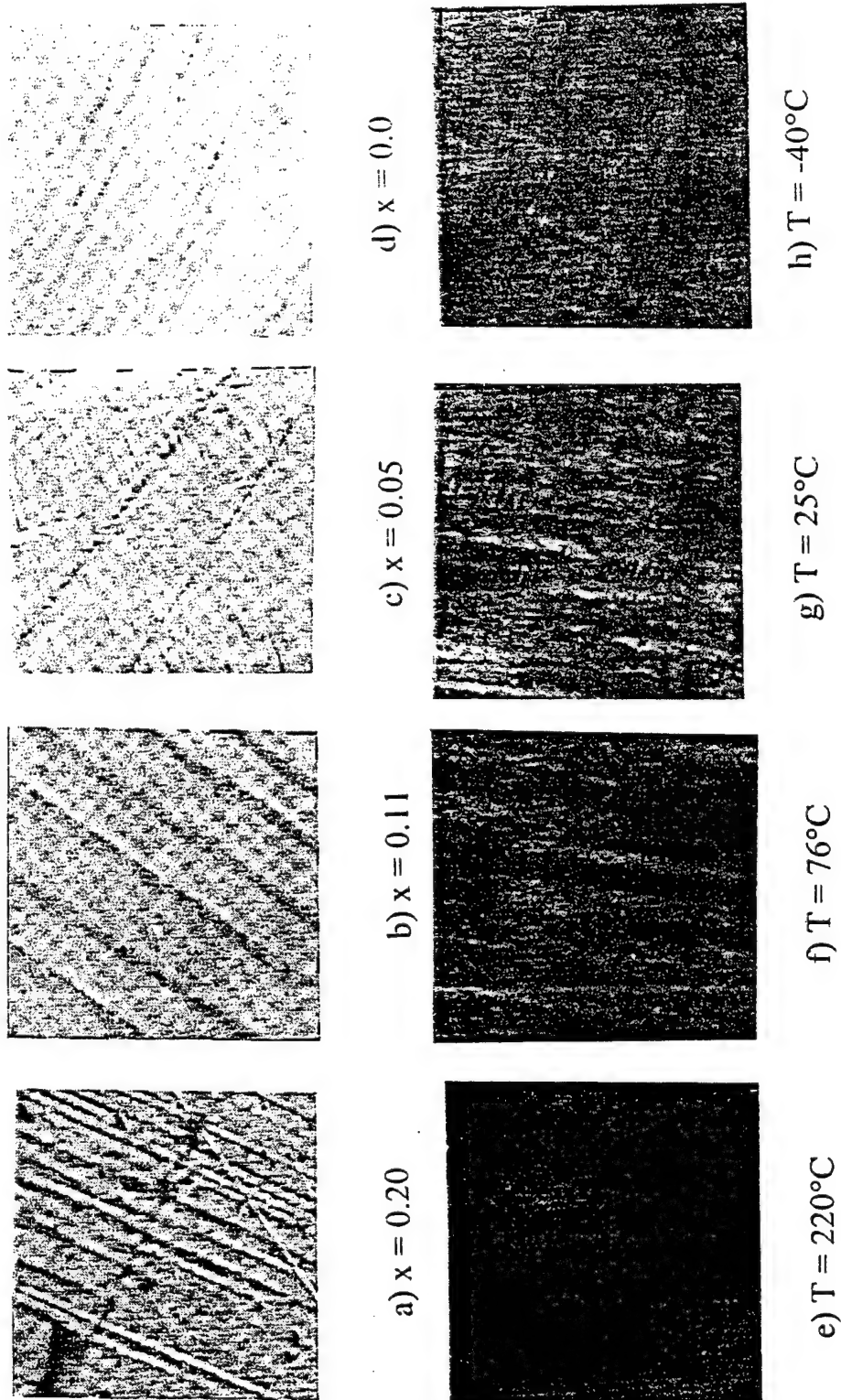


Figure 4 Changes in the domain configuration in (1-x)PZN - x PT with varying amount of x(PT) content at room temperature with field 12kv/cm along [111], data taken from ref. 9 [a) - d)]. Changes in the domain configuration in 0.90PZN - 0.10PT with decreasing temperature T and field of 3kv/cm along [111]. Present data [ e) - h)]

It can be summarized that the domain evolution with field along [111] and reducing temperature for 0.90PZN - 0.10 PT crystals are similar to that formed at constant temperature and decreasing amount of PT content in the crystals. This type of domain hierarchy in combination with orientation dependence of the piezoelectric properties may be having some contributing role for the high  $k$  observed in these materials. Further studies are required to quantify these results.

#### ACKNOWLEDGEMENTS

This work is being supported by Office of Naval Research, USA  
(fund # N00014-91-J-4145)

#### References

- [1] J. Kuwata, K. Uchino and S. Nomura, *Ferroelectrics*, **37**, 579 (1981).
- [2] S. E. Park and T. R. Shrout, J. Mateer, *Res. Innovations* **1**, 20 (1997).
- [3] T. R. Shrout, Z. P. Chang, N. Kim and S. Markgraf, *Ferroelectrics Letter Section*, **21**, 63 (1990c).
- [4] Y. Yamashita, *Jpn. J. Appl. Phys.*, **33**, 5328 (1994).
- [5] J. Kuwata, K. Uchino and S. Nomura, *Jpn. J. Appl. Phys.*, **21**, 1298 (1982).
- [6] X. H. Du, U. Belegundu and K. Uchino, *Jpn. J. Appl. Phys.*, **36**, 5580 (1997).
- [7] G. Arlt and P. Sasko, *J. Appl. Phys.*, **51**, 4956 (1980).
- [8] C. A. Randall, D. J. Barber and R. W. Whatmore, *J. Mater. Sci.*, **122**, 925 (1987).
- [9] R. Ujiie and K. Uchino, Proc. IEEE Ultrasonic Symp. '90, Hawaii, **12**, 725 (1990).

# **APPENDIX 80**

## In Situ Observation of Domains In $0.9\text{Pb}(\text{Zn}_{1/3}\text{Nb}_{2/3})\text{O}_3 - 0.1\text{PbTiO}_3$ Single Crystals

UMA BELEGUNDU, X. H. DU, L. E. CROSS and KENJI UCHINO

*International Center for Actuators and Transducers, Materials Research Laboratories, The Pennsylvania State University, University Park, PA 16802*

Domains in  $0.9\text{Pb}(\text{Zn}_{1/3}\text{Nb}_{2/3})\text{O}_3 - 0.1\text{PbTiO}_3$  or "PZN-PT" single crystals under the application of electric field were investigated with an optical microscope. The dynamic response of the domains was studied under an electric field on PZNPT crystals is reported. In this study, electric field applied along [001]. The domain formation with the changing temperature showed the successive phase transitions from cubic to tetragonal and then to rhombohedral with decreasing temperature. The room temperature configuration showed the co-existence of both rhombohedral and tetragonal domains. Under the given experimental conditions we found that a single domain state could be induced only in the tetragonal state. Even though the temperature was lowered to  $-100^\circ\text{C}$ , complete transformation to the rhombohedral state was not observed.

**Keywords:** Relaxor Ferroelectric; Domain studies; Single crystals

### INTRODUCTION

Relaxor materials such as  $\text{Pb}(\text{Zn}_{1/3}\text{Nb}_{2/3})\text{O}_3$  (PZN) and their solid solutions with  $\text{PbTiO}_3$  (PT) have come into prominence due to their very high electromechanical coupling factors  $k^{1,2}$ . In 1982, Kuwata, Uchino and Nomura discovered that poling along the [001] direction for rhombohedral crystals led to a very high value of  $k_{33}$  of 92%. Since the spontaneous polarization direction for the rhombohedral symmetry is along [111] direction, some hierarchical domain configuration is expected in the [001] poled sample. In general, the properties such as permittivity and piezoelectric properties are significantly affected by the domain motion. It is well known that the relative volume of domain orientation can be changed by the application of electric field in ferroelectrics and that these relative volumes affect the properties. In the present experiment, we have tried to understand and identify the various domains formed in the crystal under the influence of electric field.

PZN, is a relaxor ferroelectric<sup>3</sup> with a broad and frequency dependent phase transition near 140 °C and PT is a regular ferroelectric with a sharp phase transition at 490 °C. PZN has rhombohedral symmetry and PT has tetragonal symmetry. The composition chosen lies at the morphotropic phase boundary of the solid solution of these two systems.

For the present studies, single crystals 0.9PZN-0.1PT composition were grown in the laboratory. The different domains formed, their switching behaviour due to temperature variation with field applied along [001] direction, is reported herein.

#### PREPARATION OF THE SINGLE CRYSTAL SAMPLE

Single crystals of 0.9PZN- 0.1PT composition were grown by the conventional flux method. The crystallographic direction [011], [001] and [111] were determined by Laue Back Reflection method. The plate of the crystal lies in (110) plane so as to apply the field along [001] direction. The sample was then ground to a thickness of 100  $\mu\text{m}$  using SiC powder and polished to mirror finish using diamond paste. Sputtered gold electrodes were deposited and silver lead wires were connected to the sample using air dry silver paste. The surface electrode gap was 400  $\mu\text{m}$ .

The domain observation was carried out using Nikon Transmission Microscope under crossed polarizers. A temperature controlled sample stage ( Linkam ) was used to observe the domains as a function of the temperature. A VCR with the monitor connected to the microscope allowed the data to be recorded dynamically. A function generator was used to apply a triangular wave type with a frequency of 0.05 Hz ( 20 sec period ) and the maximum value of 7 kV/cm to the sample. The temperature of the crystal was changed from  $-100^{\circ}\text{C}$  to  $+250^{\circ}\text{C}$  at the rate of  $10^{\circ}\text{C/min}$ . In the figures given, the electrodes are located at top and bottom of the pictures. The plane of the picture ( plane of the crystal ) is perpendicular to [110] and [001] lies along top to bottom of the picture.

#### RESULTS

The 0.9PZN-0.1PT crystal showed the co-existence of both the rhombohedral and tetragonal domains at room temperature. "Needle shaped" domains are associated with rhombohedral symmetry and the "stripe pattern" with the tetragonal domains. As the temperature was lowered to  $-37^{\circ}\text{C}$ , the needle shaped domains associated with rhombohedral symmetry emerged more clearly. Some tetragonal distortion remained at  $-100^{\circ}\text{C}$  and complete transformation to rhombohedral state was not observed probably due to spatial

composition variation in the crystal. As the sample was heated, the transition from rhombohedral to tetragonal occurred over a wide temperature range and complete tetragonal state was observed at 90° C. With increasing temperature, these tetragonal domains increased in width to 40  $\mu\text{m}$  finally disappearing at 228°C. On cooling, these domains appeared around 225°C, finally having a mixture of both tetragonal and rhombohedral domains at room temperature. The domain patterns at different temperatures, while heating are shown in Fig. 1a, 1b, 1c.

On application of the field  $\pm 7\text{kV/cm}$ , the color changes associated with the birefringence occurred at 220°C. As the temperature was reduced, no clear stripe pattern associated with tetragonal domains was observed. Rather, the whole region between the electrodes switched in uniform manner. A small number of stripes were observed near the electrodes possibly due to electrode effect. Figure 1f shows the domain pattern at 148°C with the application of the field. Figure 1c shows the clear tetragonal pattern obtained at the same temperature without field. This temperature corresponds to stable tetragonal state with the polarization direction along [001]. Since in our experiment, the field is along [001] almost monodomain tetragonal phase was achieved, providing a few number of domain walls.

On further cooling near 135° C, some interesting results were observed. As mentioned above, complete tetragonal state was observed above 90° C without the electric field. Figure 2 shows the domain formation at zero field and maximum applied field at 125° C and 85° C. Figures a and c correspond to zero field, where a domain resembling a "needle" needle shape was induced. These disappeared for the maximum value of the field (Fig 2. b and d ). The switching of these speculated rhombohedral domains took place in wave like motion. It appears that the rhombohedral phase is being induced at this temperature. Also the reduction in tetragonal domain width and the increase in their number began at this temperature. As the temperature was reduced further, these rhombohedral domains split into smaller needle shape microdomains<sup>4</sup>. This is shown in Fig. 1d. The switching of the domains continues till -25°C and freezes thereafter. Below this temperature, the rhombohedral domains increase in number.

#### ACKNOWLEDGEMENTS:

The support provided by Office of Naval Research, fund N00014-91-J-4145 is greatly acknowledged



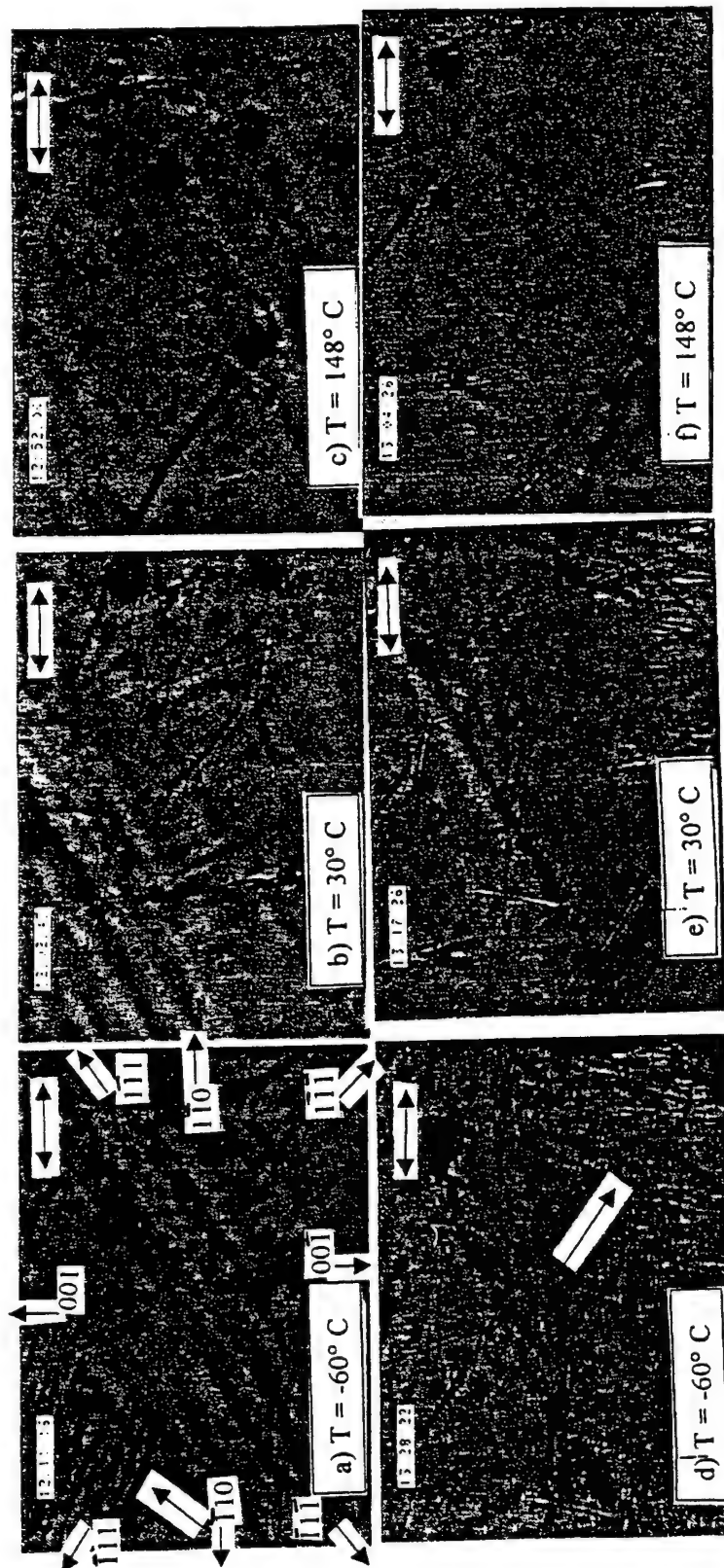


Fig. 1 Domain patterns formed with varying temperature and applied electric field. The electrodes are located at the top and bottom of the figures. The plane of the photograph is perpendicular to  $[110]$  and the relevant crystal directions are shown in the first figure. Figures a), b) and c) show the domains at different temperatures without the application of the field. The rhombohedral domains are indicated by the arrow. Figures d), e) and f) show the effect of field + 7kV/cm Monodomain state obtained by the application of field is clear in f). The bar on right top corner represents 20  $\mu\text{m}$  length ( $\longleftrightarrow$ )

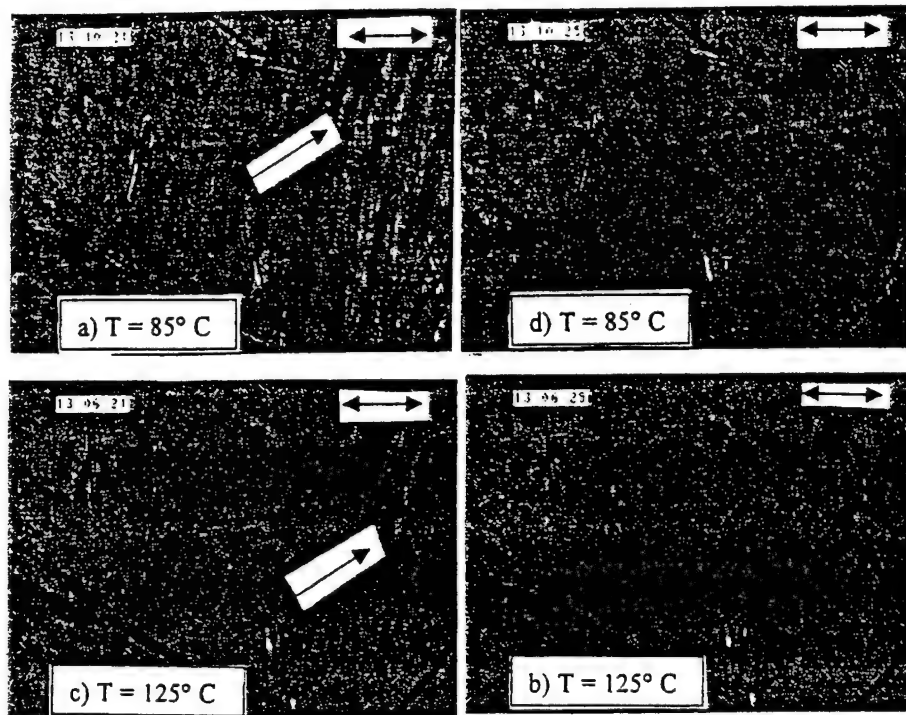


Fig. 2 Domain formation at zero field and maximum applied field of 7 kV/cm at 125° C and 85° C. Figures a) and c) correspond to zero field, where a domain resembling a "needle" (needle shape) was induced. ( indicated by the arrow). The plane of the photograph is perpendicular to [110], the relevant crystal directions are shown in the Fig. 1 a).

### References

- [1] J. Kuwata, K. Uchino and S. Nomura, *Ferroelectrics.*, **37**, 579 (1981)
- [2] S. E. Park and T. R. Shrout, *IEEE Transactions on Ultrasonics Ferroelectrics and Frequency Control*, (1997)
- [3] G. A. Smolenski and A. I. Agranovskya, *Sov. Phys. Sol.-State.*, **1**, 1429.(1959)
- [4] M. L. Mulvihill, L. E. Cross and K. Uchino, *J. Am Ceram. Soc.*, **78**, 3345, (1995)

# **APPENDIX 81**

## Determination of Domain and Domain Wall Formation at Ferroic Transitions

D. M. HATCH<sup>a</sup> and W. CAO<sup>b</sup>

<sup>a</sup>*Department of Physics and Astronomy, Brigham Young University, Provo, Utah 84602; and* <sup>b</sup>*Materials Research Laboratory, The Pennsylvania State University, University Park, Pennsylvania 16802*

Through the example of the  $Pm\bar{3}m - I4/mmm$  structural phase transition in  $\text{LaAg}_{1-x}\text{In}_x$  ( $x=0.2$ ), a general procedure is given in this paper to model and predict the domain pair and domain wall formation using a group theoretical approach and a Landau-Ginzburg type continuum theory. The heterogeneous order parameter profile can then be calculated by using an initial value scan method based on the equilibrium conditions of the order parameter and the minimization of the total elastic energy. The dependence of the domain wall profile on different expansion coefficients of the free energy is demonstrated numerically in several examples.

**Keywords:** Group theory; Domains; Domain walls; Phase transitions; Ferroelastic; Landau-Ginzburg theory

### INTRODUCTION

Group theoretical methods provide the tools to obtain a great deal of information about phase transitions and the resulting domain structures. The symmetry change at a transition allows us to obtain the following: (1) the Landau-Ginzburg free energy, including gradient and secondary order-parameter (OP) invariants, (2) the number and the physical properties of possible homogeneous domains,

- (3) the classification of equivalent domain and twin pairs and their symmetry,  
 (4) the sets of non-linear equations which define the domain wall profiles in the heterogeneous structures, (5) the criteria for stability, and (6) the merging and splitting of domain walls.

In this paper we use the improper ferroelastic phase transition in a CsCl structure to illustrate the methodology of the symmetry approach. The transition is from a  $Pm\bar{3}m$  to  $I4/mmm$  structure<sup>1</sup> and is induced by an  $M_5^-$  mode softening in the pseudo-binary rare earth alloy  $\text{LaAg}_{1-x}\text{In}_x$  ( $x=0.2$ ). Structural details of the transition in CsCl are given in Ref. 1. We use the software program *ISOTROPY*<sup>2</sup> by Stokes and Hatch to quickly obtain some of the pertinent details of the invariants and domain twins.

#### THE LANDAU-GINZBURG FREE ENERGY

The symmetry of the  $I4/mmm$  distorted phase with cell quadrupling initially gives two possible choices<sup>3</sup> for this symmetry change from  $Pm\bar{3}m$ . However, comparison with the observed displacements leads uniquely to the realization that the transition is induced by the soft mode of the  $M_5^-$  irreducible representation, corresponding to a six-component OP  $\eta = (\eta_1, \eta_2, \eta_3, \eta_4, \eta_5, \eta_6)$ , with the direction<sup>1</sup> of  $P_{10} = (a, a, 0, a, -a)$ . The Landau-Ginzburg free energy is constructed by forming polynomials which are invariant under the complete set of transformations of the higher symmetry group  $Pm\bar{3}m$ . The invariants obtained from *ISOTROPY* can be collected into two parts. The first, the Landau energy part, is composed of invariant polynomials of the primary and secondary OPs. These terms are indicated in the following manner  $F_L(\eta) = F_{\text{primary}} + F_{\text{secondary}} + F_{\text{couplets}}$  with invariants up to sixth order in the primary and fourth order in secondary OPs, and terms coupling these two sets of parameters<sup>1</sup>. As far as the space group symmetry change is concerned, the first order vs second order nature of a transition does not play a prominent role, therefore, we take the expansion

for the primary OP only up to fourth order in this paper, which allows us to obtain some simple analytic and numerical solutions. The Ginzburg portion,  $F_G$ , is an invariant combination of spatial derivatives of the primary OP. The free

$$F_G = b_1 \left( \frac{1}{6} (\eta_{1,x})^2 - \frac{1}{\sqrt{3}} (\eta_{1,x}) (\eta_{1,y}) + \frac{1}{2} (\eta_{1,y})^2 + \frac{1}{3} (\eta_{2,x})^2 + (\eta_{2,y})^2 \right. \\
+ \frac{5}{6} (\eta_{3,x})^2 + \frac{1}{\sqrt{3}} (\eta_{3,x}) (\eta_{3,y}) + \frac{1}{2} (\eta_{3,y})^2 \\
+ b_2 \left( -\frac{1}{2\sqrt{3}} (\eta_{1,x})^2 + (\eta_{1,x}) (\eta_{1,y}) + \frac{1}{2\sqrt{3}} (\eta_{1,y})^2 + \frac{1}{\sqrt{3}} (\eta_{2,x})^2 - \frac{1}{\sqrt{3}} (\eta_{2,y})^2 \right. \\
- \frac{1}{2\sqrt{3}} (\eta_{3,x})^2 - (\eta_{3,x}) (\eta_{3,y}) + \frac{1}{2\sqrt{3}} (\eta_{3,y})^2 \\
+ b_3 \left( \frac{1}{2} (\eta_{1,x}) (\eta_{1,z}) + \frac{\sqrt{3}}{2} (\eta_{1,y}) (\eta_{1,z}) - (\eta_{2,x}) (\eta_{2,z}) \right. \\
+ \frac{1}{2} (\eta_{3,x}) (\eta_{3,z}) - \frac{\sqrt{3}}{2} (\eta_{3,y}) (\eta_{3,z}) \left. \right) + b_4 ((\eta_{1,z})^2 + (\eta_{2,z})^2 + (\eta_{3,z})^2) \quad (1)$$

energy form for this portion is given in Eq. (1). Euler's equations then lead to six coupled partial differential equations in  $\eta$  and three equations in stress as shown in Eq. (2),

$$\sum_m \frac{\partial}{\partial x_i} \left[ \frac{\partial F}{\partial \eta_{i,j}} \right] - \frac{\partial F}{\partial \eta_i} = 0, \quad (j=1,2,3; i=1,\dots,6), \quad (2)$$

$$\sum_m \sigma_{nm} = 0, \quad (m,n=1,2,3).$$

#### DOMAIN TWINS

The transition from  $Pm\bar{3}m$  to  $I4/mmm$  produces twelve homogeneous single domain states, labeled  $S_1, S_2, \dots, S_{12}$ . The set of all elements of the parent group that do not change  $S_1$  comprise the isotropy group  $I4/mmm$  of the first domain. We label this group  $F_1$ , which is a subgroup with basis vectors  $(2,0,0)$ ,  $(0,2,0)$ ,  $(0,0,2)$  and origin  $(\frac{1}{2}, \frac{1}{2}, 0)$  with respect to the parent group. Those elements of the

parent group that transform  $S_1$  into the particular domain  $S_i$  will form a left coset with respect to  $F_1$  and the cosets can be used to write the parent group, denoted as  $G$ , in the form  $G = F_1 + g_{2,1}F_1 + g_{3,1} + \dots g_{12,1}F_1$ , where  $g_{i,1}$  is an element that transforms  $S_1$  to domain  $S_i$ . The isotropy group of  $S_i$  is  $g_{i,1}F_1g_{i,1}^{-1} = F_1$ .

A domain pair is of the form  $(S_i, S_j)$  and is made up of two domains which simultaneously exist in space without being combined and without interacting. Two domain pairs are said to be equivalent if there is some element  $g$  of the parent group  $G$  for which  $g(S_i, S_j) = (gS_i, gS_j) = (S_k, S_l)$ . This procedure allows all possible domain pairs for the  $\text{LaAg}_{1-x}\text{In}_x$  transition to be grouped into four classes. The identity class  $(S_1, S_1)$ , two antiphase classes exemplified by the domain pairs  $(S_1, S_{10})$  and  $(S_1, S_2)$ , and an orientation class exemplified by the pair  $(S_1, S_3)$ . Equivalent domain pairs are indicated in Table I. We will not

Table I Equivalent domain pairs.  $k, m, n$  are positive integers;  $k+3m, k+3n+1, k+3n+2$  are smaller than 12.

Domain Pair	Equivalent Pairs
(1,10)	(2,11), (3,12), (4,7), (5,8), (6,9)
(1,4)	( $k, k+3m$ ) without pairs in type (1,10)
(1,2)	( $k, k+3n+1$ ), ( $k, k+3n+2$ )

discuss here the case of the identity class. The study of domain walls will then be reduced to studying one representative from each of three classes.

A domain twin is defined as two semi-infinite single domain regions separated by a thin planar wall, with normal  $\mathbf{n}$ , and containing the point  $\mathbf{p}$ . Following Janovec's notation<sup>3</sup>, this twin will be labeled  $(S/n, \mathbf{p}/S_j)$ . Its symmetry group (hereafter called its twin group) consists of four parts:

$$J_{ij} = \hat{F}_{ij} + \hat{L}'_{ij} \hat{F}_{ij} + \hat{r}_{ij} \hat{F}_{ij} + \hat{s}'_{ij} \hat{F}_{ij} \quad (3)$$

Here,  $\hat{F}_{ij}$  contains those elements that leave  $S_i, S_j$ , and  $\mathbf{n}$  invariant;  $\hat{L}'_{ij} \hat{F}_{ij}$  contains those elements that interchange  $S_i$  and  $S_j$ , and reverse  $\mathbf{n}$ ;  $\hat{r}_{ij} \hat{F}_{ij}$  contains those elements that leave  $S_i$  and  $S_j$  invariant and reverse  $\mathbf{n}$ ; and  $\hat{s}'_{ij} \hat{F}_{ij}$  contains those elements that interchange  $S_i$  and  $S_j$ , and leave  $\mathbf{n}$  invariant; while all of the above leave  $\mathbf{p}$  invariant. Representative twin groups are indicated in Table II.

Table II Representative Twin Groups in  $\text{LaAgIn}$   
(in terms of the parent cubic setting)

Twin, Group, Basis, Origin	$\hat{F}_{ij}$	$\hat{L}'_{ij} \hat{F}_{ij}$	$\hat{s}'_{ij} \hat{F}_{ij}$	$\hat{r}_{ij} \hat{F}_{ij}$
(1/(0,0,1),(0,0,0)/10) P4/m2/m2/m (1,-1,0),(-1,-1,0) (1/2,1/2,0)	P4mm	(C2b 0,0,0)	(E -1,1,0)	(C2b -1,1,0)
(1/(0,0,1),(0,0,0)/4) P2/m2/m2/m (0,2,0),(-1,0,0) (0,1/2,0)	P2mm	(C2y 0,0,0)	(E -1,0,0)	(C2y -1,0,0)
(2/(1,1,0),(0,0,0)/3) C2mm (0,0,2),(2,-2,0) (0,0,-1/2)	C11m	none	(C2a 0,0,1)	none
(2/(-1,1,0),(0,0,0)/3) Cmm2 (-2,2,0),(2,2,0) (0,-1,0)	C11m	none	none	(C2a 0,0,1)

## DOMAIN WALL SOLUTIONS

(1) The (1,10) antiphase boundary (APB) is formed between  $P_1(\eta') = (-\sqrt{2} a, 0, 0, \sqrt{2} a)$  and  $P_{10}(\eta') = (-\sqrt{2} a, 0, 0, 0, -\sqrt{2} a)$ . For convenience new OP components have been defined where  $\eta'_i = \sqrt{2}(\eta_i + \eta_{i-1})$  or  $\eta'_i = \sqrt{2}(\eta_i - \eta_{i-1})$  for  $i$  even or odd, respectively. The APB is formed by half a lattice constant

translation of the lower symmetry phase along the  $z$  direction. The single domain states serve as boundary conditions for heterogeneous solutions, and we consider the *inverse* boundary value problem based on the assumption that both the primary and the secondary OP depend only on the position coordinate  $z$  perpendicular to the domain wall, thus  $\eta' = \eta'(z)$ . The strains are subjected to

$$-(2D_4 - D_1) \frac{d^2 \eta'}{dz^2} + k^* \eta' + (A_6^* + A_6') \eta'^2 = 0. \quad (4)$$

compatibility relations<sup>4</sup>. Assuming  $\eta'_2 = \eta'_3 = \eta'_4 = \eta'_5 = 0$ , the Euler equations reduce to two non-linear coupled second-order ordinary differential equations for  $\eta'_1(z)$  and  $\eta'_6(z)$ . Both order parameter components satisfy the same equation. The solutions are  $\eta'_1 = \eta'_6 = a \tanh(z/\xi_{APB})$ , where  $\xi_{APB} = [-2(2D_4 - D_1)/k^*]^{1/2}$  is the half width of the APB and  $k^*$  is a renormalized second-order coefficient.

(II) The (1,4) antiphase boundary is formed between  $P_1(\eta') = (\sqrt{2} a, 0, 0, 0, 0, 0,$

$$\begin{aligned} -(2D_4 + D_1) \frac{d^2 \eta'_1}{dz^2} + k_1^* \eta'_1 + A_1^* \eta'^2 + A_{1,2}^* \eta'_1 \eta'^2 &= 0, \\ -2D_3 \frac{d^2 \eta'_6}{dz^2} + k_6^* \eta'_6 + A_6^* \eta'^2 + A_{6,2}^* \eta'_6 \eta'^2 &= 0. \end{aligned} \quad (5)$$

$\sqrt{2} a$ ) and  $P_4(\eta') = (-\sqrt{2} a, 0, 0, 0, 0, \sqrt{2} a)$ . This APB is formed by half a lattice constant translation of the lower symmetry phase along the  $x$  direction. We assume  $\eta'_2 = \eta'_3 = \eta'_4 = \eta'_5 = 0$  and a domain wall perpendicular to  $x$ . The set of coupled nonlinear equations are given in Eq. (5). If we take no coupling, i.e.,  $A_{1,6}^* = 4A_1^* + 2A_3^* = 0$ , we can find the following solution:  $\eta'_1 = \sqrt{2} a \tanh(x/\xi_{APB})$ ,  $\eta'_6 = \sqrt{2} a$ , and  $\xi_{APB} = [-2(2D_4 + D_1)/k_1^*]^{1/2}$ . In addition, the strain components  $e_1, e_3$  are constant and  $\sigma_{12} = \sigma_{23} = \sigma_{13} = \sigma_{11} = 0$ .

(III) The (2,3) orientation twin boundary (OTB) is formed between  $P_2(\eta') = (0, 0, 0, \sqrt{2} a, 0)$  and  $P_3(\eta') = (0, \sqrt{2} a, 0, 0, 0)$ . The domains 2 and 3 are related by a three-fold rotation along the  $[111]$  direction of the  $Pm\bar{3}m$  structure. Note that the (2,3) OTB is equivalent to the (1,2) OTB. In contrast to

the antiphase domains, orientation twin domains are distinguished by their ferroic properties, i.e., the two twin domains have *different* strains which can be detected optically or with x rays. The order-parameter profile representing the twin boundary has the following form:  $\eta' = (0, \eta'_2, \eta'_3, \eta'_4, \eta'_5, 0)$  and contains the  $x = y$  plane. For the special case  $Q_1 = \eta_2^2 = \eta_3^2$ ,  $\eta_4^2 = \eta_5^2 = Q_2$  we get the two coupled differential equations:

$$\begin{aligned} D^* \frac{d^2 Q_1}{ds^2} + 2k_1^* Q_1 + 4A_1^* Q_1^2 + 2A_{1,2}^* Q_1 Q_2 &= 0, \\ D^* \frac{d^2 Q_2}{ds^2} + 2k_2^* Q_2 + 4A_2^* Q_2^2 + 2A_{1,2}^* Q_1 Q_2 &= 0. \end{aligned} \quad (6)$$

Assuming  $A_{1,2}^* = 0$  and by defining  $\xi_{TB} = \sqrt{D^*/k_2^*}$ , we get  $Q_1 = 1/\sqrt{2}a[1 + \tanh(s/\xi_{TB})]$ , and  $Q_2 = 1/\sqrt{2}a[1 - \tanh(s/\xi_{TB})]$ . The domain wall energy is  $E = -\xi_{TB}(\frac{10}{3}k_2^*a^2 + \frac{8}{3}A_1^*a^4 + 2A_{1,2}^*a^4)$ . The strains  $e'_1, e'_3$  are constant and  $\sigma_{11} = 0$ , where  $r$  and  $s$  denote the  $[110]$  and  $[1\bar{1}0]$  directions, respectively.

(IV) *Numerical Solutions:* General solutions for both the antiphase and twin boundaries can be obtained by numerically solving the nonlinear coupled differential Eqs. (4), (5), and (6). From the mathematical formulations, the differential equations for the OTB (2,3) is the same as that for the AP twin boundary (1,4); therefore, we will analyze the equations for (1,4) using normalized variables and the normalized equations can also apply to the OTB case. The differential equations for a (1,4) AP boundary were given in Eq. (5). This set of coupled nonlinear differential equations can be solved by using the initial value scan method<sup>5</sup>, and the solutions are expected to be similar to the solutions of Cao and Barsch<sup>6</sup>.

The solutions for  $A_{1,6}^* = 0$  were given in our discussion after Eq. (5). For the more general case,  $A_{1,6}^* \neq 0$ , we must solve Eq. (5) numerically. To simplify the mathematical problem, the following substitutions are introduced:

$$q_1 = \frac{\eta_1}{\sqrt{2}\alpha}, \quad q_2 = \frac{\eta_2}{\sqrt{2}\alpha}, \quad (7a,b)$$

$$\alpha = \sqrt{\frac{2D_1 k_1}{k_2(2D_1 + D_2)}}, \quad \beta_1 = \frac{A_{10}}{A_1 + A_{10}}, \quad \beta_2 = \frac{A_{20}}{A_2 + A_{20}}, \quad (7c,d,e)$$

$$x = \gamma\xi, \quad \gamma = \sqrt{\frac{(2D_1 + D_2)D_1}{k_1 k_2}}, \quad (7f,g)$$

With these substitutions, Eqs. (6a,b) becomes dimension-less, i.e.,

$$\frac{1}{\alpha} \frac{d^2 q_1}{d\xi^2} = q_1 + (1 - \beta_1)q_1^3 + \beta_1 q_1 q_2^2, \quad (8a,b)$$

$$\alpha \frac{d^2 q_2}{d\xi^2} = q_2 + (1 - \beta_2)q_2^3 + \beta_2 q_2 q_1^2,$$

and the boundary conditions become

$$\lim_{\xi \rightarrow \pm\infty} q_1 = \pm 1, \quad \lim_{\xi \rightarrow \pm\infty} q_2 = 1. \quad (9a,b)$$

From Eqs. (8) and (9), the function  $q_1(\xi)$  should be an odd function,  $q_2(\xi)$  should be an even function, and the following conditions hold:

$$q_1(0) = 0, \quad \frac{dq_2(0)}{d\xi}. \quad (10a,b)$$

One integral exists for Eqs. (8a,b), and is shown in Eq. (11),

$$\beta_2^2 \left( \frac{dq_1}{d\xi} \right)^2 + \alpha^2 \beta_1 \left( \frac{dq_2}{d\xi} \right)^2 + \alpha \beta_1 (q_1^2 - 1) - \frac{\alpha}{2} \beta_2 (1 - \beta_1)(q_1^4 - 1) + \alpha \beta_1 (q_2^2 - 1) - \frac{\alpha}{2} \beta_1 (1 - \beta_2)(q_2^4 - 1) - \alpha \beta_1 \beta_2 (q_1^2 q_2^2 - 1) = 0. \quad (11)$$

Analyzing Eqs. (8a,b), one finds that stability requires  $\beta_2 < 1$ , which means that the coefficients  $A_{10}$  and  $A_{20}$  must have the same sign. The coefficient  $\alpha$  should be on the order of one and positive. There are three independent parameters in Eqs. (8a,b),  $\beta_1$ ,  $\beta_2$  and  $\alpha$ , which control the variation of the

order parameter across a domain wall or an AP boundary. Fig. 1 shows the influence of  $\beta_1$  while the parameters  $\alpha$  and  $\beta_2$  are fixed. One can see that the anti-symmetric component  $q_1$  of the order parameter changes the most while  $q_2$ , the symmetric component, shows little change. In

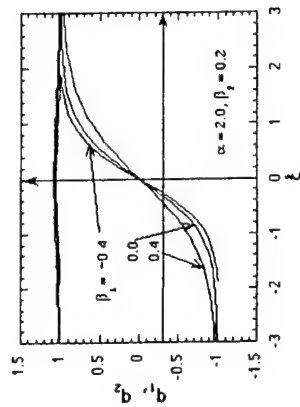


Figure 1 Numerical solutions for Eq. (8a,b) with the coefficients  $\alpha = 2.0$ ,  $\beta_2 = 0.2$  and  $\beta_1 = -0.4$ , 0.0 and 0.4, respectively.

Fig. 2,  $\alpha$  and  $\beta_1$  are fixed and  $\beta_2$  changes from -0.4 to 0.2. For this case, only the symmetric component of the OP  $q_2$  changes its amplitude while  $q_1$  is practically unchanged. For both cases, only the amplitude of the OP varies but the thickness of the transition region is almost unchanged by the variation of  $\beta_1$  and  $\beta_2$ . In Fig. 3, both  $\beta_1$  and  $\beta_2$  are fixed but changes in  $\alpha$  go from -0.4

to 0.4. As we can see the wall thickness increases with  $\alpha$ . The OP amplitude variation across a domain wall is determined by the nonlinear coefficients in the free energy expansion while the domain wall thickness is mainly controlled by the gradient coefficients.

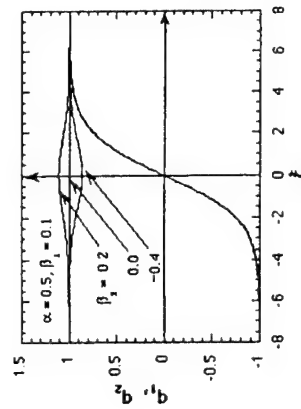


Figure 2 Numerical solutions for Eq. (8a,b) with the coefficients  $\alpha = 0.5$ ,  $\beta_1 = 0.1$  and  $\beta_2 = -0.4$ , 0.0 and 0.2, respectively.



Stronger non-local coupling (large gradient coefficients) results in broader domain walls.

## CONCLUSION

We have described a systematic method for studying the domains and also domain walls that occur in ferroic

phase transitions. Use of the continually expanding ISOTROPY program gives information about primary and secondary order parameters and their invariants, gradient invariants, domain pairs and domain twins, as well as symmetry determined physical properties. Numerical solutions for the domain walls provided additional insight into the detailed OP variation in the spatial transition region and the influence of different physical parameters in the free energy.

## References

- [1] A. Saxena, G. R. Barsch, and D. M. Hatch, *Phase Trans.* **46**, 89 (1994); see the figures and references, therein.
- [2] H. T. Stokes and D. M. Hatch, *Isotropy Subgroups of the 230 Crystallographic Space Groups*, (World Scientific, Singapore, 1988).
- [3] V. Janovec, W. Schranz, H. Warhanek, and Z. Zikmund, *Ferroelectrics* **98**, 171 (1989).
- [4] E. A. H. Love, *A Treatise on the Mathematical Theory of Elasticity* (Dover, New York, 1944), pp.49, 131.
- [5] W. Cao, Ph.D. thesis, The Pennsylvania State University, (1987).
- [6] W. Cao and G. R. Barsch, *Phys. Rev. B* **41**, 4334 (1990).

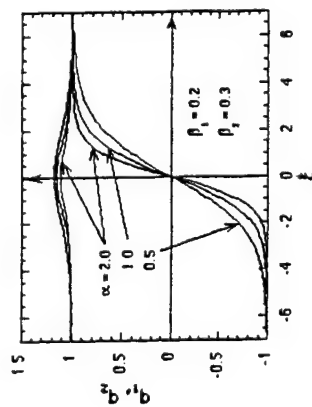


Figure 3: Numerical solutions for Eq. (8 a,b) with the coefficients  $\alpha = 2.0$ ,  $\beta_2 = 0.2$  and  $\beta_1 = -0.4$ ,  $0.0$  and  $0.4$ , respectively.

# **APPENDIX 82**

## OBSERVATION OF FERROELECTRIC DOMAINS IN $\text{LiTaO}_3$

WENWU CAO\* and SHINING ZHU

*Materials Research Laboratory, The Pennsylvania State University,  
University Park, Pennsylvania 16802, USA*

*(Received in final form 17 July 1998)*

Periodic and partially reversed  $180^\circ$  domain patterns in  $\text{LiTaO}_3$  single crystals, engineered through pulse poling, can be directly observed by using environmental scanning electron microscopy (ESEM) in secondary electron emission mode. The ESEM technique does not require surface treatment and can be used to observe ferroelectric domains on a natural cracked surface in a bulk material. This is very important since the domain patterns obtained by this technique can truly represent the domain configurations in a bulk. The domain structures are confirmed by chemical etching and scanning electron microscopy. The ESEM gives stable and high resolution images.

**Keywords:** ESEM; Ferroelectric domains; SEM; TEM; domain switching;  $\text{LiTaO}_3$

**PACS Numbers:** 61.16Bg; 77.80Dj; 61.72Mm; 77.22Ej

### INTRODUCTION

There has been a long debate regarding if the domain microstructures observed by using transmission electron microscopy (TEM) really reflect the true domain configurations in bulk materials. The reason is that the TEM samples must be thinned to a foil to allow the penetration of electron beam. Practically speaking, the samples become 2-dimensional and the boundary conditions are totally changed from that of the original 3-D bulk. If we assume that the system being observed is in thermodynamic equilibrium, then the domain patterns will change as the sample is being thinned down due to the release of constraints from one of the dimensions. In other words,

---

\*Corresponding author.

the only way to preserve the bulk domain structure in the thin foil is to lock the system in a metastable state. This may be achieved for systems with a paraelectric-ferroelectric phase transition temperature much higher than the processing and observation temperatures, for example, the lead zirconate titanate which has the transition temperature of 375°C.<sup>[1]</sup> However, in general, it becomes questionable if the domain structures observed by TEM really reflect the pattern in a 3-D structure, particularly when the transition temperature is relatively close to the observation temperature. In many cases, the change of domain microstructures due to local electron beam heating is clearly visible under the microscope. As a result, the TEM observations can not convincingly prove or disapprove the theoretical prediction of the relationship,  $D \propto \sqrt{l}$ , between the domain size  $D$  and grain size  $l$ .

With the development of fine structure materials, the study of domain microstructures become increasingly important for materials engineering to produce materials of improved properties, such as high dielectric, piezoelectric and elastic properties. With the problem of low resolution of optical microscopy and the geometrical limitation of the TEM, there is an urgent need to develop better means for the observation of domain microstructures in a 3-D structure.

The traditional techniques used in domain pattern observation include optical microscopy, scanning electron microscopy and transmission electron microscopy. The first two techniques require the sample surface being etched so that a topographic pattern appear due to different etching rates in domains of different polarity or at the domain boundaries where are high stress concentrations. The acid etching not only leads to damaged surfaces but also could not distinguish the topographic pattern of defects, stress concentrations and polarization effects. The resolution of the etching technique is also too low to give subtle details of submicron domains and domain walls. While the TEM technique does not need surface etching and has high resolution, the samples need to be thinned down to a very thin foil of less than 1000 Å in order to allow the electron beam to penetrate through and to avoid the overlapping of layered domain images. Therefore, the domain structures obtained by TEM may not account for the domain patterns in a 3-D structure. The scanning force microscopy has opened up a new method to study the domain structures in ferroelectrics,<sup>[2]</sup> it has shown a great success for TGS which has atomically flat cleavage planes,<sup>[3]</sup> however, the interpretation of the images for a general ferroelectric system is still not satisfactory. The demand on the sample surface makes it difficult to be used for a general ferroelectric system.

In recent years, a new method began to evolve using low current scanning electron microscopy (SEM) to observe unetched ferroelectric materials.<sup>[4-10]</sup> The basic idea is to use low accelerating voltage and low current to reveal adjacent domains of opposite polarity in secondary electron emission mode. The technique does not require etching but the images only appear for certain length of time. The key to obtain the polarization domain images using the low field secondary electron SEM method is to avoid surface charge accumulation onto an insulating crystal from electron beam deposition. The choice of probe current and accelerating voltage are very critical, no contrast can be found if the parameters are not properly chosen. In addition, the contrast image is short-lived, it disappears under the illumination of electron beam after a few seconds to, at most, a few minutes. The observable time for the contrast image shortens with the increase of accelerating voltage. Consequently, it is not possible to obtain a contrast image with high resolution<sup>[4,5]</sup> due to the insufficient number of electrons to brighten the contrast image.

Recently, we have tried to use the environmental scanning electron microscopy (ESEM) for the observation of ferroelectric domains in  $\text{LiTaO}_3$  and achieved an amazing success.<sup>[11]</sup> Because the ESEM<sup>[12,13]</sup> can operate at pressures ten thousand times higher than that of standard SEM, the free ions created by collisions between moving electrons and neutral gas molecules can provide a conductive path for beam-deposited surface charges. This allows us to observe unprepared, uncoated insulating samples with high resolution. More importantly, the domain contrast obtained from ESEM is very stable, the images are unchanged for several hours in the case of  $\text{LiTaO}_3$  crystals.

## SAMPLE PREPARATION

The samples used in our experiments are  $\text{LiTaO}_3$  with engineered periodic and triangular domain structures. Starting with a monodomain c-cut single crystal of 3m symmetry, the spontaneous polarization  $P_s$  is reversed in selected regions using a pulse electric field at room temperature.<sup>[14]</sup> Preliminary examination of the domain structures in a poled  $\text{LiTaO}_3$  sample can be made by optical microscopy on an etched surface. The procedure described in Ref. [14] consists of making two kinds of aluminum electrodes: one is periodic, and the other is uniform plane. Through pulse poling, stripe and triangular shaped domains were produced by using these two kinds of electrodes mentioned above. Both the level of poling field and the duration

of the pulse can influence the final domain pattern in the system. More details of the fabrication technique has been discussed elsewhere in Refs. [14–15].

### DOMAIN OBSERVATION

The domain observations were performed using an ESEM (ElectroScan Model E-3, Wilmination, MA) in secondary electron emission mode. For comparison, we have performed the experiments in two stages:

First, a periodically poled sample was etched in a solution containing 2 parts  $\text{HNO}_3$  and 1 part HF for 15 hours at room temperature. The etched sample was attached to an aluminum sample mount using a double faced tape for observation. The aluminum sample mount was grounded. Figure 1 is a schematic diagram of the experimental arrangement and the crystal orientation of the sample.

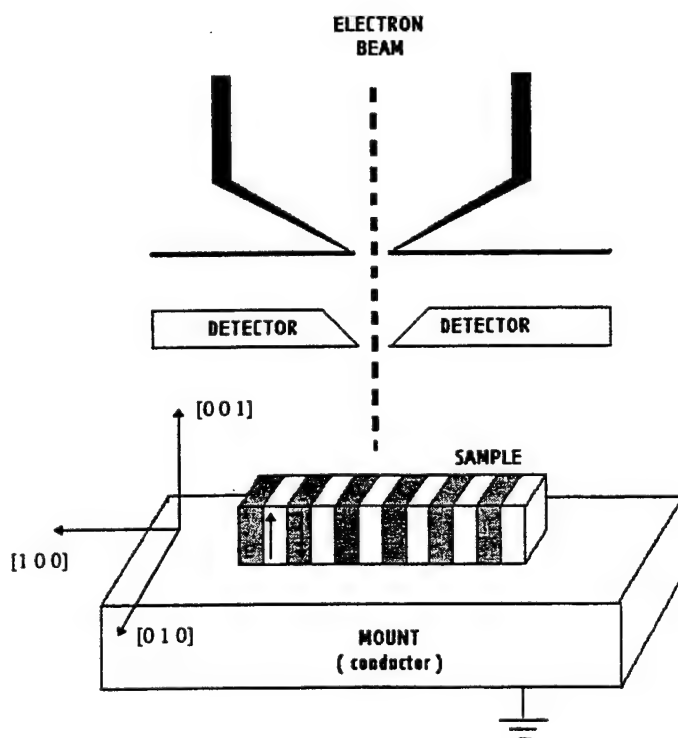


FIGURE 1 Schematic diagram of the experimental arrangement and sample orientation.

The unit vectors for the Cartesian coordinate system was chosen as the following:  $z$  is along the poling direction,  $y$  is in one of the mirror planes of the symmetry group in  $z = 0$  plane and perpendicular to  $z$ , and  $x$  is perpendicular to  $y$  and  $z$ .

Under normal observation conditions, viz.: Wet mode, Chamber pressure = 3–3.5 Torr, Accelerating voltage = 15 kV, Condenser = 40, Scan rate = 8–30 sec./frame and beam aperture size = 30  $\mu\text{m}$ , we got a topographic image of the periodic domain pattern on the original  $+c$  surface, as shown in Figure 2(a), which is in  $[001]$  of the orthogonal coordinate system described above. Water vapor was chosen as the imaging gas. In the image obtained, the surfaces of  $-P_r$  domains are lower than that of  $+P_r$  domains. The formation of the surface steps is due to different etching rate of positive and negative domains in the acid. A wider stripe and some island domains shown in the figure are attributed to imperfect poling or stress concentrations. One can see that the contrast image only outlines the domain boundaries which are brighter than the interior of domains, reflecting the fact that more secondary electrons are emitted at the edges of the etching steps. No contrast was revealed between the positive and negative domains due to the screening of the polarization  $P_r$  by the probing current. In other words, the positive and negative domains have nearly equal secondary electron emission rate if the depolarization field is screened by the charged ions and the beam deposition electrons.

In the second stage, the etched sample was taken out from the chamber and the  $[001]$  surface was polished. When the polished sample was re-examined using ESEM under the same condition, nothing interesting was seen except some topographic images of polishing scratches on the surface. We then changed the experimental conditions by decreasing the chamber pressure, decreasing the condenser setting and increasing the accelerating voltage, magically, contrast stripes began to appear (shown in Fig. 2(b)) and they stay stable. The locations and shapes of the contrast patterns in Figure 2(b) exactly match the etched patterns in Figure 2(a). This confirms that the contrast stripes are originated from the anti-parallel domains.

With a slight tilt of the sample, we could simultaneously observe the previously etched patterns of the periodic structure on  $[010]$  surface of the sample which was not polished (see the bottom of Fig. 2(b)). The image patterns on the two adjacent  $[001]$  and  $[010]$  faces are consistent. However, if we tilt the sample to the  $[0\bar{1}0]$  surface which was polished, not contrast stripes were found. This means that only the polar surfaces can show the domain contrast images, which indirectly telling us that the images are related to the unscreened portion of the depolarization field.

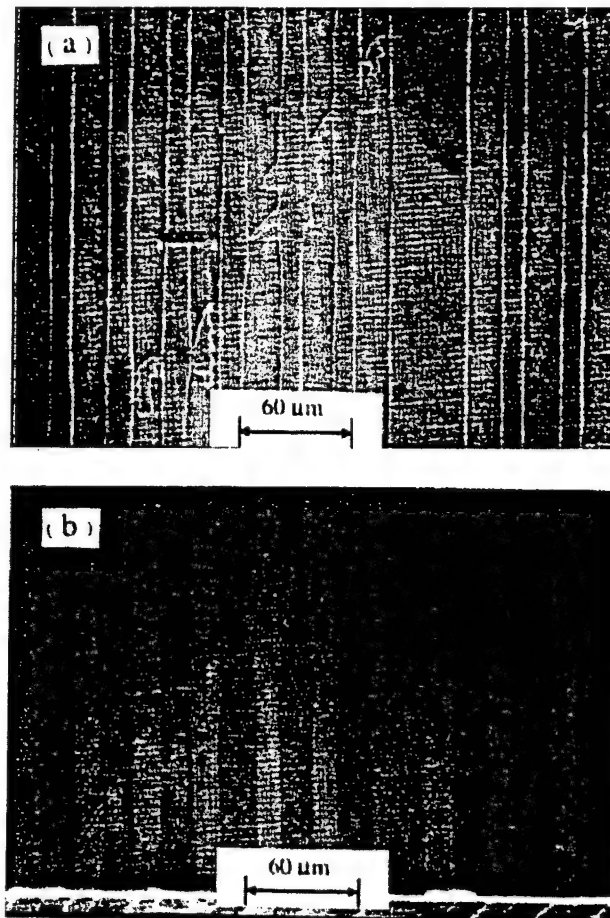


FIGURE 2 Comparison of ESEM images of a surface portion in a c-cut  $\text{LiTaO}_3$  with antiparallel domains: (a) Etched surface; (b) Polished surface.

In the ESEM technique, the visualization of domain contrast is also independent of surface roughness. We could clearly observe the contrast image of domains on a crack surface as shown in Figure 3 with appropriate experimental conditions. The sample in Figure 3 was partially poled under a pair of uniform plane aluminum electrodes. After poling, the electrodes were removed in NaOH solution which only resolves the aluminum but not the  $\text{LiTaO}_3$  crystal. In Figure 3 some triangular domains with positive polarity are shown as lighter regions on the dark background of negative polarity.



Such triangular domain pattern was produced by using a moderate field,  $E = 21 \text{ kV/mm}$ . The sides of the triangles corresponding to domain walls are parallel to crystallographic  $x$ -directions. The domains in Figure 3 have different sizes, which reveals that the polarization reversal in the  $\text{LiTaO}_3$  crystal is through nucleation and growth mechanism. At first, large number of inverted domains are nucleated at different sites, then they grow and coalesce to complete the domain reversal process in the single crystal system. Using a scanning electron microscope on a polished surface of a  $c$ -cut  $\text{LiTaO}_3$  crystal, we have confirmed our domain pattern observations shown in Figure 4. In comparison with Figure 3, one can see the difference between the two imaging methods. Here the image is formed through piezoelectric effect, *i.e.*, the surface charge accumulation expands the positive polar regions to give a topographic image on a negative polar background.<sup>[16]</sup> The density of the secondary electrons produced by the positive and negative polar regions are apparently the same in the SEM secondary electron method, since the image intensities are the same except at the domain boundaries.

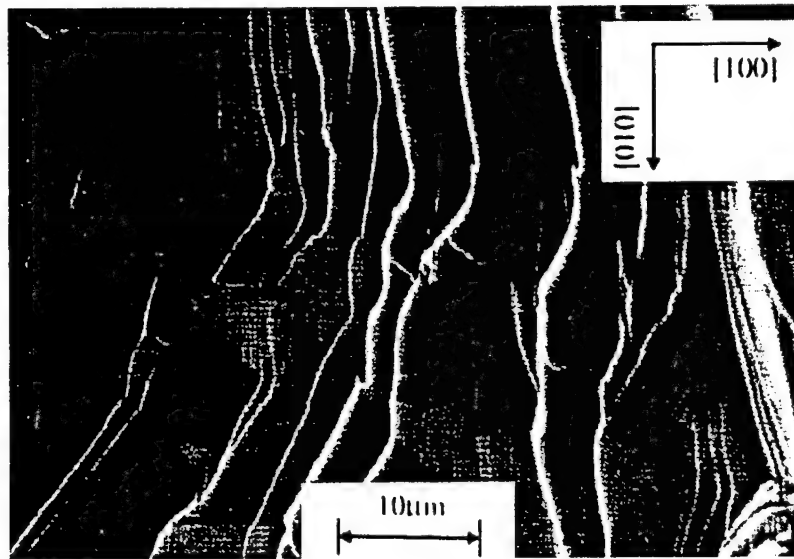


FIGURE 3 ESEM image of a crack surface of  $\text{LiTaO}_3$  crystal with nearly  $[00\bar{1}]$  orientation. The sample was partially poled by a poling field of  $E = 21 \text{ KV/cm}$ . The triangular anti-parallel domains with positive polarity are shown as brighter regions on the darker background.

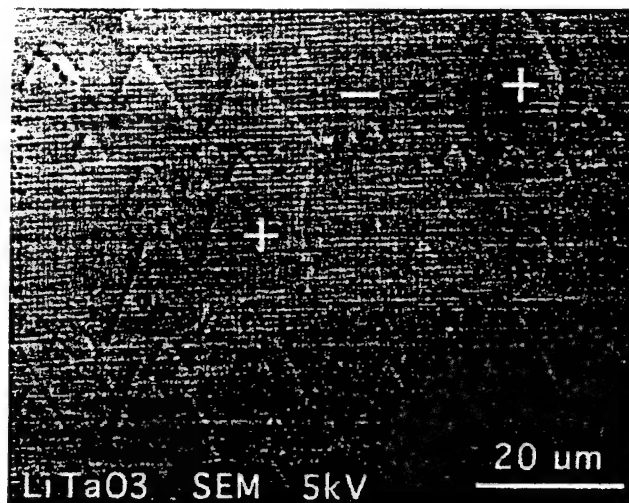


FIGURE 4 SEM secondary electron image of partially reversed domains in a  $\text{LiTaO}_3$  single crystal. The triangular domains are positive polar regions in a negative polar background.

### CONCLUSIONS

In conclusion, we have successfully observed stable contrast image of anti-parallel domains in poled  $\text{LiTaO}_3$  single crystals using ESEM technique. The images obtained from ESEM are further confirmed by chemical etching and the SEM secondary electron microscopy on polished surfaces.

The ESEM technique is very promising for the study of domain configurations in a 3-D bulk since it allows us to directly observe anti-parallel domains in an unprepared insulating sample surface. Because the technique allows the use of higher accelerating voltage with higher magnification, much better resolution than that of the low voltage low current SEM can be obtained. The technique also allows the measurement of rough surfaces, providing a reliable way to study the true 3-D domain configuration without the influence of polishing damages to the sample surface.

### Acknowledgement

This research is sponsored by the Office of Naval Research.

### References

- [1] Cao, W. and Randall, C. A. (1996). *J. Phys. Chem. Solids*, **57**, 1499.
- [2] Franke, K., Hülz, H., Weihnacht, M., Häbler, W. and Besold, J. (1994). *Ferroelectrics*, **172**, 397.
- [3] Eng, L. M., Fousek, J. and Günter, P. (1996). *Ferroelectrics*, **190**, 419.
- [4] Binhlan, R. L. (1989). *Ferroelectrics*, **97**, 19.
- [5] Sogr, A. A. (1989). *Ferroelectrics*, **97**, 47.
- [6] Ozaki, T., Fujii, K. and Aoyagi, S. (1996). *J. Appl. Phys.*, **80**, 1697.
- [7] Rosenman, G., Skliar, A. and Lareah, Y. *et al.*, (1996). *J. Appl. Phys.*, **80**, 7166.
- [8] Hilczer, B., Szczesniak, L. and Meyer, K. P. (1989). *Ferroelectrics*, **97**, 59.
- [9] Roshchupkin, D. V. and Brunel, M. (1993). *Scan. Micro.*, **7**, 543.
- [10] Oleinik, A. S. and Bokov, V. A. (1975). *Sov. Phys. Solid. State.*, **17**, 560.
- [11] Zhu, S. N. and Cao, W. (1997). *Phys. Rev. Letter*, **79**, 2558.
- [12] Danilatos, G. D. (1988). *Advances in Electronic and Electron Physics*, **71**, 109.
- [13] Danilatos, G. D. (1989). *Advances in Electronic and Electron Physics*, **78**, 1.
- [14] Zhu, S. N., Zhu, Y. Y. and Ming, N. B. *et al.* (1995). *J. Appl. Phys.*, **77**, 5481.
- [15] Chen, Y. F., Zhu, S. N., Zhu, Y. Y. and Ming, N. B. (1997). *Appl. Phys. Lett.*, **70**, 592.
- [16] Rosenman, G., Skliar, A., Lareah, Y., Angert, N., Tseitlin, M. and Roth, M. (1996). *Phys. Rev. B*, **54**, 6222.

# **APPENDIX 83**

phys. stat. sol. (a) **173**, 495 (1999)

Subject classification: 77.80.Dj; 61.16.Bg; S10.15

## Imaging of 180° Ferroelectric Domains in LiTaO<sub>3</sub> by Means of Scanning Electron Microscopy

S. ZHU<sup>1</sup>) and W. CAO

*Materials Research Laboratory, The Pennsylvania State University,  
University Park, Pennsylvania 16802, USA*

(Received February 19, 1999)

The 180° ferroelectric domains, engineered through field poling in single crystalline LiTaO<sub>3</sub> were directly observed by means of scanning electron microscopy (SEM) on its polished polar surfaces without metal coating. Two kinds of domain images, the brightness-contrast image and topographic-boundary image, were found with slow scan rate under the condition of a cathode voltage of  $V_0 = 3$  to 5 kV and a probing beam current of  $I_b = (4 \text{ to } 20) \times 10^{-11}$  A. They appeared at the initial and subsequent frames of scanning, respectively. The formation of these two kinds of images is explained as pyroelectric and piezoelectric effects which originated from the beam electron heating and the charge accumulation on the top surface of a LiTaO<sub>3</sub> crystal.

### 1. Introduction

The study of domain microstructures becomes increasingly important for materials engineering. Therefore, visualization of domains has gained broad interests in both physics and materials science communities. Since the 1980's, scanning electron microscopy (SEM) has been used for the observation of ferroelectric domain structures by Le Bihan, Sogor, and others [1 to 3]. Some useful ferroelectric crystals, such as BaTiO<sub>3</sub>, LiNbO<sub>3</sub> and KTiOPO<sub>4</sub>, have been studied by using this method [4 to 6]. For most ferroelectric crystals, the secondary electron emission yield is close to one under the condition of a probing beam electron energy  $E \approx 1$  to 5 keV. Therefore, there is no severe charge accumulation on the surface of an insulating sample.

LiTaO<sub>3</sub> is also an important ferroelectric crystal possessing excellent optical and acoustic properties [7]. The 180° engineered domains in the crystal have been used for the generation of second and third harmonics of laser radiation by quasi-phase-matching, and the excitation and reception of high frequency acoustic wave [8 to 10]. The domain structure in a poled LiTaO<sub>3</sub> sample can be evaluated by optical microscopy on its etched surface. In order to eliminate the damage of etching in the study of domain configuration, it is desirable to develop new convenient nondestructive methods for the observation of engineered domain patterns on an unprepared polar surface of a LiTaO<sub>3</sub> crystal.

Recently, we have successfully observed a 180° domain contrast by using the environmental scanning electron microscopy (ESEM) technique [11]. The ESEM observation is performed under finite atmosphere pressure. Up to now, there are no reports on characterizing the domain structure of LiTaO<sub>3</sub> using conventional SEM. This paper reports

<sup>1</sup>) Permanent address: National Laboratory of Solid State Microstructures and Physics Department, Nanjing University, Nanjing 210093, People's Republic of China.

our SEM results and analyzes the interesting physical principles associated with the images.

In conventional SEM, the sample is put in a high vacuum chamber with a pressure  $p < 10^{-6}$  Torr. Therefore, the observation can only be performed under the conditions of a low acceleration voltage and a small beam current in order to avoid severe charge accumulation on the insulating surface of the sample. Two kinds of domain images of  $\text{LiTaO}_3$  were found in our SEM observation: brightness-contrast images and domain-boundary images. They appeared at the initial and subsequent frames of scanning, respectively.

## 2. Experimental Conditions

The probed samples with  $180^\circ$  anti-parallel domains were fabricated by using pulse-field poling on a single domain  $\text{LiTaO}_3$  crystal at room temperature [12]. Under different electrodes, i.e. stripe and plane electrodes, two types of domain morphology were produced exhibiting stripe and triangular shapes, respectively. The samples were  $\approx 0.5$  mm thick with a pair of parallel polar surfaces. The poled samples were first etched. Some inverted domains with triangular shape or stripe shape on the  $-c$  and  $+c$  faces were confirmed by optical microscopy. Afterwards, the etched surfaces were re-polished in order to remove the topographic domain patterns and the samples were transferred into the SEM sample chamber. The bottom surface of the sample was loosely fixed to a conducting holder and the probing beam current  $I_b$  was directed towards the surface. The conducting sample holder was connected to the ground as shown in Fig. 1. The SEM investigations were performed with a scan rate of 8 to 20 s per frame by using a JEOL JSM-6300 scanning electron microscope in the secondary electron emission mode. The experimental conditions are as follows: chamber pressure  $p < 10^{-6}$  Torr, probe current  $I_b = 4$  to  $20 \times 10^{-11}$  A, and a cathode voltage of  $V_0 = 3$  to 5 kV. The small probe current and the low voltage ensure a longer effective observation time.

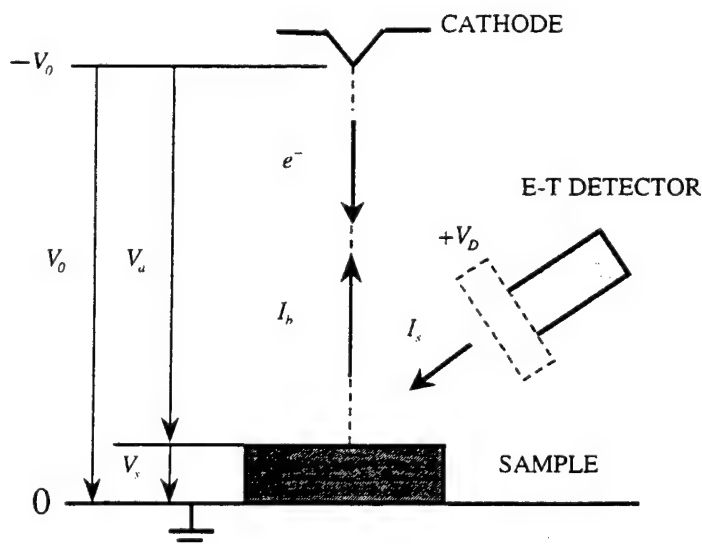


Fig. 1. Definition of the electrical potential levels of the experimental set-up

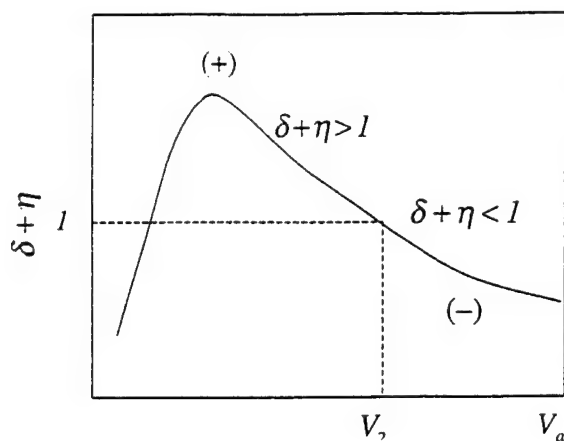


Fig. 2. Sum of the secondary and backscattered electron yield versus the effective acceleration voltage  $V_a$  of the probing beam electrons for an insulating crystal

When the primary probing beam scans the surface of the sample, the irradiated surface emits secondary and backscattered electrons. The total emitted electron coefficient  $\delta + \eta$  as a function of the acceleration voltage  $V_a$  of the probing beam electrons is shown in Fig. 2, where  $\delta$  and  $\eta$  are the yields of secondary and the backscattered electrons of the sample, respectively, and  $V_2$  is the voltage at the equilibrium point at which the sum of the emitted electron coefficient is unity,  $\delta + \eta = 1$ . If the cathode voltage  $V_0$  can be set to  $V_0 = V_2$ , the charges directed to the sample by the probing beam would be the same as the totally emitted charges. Thus, no net charge accumulation would occur on the top surface of the sample. If the cathode voltage  $V_0$  is set to be greater than  $V_2$ , we obtain the condition of  $\delta + \eta < 1$ , which means that the sample is charged negatively that produces a negative voltage  $V_s$  across the sample. The acceleration voltage  $V_a = V_0 - V_s$  will continue to increase until  $V_a = V_2$ . If the cathode voltage can be set to  $V_0 < V_2$ , more electrons are emitted and the sample will be charged positively until  $V_a = V_0 + V_s = V_2$ . With the approximation of a parallel plate capacitor, the electrical potential of the top surface can be written as  $V_s = (ql)/(\epsilon\epsilon_0 a^2)$ , where  $q$ ,  $l$  and  $a$  are the surface charge, the sample thickness and the beam radius, respectively, while  $\epsilon$  and  $\epsilon_0$  are the relative dielectric constant and free space permittivity, respectively. When  $\delta + \eta \neq 1$ , the effective potential from the cathode to the sample surface  $V_a$  is equal to  $V_0 + |V_s|$  for  $V_s < 0$  and  $V_0 - |V_s|$  for  $V_s > 0$  [13,14]. In our experimental conditions, the cathode voltage was set to  $V_0 > V_2$ , based on the fact that the sample surface was negatively charged during the scan.

### 3. Results and Discussion

Two kinds of SEM contrast images were obtained in our experiments. The first was a brightness-contrast image between the positive and negative domains, and the second was a domain-boundary image. The brightness contrast was shown only at the initial frame of probing electron beam scanning. The image of positive domains was brighter than that of the negative domains as shown in Fig. 3. This means that the secondary electron emission yield from the surface of positive domains is larger than that from the surface of negative domains. In the subsequent frames, the brightness contrast disap-

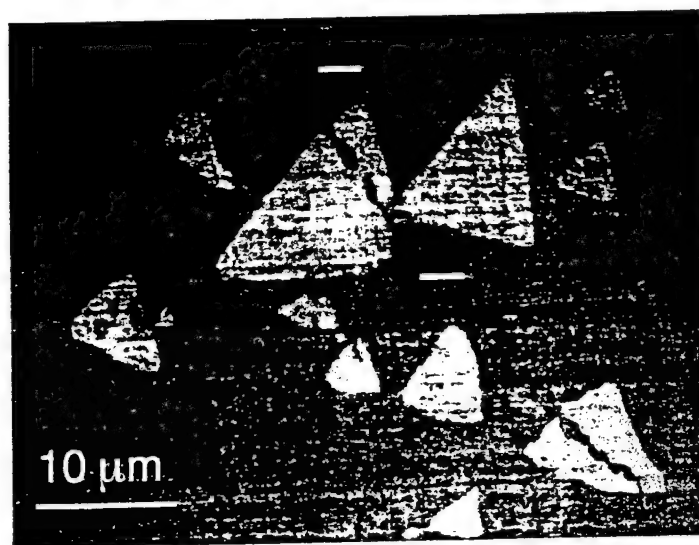


Fig. 3. Domain contrast on the  $-c$  polar surface of a  $\text{LiTaO}_3$  single crystalline surface at the initial scanning frame. The triangular positive domains surrounded by the negative domains are brighter

pears while the domain boundary contrast begins to appear. Fig. 4 reveals a topographic image with the higher lying surface to be the positive domains. The topographic origin of the image can be seen from the shadowing effect in Fig. 4. Some authors also reported similar results in their SEM observations of KTP [15]. These two kinds of contrasts can be of different physical origin as analyzed in more detail below.

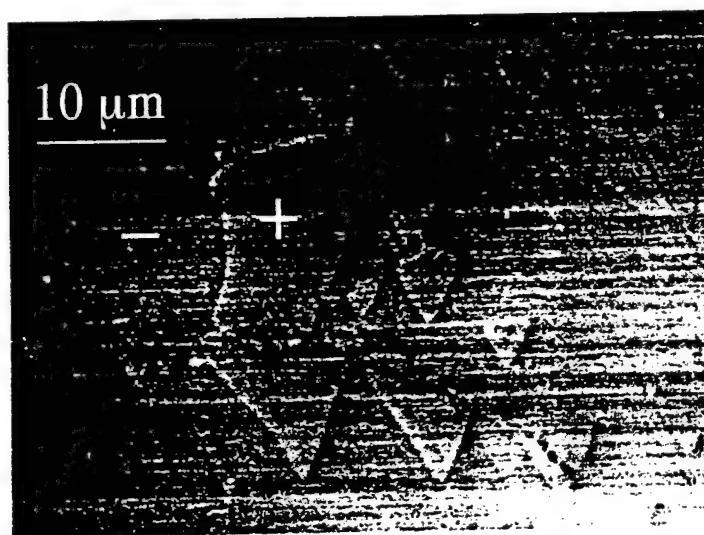


Fig. 4. In the subsequent frames, only a boundary contrast can be observed on the polar surface of the  $\text{LiTaO}_3$  sample



### 3.1 Pyroelectric imaging

Single crystalline LiTaO<sub>3</sub> is a ferroelectric material revealing strong pyroelectric and piezoelectric effects. These effects allow secondary-electron emission from the opposite polar surfaces or their boundaries to have different yield rates which produce domain images.

According to our experimental conditions and the material parameters of LiTaO<sub>3</sub>, we can roughly estimate the influence of these effects on the parameters of the secondary-electron and backscattered-electron yields,  $\delta$  and  $\eta$ , respectively. The average energy per incident electron is  $E_a = eV_a$  before they hit the sample. A portion of this energy is used to excite the secondary and backscattered electrons, while the rest of this energy is absorbed by the sample and is converted into heat. Since, the thermal conductivity of the sample is finite, there will be some temperature difference  $\Delta T$  between the irradiated region and the rest of the sample. This temperature rise can be estimated by using the following formula:

$$\Delta T = \frac{t_d \{ I_b (E_a - \delta \bar{E}_s - \eta \bar{E}_b) / e - L \}}{\nu \varrho c_p} \quad (1)$$

where  $I_b$  is the probe current,  $e = 1.60 \times 10^{-19}$  C is the basic charge unit,  $\nu = \pi a^2 h$  is the irradiated volume,  $h$  is the average penetration depth of the electron,  $a$  is the beam radius,  $c_p$  is the heat capacity per unit volume,  $\varrho$  is the density of crystal,  $\bar{E}_s$  and  $\bar{E}_b$  are the averaged energies of secondary and backscattered electrons. The dwell time  $t_d$  of the probing beam can be evaluated from its line scan length and line scan time. In Eq. (1), the product  $t_d I_b E_a / e$  is the incident energy of probing beam electrons. If this energy is totally converted into heat, the temperature rise in the irradiated local region for a LiTaO<sub>3</sub> crystal ( $\varrho = 7.456$  g cm<sup>-3</sup> [16] and  $c_p = 0.424$  J g<sup>-1</sup> K<sup>-1</sup> [17]) – could be near 100 K. However, a real temperature increase is much lower than this estimated value because two factors prevent the local temperature rise. In Eq. (1),  $t_d I_b (\delta \bar{E}_s + \eta \bar{E}_b) / e$  represents the energy carried away by backscattered and secondary electrons, and  $L$  is the energy loss related to the thermal conductions. According to Ref. [18], a temperature rise of a few degrees Celsius was determined for some bulk samples with a typical SEM probing beam current of  $I_b = 1 \times 10^{-9}$  A [18]. In our case, the beam current was smaller but the scan rate was slower. Thus, it is expected that an increase in temperature of the same order of magnitude compared to the reported values occurred in the irradiated local region. This rise in temperature can generate a pyroelectric potential on the sample surface given by

$$U_{\text{pyro}} = \frac{\kappa \Delta T h}{\varepsilon_0 \varepsilon} \quad (2)$$

where  $\kappa$  is the pyroelectric coefficient of the sample. For single crystalline LiTaO<sub>3</sub> [17],  $\kappa = -17.6 \times 10^{-5}$  CK<sup>-1</sup> m<sup>-2</sup> and  $\varepsilon = 43.4$ . Assuming a small local rise in temperature of  $\Delta T \approx 3$  K, the generated surface potential will be  $U_{\text{pyro}} = -2.5$  V (+2.5 V) for the positive (negative) domains. Therefore, the pyroelectric potential difference  $\Delta U_{\text{pyro}}$  between the positive and negative domains can amount to 5.0 V. This potential difference is large enough to produce a potential contrast on the surfaces of the positive and negative domains because secondary electrons are low in energy (less than 10 eV) making them sensitive to the effects of surface potential and the electric field gradients. If

$U_{\text{pyro}} = +2.5$  V for the negative domains, the secondary electrons with energies less than 2.5 eV will not escape the sample. Thus, a smaller amount of electrons will be detected by the Everhart-Tornley detector. On the other hand, the thermally induced bias of  $-2.5$  V for the positive domains — as calculated above — will act as a booster for the escape of secondary electrons and, hence, a larger amount of electrons will arrive at the detector. Experimentally, a higher yield of the secondary electrons was observed for surfaces of positive domains making them brighter which is consistent with our analysis. According to the above discussions, it is obvious that the contrast resulting from the pyroelectric effect is a reflection of electrical potential contrast [19]. We expect that the same effect can be produced by applying a pressure to a multi-domain single crystalline sample since the piezoelectric effect induces an electric potential difference between the end faces of the positive and the negative domains.

$\text{LiTaO}_3$  is a good insulator with a very small electrical conductivity ( $\sigma < 10^{-11} \Omega^{-1} \text{m}^{-1}$ ) [20]. In the case that the cathode voltage  $V_0 > V_2$  and the total emitted electron coefficient  $\delta + \eta < 1$ , the electrons tend to accumulate on the irradiated surface, producing an additional electric field in the interior of the sample. In our experiment (20 s/frame), the dwell time  $t_d$  of the probing beam is approximately  $10^{-5}$  s, therefore, the incident charge density per frame is estimated to be  $2 \times 10^{-5} \text{ C/cm}^2$ . The effective charge density for the surface build up was much smaller because a significant fraction of the charge was scattered and emitted in the form of secondary electrons. These accumulated charges can be dissipated through the Maxwell relaxation process with a typical relaxation time of  $\tau_m = \epsilon\epsilon_0/\sigma$ . For a  $\text{LiTaO}_3$  crystal, the relaxation time is  $\tau_m > 30$  s. Therefore, the accumulated charges cannot be sufficiently relaxed within the dwell time  $t_d$ . There are still remaining charges on the surface from the previous scan even after the frame interval time  $t_f$  ( $\approx 20$  s). This charge accumulation will cause the reduction of the effective acceleration potential  $V_a$  between the sample and the cathode causing reduction of the velocity of the injected electrons. The situation will continuously accompany the scan process until the condition  $\delta + \eta = 1$  is reached, at which time, the total charges on the sample surface reach a dynamical equilibrium.

Before the dynamic equilibrium is reached, the amount of surface charges is time-dependent and follows the simple rule of  $q = q_0(1 - e^{-t/\tau})$ , where  $q_0$  is the surface charge at equilibrium,  $t$  is the observation time, and  $\tau$  is the effective relaxation time. This time  $\tau$  depends on the conductivity of the sample, the voltage and the current of the probing beam, the quality of vacuum in the chamber, and so on. Thus, the surface potential  $V_s$  can be written as

$$V_s = (V_0 - V_2)(1 - e^{-t/\tau}). \quad (3)$$

The average energy of an incident electron becomes

$$E_a = e(V_0 - V_s) = eV_2 + e(V_0 - V_2)e^{-t/\tau}. \quad (4)$$

When the observation time  $t \gg \tau$ , the average energy  $E_a$  approaches  $eV_2$ . Equation (4) indicates that the energy of the probing beam is a function of the observation time  $t$ . At the initial stage of scan,  $V_s \approx 0$ ,  $E_a \approx eV_0$ . According to Eqs. (1), (2), (3), and (4), the resulting surface pyroelectric potential can be estimated as

$$U_{\text{pyro}} = \frac{\alpha I_b t_d [V_2 + (V_0 - V_2)e^{-t/\tau} - L]}{\epsilon_0 \epsilon \pi a^2 c_p Q}, \quad (5)$$

where  $L$  represents the total energy loss as in Eq. (1). The pyroelectric potential on the LiTaO<sub>3</sub> surface will decrease monotonously with time during the scan process. The surface potential  $V_s$  of the positive and negative domains will differ by  $2U_{\text{pyro}}$ . When the observation time is short, i.e.  $t \ll \tau$  the surface potential  $V_s \approx U_{\text{pyro}}$  and the dominant effect producing the image is the pyroelectric potential. On the other hand, when  $t \gg \tau$ ,  $V_s \gg U_{\text{pyro}}$  and the potential difference between the positive and negative domains becomes negligible. The pyroelectric image fades away rapidly with the increase of  $V_s$ . Experimentally, the pyroelectric domain contrast can only be observed unambiguously in the first frame of the scan.

### 3.2 Piezoelectric imaging

The piezoelectric effect becomes more and more visible with the build up of the surface potential  $V_s$ , which leads to a topographic domain pattern. The electric field induced by the surface charge accumulation along the thickness direction is  $E = V_s/l$ , where  $l$  is the thickness of the sample, which induces an elastic strain of  $S = \Delta l/l = d_{33} E$  in the poling direction through the converse piezoelectric effect. For LiTaO<sub>3</sub>,  $d_{33} = 9.2 \times 10^{-12} \text{ CN}^{-1}$  [21]. Thus, the surface displacement  $\Delta l$  is given by

$$\Delta l = d_{33} V_s = d_{33} (V_0 - V_2) (1 - e^{-t/\tau}). \quad (6)$$

When  $t \gg \tau$  and  $V_s \approx 3 \text{ kV}$ ,  $\Delta l \approx \pm 0.03 \text{ } \mu\text{m}$ . For positive domains, the electric field vector  $\mathbf{E}$  is parallel to the polarization vector  $\mathbf{P}$  so that the displacement  $\Delta l$  is positive. The electric field vector  $\mathbf{E}$  is anti-parallel to  $\mathbf{P}$  for the negative domains resulting in a negative displacement  $\Delta l$ . Since the bottom side of the sample surface is only weakly fixed to the sample holder and free to deform, the surface displacement difference between the positive and negative domain on the top surface is only  $0.03 \text{ } \mu\text{m}$ . The domain-boundary contrast is a topographic one, which originates from the high surface potential built by the beam deposited charge accumulation. In Fig. 4 the boundaries between

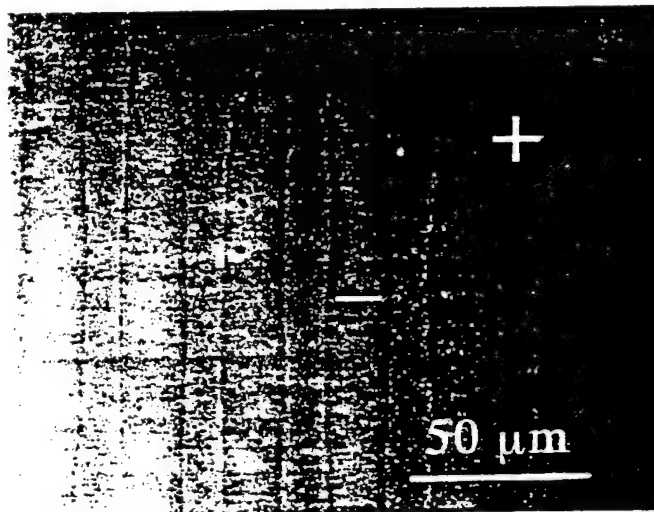


Fig. 5. Domain image of a periodically poled LiTaO<sub>3</sub> sample

the positive and negative domains indeed show sub-micron steps. We also observe the boundary contrast for lower values of  $V_0$  ( $V_0 \approx 3$  kV); the image was the same except of a shallower boundary step as expected. This fact revealed that the equilibrium potential  $V_2$  of the secondary electron emission in LiTaO<sub>3</sub> is lower than 3 kV. We used the SEM technique to check LiTaO<sub>3</sub> samples poled periodically and quasi-periodically and satisfactory images were obtained in both cases. Fig. 5 is an image of a periodic domain structure of a LiTaO<sub>3</sub> surface.

#### 4. Conclusions

In conclusion, the two different kinds of domain contrast images, i.e., the brightness contrast and the domain-boundary contrast, were observed on the polar single crystalline surface of LiTaO<sub>3</sub> by using conventional SEM. At the initial frame, the pyroelectric potential leads to different secondary-electron yields from the positive and the negative domain surfaces and, thus, forming a brightness contrast and produced a domain image. The topographic domain patterns were produced by the piezoelectric effect in subsequent scan frames with the increase of the charge accumulation at the polar sample surface due to the insulating nature of the sample. Hence, a domain boundary image was observed. Our results showed that the 180° anti-parallel engineering domains of single crystalline LiTaO<sub>3</sub> surfaces can be imaged by the conventional SEM under the conditions of non-surface etching and non-coating. This establishes a nondestructive method for the observation of the engineering domain structures of single crystalline LiTaO<sub>3</sub> samples.

**Acknowledgement** This research was sponsored by the U.S. National Science Foundation Grant # DMS-9704714.

#### References

- [1] R. LE BIHAN, *Ferroelectrics* **97**, 19 (1989).
- [2] A. A. SOGR and I. B. KOPYLOVA, *Ferroelectrics* **191**, 193 (1997).
- [3] A. SKLIAR et al., *Ferroelectrics* **191**, 187 (1997).
- [4] G. ROSENMAN, A. SKLIAR, Y. LAREAH et al., *J. Appl. Phys.* **80**, 7166 (1996).
- [5] D. V. ROSHCHUPKIN and M. BRUNEL, *Scanning Microscopy* **7**, 543 (1993).
- [6] T. OZAKI, K. FUJII, and S. AOYAGI, *J. Appl. Phys.* **80**, 1697 (1996).
- [7] Y. XU, *Ferroelectric Materials and Their Applications*, North-Holland Publ. Co., New York 1991.
- [8] S. N. ZHU, Y. Y. ZHU et al., *Phys. Rev. Lett.* **78**, 2752 (1997).
- [9] S. N. ZHU, Y. Y. ZHU, and N. B. MING, *Science* **278**, 843 (1997).
- [10] Y. F. CHEN, S. N. ZHU, Y. Y. ZHU, and N. B. MING, *Appl. Phys. Lett.* **70**, 592 (1997).
- [11] S. N. ZHU and W. CAO, *Phys. Rev. Lett.* **79**, 2558 (1997).
- [12] S. N. ZHU, Y. Y. ZHU et al., *J. Appl. Phys.* **77**, 5481 (1995).
- [13] R. LE BIHAN and M. MAUSSON, *Rev. Phys. Appl.* **9**, 427 (1974).
- [14] P. R. THORNTON, *Scanning Electron Microscopy*, Chapman & Hall, London 1968.
- [15] G. ROSENMAN et al., *Phys. Rev. B* **54**, 6222 (1996).
- [16] S. C. ABRAHAMS and S. C. BERNSTEIN, *J. Phys. Chem. Solids* **28**, 1685 (1967).
- [17] H. P. BEERMAN, *Infrared Phys.* **15**, 225 (1975).
- [18] J. I. GOLDSTEIN, *Scanning Electron Microscopy and X-Ray Microanalysis*, Plenum Press, New York 1992.
- [19] L. REIMER and G. PFEFFERKORN, *Raster-Elektronen Mikroskopie*, Springer-Verlag, Berlin 1973.
- [20] G. I. ROZENMAN, J. S. REZ, TU. L. CHEPELEV, and N. B. ANGERT, *Soviet Phys. — Tech. Phys.* **26**, 234 (1981).
- [21] T. YAMADA, H. IWASAKI, and N. NIIZEKI, *Jpn. J. Appl. Phys.* **8**, 1127 (1969).

# **APPENDIX 84**

## Nonlinear Ferroelectric Domain Wall Response

VOLKMAR MUELLER<sup>a</sup>, HORST BEIGE<sup>a</sup> and Q.M. ZHANG<sup>b</sup>

<sup>a</sup>*FB Physik, Universität Halle, F.-Bach-Platz 6, D-06108 Halle, Germany; and*

<sup>b</sup>*Mat. Res. Lab. Pennsylvania State University, University Park, PA 16802*

The ac-field dependence of complex dielectric coefficients in the improper ferroelectric phase of incommensurate  $\text{Rb}_2\text{ZnCl}_4$  crystals is analyzed and compared with those observed in donor doped lead zirconate titanate (PZT) piezoceramics. For all coefficients examined, a threshold field for the onset of nonlinearity exists leading to qualitatively the same non-analytic scaling behavior above threshold. Due to the similar nonlinear behavior of very different ferroelectric systems, we suggest that a universal mechanism may exist in a larger class of ferroelectrics causing nonlinearity at moderate field level. This may be related to the dynamics of randomly pinned elastic interfaces driven at field strengths slightly above threshold for collective interface motion.

**Keywords:** ferroelectric domain walls; dielectric nonlinearity; pinning

### INTRODUCTION

The behavior of ferroelectric materials in external electric fields is substantially influenced by their ferroelectric domain structure. In strong fields, the redistribution of volume parts occupied by domains with different orientations of the spontaneous polarization takes place causing a strongly nonlinear and hysteretic field dependence of the macroscopic polarization.<sup>[1]</sup> The understanding of the repolarization process leading to the ferroelectric hysteresis loop is essential for technical applications such as nonvolatile ferroelectric

memory devices. On the other hand, the switching of spontaneous polarization is not desired in various other applications. For example, in PZT piezoceramics widely used in actuators, transducers and motors,<sup>[2]</sup> repolarization may destroy the poling of the ceramic. However, piezoceramics are often subjected to rather large fields in which the field dependence of the polarization is clearly hysteretic and nonlinear and can be described by the Rayleigh law.<sup>[3]</sup> Accordingly, the behavior of ferroelectrics in the field range of Rayleigh loops was subject of several studies.<sup>[3-6]</sup>

In soft PZT piezoceramics, two different thresholds for the onset of nonlinearity of effective piezoelectric and dielectric coefficients were found at ac-fields  $E_{c1} \approx 100 \text{ V/cm}$  and  $E_{c2} \approx 1 \text{ V/cm}$ , respectively.<sup>[5]</sup> Both lead to a non-analytic scaling behavior

$$X(E^{(ac)}) = X_0 + X_{n1} (E^{(ac)} - E_c)^\phi \quad (1)$$

above the respective threshold. The exponent  $\phi = 1.5 \pm 0.1$  was observed in weak fields whereas the nonlinearity is anisotropic in medium fields and can be characterized by exponents  $\phi = 1.2 \pm 0.1$  and  $\phi = 1.0 \pm 0.1$  in fields perpendicular and parallel to the polar direction, respectively. Moreover, all exponents are apparently independent of the particular ceramic system indicating a universal behavior of soft PZT. However, the complex domain structure, the phase coexistence for compositions close to the morphotropic phase boundary (MPB) and clamping of the grains<sup>[7]</sup> makes the interpretation of experimental results obtained in this polycrystalline material more difficult.

In contrast to the complex electromechanical system PZT, the conditions in most ferroelectric single crystals are much simpler. Thus, it would be interesting to find single crystals that show a similar nonlinear behavior. The improper ferroelectric lock-in phase of  $\text{Rb}_2\text{ZnCl}_4$  (RZC) crystals, for example, exhibits an especially simple domain structure which is built up of planar

non-ferroelastic  $180^\circ$  domain walls (DW's) oriented parallel to the crystallographic c-axis. More importantly, the ferroelectric domain structure follows in the incommensurate - commensurate (IC-C) phase transition from a regular phase soliton lattice of the IC-phase.<sup>[9,10]</sup> This is the cause that polarization reversal proceeds in RZC in the simplest way possible in a ferroelectric system: by sideways shifts of a field independent number of DW's.<sup>[11,12]</sup> Since the field induced domain nucleation has not to be taken into consideration, RZC represents a unique model system for the study of DW-defect interaction. In this paper, the ac-field dependence of the dielectric response of purified RZC single crystals is analyzed and compared with those of soft PZT piezoceramic. Despite the big differences between PZT and RZC, the same scaling behavior is found in the improper ferroelectric phase of RZC as observed recently in soft PZT.<sup>[5]</sup> Thus, the experimental data indicate that a mechanism common to a larger class of ferroelectrics may exist causing nonlinearity at medium field level.

## EXPERIMENTAL

The same purified RZC crystal, obtained by repeated recrystallization from the aqueous solution, was investigated as in a previous paper.<sup>[12]</sup> The behavior of RZC is compared with those of the commercial piezoceramic PZT-5A (Morgan Matroc) which is a poled donor doped (soft) PZT close to the MPB. The current flowing through the sample subjected to a harmonic ac-field  $E^{(ac)}$  ( $f=110\text{Hz}$ ) was amplified by a current amplifier (Stanford SR540) and analyzed using a digital lock-in amplifier (Stanford SR830). Thus, the ac-field dependence of the complex effective dielectric coefficient  $\epsilon = P/E^{(ac)}$  was obtained. The sample was slowly cooled through the IC-C transition to the desired temperature which was stabilized with an accuracy of  $\Delta T = \pm 0.05\text{K}$ .



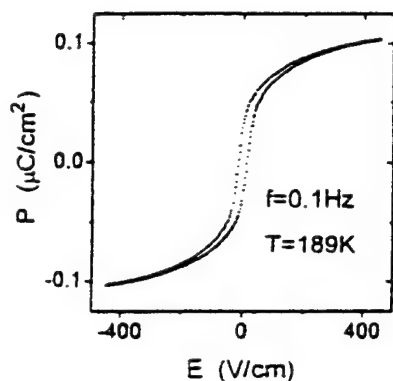


FIGURE 1 Quasistatic hysteresis loop of RZC.

## RESULTS

The quasistatic hysteresis loop of RZC obtained close below the IC-C transition temperature  $T_L$  (Fig. 1) differs strongly from the well known ferroelectric hysteresis of PZT.<sup>[8,13]</sup>

This is attributed to the completely different phase transition mechanism, different domain structure and, most importantly, different repolarization mechanism in RZC. Polarization reversal in the proper ferroelectric phase of PZT includes nucleation, growth and coalescence both of non-180° and 180° domains. On the other hand, the unique repolarization mechanism in the improper ferroelectric phase of RZC causes the "swan neck" shape of the hysteresis loop reflecting the DW interaction.<sup>[12]</sup>

Despite the different repolarization mechanism, shape and ac-field dependence of Rayleigh loops  $P(E)$  in RZC are quite similar than in PZT

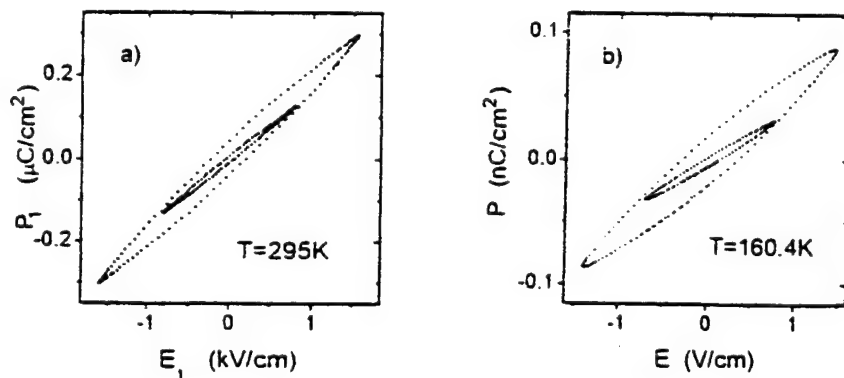


FIGURE 2 Rayleigh loops  $P(E)$ : a) PZT-5A; b) RZC.

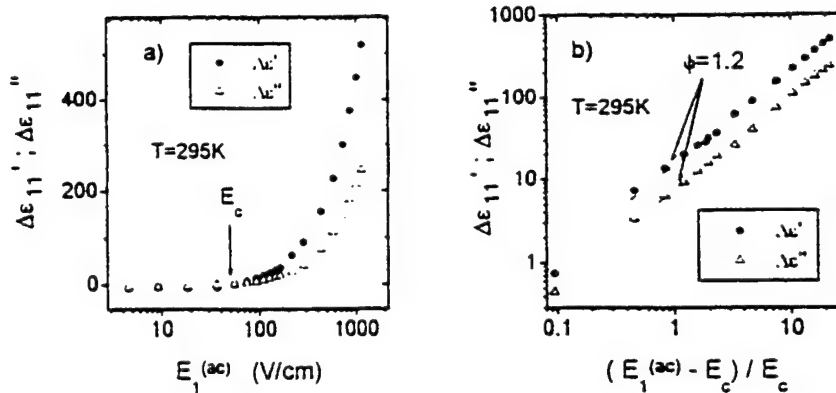


FIGURE 3 Nonlinearity of the complex permittivity  $\epsilon_{11}^*$  of PZT-5A:  
 a) ac-field dependence of  $\Delta\epsilon_{11} = \epsilon_{11}(E_1^{(ac)}) - \epsilon_0$ ; b) non-analytic scaling behavior above threshold  $E_c = 50\text{V/cm}$ .

(Fig. 2a,b). However, due to the different DW mobility, the field range in which Rayleigh loops occur differs considerably between both systems. An example for the nonlinearity observed recently in soft PZT above medium field threshold<sup>[5]</sup> is given in (Fig. 3a,b). Interesting to note that the imaginary part  $\epsilon_{11}''$  of the permittivity can be scaled in the same way and yield to the same exponent  $\phi = 1.2 \pm 0.1$  as the real part. Thus, the "nonlinear phase angle"  $\tan_{nl}\delta = \epsilon_{11}'' / \epsilon_{11}'$  is independent of the ac-field. The ac-field dependence of the dielectric coefficient of RZC, measured at a temperature  $T = 160.4\text{K}$  is shown in Fig. 4a. The close similarity to the behavior observed in soft PZT is apparent. In particular, a threshold for the onset of nonlinearity seems to exist at  $E_c \approx 0.07\text{V/cm}$ , that is, at smaller field level than in soft PZT. Moreover, both the real and the imaginary part of the permittivity of RZC can be scaled according to Eq.(1) (Fig. 4b) and lead to the same exponent  $\phi = 1.5 \pm 0.1$  as obtained in soft PZT above weak field threshold.

In order to investigate the influence of temperature, the experiment was repeated at  $T = 187.5\text{K}$ , that is, slightly below  $T_L$ . Clearly, the threshold character of the dielectric weak field nonlinearity is preserved (Fig.5a).

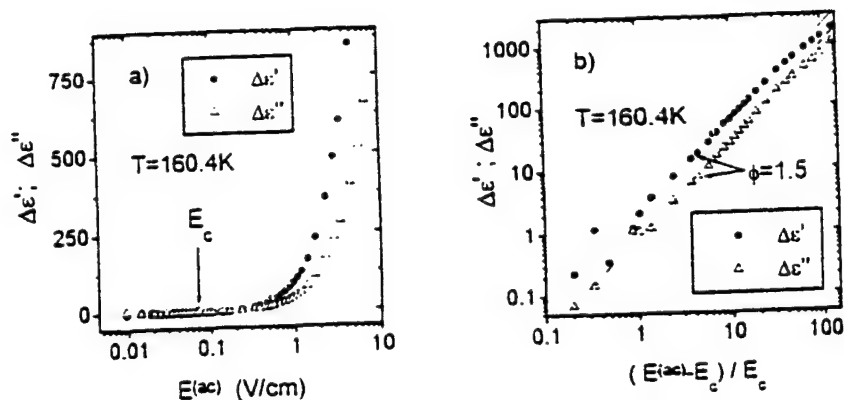


FIGURE 4 Nonlinearity of the complex permittivity of RZC far below  $T_L$ : a) ac-field dependence of  $\Delta\epsilon = \epsilon(E^{(ac)}) - \epsilon_0$ ; b) non-analytic scaling behavior above threshold  $E_c = 0.07 \text{ V/cm}$ .

Though the coercive field of the (large field) hysteresis loop is significantly smaller at this temperature,<sup>[12]</sup> the analysis of the weak field results comes to a threshold field  $E_c \approx 0.15 \text{ V/cm}$  larger than those at  $T = 160.4 \text{ K}$ . In addition, scaling of the data at  $T = 187 \text{ K}$  yields the same exponent  $\phi = 1.5 \pm 0.1$  as obtained at  $T = 164.5 \text{ K}$  (Fig. 5). However, at  $T = 187 \text{ K}$ , deviations from the straight lines occur at lower field level  $E^{(ac)} \approx 4E_c$  than at  $T = 160.4 \text{ K}$ .

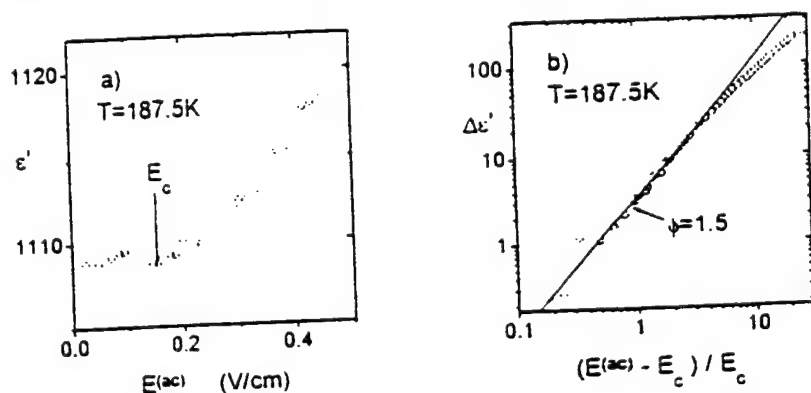


FIGURE 5 Nonlinearity of RZC slightly below  $T_L$ : a) ac-field dependence of  $\Delta\epsilon$ ; b) non-analytic scaling behavior above threshold  $E_c = 0.15 \text{ V/cm}$ .

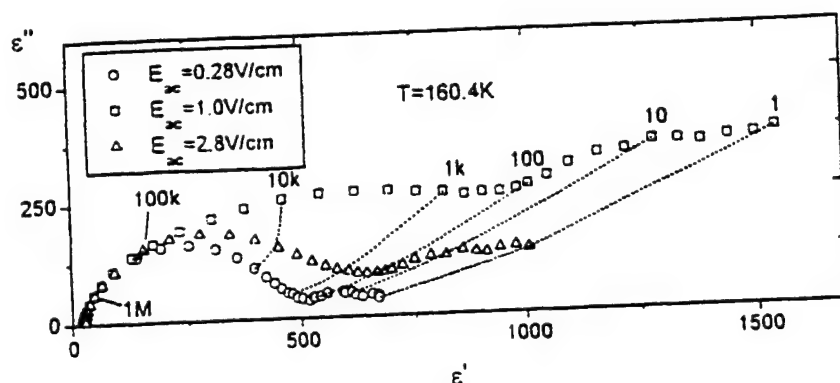


FIGURE 6 AC-field dependence of the dielectric dispersion of RZC.

Finally, at  $T=160.4\text{K}$ , the frequency range was determined in which the strong ac-field dependence of the complex permittivity appears. For small amplitudes  $E^{(ac)}=0.28\text{V/cm}$ , the dielectric dispersion in the frequency range  $1\text{kHz} < f < 10\text{MHz}$  is of the Cole-Cole type (Fig. 7) with a mean relaxation frequency  $f_r \approx 30\text{kHz}$ . This relaxation region is related to the dielectric contribution of pinned DW's that respond to the electric field in the same way as an elastic membran.<sup>[14]</sup> In comparison to this dispersion region, additional dielectric contributions discernible at low frequencies  $f < 1\text{kHz}$  are small at this field level. However, with increasing ac-field amplitude, the low frequency dispersion, characterized by a very broad distribution of relaxation times, becomes increasingly important and governs the dielectric response in high fields. Obviously, the ac-field dependence of the permittivity is largest at frequencies  $f=f_r$  corresponding to the low frequency end of the weak field Cole-Cole arc whereas there is almost no ac-field dependence at  $f > f_r$ .

## DISCUSSION

The observed nonlinearity in PZT and RZC is clearly related to the response of ferroelectric DW's. In order to illuminate possible reasons for the similar

nonlinear behavior of ferroelectrics that are, in first view, completely different, it may be helpful to point out some common features of the dielectric domain wall response in PZT and RZC.

First, due to its peculiar repolarization mechanism, the number of DW's in RZC does not depend on electric field even at field strengths where fully developed ferroelectric hysteresis loops are obtained. In La doped PZT, switching takes place if the internal electric field within the grain exceeds a critical field  $E_s \approx 10 \text{ kV/cm}$ .<sup>[13]</sup> Thus, the Rayleigh loop of soft PZT should be determined by the motion of existing DW's rather than by the nucleation of new domains. This is supported by the linear polarization strain dependence  $S_5(P_1)$  in PZT.<sup>[6]</sup> Apparently, the observed scaling behavior is restricted to systems for that the primary nucleation of domains can be neglected.

In first view, it may be surprising that differences concerning crystal symmetry, domain structure and phase transition mechanism do not make a difference in the nonlinear response. Even within the PZT compositions close to the MPB examined previously,<sup>[5]</sup> tetragonal and rhombohedral phase and, thus,  $180^\circ$  and different types of non- $180^\circ$  walls coexist. However, only a small part of the spontaneous polarization of RZC and PZT, respectively, is switched in the field range of Rayleigh loops (Fig. 2a,b). Thus, the DW's are shifted only slightly by a distance  $\Delta x$  from their equilibrium position. Due to the strong anharmonicity of the DW potential energy  $U(\Delta x)$ ,<sup>[12]</sup> DW's moving on the flat bottom of the potential box do not probe the specific properties of the potential and the nonlinearity related to the potential energy of the DW should be small. This is corroborated by the amplitudes of higher harmonics (Fig. 7a,b) that are small in comparison to the strong nonlinearity observed in the first harmonic. From this point of view, the non-analytic scaling behavior seems to be restricted to fields in which DW's do not come that close to each other that DW interaction becomes important. In RZC, this may cause the deviations from the scaling behavior in large fields.

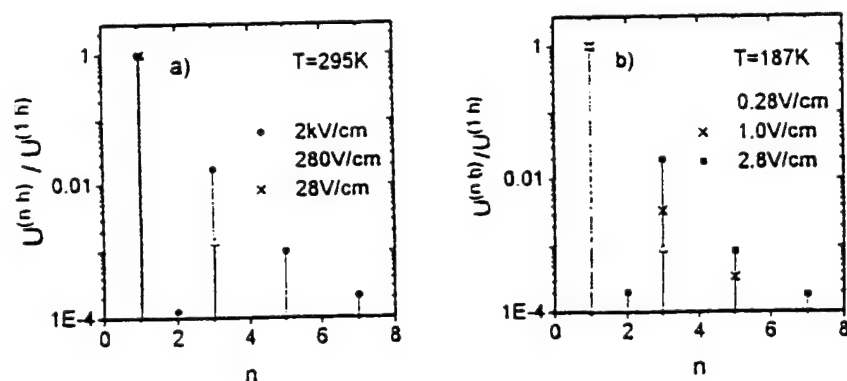


FIGURE 7 Ratio  $U^{(n,h)}/U^{(1,h)}$  between higher harmonics and first harmonic: a) PZT-5A; b) RZC.

A common feature of the ferroelectrics examined is their large DW mobility. Apparently, no major obstacles for DW displacements exists but DW interaction with a matrix of randomly distributed "small" defects is relevant. For the temperature and frequency range of our experiments, these defects can be regarded as immobile. Thus, the DW can be treated as an elastic interface in a medium with quenched disorder. Theoretical considerations (see, e.g.,<sup>[15,16]</sup>) predict that the interface motion is basically jerky as long as external pressure (due to the driving field) and pinning pressure are comparable. Thus, it is conceivable that the observed nonlinearity is related to the dynamics of pinned DW's.

In weak fields, dielectric contributions occur due to depinning of parts of the DW. Theoretical considerations lead to a logarithmic frequency dependence of  $\epsilon'$  at low frequencies<sup>[15]</sup> which was experimentally observed both in PZT<sup>[4]</sup> and, in the present study, in RZC. Additionally, nonlinearity of the dielectric response was predicted.<sup>[15]</sup> However, our experimental results indicate that a finite threshold  $E_c > 0$  for the onset of nonlinearity exists. In a theoretical study, the depinning transition of interfaces was treated as dynamical critical phenomenon.<sup>[16]</sup> Above threshold for the onset of collective

interface motion, a nonlinear relationship  $v \sim (F - F_c)^\psi$  was predicted between the mean interface velocity  $v$  and the driving force  $F$ . Interestingly, the mean field result<sup>[16]</sup> for the critical exponent  $\psi = 1.5$  coincides with the exponents obtained in weak fields on soft PZT<sup>[5]</sup> and RZC. Unfortunately, due to accuracy limitations of our experimental setup, no information could be obtained within the critical region treated by the theory.

To conclude, a non-analytic scaling behavior of effective dielectric coefficients was observed in very different ferroelectric systems. Therefore, we suggest that a universal mechanism may exist in a larger class of ferroelectrics causing nonlinearity at moderate field strengths. This mechanism may be related to the dynamics of driven elastic interfaces moving in pinning media with quenched disorder.

### References

- [1] M.E. Lines and A.M. Glass, *Principles and Applications of Ferroelectrics and Related Materials* (Clarendon, Oxford, 1977).
- [2] L. E. Cross, *Ferroelectric Ceramics. Tailoring Properties for Specific Applications in Ferroelectric Ceramics*, edited by N. Setter and E. L. Colla (Birkhaeuser, Basel, 1993).
- [3] D. Damjanovic and M. Demartin, *J. Phys. C*, **9**, 4943 (1997).
- [4] D. Damjanovic, *Phys. Rev. B*, **55**, R649 (1997).
- [5] V. Mueller and Q.M. Zhang, to appear in *Appl. Phys. Lett.*.
- [6] V. Mueller and Q.M. Zhang, *J. Appl. Phys.*, **83**, 3754 (1998).
- [7] G. Arlt, *J. Mater. Sci.*, **25**, 2655 (1990).
- [8] B. Jaffe, J. Cook and H. Jaffe, *Piezoelectric Ceramics* (Academic, London, 1971).
- [9] H. Z. Cummins, *Phys. Rep.*, **185**, 211 (1990).
- [10] V. Novotná, H. Kabelka, J. Fousek, H. Havráňková and H. Warhanek, *Phys. Rev. B*, **47**, 11019 (1993).
- [11] A. Levstik and H.-G. Unruh, *Phys. Rev. B*, **36**, 872 (1987).
- [12] T. Hauke, V. Mueller, H. Beige and J. Fousek, *Phys. Rev. B*, **57**/17, in press (1998).
- [13] G. Arlt, *Ferroelectrics*, **189**, 103 (1996).
- [14] V. Mueller, T. Hauke, H. Beige and J. Fousek, *Ferroelectrics*, **176**, 107 (1996).
- [15] T. Nattermann, Y. Saphir and I. Vilfan, *Phys. Rev. B*, **42**, 8577 (1990).
- [16] D. S. Fisher, *Phys. Rev. B*, **31**, 1396 (1985).

# **APPENDIX 85**



## Optical observation of dynamic ferroelectric phase transition and static domain structures in crystal ion sliced (CIS) LiNbO<sub>3</sub> film

Ruibin Liu <sup>a,\*</sup>, Ruyan Guo <sup>a</sup>, Amar S. Bhalla <sup>a</sup>, L.E. Cross <sup>a</sup>, M. Levy <sup>b</sup>,  
R.M. Osgood Jr. <sup>b</sup>

<sup>a</sup> Materials Research Laboratory, The Pennsylvania State University, University Park, PA 16802, USA

<sup>b</sup> Department of Applied Physics, Columbia University, New York, NY 10027, USA

Received 3 December 1998; accepted 6 December 1998

### Abstract

Crystal ion slicing (CIS) is a novel approach to produce films from bulk crystalline materials. A LiNbO<sub>3</sub> film with dimensions of  $1.29 \times 0.9 \times 0.01$  mm was detached from a poled bulk crystal. The ferroelectric domain characteristics and phase transition behavior of the detached film were studied using transmission optical microscopy and recorded continuously by VCR tape recorder through a CCD camera. The sample was heated gradually from room temperature to 1190°C, and then cooled down to room temperature. The phase transition from the ferroelectric to paraelectric was observed at 1163°C. High density domain structures were also observed when the sample was cooled to room temperature after it was annealed at a temperature around the Curie temperature. The experimental results show that the virgin CIS LiNbO<sub>3</sub> film is still in a ferroelectric state and preserves the single domain state of a poled bulk crystal. The CIS film has clear advantages over the film prepared by other techniques for various integrated applications. © 1999 Elsevier Science B.V. All rights reserved.

PACS: 81.20.-n; 42.82.-m; 77.80.Dj

**Keywords:** Ferroelectric film; Crystal ion slicing technology; Ferroelectric phase transition and domain; Integrated optics

### 1. Introduction

Fabrication of ferroelectric materials in thin ( $< 1$   $\mu\text{m}$ ) and thick ( $< 10$   $\mu\text{m}$ ) film is important for their applications related to memories, MEMS, thermal detecting arrays and integrated optics [1].

Efforts have been made to develop high quality ferroelectric thin and thick films by various methods

including CVD, sol-gel, rf sputtering, laser ablation deposition, tape casting and screen printing [2]. Recently, a novel approach known as crystal ion slicing (CIS) has been used to fabricate ferroelectric films from a poled LiNbO<sub>3</sub> crystal [3]. A 10  $\mu\text{m}$  thick LiNbO<sub>3</sub> film was successfully separated by the CIS technique from the poled bulk crystal. In the CIS processing, the surface of the bulk crystal material is subject to deep ion implantation, which creates a damage layer several microns below the sample surface. Etching selectively between the damage layer and rest of the bulk material is much different. Thus,

\* Corresponding author. Fax: +1-814-863-1327; E-mail: rxl23@psu.edu

the top layer can be split from its matrix. Beside  $\text{LiNbO}_3$  crystals, this method can also be applied to other ferroelectric and nonferroelectric crystals.

The CIS  $\text{LiNbO}_3$  film is of particular interest because of its wide range of applications in electro-optic devices. The CIS film in a freestanding state can easily be transferred onto other substrates. In addition, the detached film should preserve good electro-optic properties, and ferroelectric characteristics such as spontaneous polarization, phase transition, etc. [4,5]. Earlier reports on X-ray and electrical measurements suggest that the detached films have similar structure and room-temperature dielectric constant as its bulk crystal [3].

In this paper, we report the optical microscopic investigation of the CIS  $\text{LiNbO}_3$  film. The detached  $\text{LiNbO}_3$  film with dimensions of  $1.29 \times 0.9 \times 0.01$  mm was placed on a sapphire substrate and subject to a controlled heating and cooling cycle between room temperature and  $1190^\circ\text{C}$ . Ferroelectric phase transition was observed around  $1163^\circ\text{C}$ . The film showed the multidomain structure after it was annealed at temperature around the Curie temperature. This observation also provides direct evidence of the ferroelectric single domain state of the as-prepared CIS film.

## 2. Experimental procedure

The poled bulk  $\text{LiNbO}_3$  crystal was mounted on a water-cooled substrate. The 3.8 MeV helium ions were implanted on the unmasked surface perpendicular to the [001] axis. The depth of the damage layer can be controlled by the implanted ion beam energy. The implant dose for all samples was  $5 \times 10^{16}$  ions/ $\text{cm}^2$ . The ion implanted bulk crystal was then etched in diluted 5% hydrofluoric acid for 24 h. Ten micrometer-thick freestanding film with 1.29 mm length and 0.9 mm width was obtained after the completion of the etching process. Fig. 1 shows the as-prepared CIS  $\text{LiNbO}_3$  film. The surface features show the microdomains were created during the ion implantation and etched in the process of separating the film from its bulk crystal. The film was then placed on an optical isotropic transparent sapphire disc. The disc was inserted into a heating crucible of

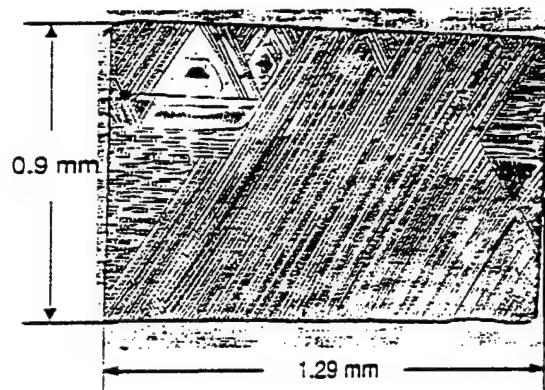


Fig. 1. As-prepared CIS  $\text{LiNbO}_3$  film, showing the etched microdomains.

the TH 1500 (Liakam, Japan) high-temperature stage, and observations were made of plane-polarized light under crossed polarized conditions in a transmission mode of operation. The heating and cooling was controlled by a programmable controller at a rate of  $10^\circ\text{C}/\text{min}$ . The transmitted light image of the crystal was continuously recorded by a Sony video tape recorder and using a Hamamatsu CCD video camera.

## 3. Experimental results and discussions

The two most important characteristics, in general, of a ferroelectric material are (1) its ferroelectric to paraelectric phase transition and (2) dielectric hysteresis loop. These characterizations of ferroelectric properties are usually obtained by (1) measurement of the dielectric anomaly at the phase transition temperature and (2) the measurement of dielectric hysteresis loop at temperatures below the Curie temperature [6]. However, in case of  $\text{LiNbO}_3$ , the Curie temperature, between  $1150^\circ\text{C}$ – $1180^\circ\text{C}$  for stoichiometrical composition, is too high and the coercive field is too large at room temperature to measure the dielectric hysteresis loop [7]. Therefore, both of these investigation are difficult to perform.

As an alternative approach, optical microscopic investigation can reveal the phase transition characteristics of  $\text{LiNbO}_3$ . Large changes in the optical transmission ( $\text{LiNbO}_3$  is an excellent electro-optic crystal) could be sufficient to mark the phase transi-

tion dynamics. Fig. 2 shows several stages of the phase transition (selected from the continuous recording of the phase transition process). Ferroelectric to paraelectric phase transition in CIS  $\text{LiNbO}_3$  film occurs around  $1163^\circ\text{C}$  and this value is in agreement with the  $T_c$  reported for a bulk crystal. The time taken for the phase transition from beginning to the finish was 24 s. This corresponds to a  $4^\circ\text{C}$  temperature change, based on the heating rate and calibration conditions set in our experimental set-up. From the intensity recording and the rate of change of intensity, this phase transition appears to be of the second order as is expected in bulk  $\text{LiNbO}_3$ .

After heating above its Curie temperature and then cooling to below  $T_c$  without bias, the crystal

becomes polydomain. As the  $T_c$  is close to the melting temperature ( $1260^\circ\text{C}$ ) of this crystal, there is a slight thermal etching, which occurs at high temperature ( $< T_c$ ) and leaves its signature as etched domains. The new domains sets are different from those observed in the as-prepared CIS film which revealed as line pattern after the separation of the film from the bulk. When the sample was cooled down to room temperature, some cracks occurred during the cooling. High-density polydomain structures appear on the annealed sample at room temperature (Fig. 3b). The as-prepared film did not show such trigonal polydomain structure (Fig. 3a). The crystalline symmetry changes from  $\bar{3}m$  to  $3m$  during the phase transition from paraelectric to ferro-

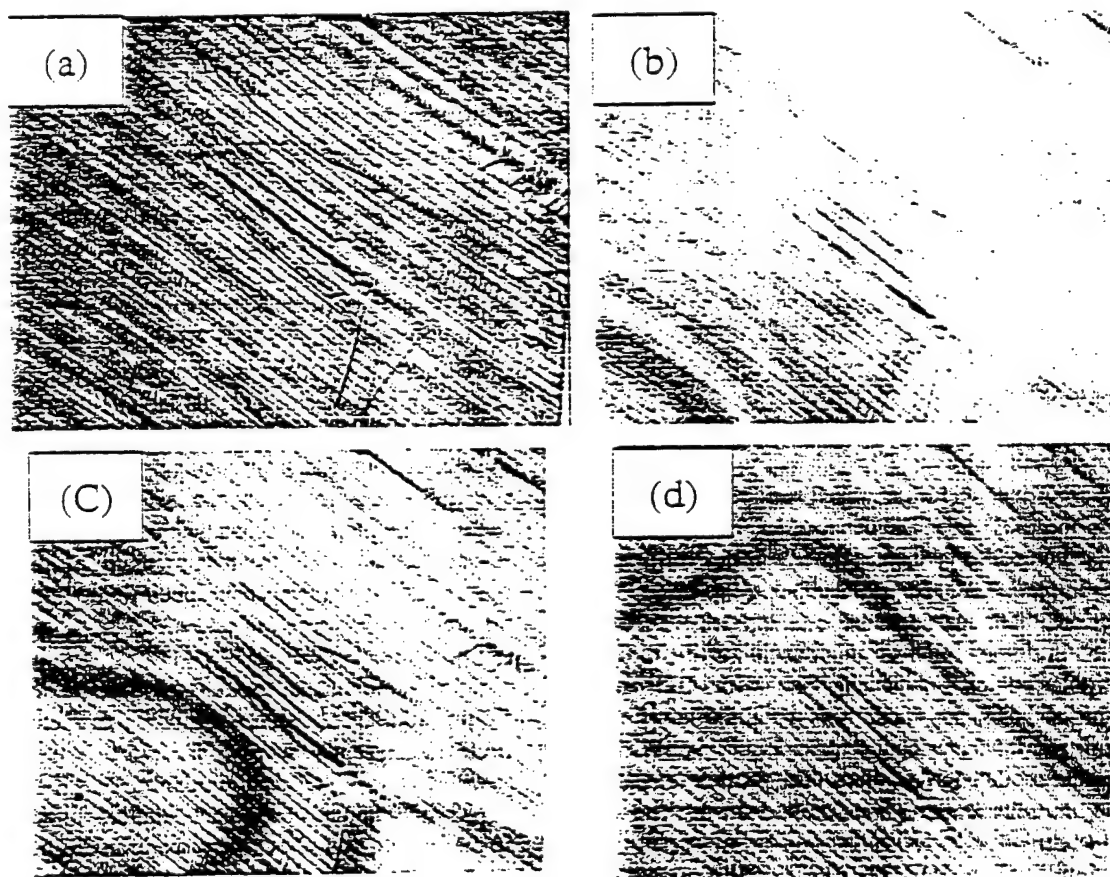


Fig. 2. Observation of ferroelectric phase transition: (a) room temperature, (b) the beginning of the phase transition,  $1163^\circ\text{C}$ , (c) middle stage of phase transition, (d) final stage of phase transition.

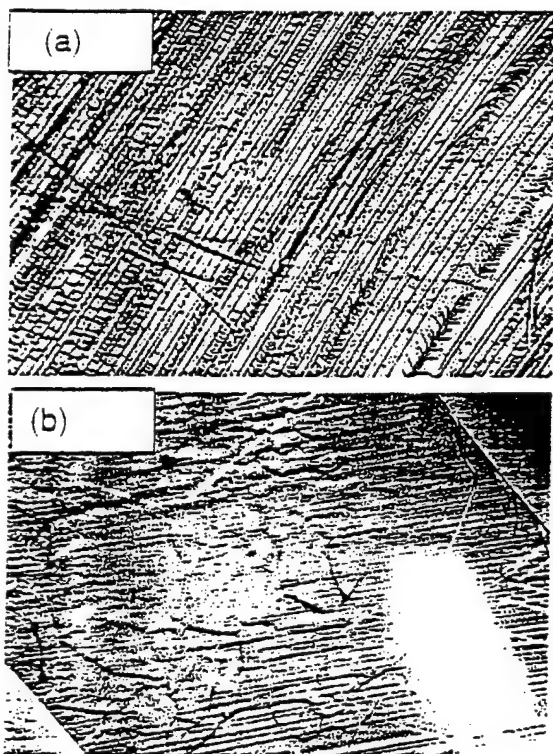


Fig. 3. Domain structure of the CIS film as observed at room temperature: (a) as-prepared. (b) after thermal treatment.

electric.  $180^\circ$  domains exist in the ferroelectric phase. In the plane perpendicular to the polarization axis, the domain walls depict a typical angle of  $120^\circ$  to each other. The observed domain pattern in annealed CIS film indicates the ferroelectric character of the CIS films.

#### 4. Conclusions

Direct optical observation suggests the CIS films preserve the ferroelectric character and goes through a phase transition to paraelectric at  $1163^\circ\text{C}$ . During the ion bombardment there are microdomains occurring in the vicinity of the surface layer that are revealed by etching during the process of separation of the film from the bulk, but the majority of the sample preserves the single domain state of the original crystal.

#### Acknowledgements

This work is supported by the DARPA FAME Program under the contract No. DABT63-98-1-002 for Penn State and N00173-98-1-G014 for Columbia University.

#### References

- [1] J.F. Scott, *Ferroelectric Rev.* 1 (1) (1998) 111.
- [2] R.C. Richard Wu, R.W. Vest, in: B.V. Haremath (Ed.), *Ceramic Transactions*, Vol. 11, American Ceramic Society, 1989, p. 319.
- [3] M. Levy, R.M. Osgood Jr. et al., *Appl. Phys. Lett.* 73 (1998) 2293.
- [4] K. Nashimoto, H. Moriyama, E. Osakabe, *Jpn. J. Appl. Phys.* Part 1 35 (1996) 4936.
- [5] S. Ono, S. Hirano, *J. Am. Ceram. Soc.* 80 (1997) 2869.
- [6] F. Jona, G. Shirane, *Ferroelectric Crystals*, Chap. 1, Dover Publications, 1993.
- [7] A.M. Prokhorov, Yu S. Kuz'minov, in: *Physics and Chemistry of Crystalline Lithium Niobate*, Chap. 1, English edn., IOP Publishing, Bristol, 1990.

# **MODELING and CHARACTERIZATION**

***Electrostriction***

# **APPENDIX 86**

# Converse electrostriction in polymers and composites

Sylvie Eury, Rattikorn Yimnirun, V. Sundar, Paul J. Moses, Sei-Joo Jang, Robert E. Newnham\*

251-A Materials Research Laboratory, Pennsylvania State University, University Park, PA 16802, USA

## Abstract

The evaluation of electrostrictive properties of low permittivity dielectrics requires extremely sensitive instrumentation. In the present work, a modified compressometer capable of resolving fractional changes in capacitance of the order of  $10^{-6}$  is used. In the compressometric method, a high sensitivity capacitance bridge, GenRad 1615, is coupled with two lock-in amplifiers to detect attofarad ( $10^{-18}$ F) level capacitance changes caused by in-phase cyclic uniaxial stresses on the samples. In studying low-permittivity polymers, we have obtained extensive electrostriction data, which along with widely accepted data on ferroelectric materials and soft polymers, verify the linear relationship between electrostriction coefficient ( $Q$ ) and the ratio of elastic compliance and dielectric permittivity ( $s/\epsilon_0\epsilon_r$ ). This leads to an effective way to predict the electrostriction coefficient in dielectric materials. © 1999 Elsevier Science S.A. All rights reserved.

**Keywords:** Electrostriction; Polymers; Composites

## 1. Introduction

Electrostriction is the fundamental mechanism of electromechanical coupling in all insulator materials. The electric field induced strains range from small values in low permittivity dielectrics to very large values in ferroelectrics. From a practical point of view, electrostrictive stresses can either be seen as a benefit for electromechanical devices, when high strain materials are required, or as a drawback in microelectronics and high voltage devices where the mechanical stresses can lead to breakdown in insulator materials [1]. In ferroelectric ceramics and elastomers, the electrostrictive properties have been extensively studied, but there is very little reliable experimental data for other low-permittivity dielectrics. This study was undertaken to provide reliable data for theoretical studies of this fundamental electromechanical phenomenon.

Electrostriction is a fourth rank tensor property relating mechanical strain  $x$  to an applied electric field  $E$  or to polarization  $P$ . The electromechanical interactions can be expressed in a power series to the second order as [2,3]:

$$x_{ij} = s_{ijkl}^E X_{kl} + d_{mij} E_m + M_{ijmn} E_m E_n, \quad (1)$$

$$x_{ij} = s_{ijkl}^P X_{kl} + g_{mij} P_m + Q_{ijmn} P_m P_n. \quad (2)$$

In these expressions,  $s_{ijkl}$  is the elastic compliance tensor under appropriate boundary conditions,  $X_{kl}$  the elastic stress component and  $g_{mij}$  and  $d_{mij}$  the piezoelectric tensors. From

these equations three electrostriction effects can be derived and expressed as

$$M_{ijmn} = \frac{1}{2} \left( \frac{d^2 x_{ij}}{dE_m dE_n} \right)_{T,X}, \quad (3)$$

$$Q_{ijmn} = \frac{1}{2} \left( \frac{d^2 x_{ij}}{dP_m dP_n} \right)_{T,X}, \quad (4)$$

for the 'direct' effect,

$$M_{ijmn} = \frac{1}{2} \left( \frac{d\eta_{mn}}{dX_{ij}} \right)_{T,E}, \quad (5)$$

$$Q_{ijmn} = -\frac{1}{2} \left( \frac{d\chi_{mn}}{dX_{ij}} \right)_{T,P}, \quad (6)$$

for the 'first converse' effect, obtained by introducing the dielectric susceptibility  $\chi_{ij}$  and its inverse the dielectric stiffness  $\eta_{ij}$  in the defining equations. The 'second converse' effect is the polarization dependence of the piezoelectric voltage coefficients.

The direct and first converse electrostriction effects offer two independent and equivalent techniques for measuring the electrostriction coefficients [4]. This allows the coefficients to be double-checked for accuracy [1,3].

## 2. Electrostriction measurement

In previous studies, several different techniques have been used to determine electrostriction coefficients. Some used

\*Corresponding author. Tel.: +1-814-865-1612; fax: +1-814-865-7593.

the direct effect by measuring the strain developed as a function of an applied field using interferometric or strain gauge methods [4–7]. Others measured the converse effect with a capacitance dilatometer or compressometer [4,8,9]. These latter two techniques require highly accurate dielectric measurements of the samples tested.

In this work the change in permittivity was measured as a function of stress using a dynamic compressometer, which is mechanically, electrically, and thermally stable, and well isolated from electrical and mechanical noise. The system was designed to apply a homogeneous pressure on the sample surface with completely uniaxial loading. To prevent shear deformations arising from elastic mismatch between the metal ram and the polymer sample, the specimen was held between Plexiglas ram extenders. To avoid barreling of the sample, thin mylar films were placed between the sample and the plexiglas extenders were used to take up any surface irregularities.

The dynamic compressometer (Fig. 1) was obtained from the original compressometer design [1] by adding a motorized stressing system. This allowed us to apply a periodic stress that was uniaxially transferred to the sample through extension rams. To optimize the measurement conditions, the mechanical frequency was set at 0.4 Hz. Then by using an appropriate spring with the stepping motor, a heavy load of 9.96 kg on the sample was used to achieve a substantial change in capacitance. The capacitance of the sample is first measured to a resolution of 0.0001 pF on a GenRad 1615 capacitance bridge at 1 kHz. A Stanford SR830 DSP Lock-In Amplifier is used to read the bridge balancing null. On applying a cyclic load, the first lock-in amplifier output voltage gives a signal proportional to the capacitance change  $\Delta C$  (Fig. 2). The output from this amplifier is then used as input ( $V_{pp}/2\sqrt{2}$ ) for a second Stanford SR830 DSP Lock-In Amplifier. This second lock-in amplifier is added to the system to couple the motion of the stepping motor and the system (Fig. 1). It is set up at the same frequency as the applied cyclic stress ( $f_{\text{mechanical}}=0.4$  Hz). The output voltage of the second lock-in gives then a precise fractional change in capacitance of the sample. The sensitivity of the Lock-in

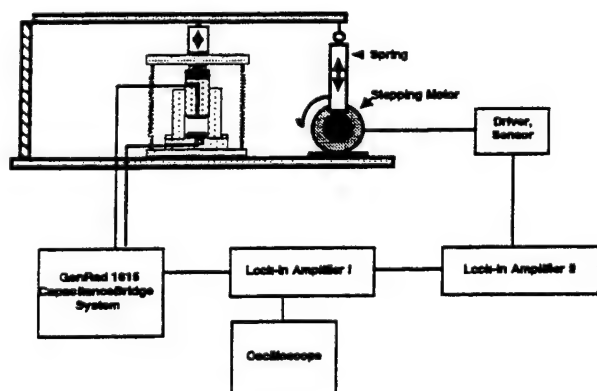


Fig. 1. Schematic drawing of the dynamic compressometer.

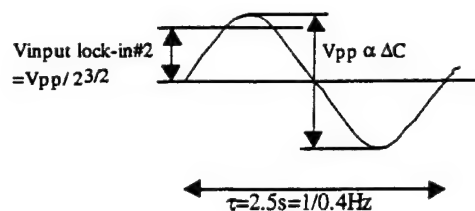


Fig. 2. Signal at the output of Lock-In no. 1.

no. 2 being 500 mV.

$$V_{\text{output lock-in no. 2}} = \frac{10 \text{ V}}{500 \text{ mV}} V_{\text{input lock-in no. 2}}, \quad (7)$$

$$V_{\text{output lock-in no. 2}} = 20 \frac{V_{pp}}{2\sqrt{2}}, \quad (8)$$

$$V_{\text{output lock-in no. 2}} = \frac{10}{\sqrt{2}} V_{pp} \sim \Delta C, \quad (V_{pp} \sim \Delta C). \quad (9)$$

The voltages  $V_{pp}$  and  $V_{\text{aver}}$  corresponding to the output of the first and second lock-in, respectively, were read on an oscilloscope. Both thermal and mechanical noises were electronically rejected from the measurements by using two lock-in amplifiers.

### 3. Experimental procedures

#### 3.1. Compressometric equations

The equation for the capacitance of a parallel plate insulator,  $C = \epsilon_0 \epsilon_r A/d$ , may be separated and differentiated with respect to the applied stress to give [1]

$$\frac{\delta \ln \epsilon_r}{\delta X} = \left[ \frac{\Delta C/C}{\Delta X} - \frac{\delta \ln(A/d)}{\delta X} \right] = B_i(\text{measured}) - S_i, \quad (10)$$

where  $S_i$  are linear combinations of elastic compliances, and  $B_i$  pressure dependencies of the capacitance for various cuts. Then  $Q$  and  $M$  are obtained from

$$Q = \frac{\epsilon_r}{2\epsilon_0(\epsilon_r - 1)^2} [B_i - S_i], \quad (11)$$

$$M = \frac{\epsilon_0 \epsilon_r}{2} [B_i - S_i]. \quad (12)$$

Most of the polymers studied were isotropic. So  $S_i$  may be expressed simply as a function of Young's modulus  $E$  and the shear modulus  $G$  or Poisson's ratio  $\nu$

$$S_i = \frac{1}{E} - \frac{1}{G} = -\frac{1+2\nu}{E} \leq 0. \quad (13)$$

From our measurements  $B$ , the fractional change in dielectric constant with compressive stress was found negative. In general  $|B_i| \geq |S_i|$ , as a result most of the electrostriction coefficients  $M_{33}$  and  $Q_{33}$  found were negative.

#### 3.2. Sample preparation

We studied several types of polymers: a polystyrene, some classical polyolefins (high-density polyethylene and



polypropylene), polyesters (Polyethylene Terephthalate and PolyButylene Terephthalate), polyamides (nylon 6.6 and nylon 6.12), and polyacetal resins. HDPE, PP and PS were purchased from Goodfellow (Berwyn, PA), and DuPont (Wilmington, DE) supplied the others. Measurements were carried out on plates 1–3 mm thick. The samples were cut into disk shape with plane parallel faces and a typical diameter of 24 mm. Gold electrodes were sputtered on the samples and a guard ring was scribed to avoid edge effects and fringing field errors.

#### 4. Experimental results

In a dynamic compressometer experiment, two frequencies are involved, first the mechanical frequency corresponding to the rotation speed of the motor, then the electrical frequency at which the capacitances were measured. The compressometer measurements were done under quasi-static conditions, which means that we were close to an equilibrium state and no time dependence should be involved. However by increasing the mechanical frequency, we expect a change in the electrostriction coefficients, especially near the glass transition where mechanical or dielectric relaxations takes place.

All the measurements of the  $B$  factor were performed at room temperature, electrical frequency 1 kHz, and mechanical frequency 0.4 Hz. Since the mechanical frequency is very low, we used the value of Young's modulus measured by ASTM D 638 to calculate the  $Q$  and  $M$  coefficients. In general these values and the Poisson's ratio  $\nu$  were given by the suppliers of the materials. However, we had to estimate Poisson's ratios for HDPE, PBT and Nylon 6,12 from sound wave velocities. Two additive molar elastic wave functions Rao-function  $U_R$  and Hartmann-function  $U_H$  are introduced. They are 'independent of temperature or polymeric phase state and can be calculated from additive group contributions' [10]. Thus from Eq. (14), and the tables of  $U_R$  and  $U_H$  given in Krevelen's book [10], the Poisson's ratio  $\nu$  can be predicted.

$$\nu = \frac{1 - 2/3(U_H/U_R)^6}{2(1 + 1/3(U_H/U_R)^6)} \quad (14)$$

Table 1 listed the hydrostatic electrostriction coefficient  $Q_h$  of the polymers studied in this work and other common dielectric materials for comparison. For isotropic materials  $Q_h$  may be estimated from  $Q$  and  $\nu$ , the Poisson's ratio, using the relation

$$Q_h = Q_{33}(1 - 2\nu). \quad (15)$$

Ceramics, glasses and ferroelectric materials have very low  $Q_h$  coefficients, while polymers' values range from 0.8 up to 230  $\text{m}^4/\text{C}^2$  for very soft polymers like polyurethane.

#### 5. Prediction of electrostriction coefficients [4]

Under the action of an applied electric field, the cations and anions in a crystal structure are displaced in opposite directions by an amount  $\Delta r$ . This displacement is thought to be responsible for most of the electric polarization, the dielectric permittivity, and the electrostrictive strain. We may express the relation between these as [4]

$$Q = \frac{x}{P^2} \sim \frac{\Delta r}{(\Delta r)^2} = \frac{1}{\Delta r} \sim \frac{1}{\epsilon_0 \epsilon_r}. \quad (16)$$

Large strains in compliant solids such as polymers can introduce large changes in the dielectric stiffness and in anharmonic potentials. Electrostrictive strain  $x$  is displacive and acts against the elastic forces in a material. Introducing the elastic compliance  $s$  into the  $Q$  versus  $1/\epsilon_0 \epsilon_r$  relationship can better express the correlation between these properties. Through the first converse effect, electrostriction is proportional to the change of dielectric stiffness  $\eta$  with stress  $X$ , which may be expressed as

$$Q \sim \frac{\Delta \eta}{X} \sim \frac{x}{(x/s)} \sim s. \quad (17)$$

Empirically,  $\log(Q_h)$  is found to vary linearly with  $\log(s/\epsilon_0 \epsilon_r)$  (Fig. 3). This combination of the compliance and the dielectric properties of materials may be used to predict the magnitude of electrostriction in insulators.

#### 6. Effect of fillers on mechanical and dielectric properties of composites

Polymers are very complex materials. In addition to the temperature and frequency dependence of the dielectric and mechanical properties, different processing methods can produce various types of polymers, with different characteristics and probably different electrostriction coefficients for the same chemical repeating units. The number of polymer applications is continually increasing in volume

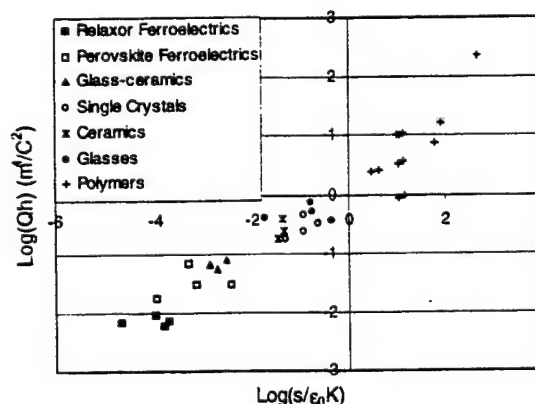


Fig. 3. Evolution of  $\text{Log}(Q_h)$  with  $\text{Log}(s/\epsilon_0 K)$ .

Table 1

List of dielectric constants, elastic constants, and electrostriction coefficients of common dielectrics

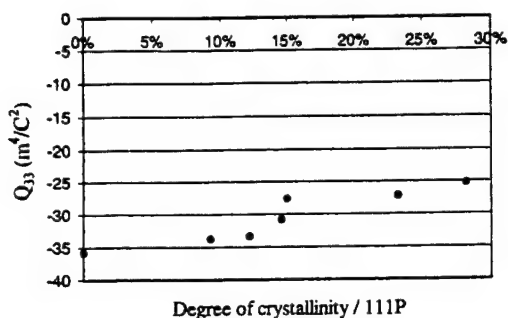
Materials	$K$	$S(\times 10^{-12})$ (m <sup>2</sup> /N)	$S/\epsilon_0\epsilon_r(\times 10^{-4})$ (m/FN)	$ Q_{33} $ (m <sup>4</sup> /C <sup>2</sup> )	References
<i>Relaxor Ferroelectrics</i>					[11–13]
PLZT (11/65/35)	5900	9.50	1.82	0.007	
BaTi <sub>0.38</sub> Sn <sub>1-0.38</sub> O <sub>3</sub>	10 300	8.90	1.01	0.0099	
BaSr <sub>0.35</sub> Ti <sub>1-0.35</sub> O <sub>3</sub>	25 000	4.55	0.21	0.0069	
La/PMN-PT (1/93/97)	13 000	16.42	1.43	0.006	
<i>Perovskite Ferroelectrics</i>					[13]
SrTiO <sub>3</sub>	450	1.82	4.57	0.07	
PbTiO <sub>3</sub>	270	7.81	32.6	0.03	
BaTiO <sub>3</sub>	1070	6.02	6.36	0.03	
Pb(Ti <sub>1-x</sub> Zr <sub>x</sub> )O <sub>3</sub>	1700	1.52	1.01	0.018	
<i>Glass-Ceramics</i>					[11]
Corning 888VE	300	7.25	27.31	0.079	
Corning 888YT	370	5.85	17.87	0.055	
Corning 888ZF	440	4.93	12.66	0.064	
<i>Single crystal</i>					[3,14]
CaF <sub>2</sub>	6.8	6.92	1150	0.47	
BaF <sub>2</sub>	7.4	15.3	2342	0.33	
KMnF <sub>3</sub>	9.8	9.72	1121	0.24	
MgO	9.8	4.03	465	0.18	
<i>Ceramics</i>					[4]
Al <sub>2</sub> O <sub>3</sub>	9.9	2.90	312	0.18	
AlN	8.3	3.03	360	0.40	
Si <sub>3</sub> N <sub>4</sub>	7.9	3.13	406	0.25	
<i>Glasses</i>					[3,4,15]
Na-Aluminosilicate	10.2	15.3	1696	0.519	
Fused-SiO <sub>2</sub>	3.8	14.0	4163	0.37	
Na <sub>2</sub> O.3SiO <sub>2</sub>	11.3	16.3	1629	0.765	
Spodumene Glass	7.9	1.18	169	0.43	
<i>Polymers</i>					[4,16,17]
PVDF	16	420	29 660	2.4	This work
VDF/TrFE	11	400	41 090	2.5	
PVC	3.4	333	110 700	10.1	
Polystyrene	2.6	312	133 500	10.4	
Polypropylene	2.3	1562	765 296	16.0	
HDPE	2.4	1250	588 267	7.4	
PET	3.6	333	104 624	3.1	
PBT	3.2	370	129 166	3.7	
Acetal resin (Delrin 500P)	3.5	308	98 771	10.0	
Nylon 6.6	3.9	353	102 905	0.8	
Nylon 6.12	4.0	493	138 120	1.0	
Polyurethane	6.5	25 000	4 346 000	230	

and in new fields. To respond to these demands, polymers with special properties are engineered, usually by incorporating additives like glass reinforcement or by blending some polymers together.

### 6.1. Crystallinity influence

Fig. 4 shows the decrease of  $Q_{33}$  amplitudes with increasing degree of crystallinity in polyacetal resins. The relative crystallinities of the resins to Delrin 111P (DuPont trade names for polyacetal homopolymer) were obtained by DSC.

Indeed by enhancing the crystallization, we enhance the tensile modulus slightly. In this way we decrease the micro regions where the polymer is amorphous. Therefore because more of the polymer chains are trapped in a crystal network, only a few polymer chains are able to move and mechanically deform the sample under an electric field. In our case, by applying a stress to the sample, fewer macromolecular chains are free to move to order themselves and increase the polarization. This explains the low changes in capacitance with pressure observed and then the low changes in dielectric constant with pressure.

Fig. 4.  $Q$  versus the degree of crystallinity.

### 6.2. Glass reinforcement influence

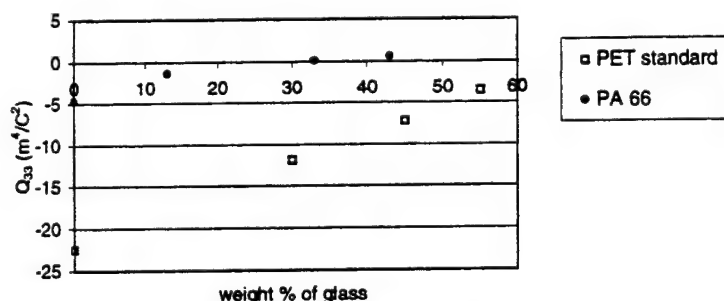
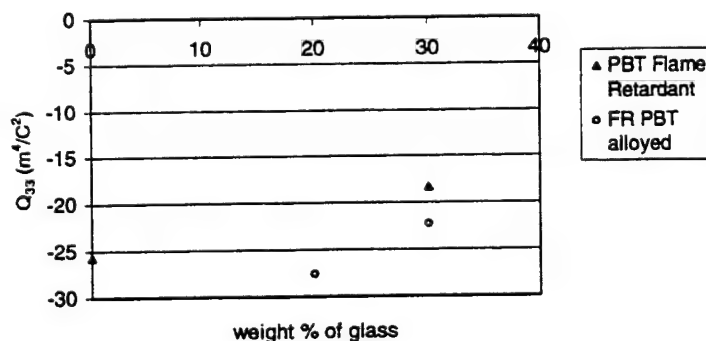
In the following discussion, the influence of glass reinforcement is described for nylon 66 and PET. In both cases, it is observed that the amplitudes of the  $M_{33}$  and  $Q_{33}$  coefficients decrease with the percentage of glass reinforcement in the material (Fig. 5).

Under an electric field the dipoles in the polymers align, and if the motion of the molecule is not impeded, the material will deform. In composites with high glass reinforcement, the molecules are partially trapped in the glass particle network, reducing their freedom degree of motion. Therefore lower electrostriction coefficients are found with increasing glass percentage. If we consider how the pre-

sence of glass affects the dielectric and mechanical properties, we observe that the dielectric constant  $K$  increases. However, the main contribution in the decrease of the electrostriction coefficients is due to the large increase in the Young's modulus of the material, making it stiffer. The increase in  $K$  simply influences the amplitude of the decrease. In this case, it is more important how the material deforms rather than how it polarizes that influences the final result.

### 6.3. Blend of polymers

In the DuPont samples, PBT is blended with an unspecified polymer to improve the dimensional properties. The alloyed PBT have lower  $E$  and  $K$  values. At 30 wt.% glass, they are respectively  $-33.3\%$  and  $-7.2\%$  lower than the Flame Retardant PBT values, making the alloy more compliant and less polarizable. For this same percentage of glass reinforcement, the alloy exhibits higher electrostrictive amplitudes than Flame Retardant Glass Reinforced PBT (Fig. 6). Therefore even if fewer dipoles are susceptible to alignment with an applied electric field, their motions in the alloyed polymer will be less hindered. The polymer alloyed to PBT was probably of a similar chemical structure to assure good mixing with more alkyl group in the backbone to increase the flexibility of the chain and decrease the density of polarizable groups.

Fig. 5.  $Q_{33}$  versus weight % of glass for PET and nylon 6,6 resins.Fig. 6.  $Q_{33}$  versus weight % of glass for PBT and alloyed PBT Resins.

## 7. Conclusions

In this study, an extremely sensitive instrument, a dynamic compressometer, was described. Electrostriction coefficients of various polymers were measured. We observed that the influence of crystallinity, glass reinforcement, and blending were affecting the electrostriction behavior because it is mainly governed by the elastic properties in low-permittivity polymers. The results confirmed the linear relationship between the electrostriction coefficient ( $Q_h$ ) and the ratio of elastic compliance and dielectric permittivity ( $s/\epsilon_0\epsilon_r$ ). Completing the data on low-permittivity materials leads us to an effective way to predict the electrostriction coefficient in dielectric materials.

## Acknowledgements

We take pleasure in dedicating this paper to Prof. Shigeyuki Somiya. For many years he has been a pioneering “bridge builder” between Japanese and American ceramists and materials scientists. His many friends here at Penn State are proud to pay homage to Prof. Somiya, a great scientist, inspiring teacher, and true friend.

The authors thank Dr. Kosinski, DuPont Inc., for providing us with most of our samples. This work is supported by the National Science Foundation through contract DMR-9634101.

## References

- [1] V. Sundar, R.E. Newnham, *Mater. Res. Bull.* 31(5) (1996) 545.
- [2] V. Sundar, R.E. Newnham, *J. Mater. Sci. Lett.* 13 (1994) 799.
- [3] V. Sundar, J.-F. Li, D. Viehland, R.E. Newnham, *Mater. Res. Bull.* 31(5) (1996) 555.
- [4] R.E. Newnham, V. Sundar, R. Yimnirun, J. Su, Q.M. Zhang, *J. Phys. Chem. B* 101(48) (1997) 10141.
- [5] G. Kloos, *Polym. Eng. Sci.* 37(3) (1997) 640.
- [6] M. Zhenyi, J.I. Scheinbeim, J.W. Lee, B.A. Newman, *J. Polym. Sci., Part B* 32 (1994) 2721.
- [7] J.-F. Li, P. Moses, D. Viehland, *Rev. Sci. Instrum.* 66(1) (1995) 215.
- [8] K. Nakamura, Y. Wada, *J. Polym. Sci., Part A-2* 9 (1971) 161.
- [9] K. Rittenmyer, Ph.D. Thesis, Pennsylvania State University, University Park, PA, 1984.
- [10] D.W. Van Krevelen, *Properties of Polymers*, 3rd ed., Elsevier, Amsterdam, 1990.
- [11] V. Sundar, K. WaGachigi, D. McCauley, K.A. Markowski, R.E. Newnham, *Proceedings of the ISAF*, 1994.
- [12] Landolt-Bornstein, *Numerical Data on Functional Relations in Science and Technology; New Series Group III*, vol. 24, Springer, New York, 1990.
- [13] K. Uchino, L.E. Cross, *Jpn. J. Appl. Phys.* 19 (1980) L171.
- [14] G. Simmons, H. Wang, *Single-Crystal Elastic Constants and Calculated Aggregate Properties. A Handbook*, MIT Press, Cambridge, MA, 1971.
- [15] Y. Sun, W.W. Cao, L.E. Cross, *Mater. Lett.* 4 (1986) 329.
- [16] T. Furukawa, N. Seo, *Jpn. J. Appl. Phys.* 29 (1990) 675.
- [17] J. Brandrup, E.H. Immergut, *Polymer Handbook*, Interscience Publishers, New York, 1966.

# **APPENDIX 87**

# Electrostriction Measurements on Low Permittivity Dielectric Materials

Rattikorn Yimmirun,\* Sylvie M.-L. Eury, V. Sundar, Paul J. Moses, Sei-Joo Jang and Robert E. Newnham

Materials Research Laboratory, The Pennsylvania State University, University Park, PA 16802-4801, USA

## Abstract

To measure the electrostrictive effects in low permittivity materials, extremely sensitive instrumentation is required. A modified compressometer for resolving fractional changes in capacitance on the order of  $10^{-6}$  is used in this work, along with a modified single beam interferometer capable of sub-angstrom resolution in displacement. For the compressometric method, a high sensitivity capacitance bridge, GenRad 1615, is coupled with two lock-in amplifiers to detect attofarad ( $10^{-18}$  F) level capacitance changes caused by in-phase cyclic uniaxial stresses on samples. The interferometer is a Michelson–Morley type instrument modified to detect changes in interference fringe intensity for very small changes in path length. The measurements confirmed by both techniques are used to establish a set of reliable and accurate data of electrostriction coefficients for low permittivity materials. Using these recent data, along with widely accepted data on ferroelectric materials and soft polymers, the linear relationship between electrostriction coefficient ( $Q$ ) and the ratio of elastic compliance over dielectric permittivity ( $s/\epsilon_0\epsilon_r$ ) is obtained. This leads to an effective way to predict the electrostriction coefficient in dielectric materials. © 1999 Elsevier Science Limited. All rights reserved

**Keywords:** electrostriction, dielectric properties.

## 1 Introduction

Electrostriction is the fundamental mechanism of electromechanical coupling in all insulator materials. Its magnitudes can range from very minute in

low permittivity dielectrics to very large in ferroelectrics. Theoretical studies of this fundamental phenomenon are handicapped by the absence of reliable and accurate experimental data in simple low permittivity dielectrics. In practical applications, electrostrictive stresses can cause breakdown in insulator materials in microelectronics and high voltage devices.<sup>1</sup> Therefore, this study was undertaken with the primary goal of establishing reliable and accurate electrostriction coefficients for low permittivity dielectrics.

Electrostriction is defined as the quadratic coupling between strain ( $x$ ) and electric field ( $E$ ), or between strain and polarization ( $P$ ). This is a fourth-rank tensor expressed by the following relationships:<sup>2,3</sup>

$$x_{ij} = s_{ijkl}^E X_{kl} + M_{ijmn} E_m E_n \quad (1)$$

$$x_{ij} = s_{ijkl}^P X_{kl} + Q_{ijmn} P_m P_n \quad (2)$$

where  $s_{ijkl}$  is the elastic compliance tensor under appropriate boundary conditions and  $X_{kl}$  is the elastic stress component. From these, the ‘direct’ effect  $Q$  and  $M$  electrostriction coefficients are defined as:

$$M_{ijmn} = 1/2(d^2 x_{ij}/dE_m dE_n)_X \quad (3)$$

$$Q_{ijmn} = 1/2(d^2 x_{ij}/dP_m dP_n)_X \quad (4)$$

Alternatively, by application of Maxwell relations to the above equations, one can derive the ‘first converse’ effect  $Q$  and  $M$  coefficients in terms of the dielectric susceptibility ( $\chi_{ij}$ ) and its inverse, the dielectric stiffness tensor ( $\eta_{ij}$ ) as:

$$M_{ijmn} = 1/2(d\eta_{ij}/dX_{mn})_P \quad (5)$$

\*To whom correspondence should be addressed. Fax: +1-814-865-2326; e-mail: rxy8@psu.edu

$$Q_{ijmn} = -1/2(d\chi_{ij}/dX_{mn})_P \quad (6)$$

The 'second converse' effect is the polarization dependence of the piezoelectric voltage coefficient ( $g_{nij}$ ) and can be defined as:

$$Q_{ijmn} = \delta g_{nij}/\delta P_m \quad (7)$$

$$M_{ijmn} = \epsilon_0(\epsilon_{ij} - 1)^2 \delta g_{nij}/\delta P_m \quad (8)$$

The direct and converse electrostriction effects are of importance because they offer two independent and equivalent techniques for electrostriction measurements. Measurements confirmed by both the direct and converse methods would result in more reliable and accurate electrostriction coefficients in materials of interest, such as low permittivity dielectrics.<sup>1,3,4</sup>

## 2 Electrostriction Measurement Techniques

Various techniques can be used to determine electrostriction coefficients. Widely used experimental techniques include the strain gauge method, the capacitance dilatometer, and laser ultradilatometer based on Michelson interferometer. In this work, two independent experimental approaches were used to determine electrostriction coefficients: a modified Michelson–Morley interferometer, measuring the strains induced in materials in response to applied fields or induced polarizations using the direct effect, and a dynamic compressometer, measuring the change in permittivity under appropriate stress using converse effect.

### 2.1 The dynamic compressometer

In the converse method the change in permittivity was measured as a function of stress using a mechanically stable compressometer isolated from electrical and mechanical noises. The system was designed to apply a homogeneous pressure on the sample surface from a completely uniaxial loading. The sample was held between Plexiglas ram extenders. This prevented shear deformations arising from elastic mismatch between the metal ram and samples.

Significant modifications were made to the original compressometer design<sup>1</sup> involving a cyclic loading system and a revised measurement technique. The redesigned compressometer is shown in Fig. 1. A stepping motor and spring were used to apply cyclic stress, which was uniaxially transferred to the sample through extension rams. The capacitance of the sample was first measured to a resolution of

0.0001 pF on a GenRad 1615 capacitance bridge. A Stanford SR830 DSP Lock-In Amplifier was used to read the bridge balancing null. The output from this amplifier was then used as input for a second lock-in amplifier, which was electronically locked to the revolving frequency of the stepping motor using a reflecting sensor. During cyclic loading, the first lock-in amplifier produced an electrical signal proportional to capacitance change, then a precise fractional change in capacitance of the sample was calculated from the output of the second lock-in amplifier. Thermal and mechanical noises were electronically rejected from the measurements with use of both lock-in amplifiers.

These compressometric measurements were performed at 1 kHz, corresponding to the frequency of the first lock-in amplifier. To optimize the measurement conditions, a stepping motor frequency was appropriately set to provide a cyclic loading at 0.4 Hz, at which a second lock-in amplifier was also automatically set through a sensor. Throughout the experiment, a maximum load of 9.96 kg was used to achieve relatively high level of capacitance changes.

### 2.2 The interferometric ultradilatometer

A modified Michelson–Morley interferometer was constructed specifically for this study.<sup>5</sup> In the interferometric method, the sample under investigation was subjected to an AC field, and was interrogated with a polarized beam from a Helium–Neon laser. The path difference between the beam reflected from the sample surface and a reference beam produced interference, and resultant intensity variations were sensed by a photodiode. A schematic of the system is shown in Fig. 2. It is a compact system with very light and rigid optical components. The total optical path length in the system is small, which is of utmost importance in reducing mechanical noise. The difference in the lengths of the optical path traveled by the two interferometer arms was kept small by mounting the sample, laser, photodetector and the electrostrictive stack on the circumference of a Plexiglas ring ~0.5 m in diameter. This minimized laser coherence length problems, reduced thermal drift, and compensated for beam divergence problems. The system is mounted on a pneumatically supported table to reduce the effect of ambient vibrations. Temperature and electrical stability was achieved by fitting the sample with an aluminum lined foamboard lid. The laser used is a 2 mW polarized He–Ne laser (Uniphase,  $\lambda = 632.8$  nm). The reference mirror, that reflects the reference beam, is mounted on an electrostrictive actuator stack connected to a feedback loop. This loop stabilizes the system at a point where the path difference is  $\lambda/4$ , the ' $\pi/2$  point',

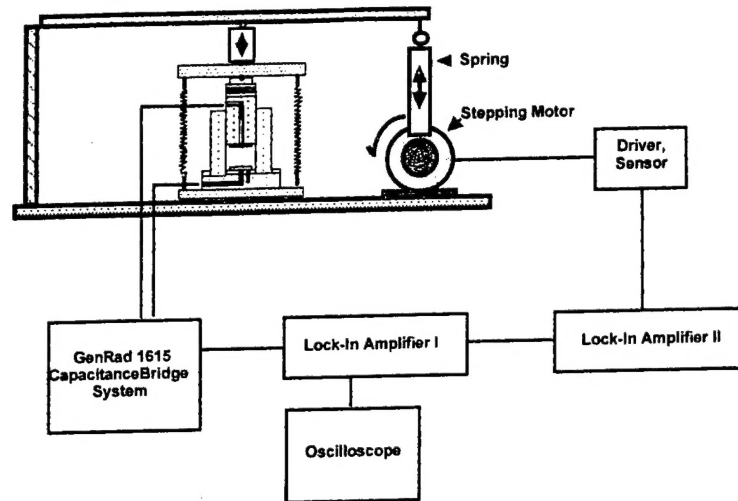


Fig. 1. Schematic of dynamic compressometer.

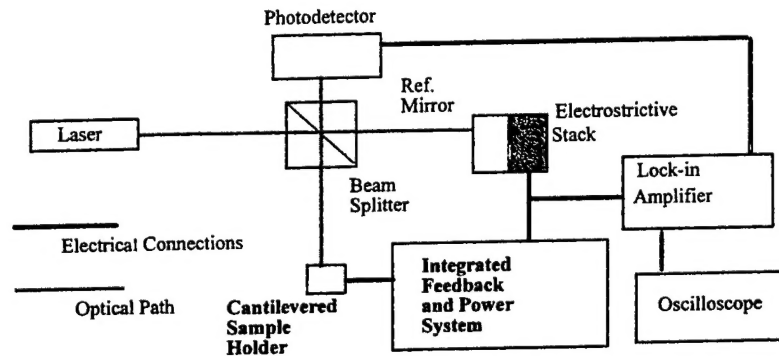


Fig. 2. Schematic of laser interferometer.

where light intensity change is maximized for a small change in the displacement  $\Delta d$  of the sample surface. When an AC field is applied to the sample, small sinusoidal displacements are obtained, giving interference intensity changes at the point of detection. This optical signal is converted to a voltage change by a biased photodiode (Motorola MRD500). The photocurrent is then converted to a voltage using a high frequency current to voltage converter with a gain of  $10^4 \text{ VA}^{-1}$ . This voltage is detected by a lock-in amplifier (Stanford Research Systems 830) as  $V_{out}$ , an rms value. The interference fringe shifts are observed using an oscilloscope (Hewlett-Packard 54600B).

$$\frac{\delta \ln \epsilon_r}{\delta X} = \left[ \frac{\Delta C/C}{\Delta X} - \frac{\delta \ln(A/D)}{\delta X} \right] = B_i(\text{measured}) - S_i \quad (9)$$

where  $S_i$  are linear combinations of elastic compliances, and  $B_i$  pressure dependencies of the capacitance for the given cut.  $M'$  and  $Q'$ , the coefficients for the given cut for the first converse effect, are given by:

$$Q = [\epsilon_r/2\epsilon_0(\epsilon_r - 1)^2][B_i - S_i] \quad (10)$$

$$M = (\epsilon_0\epsilon_r/2)[B_i - S_i] \quad (11)$$

### 3 Experimental Procedure

#### 3.1 Compressometry equations

The equation for the capacitance of a parallel plate insulator,  $C = \epsilon_0\epsilon_r A/d$ , may be separated and differentiated with respect to stress applied to give:<sup>1</sup>

#### 3.2 Interferometry equations

For monochromatic light with a wavelength  $\lambda$ , interfering with a reference beam, the interference intensity detected may be expressed as:<sup>3</sup>



$$I = I_p + I_r + 2I_p I_r \sin(4\pi \Delta d / \lambda) \quad (12)$$

where  $I_p$  and  $I_r$  are the intensities of the probe and reference beams, respectively. For small displacements  $\Delta d$  about the  $\pi/2$  point, one may rewrite the intensity detected as:

$$I = 1/2(I_{\max} + I_{\min}) + 1/2(I_{\max} - I_{\min})\sin(4\pi \Delta d / \lambda) \quad (13)$$

For such a small displacement, one may assume  $\sin x \sim x$ . This implies the interference intensity change is linearly proportional to the induced displacement. The displacement may now be expressed as:

$$\Delta d = \left( \frac{\lambda}{\sqrt{2\pi}} \right) \left( \frac{V_{\text{out}}}{V_{p-p}} \right) \quad (14)$$

This displacement is plotted as a function of applied voltage to calculate the electrostriction coefficients. For this direct method, the attractive coulombic forces between the free charges on the electrodes of the sample causes a change in sample dimension. This is called 'Maxwell strain'. For a parallel plate capacitor, the attractive stress is given as:<sup>3</sup>

$$X_m = -1/2(\epsilon_{11}\epsilon_0 E^2) \quad (15)$$

A corresponding value to the measured strain is added to correct for the Maxwell strain. Hence, the true direct effect electrostrictive coefficients are given by:

$$M'_{11} = M'_{11}(\text{measured}) + 1/2(s'_{11}\epsilon_0\epsilon_{11}) \quad (16)$$

### 3.3 Sample preparation

Single crystals of orientations,  $\langle 100 \rangle$ ,  $\langle 110 \rangle$ ,  $\langle 111 \rangle$ ; were used for cubic samples  $\text{CaF}_2$ ,  $\text{BaF}_2$ ,  $\text{SrF}_2$ , and  $\text{KMnF}_3$ . For  $\text{MgO}$ ,  $\text{BeO}$ , and  $\text{CaCO}_3$ , single crystals with  $\langle 100 \rangle$  orientation were obtained.

Preliminary compressometric studies were also carried out on ceramics, such as  $\text{ZrO}_2$ ,  $\text{Al}_2\text{O}_3$ ,  $\text{AlN}$ , and  $\text{Si}_3\text{N}_4$  and on polymers, such as polystyrene (PS) and polyethylene terephthalate (PET).

For the compressometer, the samples are thin discs with plane parallel faces. The sample dimensions are approximately 20 mm in diameter and 1 mm in thickness. On the other hand, 1 mm<sup>3</sup> cubes are used in the interferometer. Gold electrodes are sputtered on samples polished to optical finish.

## 4 Experimental Results

$Q$  coefficients for the samples from both techniques are given in Table 1. It may be seen in the tabulation that all results agree well. This helps us achieve our primary aim of establishing the reliable and accurate electrostriction coefficients, particularly in low permittivity dielectrics.

## 5 Prediction of Electrostriction Coefficients

Under the action of an applied electric field, the cations and anions in a crystal structure are displaced in opposite directions by an amount  $\Delta r$ . This displacement is responsible for the electric polarization, the dielectric permittivity, and the electrostrictive strain. We may express the relation between these as:

$$Q = x/P^2 \sim (\Delta r)/(\Delta r)^2 = 1/\Delta r \sim 1/\epsilon_0\epsilon_r \quad (17)$$

Large strains in compliant solids such as polymers can introduce large changes in the dielectric stiffness and in anharmonic potentials. Electrostrictive strain is displacive and acts against the elastic forces in a material. Introducing the elastic compliance  $s$  into the  $Q$  versus  $1/\epsilon_0\epsilon_r$  relationship can better express the correlation between these properties. Through the first converse effect, electrostriction is proportional to the change of dielectric stiffness  $\eta$  with stress  $X$ , which may be expressed as:

$$Q \sim (\Delta\eta)/(X) \sim x/(x/s) \sim s \quad (18)$$

Table 1. Results from direct and converse effects<sup>4</sup>

Material		Direct $Q \text{ m}^4/\text{C}^2$	Converse $Q \text{ m}^4/\text{C}^2$
$\text{BaF}_2$	$Q_{11}$	-0.33	-0.31
	$Q_{12}$	-0.29	-0.29
	$Q_{44}$	1.46	1.48
$\text{CaF}_2$	$Q_{11}$	-0.48	-0.49
	$Q_{12}$	-0.48	-0.48
	$Q_{44}$	-0.33	-0.33
$\text{SrF}_2$	$Q_{11}$	-0.33	-0.33
	$Q_{12}$	0.38	0.39
	$Q_{44}$	2.01	1.90
$\text{KMnF}_3$	$Q_{11}$	0.51	0.49
	$Q_{12}$	-0.09	-0.10
	$Q_{44}$	1.16	1.15
$\text{MgO}$	$Q_{11}$	0.33	0.34
$\text{BeO}$	$Q_{11}$	1.45	1.48
Calcite	$Q_{11}$	1.20	1.19
$\text{Al}_2\text{O}_3$	$Q_{33}$	-	-0.20
$\text{ZrO}_2$	$Q_{33}$	-	0.06
$\text{AlN}$	$Q_{33}$	-	-0.27
$\text{Si}_3\text{N}_4$	$Q_{33}$	-	-0.36
PS	$Q_{33}$	-	-35
PET	$Q_{33}$	-	-22

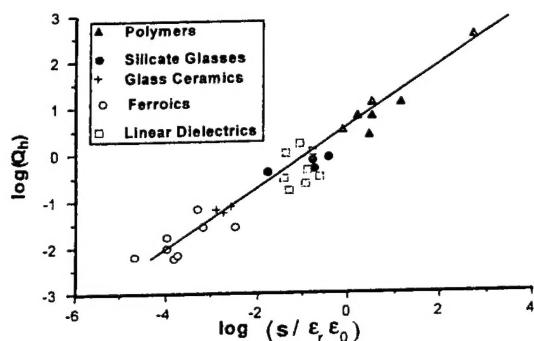


Fig. 3. Variation of  $\log Q_h(\text{m}^4/\text{C}^2)$  with  $\log (s/\epsilon_0 \epsilon_r)$ .

Empirically,  $\log(Q_h)$  is found to vary linearly with  $\log(s/\epsilon_0 \epsilon_r)$  (Fig. 3). This combination of the compliance and the dielectric properties of materials may be used to predict the magnitude of electrostriction in insulators.

## 6 Conclusions

In this present work, two extremely sensitive instrumentations, a modified single beam interferometer and a dynamic compressometer, were described. The measurements confirmed by both

techniques were used to establish a set of reliable and accurate data of electrostriction coefficients for low permittivity materials. Finally, the linear relationship between electrostriction coefficient ( $Q$ ) and the ratio of elastic compliance over dielectric permittivity ( $s/\epsilon_0 \epsilon_r$ ) was obtained. This leads to an effective way to predict the electrostriction coefficient in dielectric materials.

## Acknowledgements

This study is supported through National Science Foundation Grant DMR-9634101, Electrostriction in Ceramics and Glasses.

## References

1. Sundar, V. and Newnham, R. E., *Materials Research Bulletin*, 1996, **31**(5), 545.
2. Sundar, V. and Newnham, R. E., *Journal of Materials Science Letters*, 1994, **13**, 799.
3. Sundar, V., Li, J.-F., Viehland, D. and Newnham, R. E., *Materials Research Bulletin*, 1996, **31**(5), 555.
4. Newnham, R. E., Sundar, V., Yimnirun, R., Su, J. and Zhang, Q. M., *Journal of Physical Chemistry B*, 1997, **101**(48), 10141.
5. Li, J.-F., Moses, P. J. and Viehland, D., *Review of Scientific Instruments*, 1995, **66**(1), 215.